MODELLING OF COMBUSTION AND EMISSIONS OF A DIRECT INJECTION COMPRESSION IGNITION HEAVY-DUTY ENGINE FUELLED WITH CASHEW NUTSHELL LIQUID BIODIESEL

by

ROBERT KWADZO BISCOFF

submitted in accordance with the requirements
for the degree of

DOCTOR OF PHILOSOPHY

at the

UNIVERSITY OF SOUTH AFRICA

SUPERVISOR: PROF CHRISTOPHER C. ENWEREMADU

JUNE 2023

ABSTRACT

Several studies have shown that the efficient use of bioenergy can reduce greenhouse gas emissions and keep global temperatures below 2°C. Among biofuels, cashew nut shell liquid (CNSL) biodiesel from inedible feedstock is considered sustainable, environmentally friendly, and economically beneficial. However, knowledge gaps exist regarding how to improve in-cylinder combustion phenomena and reduce emissions with the use of CNSL biodiesel in diesel engines. This research aims to explore the potential of CNSL for the production of biodiesel and further determine the combined effects of combustion chamber geometry and injection parameters on the combustion and emission characteristics of CNSL biodiesel in a direct injection compression ignition diesel engine using CFD software, ANSYS FORTE. The RNG k- ε turbulence model was used to examine physical phenomena associated with kinetic energy changes. To reduce time and cost, a sector mesh at a 45° angle with periodic boundary conditions is used instead of the entire engine geometry. The substitute for diesel fuel was n-heptane, which was modelled and simulated in five different combustion chamber piston bowl designs with varying injection parameters. Simulation results were similar to the experimental data for in-cylinder pressure, temperature, heat release rates, and exhaust emissions of CO, UHC, NOx, and soot. ANSYS CHEMKIN-PRO was used to solve complex chemical and gas reaction models by implementing the properties of CNSL biodiesel-diesel blends using methyl palmitate and methyl oleate with the merger of n-heptane in ANSYS FORTE to conduct simulations. In turn, two optimized piston bowl designs were used to model and simulate the impact of CNSL biodiesel and diesel blends (B10, B20, B30, and B50) on combustion and emissions. Results show that diesel engines can utilise CNSL B10 and B20 without significant engine modifications. A CNSL biodiesel blend emits fewer CO and UHC compared to diesel, and further reductions occur as the blend percentage increases. With an increased proportion of CNSL biodiesel in the blends, the gross indicated specific fuel consumption (GISFC) increased significantly. A larger spray-included angle and advanced injection timing increased NOx emissions marginally but reduced soot emissions and GISFC.

Keywords: CNSL, Biodiesel, Heavy-duty DICI Diesel Engine, Combustion, Emissions, Piston bowl geometry, Modelling, Simulation, CFD, ANSYS FORTE.

DECLARATION

Name: **ROBERT KWADZO BISCOFF**

Student number: **61085782**

Degree: **Doctor of Philosophy in Science, Engineering Technology**

Exact wording of the title of the thesis as appearing on the electronic copy submitted for examination:

MODELLING OF COMBUSTION AND EMISSIONS OF A DIRECT INJECTION COMPRESSION IGNITON HEAVY- DUTY ENGINE FUELLED WITH CASHEW NUT SHELL LIQUID BIODIESEL

I, **ROBERT KWADZO BISCOFF** declare that the above thesis is my own work and that all the sources that I have used or quoted have been indicated and acknowledged by means of complete references.

I further declare that I submitted the thesis to originality checking software and that it falls within the accepted requirements for originality.

I further declare that I have not previously submitted this work, or part of it, for examination at Unisa for another qualification or at any other higher education institution.

_____ 12th June 2023

SIGNATURE DATE

PUBLICATION

This section presents articles that form part of and/or include the research presented in this thesis. A paper has been published, and others are in the process of being reviewed for publication, including:

Biscoff, R.K. and Enweremadu, C.C., 2023. Cashew nutshell liquid: A potential inedible source of biodiesel for heavy duty vehicles in sub-Saharan Africa. Energy Sources, Part A: Recovery, Utilization, and Environmental Effects, 45(1), pp.905-923.

Manuscripts under review for publication

i. The combined effect of spray-included angle and piston bowl geometry on combustion and emission characteristics of the DICI diesel engine: a numerical CFD approach
ii. Influence of injection parameters and piston bowl geometry on combustion and emission in a CNSL biodiesel fuelled DICI heavy-duty diesel engine.
iii. Numerical analysis of CNSL biodiesel blend combustion and emission in the DICI heavy-duty diesel engine**.**

DEDICATION

I dedicate this work to God Almighty and to my Lord and Saviour, Jesus Christ, who reigns forever. To my lovely wife, Rose Akubia Biscoff, children, and family who stood by me through difficult times. In addition, my mother, who was concerned and always asked, "When are you completing your studies?" but passed on before I finished. I give all glory to God, who sustained and protected us.

ACKNOWLEDGEMENTS

This work would not have been possible without the guidance, counsel, patience, and wisdom of my supervisor, Professor Christopher Chintua Enweremadu. I am grateful that he recognised my potential and offered me the opportunity to be part of the Renewable Energy Systems and Thermo-fluids Research Group in the Department of Mechanical Engineering at the University of South Africa (UNISA).

I express my gratitude to Prof. Rendani Wilson Maladzhi, Head of the Department of Mechanical Engineering, and Dr. Harry M. Ngwangwa, Head of Tuition and Learning. I thank them for showing interest in the progress of my Ph.D. work. Many thanks to the members of the Renewable Energy Systems and Thermo-fluids Research Group, the late Associate Professor Samson Nnaemeka Ugwu, Mr. Shumani Ramuhaheli, and Mr. Simon Yormesor, for their collaborative academic efforts. My sincere gratitude to the Qfinsoft Support Team, who, through the kind courtesy of UNISA, gave me preliminary training on the ANSYS Forte software for simulating internal combustion (IC) engines. I owe a huge debt of gratitude to my office members at UNISA Science Campus Florida in Phapha Building Room 1-020, in the person of: Dr. Patrick M. Mubiayi, Dr. Adefemi O. Adeodu, Mr. Tolulope Babawarun, Mr. Tshamano Nemirini, Ms. Lebogang Brenda Mathebela, and Ms. Makhosasana Msibi, for their academic and moral support at any time they are available. I extend my sincere thanks to Prof. Maxwell Akple, Dr. Charles Atombo, Dr. Udoka Ogugua, Mr. Wise Klomegah, Mr. James Adzie, and Mr. Samuel Kwame for their proofreading, statistical analysis, and formatting of this work. I acknowledge with sincere thanks to the Ghana Education Trust Fund (GETFund) for the financial support through sponsorship and Ho Technical University of Ghana, which granted me part-time study leave with pay.

A special shout-out and thanks to Mrs. Aderonke Enweremadu and the family for their support, which made my stay in South Africa peaceful and successful. Thanks to my brothers and sisters for the financial and moral support, and also to my lovely wife, Mrs. Rose Akosua Akubia, and my children, Gracious, Merciful, and Divine-Favour, who consistently prayed and encouraged me to finish this PhD research by the grace of God. There were several people who helped and supported me in writing this thesis, and I say thank you to them all. Thank you, Lord God Almighty, and thank you, Christ Jesus, for granting me success.

TABLE OF CONTENTS

LIST OF FIGURES

LIST OF TABLES

ABRREVIATIONS AND NOMENCLATURE

Abbreviations

UNFCCC	United Nations Framework Convention on Climate Change
IEA	International Energy Agency
SSA	Sub-Saharan Africa
FAO	Food and Agriculture Organization
FAOSTAT	Food and Agriculture Organization Statistical Data
ASTM	American Society for Testing and Materials
ISO	International Standard Organisation
EPA	Environmental Protecting Agency
SDG	Sustainable Development Goals
DCR	Directorate of Cashew Research
SDS	Sustainable Development Scenario
2DS	Two-Degrees Scenario
IRENA	International Renewable Energy Agency
CDM	Clean Development Mechanism
COP 21	21st Conference of Parties
LLNL	Lawrence Livermore National Laboratory
SOC	Soil Organic Carbon

Nomenclature of Internal Combustion Engines

ABDC	After bottom dead centre
ATDC	After top dead centre
B/S	Bore/stroke
BSFC	Brake specific fuel consumption
BTDC	Before top dead centre
BTE	Brake thermal efficiency
CAD	Crank angle degree
CADATDC	Crank angle degree after top dead centre
CFD	Computational fluid dynamics

CI	Compression ignition
CN	Cetane number
CR	compression ratio
CS	Constant speed
DI	Direct injection
DICI	Direct injection compression ignition
DNS	Direct numerical simulation
DRG	Direct relation graph
DRGEP	Direct relation graph aided sensitivity analysis
EGR	Exhaust gas recirculation
EOI	End of injection
EP	Error propagation
EVO	Exhaust valve opening
GHG	Greenhouse gas
GIP	Gross indicated power
GISFC	Gross indicated specific fuel consumption
HDV	Heavy duty vehicles
HRR	Heat release rate
HTHR	High temperature heat release
HTR	High temperature reaction
IC	Internal combustion
ICE	Internal combustion engine
ID	Ignition delay
IMEP	Indicated mean effective pressure

IP	Injection pressure
ISFC	Indicated specific fuel consumption
IVC	Inlet valve closing
IVO	Inlet valve opening
LES	Large eddy simulation
LTC	Low temperature combustion
LTHR	Low temperature heat release
LTR	Low temperature reaction
NA	Natural aspirated
NCNSL	Natural CNSL
ON	Octane number
PBD	Piston bowl design
RANS	Reynolds averaged navier – stokes
RES	Renewable energy sources
ROHR	Rate of heat release
SA	Sensitivity analysis
SI	Spark ignition
SIA	Spray Included Angle
SOI	Start of Ignition
TDC	Top dead centre
TKE	Turbulence Kinetic Energy

Chemical Symbols and Emissions Abbreviations

B10M10	10% cardanol 80% diesel +10%methanol
B20M10	20% cardanol +70% diesel +10%methanol
B30M10	30% cardanol 60% diesel +10%methanol
B5 – B30	Biodiesel + 95% to 70% diesel by volume liquid
$C_{14}H_{30}$	Tetradecane
$C_{17}H_{34}O_2$	Methyl palmitate
$C_{19}H_{32}O_2$	Methyl linolenate
$C_{19}H_{34}O_2$	Methyl linoleate
$C_{19}H_{36}O_2$	Methyl oleate
$C1_9H_{38}O_2$	Methyl stearate
C_2H_2	Acetylene
C_7H_{16}	Normal heptane, n-heptane (nc7h16)
CC-CNSL	Catalytically cracked cashew nut shell liquid
CNS	Cashew nut shell
CNSL	Cashew nut shell liquid
CNSLB	Cashew nut shell biodiesel
CNSLME	Cashew nut shell liquid methyl ester
CNSME	Cashew nut shell methyl ester;
CNSME80P20	CNSME + 20%Pentanol
CNSME90P10	CNSME +10% Pentanol
CO	Carbon monoxide
CO_2	Carbon dioxide
cSt	Centistokes
FAME	Fatty acid methyl ester
FFA	Free fatty acid
M	Molecular weight
MB	Methyl butanoate
MD	Methyl decanoate
MD9D	Methyl-9-decenoate
ME	Methyl ethanoate
NO	Nitrogen oxide
NO_2	Nitrogen dioxide

NOx	Oxides of nitrogen (NO + NO2)
O_2	Oxygen molecule
PM	Particulate matter
SO_2	Sulphur dioxide
TC-CNSL	Thermal cracked cashew nut shell liquid
TCNSL	Technical CNSL
UHC	Unburnt hydrocarbons

Greek Symbols

ϕ	Equivalence Ratio
ν	Stoichiometric Coefficient
ω	Production Rate
σ	Surface Tension
τ	Breakup Time, KH Spray Breakup Model
Ω	Frequency
Λ	Wavelength
ρ	Density
k	species index
K	total number of species
$\tilde{u}$	flow velocity vector

CHAPTER 1

Introduction

1.0. Background

The rapid growth in human population coupled with industrialization, commercialization and accompanying soaring standard of living has overstretched the fossil non-renewable petroleum resources of energy to maximum limit. The unpredictable petroleum prices, exhaustion of fossil fuel reserves and the adverse global environmental pollution is leading to the search for fuel alternatives. This increase in population, as well as the activities that accompanied it, resulted into urban drift, widespread automobile use, and industrial expansion, all of which resulted in a high-level need for energy in all fields of human endeavour. Globally, the awareness is being created among the populace and institutions about the detrimental effects of global warming caused by the indiscriminate burning of fossil fuels. The speedy industrial and urbanized commercial activities, as well as the subsequent pollution of the atmosphere, is creating extremely dangerous and unsafe haven on earth for this and future generations (Agyemang, Zhu and Tian, 2016; Knothe and Razon, 2017). The resultant effect of increased usage of energy, conventional fossil resources are under significant strain to supply homes, commercial entities, and industries. Developing and industrialized countries continue to use fossil fuels to meet their socioeconomic expansion, causing global warming by releasing greenhouse gases from transportation, manufacturing, and electric power generation. There is no end in sight to the continued use of this fossil fuel.

All the afore-mentioned problems have prompted some academics to search into other renewable resources for alternative fuels that could possibly emit less pollutants. Globally, automobile and other manufacturing industries are subjected to strict emission standards governed by environmental and climate change concerns. To avert this global warming phenomena in the short and long term, the search for alternative renewable and sustainable energy sources are very crucial. Inedible biofuel appears to be the most favourable fuel option because it is renewable, non-toxic, eco-friendly, biodegradable, and does not compete with food security. In many developing countries, there is widespread acceptance of inedible agricultural-base biodiesel as an alternative fuel, which arose from a need to improve rural household socioeconomic

conditions (Dinesha and Mohanan, 2015; Vedharaj et al., 2015; Datta and Mandal, 2016; Sahoo et al., 2017; Kumar, Dinesha, and Rosen, 2018).

An increase in urban population would lead to an increase in food production, resulting in a relative increase in agricultural and industrial waste. Renewable resources are becoming increasingly available due to biological waste as a result of these urban relocations, thus providing a source for future sources of energy feedstocks (Knothe and Razon, 2017; Hao et al., 2018). There should be a way to transform some of these agricultural industrial waste into cheap, viable, renewable, environmentally friendly, and sustainable energy sources, keeping in mind the Sustainable Development Goals (SDGs) "7" and "13" of the United Nations Organization (UNO), namely "to ensure access to affordable, reliable, sustainable, and modern energy for all" and "to take urgent action to combat climate change and its impacts" (United Nations, 2015). Biodiesel as an alternative fuel for compression ignition (CI) engines has received a lot of attention in recent years because it is a renewable and environmentally welcoming fuel. There is no sulphur in biodiesel, and just a minor quantity of aromatic hydrocarbons. Biodiesel has a high cetane number and roughly 10-11% built-in oxygen, which helps with combustion in CI engines (Anbarasu and Karthikeyan, 2016; Yang et al., 2017; Uyumaz, 2018).

1.1. Global energy demand and renewable outlook

Global energy consumption has increased significantly over the past 50 years as a result of the industrial revolution. As a result of global climate change, the energy system may undergo large-scale changes in the next several decades. Many of these changes, however, are uncertain in terms of magnitude and direction (Newell et al., 2020). The International Energy Agency (IEA) reports that since 2010, global demand and consumption have grown at a rate that is around twice as fast as usual due to a robust global socioeconomic environment and higher heating and cooling demands in some regions of the world (IEA, 2020). Even though renewable energy sources like solar and wind grew by double digits, demand for all types of fuels surged, headed by natural gas (IEA, Ukraine, 2020).

Due to widespread state and governmental policy backing, declining technology costs, and increased usage of renewable energy in electricity delivery, renewable energy

sources accounted for the vast majority of the overall rise. Additionally, the usage of renewable energy for heating and transportation saw growth (Raturi, 2019; Newell et al., 2020). The total amount of energy consumed globally, including oil and its products, natural gas, and coal, continues to rise modestly despite all of the concerns and calls for changing energy consumption patterns as well as significant efforts to replace fossil fuels with renewable energy sources (Tvaronaviien et al., 2020). In 2019, the usage of renewable energy for heating increased marginally, with bioenergy remaining the most popular option, followed by solar thermal and geothermal. Traditional solid biomass applications, which are inefficient and have poor human health and environmental consequences, still account for the majority of bioenergy use in heating. Some countries are putting in place national strategies and policies to increase the use of renewable energy in their energy mix. (Raturi, 2019; Tvaronaviien et al., 2020; Newell et al., 2020).

Over one-third of the savings from renewables came from China alone, with the European Union contributing around 70 Mt and the United States 35 Mt (Tvaronaviien et al., 2020). In addition to increased activity in the electrical sector, renewable energy usage in transportation climbed by about 8% in 2019 (ENERGY, I.W. and Iea, A., 2020). According to reports by Tvaronaviien et al., (2020), mills increased ethanol production at the expense of sugar due to low global sugar prices, which led to a 13 percent rise in ethanol output in Brazil, a major biofuel market. The use of biofuels in China increased in 2019 due to the country's strict policy toward domestic biofuel production (Raturi, 2019; Tvaronaviien et al., 2020).

1.2. World transportation energy outlook

When economies grow, commercial transportation expands as well, enhancing the mobility of goods. Global transportation demand is being driven by various advancements in light-duty passenger vehicles and commercial transportation. It is expected that commercial transportation would increase as economic activity rises, especially in developing countries. Due to increased goods movement, heavy-duty transport accounts for the majority of the increases, however rising aviation travel also contributes as personal spending power rises (Outlook and Dudley, 2019). In spite of considerable improvements in the automobile economy and engine efficiency, an

increase in car sales is likely to drive demand growth (Tvaronaviien et al., 2020). Increasing social and commercial activities, such as moving more people and goods by bus, rail, airplane, truck, and marine vessel, will increase global transportation energy demand (Anenberg et al., 2019).

In order for humankind to grow and improve its living standards, energy resources have always been and remain one of the most important and essential elements, particularly the petroleum fuels used in automobiles and the widespread use of electricity throughout the world (Tvaronaviien et al., 2020). Thus, relying on petroleum oil for transportation will have significant effects on energy security, the environment, and human health (Outlook and Dudley, 2019). As on-road cars become more fuel-efficient and electrified, carbon emissions in the transportation sector are rising, despite significant advancements in vehicle economy and electrification. The increasing reliance on fossil fuels should be mitigated urgently to reduce greenhouse gas emissions and hence climate change to meet the SDGs (Newell et al., 2020).

1.3. Global greenhouse gas emission and second-degree scenario

In light of the fact that the energy sector accounts for two-thirds of global greenhouse gas emissions, it must necessarily play a significant role in mitigation efforts (Kraan et al., 2019; Ogunkunle and Ahmed, 2021). Globally, fossil fuel combustion contributes two-thirds of greenhouse gas emissions and the majority of CO_2 emissions, so the energy sector must lead efforts to combat climate change. Emerging economies are increasingly using fossil energy, resulting in poor air quality and serious health consequences. Among the remaining third of GHG emissions, CO_2 emissions from industrial processes, agriculture, forestry, and other land use activities are mainly responsible. Non-CO_2 emissions from the energy sector (mainly methane) are also responsible (IEA, 2020b). A number of mitigation initiatives have been undertaken by the International Energy Agency (IEA) over the past several years, including the establishment of the Second Degrees scenario (2DS), which outlines a quick decarburization pathway in accordance with international targets (Giner, Palandri and Debnath, 2019). There are all indications that bioenergy will play an essential part in climate change mitigation, according to the International Energy Agency's (IEA) Energy Technology Perspectives (IEA, 2020b). The two-degree scenario (2DS) is

consistent with a 50% chance of limiting future global average temperature to 2°C by 2100. According to studies conducted by IEA the two-degree scenario (2DS) with the modern bioenergy is an essential component of the future low carbon global energy system if global climate change commitments are to be met (IEA, 2020b). Emissions from the electricity sector have decreased as a result of the increased use of renewable energy sources (mostly wind and solar PV), the transfer from coal to natural gas, and increased nuclear power output (IEA, 2020b). In 2019, the growth of renewables was the most important factor in limiting global energy-related CO_2 emissions. Increased renewable energy deployment in almost all locations reduced projected emissions growth by over 330 Mt (IEA, 2019c). As indicated in Figure 1.1 the largest category of renewable energy remains bioenergy, although solar PV and wind power have grown at the fastest rate.

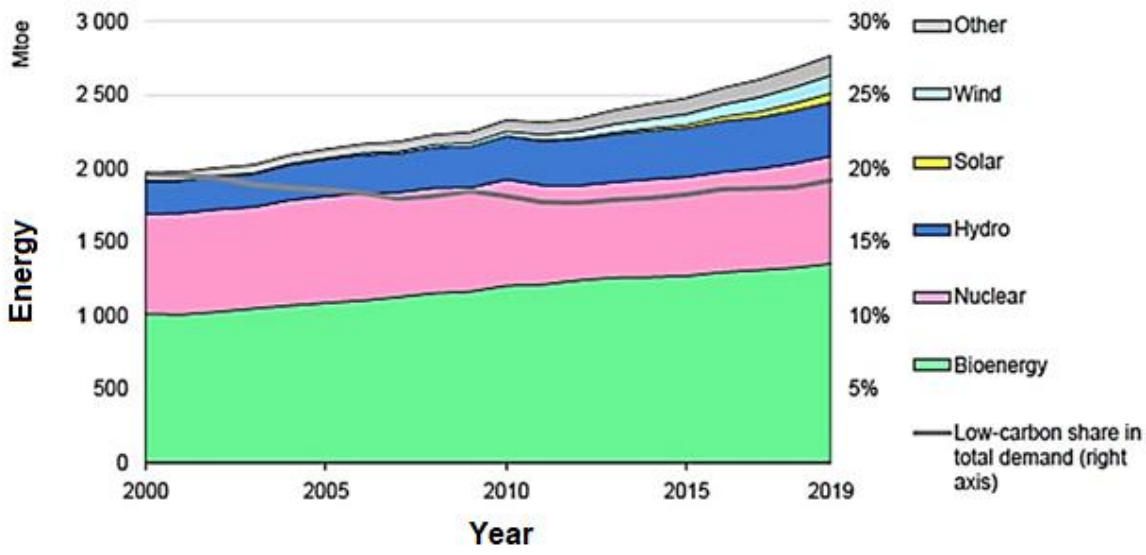

*Notes: Mtoe = million tonnes of oil equivalent.

Figure 1.1. Primary demand for low-carbon energy sources, 2000-19 (IEA, 2020a)

1.4. On-Road heavy vehicles transportation and greenhouse gas emission

The role of transport in contributing to air pollution and climate change is a serious issue. GHGs in the atmosphere are largely caused by harmful emissions from fossil fuel combustion, as measured in carbon dioxide equivalent (CO_2 eq) (Uherek et al., 2010; Lee et al., 2021). Motor vehicular movement over time has been identified as

the primary source of classical gaseous pollutants such as nitrogen oxides (NOx), volatile organic compounds (VOCs), hydrocarbons (HCs), SO_2, CO, CO_2, and particulate matter (PM). Several pollutants contribute significantly to air pollution, including CO, CO_2, HCs, NOx, and PM, which are produced by fossil fuel combustion in automobile engines (Lee et al., 2021). The United States Environmental Protection Agency (USEPA) estimates that motor vehicles, which include cars, large trucks, bulldozers, and trains, release 75% of the country's carbon monoxide. It is thought that auto emissions raise atmospheric levels of carbon dioxide and other greenhouse gases (Niculescu et al., 2019).

Growth in the global transportation sector has been accompanied by a growing reliance fossil petroleum fuel. The rising global petroleum fuel consumption by on-road vehicles has increased eightfold in the last four decades, owing to the rapid rise of freight transportation activity and the dieselization of passenger vehicles in light-duty vehicle fleets markets such as the European Union, India, South Korea, and Turkey (Miller, and Jin, 2018). Diesel fuel is also the primary fuel for more than 90% of all heavy-duty trucks and also more than 75% of all buses, accounting for more than 40% of worldwide on-road energy consumption (IEA, 2018f). Between 2010 and 2050, something drastic need to be done to reverse the fast growth in annual GHG emissions, reducing them by 40 percent to 70 percent. It is estimated that without significant and long-term mitigation measures in place, on-road transportation emissions will grow at a higher rate than emissions from other energy end-use sectors, reaching roughly 12 $GtCO_2$ by 2050 (EIA, Ukraine, 2019). Since 2000, emissions from trucks and buses (heavy-duty vehicles) have increased at a rate of 2.6 percent each year as shown in the Figure 1.2 (IEA, 2020g). Heavy-duty vehicle (HDV) energy consumption and tailpipe CO_2 emissions have increased by 2.6 percent each year since 2000, with trucks accounting for more than 80% of this increase (IEA, 2019a). Diesel engines are widely utilised in transportation and agriculture because they are fuel efficient and have a long service life. Greater thermal efficiency than conventional internal combustion (IC) engines mainly due to their higher compression ratios and lean combustion characteristics, allowing them to be used in heavy-goods vehicles. Diesel engine emissions have a negative influence on the environment and pose a health risk to living things. Diesel on-road vehicles now transport a huge percentage

of people and commodities, but this reliance on diesel technology comes at a high cost in terms of the environment and health (Miller and Jin, 2018).

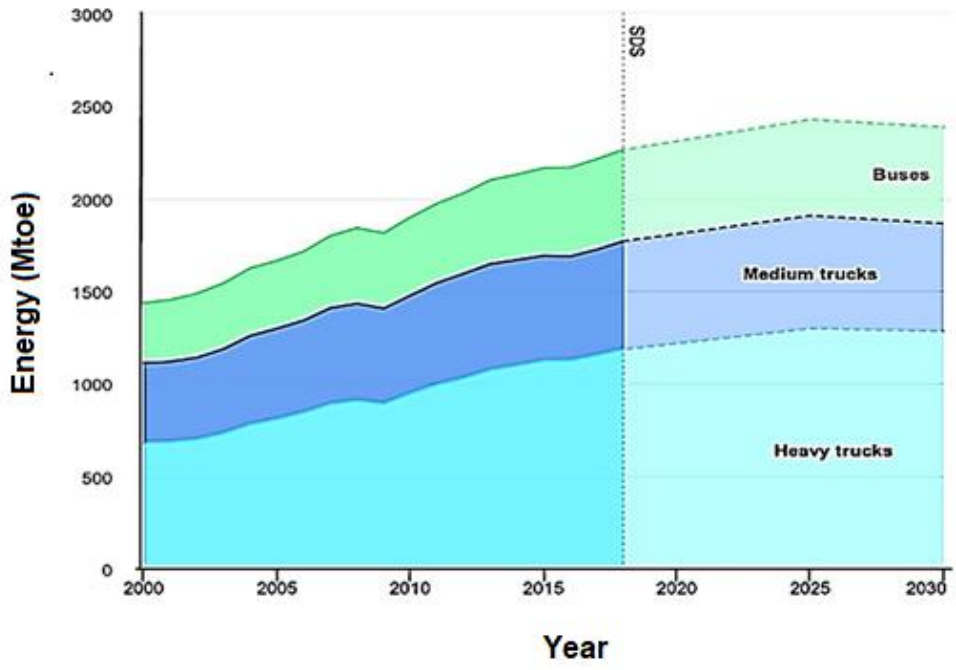

Figure 1.2. CO_2 emissions from heavy-duty vehicles in the sustainable development scenario, 2000-2030 (IEA, 2020g).

If the sustainable development goals are to be realised, biofuel production will have to contribute a large amount of effort, especially for long-haul modes of travel and freight that have limited alternatives, such as rail, aviation, and maritime transport (Giner, Palandri and Debnath, 2019; IEA ,2020g). To separate increased activity and energy usage from CO_2 emissions in the long run, low-carbon alternative fuels such as biodiesel from agricultural post-harvest residual and agro-industrial waste and powertrains improvement technologies will be required (Gnansounou et al., 2020; IEA, 2020b.

1.5. Global biofuel initiatives

The global transportation biofuel production levelled off in 2019, reaching 162 billion litres (L), equivalent to 2.8 million barrels per day (IEA, 2020b). According to the International Energy Agency (IEA, 2020b), sustainable fuels produced from non-food crop feedstock are branded as "advanced biofuels," whereas others label them as

"second-" and "third-generation" fuels. One of the most important factors is that they are biofuels, which can significantly reduce lifecycle greenhouse gas emissions when compared to fossil petroleum fuel alternatives, while not competing with food crops for agricultural land or negatively impacting the environment (Daioglou et al., 2019; Voca, and Ribic, 2020).

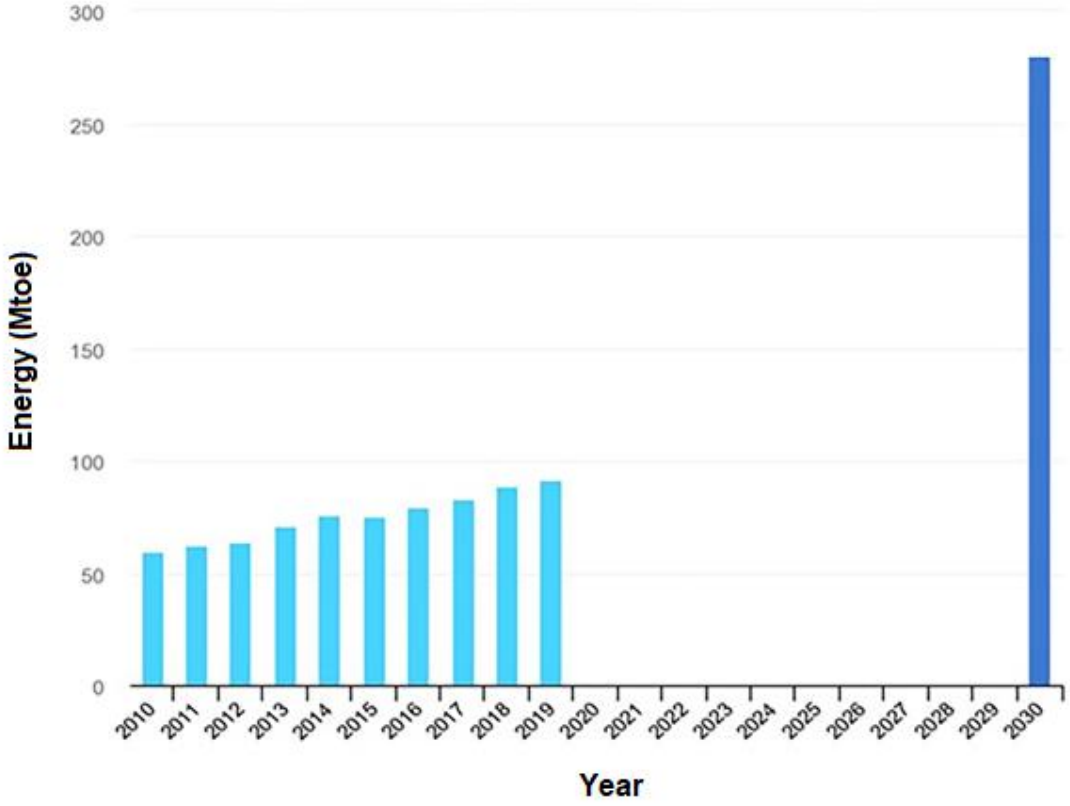

Figure 1.3. Global biofuel production 2010-2019 compared to consumption in the Sustainable Development Scenario (SDS) (IEA, 2019a).

To meet the Sustainable Development Scenario (SDS), transportation biofuel usage must nearly quadruple (to 298 Mtoe) by 2030 as shown in Figure 1.2. This corresponds to 9% of worldwide transportation fuel demand, compared to 89 Mtoe in 2018, which represents roughly 3%. Worldwide biofuel production is not keeping pace with demand for SDS (IEA, 2020d). With 12 countries accounting for 97 percent of biodiesel and ethanol fuel use, consumption is largely concentrated among a few significant players. The United States and Brazil lead the ethanol market, accounting for 50% and 27% of worldwide ethanol production, respectively. The European Union and the United States, with 39 percent and 19 percent of worldwide volumes, respectively, dominate the world in biofuel production (Voca and Ribic, 2020). In response to rising energy

demand and a desire to reduce global emissions, some industrialized countries have introduced biofuels such as methanol, ethanol, and biodiesel (Xu et al., 2019; Voca and Ribic, 2020). The European Union accounts for 38 percent of global total production of biodiesel, followed by the United States (16 percent) and Brazil (14 percent), produced mostly from rapeseed in Europe and soybean in the United States and Brazil. Indeed, some scenarios for keeping global warming at 2 degrees Celsius predict that biofuel output must meet 16% of total transportation fuels need between 2016 and 2040 (Tvaronaviien et al., 2020; IEA, 2020e). This has the added benefit of lowering fossil fuel imports and providing an opportunity to recycle agro-industrial waste, as well as perishable goods from farms, shops, and restaurants (Voca and Ribic, 2020). It is becoming increasingly evident that agricultural post-harvest and agro-industrial waste are emerging as promising biofuel feedstocks (Tchanche, 2017). In 2020, the European Union, for example, aims to meet 10% of its transport energy needs with renewable energy through the use of biofuels, which do not alter land use directly or indirectly in biodiverse and carbon-rich regions, and also reduce greenhouse gas emissions by at least 35% as compared to fossil fuels, taking biofuels into account when cultivating, processing, and transporting them (European Commission, 2015).

1.6. Global biodiesel production scenario

Global biodiesel consumption is anticipated to gradually rise over the next ten years, according to the Organisation for Economic Cooperation and Development and the UN Food and Agriculture Organization's 2016 Agricultural Outlook. An expected 68% increase in demand from developing nations, including Indonesia, Brazil, and Argentina, in 2025 as compared to 2015 (OECD/FAO 2016). In the United States, Brazil, and Argentina, canola, and soybean oils are used to produce more than 80% of biodiesel. There is a small share of vegetable-based biodiesel derived from Indonesian palm oil and other sources, such as jatropha and coconut (OECD/FAO 2016; Network, R.E.P., 2017). Although biodiesel is produced in numerous nations, only a few countries are largely responsible for its production. Globally, the EU produced 26% of all fatty acid methyl ester (FAME) biodiesel in 2016, ahead of the US (17.9%), Brazil (12.3%), Argentina (9.7%), Indonesia (9.7%), Thailand (4.5%), and

other nations as a whole, who together account for 19.8% of the total production as shown in Figure 1.4 (REN21, 2017).

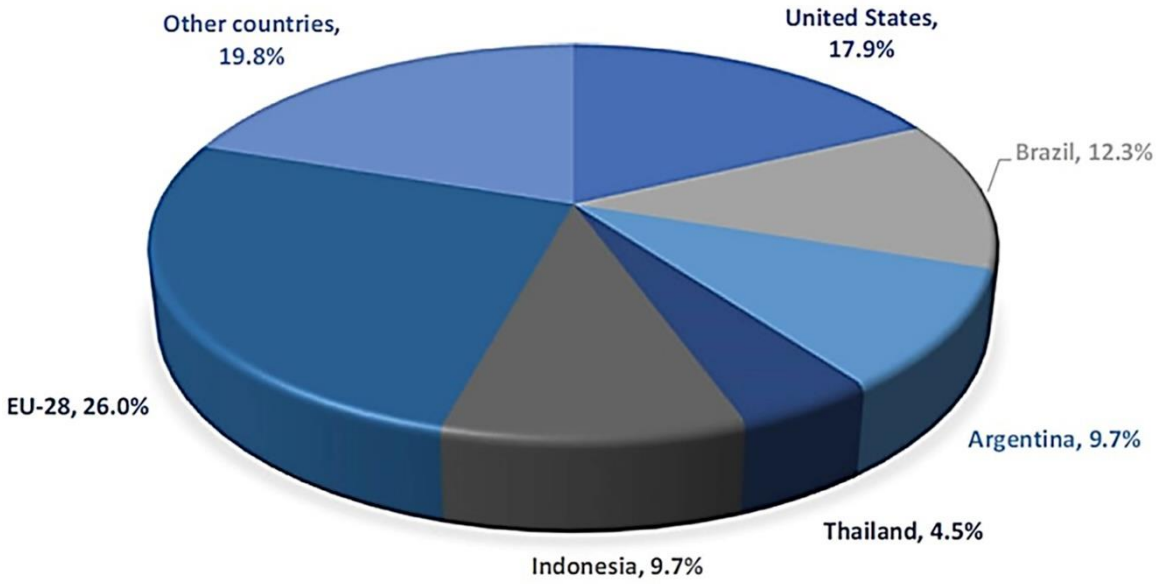

Figure 1.4. Major biodiesel-producing countries in 2016 (REN21, 2017)

Global biodiesel production is primarily driven by domestic policy incentives in the United States, Argentina, Brazil, and Indonesia, along with, to a lesser extent, the Renewable Energy Directive targets in the European Union (OECD/FAO 2016). Figure 1.5 shows the highest 14 biodiesel producing countries in 2017 as adapted from Renewable Energy Network (REN21, 2017).

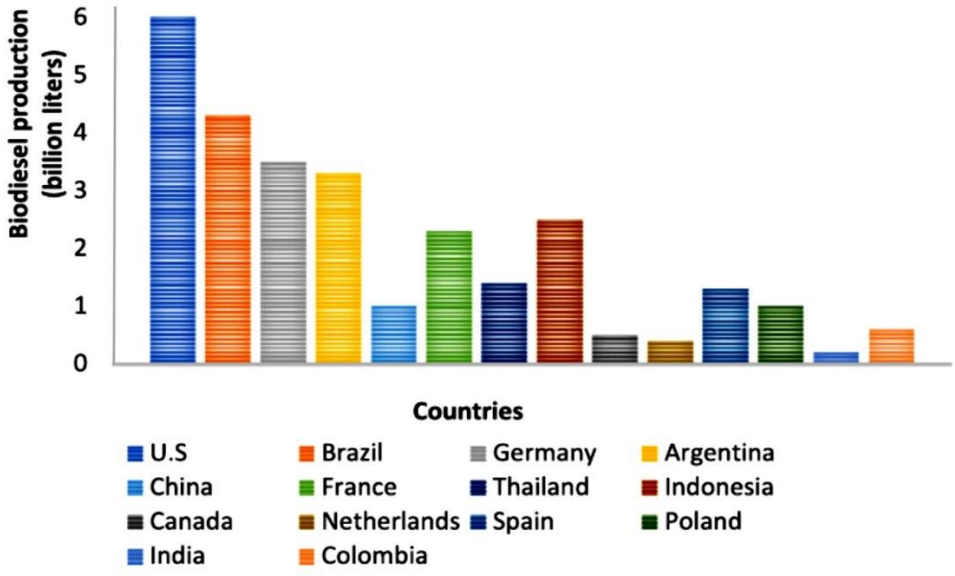

Figure 1.5. Highest 14 biodiesel producing countries in 2017(REN21, 2017).

1.7. Recent research and scientific publications on using biodiesel as fuel in CI engines

In automotive diesel engines, biodiesel combustion has been studied using various blend ratios of biodiesel to petroleum diesel. Lower blends of biodiesel, such as B5 and B10, have been effectively incorporated into petroleum diesel fuel for usage in both new and current diesel engines due to its critical lack of sulphur and aromatics and non-toxicity. The acceptable submissions are that chemically refined vegetable oil can be used to operate DICI engines for a long time without any engine modification, however studies suggest that using up to 20% of vegetable oils as an addition to diesel fuel is possible (Enweremadu, Rutto, and Peleowo, 2011; Datta and Mandal, 2016; Bae and Kim, 2017; Ogunkunle and Ahmed, 2019b).

The biodiesel was found useful as an engine fuel without engine modification. Biodiesel produced from different inedible oil seeds has been utilised in blended forms between B5 and B20, with significant similarities to that of fossil fuel combustion in DICI diesel engines (Mofijur et al., 2013; Fontaras et al., 2014; Can et al., 2017; Geng et al., 2017; Suarez-Bertoa et al., 2019; Goga et al., 2019,). Some research findings show that the most effective method of reducing emissions and improving engine performance is by adding nano additives and using emulsified fuels (Khond and Kriplani, 2016). Common additives used by researchers include di-ethyl ether, methyl oleate, orange oil, kerosene, methanol, ethanol, etc. The commonly used oxygenates are alcohols (methanol, ethanol, propanol and butanol), ether and ester. Some of these, and many other ones that are used to improve the cold flow properties of biodiesel, engine performance and emission properties were discussed by Ali et al., (2013).

Scopus analysis for scientific contributions on the application of biodiesel as vehicular engine fuel suggests how research interest in this area has increased over the years. It is evident that the utilisation of biodiesel fuel in diesel engines is gaining successful application as the publications by year showed increasing trend as reflected in Figure 1.6 (Ogunkunle and Ahmed, 2019a)

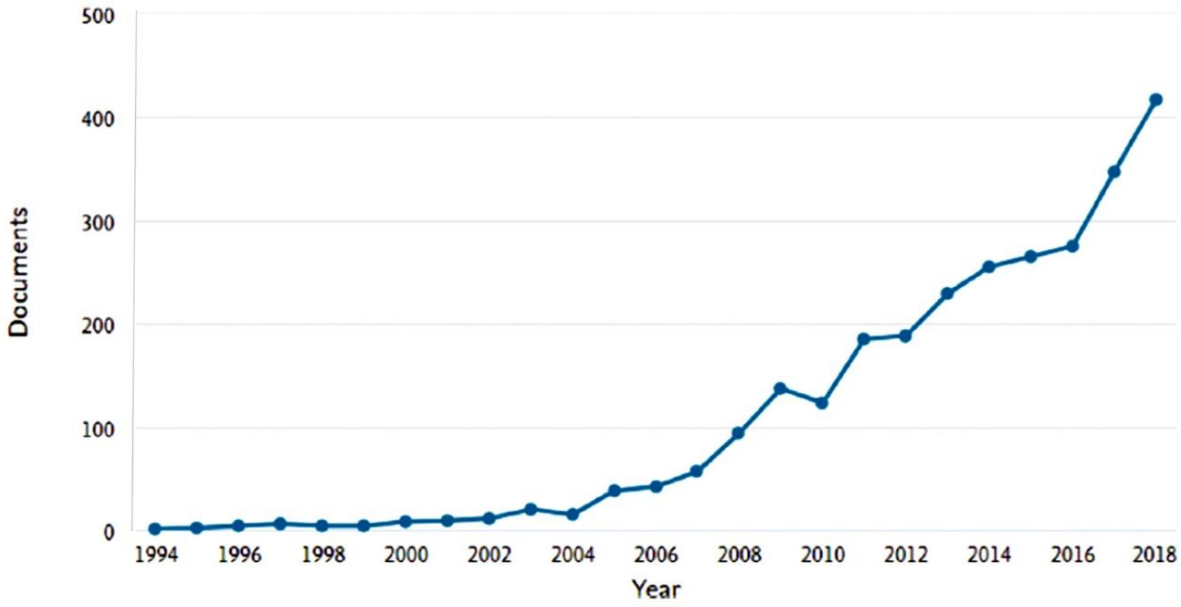

Figure 1.6. Publication trend by year on application of biodiesel in vehicular diesel engines (Ogunkunle and Ahmed, 2019a).

The results from several studies have demonstrated that cashew nut shell liquid (CNSL) is a flexible, renewable, and biodegradable biodiesel, having properties similar to petroleum diesel fuel. It is usually gotten from agricultural waste from cashew-nut processing firms in Asia Pacific, Sub-Saharan Africa, and South America (Mallikappa, Reddy and Murthy 2012; Bello et al., 2013; Velmurugan, Loganathan and Gunasekaran, 2014; Dinesha and Mohanan, 2015; Mubofu, 2016; Aruna and Vardhan, 2017; Devarajan and Nagappan, 2017; Dinesha and Mohanan, 2018; Santhanakrishnan and Ramani, 2017; Bupesh Raja and JayaPrabakar, 2019; Sahoo et al., 2019; Senthil and Thirumalini, 2020). In the light of a sustainable energy mix, the current research deems it necessary to conduct a comprehensive investigation into the detailed combustion process, and emission characteristics of the CNSL biodiesel for direct injection compression ignition (DICI) heavy duty (HD) engines and vehicles.

1.8. Problem statement

Recent literature reviewed on CNSL biodiesel, and petroleum diesel blend fuelled CI engines indicates that, greater part of research conducted only focused on engine performance parameters and emission generation characteristics. The brake thermal

efficiency (BTE), brake specific fuel consumption (BSFC), and unburned hydrocarbons (UHC), carbon monoxide (CO), nitrogen oxide (NOx), and soot were all examined. However, in most of experimental studies of CNSL biodiesel, the investigation used the identical engine specifications (bore diameter and stroke, compression ratio (CR), and combustion chamber hence piston bowl designs (Velmurugan, Loganathan and Gunasekaran, 2014; Dinesha and Mohanan, 2015; Vedharaj et al., 2016; Aruna and Vardhan, 2017; Devarajan, Munuswamy and Nagappan, 2017; Ravindra, Devarajan and Nagappan, 2017; Santhanakrishnan and Ramani, 2017; Dinesha and Mohanan, 2018; Kumar, Dinesha and Rosen, 2018; Pandian et al., 2018; Bupesh Raja and JayaPrabakar, 2019; Sahoo et al., 2019; Senthil and Thirumalini, 2020).

The engine specifications used in almost all CNSL biodiesel CI engine studies used the same bore diameters and stroke, and combustion chamber designs as their experimental settings. In most cases, researchers are constrained by the need to alter the geometry of components for further investigation because obtaining this type of result would necessitate designing and manufacturing many large numbers of prototypes for various parametric variables of the engine operating components, as well as testing many large numbers of prototypes. Consequently, a multidimensional computational fluid dynamics (CFD) software program will be employed as a tool for modelling and simulating mixture formation during injection spray atomization, spray propagation, droplet evaporation and combustion processes, depending on the geometry of a piston bowl, injector nozzle spray included angle and injection timing. In addition to this investigation, the kinematic viscosity of CNSL biodiesel would be varied using various strategies with petroleum diesel blend in DICI Heavy Duty Engine. This in-cylinder study of various combustion processes is significant when optimizing engine performance, combustion process and pollutant formation. CFD numerical modelling and simulation is the best approach to conducting these comprehensive in-cylinder fluid flow and parametric investigations because it is fast, more efficient, and more cost-effective than producing and analysing numerous prototypes (Stiesch, 2013; Tay et al., 2017; Li et al., 2018).

This research work deems it necessary to conduct detailed studies of in-cylinder flow by generation of turbulent kinetic energy (TKE) to represent combustion phenomena of CNSL biodiesel and diesel blend by considering the following factors:

i. The combustion chamber piston bowl geometry would be varied to examine mixture formation as a result of turbulent kinetic energy generation, fuel droplet evaporation and combustion process. The profile of the piston bowl geometry has a considerable impact on atomization and subsequent combustion in a direct injection compression ignition (DICI) engine, which has an impact on performance and emissions (Channappagoudra, Ramesh and Manavendra, 2018; Li et al., 2018; Channappagoudra, Ramesh and Manavendra, 2019). In investigating several open combustion chamber (CC) piston bowl geometries, Merker, Schwarz and Teichmann, (2011), Jaichandar and Annamalai, (2012), and Singh et al., (2017) discovered that CC piston bowl geometry has a great influence on air-fuel mixture formation through spray propagation, and subsequent combustion and emission generation in diesel engines.
ii. Injection timing and spray included angle would be modified in order to investigate advanced and retarded injection timing while taking into account ignition delay and combustion processes, resulting in the generation of NOx and soot. In their studies, Raeie et al., (2014) discovered that using an early injection time results in less soot and more NOx emission than using a late injection timing. The rate at which a spray propagates and forms a mixture is proportional to the amount of heat released, hence the peak pressure (Raeie, Emami and Sadaghiyani, 2014; Shameer et al., 2017; Shameer and Ramesh, 2018).
iii. The Kinematic viscosity reduction of CNSL biodiesel through blending with diesel and other additives (Mohamed Shameer et al., 2017; Yu et al., 2017; F. Li et al., 2018; Kegl and Lešnik, 2018). Battistoni and Grimaldi, (2012), discovered that the fuel injection is totally affected by high density and kinematic viscosity of the biodiesel.

1.9. Research questions

The research questions are as follows:

i. What is the potential of CNSL as a feedstock for biodiesel production?
ii. How would different piston bowl geometries generate highly required turbulent kinematic energy to enhance air fuel mixture formation?
iii. What effect would be varying injection timing and spray included angle have on air fuel mixture formation as it interacts with different combustion chambers piston bowl?
iv. What effect will percentage CNSL biodiesel blend impact CO, CO_2, UHC, soot, and NOx during the combustion process?
v. How would a combined effect of kinematic viscosity of CNSL biodiesel, varying injection included angle, injection parameters and CC piston bowl geometry improve combustion phenomena and emission generation?

1.10. Aims and objectives of the research

This research aims to explore the potential of CNSL as a feedstock for the production of biodiesel and further model the combustion and emission characteristics of the CNSL biodiesel by utilising multidimensional computational fluid dynamics (CFD) simulation work in ANSYS FORTE and a chemical mechanism generator in ANSYS Chemkin-Pro. Additionally, this research will use direct injection compression ignition (DICI) heavy duty diesel engine to model and simulate different blends of CNSL with petroleum diesel, as well as the interaction between different injection parameters and varying combustion chamber piston bowl geometry. The research will further optimize the combined effect of these four factors: varying combustion chamber piston bowl geometry, the reduced kinematic viscosity of the CNSL biodiesel blends, injection parameters with spray characteristics, and comparing with experimentally measured data.

1.10.1. Research objectives

The research objectives are as follows:

i. To explore the potential of CNSL as a feedstock for biodiesel production.
ii. To model and investigate the combined effects of varied injection timing and spray included angle as it interacts with different piston bowl geometries.
iii. To model and investigate the combined effect of varied piston bowl geometry and in-cylinder turbulent kinetic energy generation on mixture formation hence NOx and Soot formation.
iv. To determine the effects of the percentage of CNSL biodiesel blended with petroleum diesel on CO, UHC, CO_2, soot, and NOx emissions during the combustion process.
v. To model and optimize the combined effect of kinematic viscosity of CNSL biodiesel, injection pressure, injection timing, injection included angle geometries and CC piston bowl geometry on performance, combustion process, and pollutant formation.

1.12. Significance of the study

The results of this study will contribute to the understanding of engine performance during the combustion process and further enable the CNSL biodiesel and diesel petroleum blends to be employed in DICI heavy-duty diesel engines. In this regard, multidimensional CFD numerical modelling and simulation would enable faster, efficient, and effective ways to arrive at these results compared to the process of manufacturing various components for experimental investigation of numerous prototypes. The use of in-cylinder study would also help to optimize the combustion process, engine performance and help to minimize soot and NOx in the light of air/fuel mixture formation hence pollutant formation. This study would further contribute largely to the existing knowledge and broaden the understanding of biodiesel fuel usage in compression ignition engines with minor component alterations. It will also add to the knowledge base of numerous scientific discoveries which are devoted to exploring eco-friendly, sustainable, and renewable alternative fuels to replace the conventional diminishing fossil resources. This research is also very significant for these other reasons:

The trend of utilizing agro-industrial-waste as a source of renewable energy is becoming more and more feasible and CNSL cardanol biodiesel is available in many Sub-Saharan African and Asia Pacific countries, a potential feedstock of energy for farms, towns and villages. The use of biodegradable biodiesel for heavy duty DICI engines for farm machinery, earth moving equipment and commercial transport for heavy goods, will enable the reduction of carbon footprints. Furthermore, because biodiesel fuel is obtained from agricultural waste resources, a product of photosynthesis carbon fixation, it does not contribute to net atmospheric CO_2 levels.

1.13. Outline of thesis

Chapter 1: Introduction

This thesis is divided into eight chapters, including chapter one, which provides the introductory background information, the problem statement, research questions, the objective of this research, the significance of the study, and the outline of the thesis.

Chapter 2: Cashew Nut Shell Liquid Inedible Biodiesel

This chapter reviewed cashew nut shell liquid (CNSL) as a potential inedible biodiesel feedstock and its suitability as a fuel alternative for direct injection compression ignition (DICI) engines. The CNSL extraction methods and kinetic viscosity reduction procedures are discussed. Experimental and numerical investigations of CNSL biodiesel used in DICI engines were examined and reviewed for combustion and emission characteristics in order to identify the gaps in these studies.

Chapter 3: Combustion in Direct Injection Compression Ignition (DICI) Engines

This chapter discusses combustion and associated end products in the direct injection compression ignition (DICI) engines. These includes, the four phases of combustion process, influencing variables of mixture formation, step by step sub-processes in diesel DICI engine combustion, essential combustion characteristics of DICI diesel engines and finally, pollutant formation.

Chapter 4: Piston Bowl design and Injection Spray Parameters Optimisation

This chapter discusses a number of design factors that directly influence combustion processes and emission characteristics, such as piston bowl shape, injection spray

angle, and injection time. In order to determine the most optimal combustion chamber, five (5) piston bowls were designed from the baseline piston geometry and four injection timings, and four spray-included angles were chosen for optimisation in order to find the highest possible performance.

Chapter 5: Combustion Model Description and Validation

This chapter presents several computational fluid dynamics (CFD) numerical sub-models that were used in the ANSYS Forte package for simulating internal combustion engines. Direct injection compression ignition (DICI) combustion and emission characteristics, as well as in-cylinder physical and chemical kinetic were modelled using several governing equations. The model has been validated with a Low-temperature combustion (LTC) heavy-duty DICI engine experimentally measured data.

Chapter 6: Results and Discussion of Combustion Simulation of DICI Engine

In this chapter the results of the reduced normal heptane (n-heptane) kinetic mechanism are used to represent petroleum diesel as fuel surrogate to simulate combustion and emission characteristics of base bowl and five piston bowl designs in the low-temperature combustion DICI engine as discussed and the finding summarised.

Chapter 7: Results and Discussion of CNSL Biodiesel Simulation in DICI Engine

In this chapter, the results from the combustion and emission characteristics simulation of cashew nut shell liquid (CNSL) biodiesel blended with petroleum diesel (B10, B20, B30, and B50) in DICI engines are discussed.

Chapter 8: Conclusions and Recommendations for Future work

This chapter concludes with a summary of the main findings and recommendations for further research based on the study.

CHAPTER 2

Literature review

This chapter reviewed the cashew nut shell liquid (CNSL) as a potential inedible biodiesel feedstock, the main subject of the study. The chapter further discussed the global production scenarios in South America, Sub-Saharan Africa, and Asia Pacific countries and the availability of cashew fruit in year-round harvesting. The review elaborates on various extraction methods of the CNSL and kinetic viscosity reduction procedures. The CNSL biodiesel is compared to petroleum diesel according to ASTM standards. The chapter concluded by reviewing numerous experimental and numerical modelling investigations that examined combustion processes and emission characteristics of direct injection compression ignition (DICI) utilising CNSL biodiesel with other fuel additive blends to identify gaps therein.

2.1. Cashew nut shell liquid inedible biodiesel

Globally, researchers have been studying alternative biofuel sources, especially feedstocks for biodiesel production. Various edible and inedible biodiesel feedstocks have already been used in engine tests and physiochemical laboratory experiments. The use of edible oils for biodiesel is not as practicable as it once was due to the enormous economic disparity between high demand and availability of edible oils (Acharya et al., 2018). Furthermore, the price of food and commodities will increase dramatically if biodiesel feedstocks are produced from edible agricultural crops. Apparently, the suitable feedstocks to be considered are inedible agricultural crops or agricultural waste, whose production is more sustainable (Gui, Lee and Bhatia, 2008; Kumar and Sharma, 2011; Suresh, Jawahar and Richard, 2018).

It is crucial and important to consider converting agricultural and industrial wastes into renewable, sustainable, environmentally friendly, and long-term energy sources that are affordable and capable of providing long-term energy. Consequently, the by-products and agricultural wastes of the cashew industry, such as the empty shells of cashew nuts from which cashew nut shell liquid (CNSL) is obtained, have shown promising potentials as a biodiesel feedstock. The CNSL biodiesel is renewable, and compostable, have properties similar to petroleum diesel, and makes it a promising

feedstock for large-scale biodiesel production (Solanki and Javiya, 2012; Singh, Chauhan and Kumar, 2016; Kumar, Dinesha and Rosen, 2018).

Cashew plants, from which CNSL originates, are currently grown widely in Asia Pacific, Sub-Saharan Africa, and South America tropical countries, and there are a variety of end products available from this crop (Velmurugan, Loganathan and Gunasekaran, 2014; Dinesha and Mohanan, 2015; Vedharaj et al., 2015; Mubofu, 2016; Ravindra, Aruna and Vardhan, 2017; Sahoo et al., 2017; Kumar, Dinesha and Rosen, 2018).

2.2. Sustainable biodiesel from inedible feedstocks

Table 2.1 outlines the percentage oil constituent of some of the most potential inedible crops for biodiesel production. When edible oil is used to produce biodiesel, food shortages are likely to occur; therefore, producing biodiesel from inedible oil feedstocks can provide food and energy security. Many inedible oil plants grow in forests, though some thrive in less productive, degraded, and barren environments (de Figueirêdo et al., 2016; Ianda et al., 2020).

Table 2.1. Inedible oil plants, botanical name, oil content % (Seed or Shell)

Plant	Botanical Name	Oil Content % (Seed or Shell)	Ref.
Cashew nut shell	Anacardium occidentale L.	25 – 35	(b), (d)
Castor	Ricinus communis	46-55	(a)
Jatropha	Jatropha curas	20-60	(c)
Jojoba	Simmondsia chinensis	45-55	(a)
Karanja	Pongamia pinnata	25-50	(b), (d)
Mahua	Madhuca indica	35-40	(a)
Moringa	Moringa oleifera	40	(a)
Neem	Azadirachta indica	20-30	(a), (b)
Rubber oil	Hevea brasiliensis	50-60	(e)
Tobacco oil	Nicotiana tabacum	36-41	(a)

(a) Gui, Lee and Bhatia, 2008; (b) Kumar and Sharma, 2011; (c) Atabani et al., 2013; (d) Taiwo, 2015; (e) Onoji et al., 2016

Biodiesel made from inedible oil crops can assist rural people supplement their income by allowing them to collect seeds, which will help the rural economy expand. Some of these crops contain toxic components that make them unfit for human consumption, but they are suitable as biodiesel feedstocks (Jumbe, Msiska and Madjera, 2009; Atabani et al., 2013). When choosing a seed for commercial oil extraction, the oil content is an important factor to consider (Atabani et al., 2013; Onoji et al., 2016).

2.3. Production of cashew nuts with shells and land use

The production of cashew nuts with shell (CNS) is spreading across many tropical regions of the world. Between 2000 and 2019, Food and Agriculture Organization (FAO), FAOSTAT data (2020) recorded total production of 57,986,773 tons. Based on these two decades of production, the total area harvested globally increased from 3,303,615 to 7,091,275 hectares per year, a total of 114.6 percent growth of area covered with the cashew crop, as depicted in Figure 2.1 (a), which is a positive sign of reafforestation and thus a good greenhouse gas (GHG) mitigation factor.

Over the last two decades, cashew nut with shell output in Sub-Saharan Africa (SSA), where nearly all cashew crops are grown in Africa, has totalled 30,104,678 metric tons (2000-2019). This accounts for more than half of the global total production of 57,986,773 metric tons during the years under review (FAOSTAT data, 2020). As shown in Figure 2.1 (b), cashew nut with shell production in tandem with land use resulted in a significant increase in area harvested in the SSA region, from 1,157,001 hectares in 2000 to 4,704,272 hectares in 2019, a 406.5 percent increase, supporting the reforestation program.

According to Lubi and Thachil (2000) and Taiwo (2015), industrial grade CNSL accounts for about 20–25% of an empty cashew nut shell's weight, so 30,104,678 metric tons of shell can yield approximately 6,020,935 metric tons of CNSL. A study of cashew nut with shell production in Sub-Saharan Africa over the past 20 years (2000-2019) demonstrates that inedible CNSL can be used as a biodiesel feedstock in Africa (FAOSTAT, 2020).

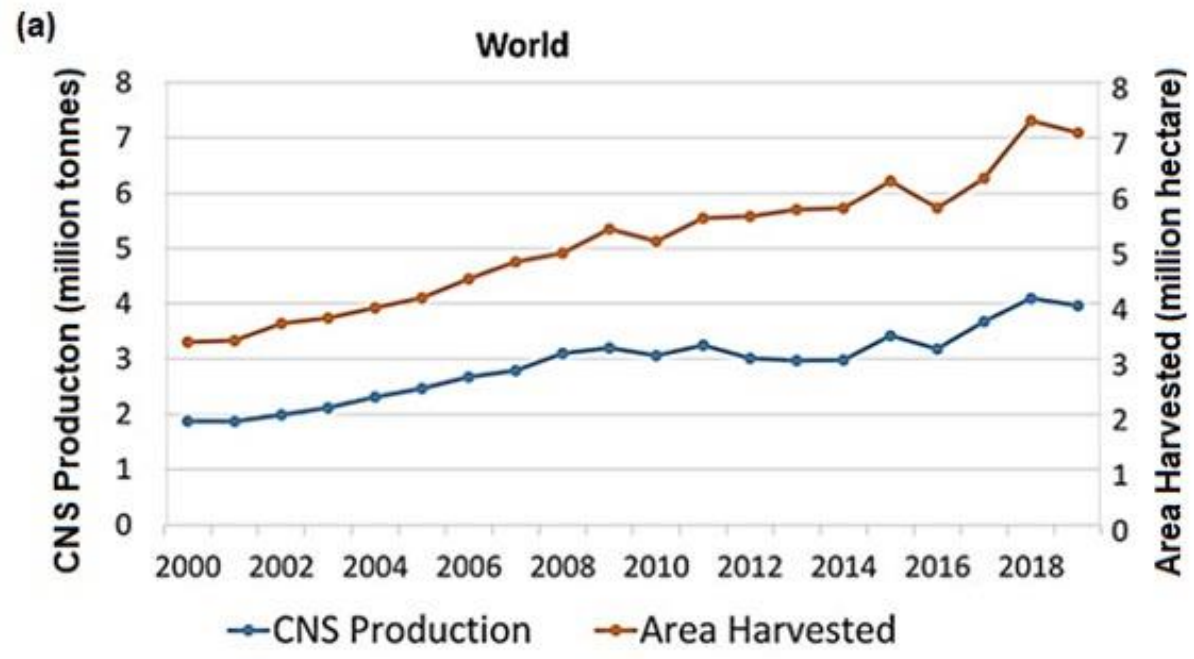

Figure 2.1. (a) World cashew nut with shell production and area harvested (2000-2019) (FAOSTAT, 2020).

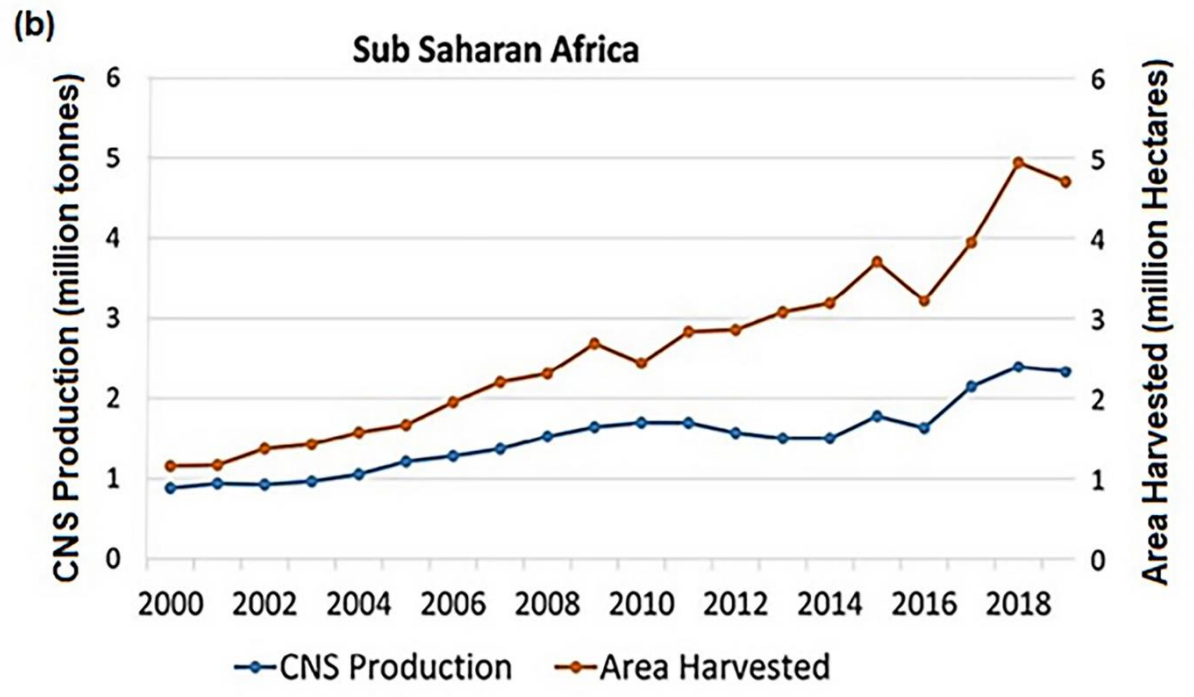

Figure 2.1. (b) Sub-Saharan Africa cashew nut with shell production and area harvested (2000-2019) (FAOSTAT, 2020).

2.3.1. Cashew plant perennial crop

The cashew tree (*Anacardium occidentale* L.) is a perennial plant that is grown in many tropical parts of the world. Cashew as a perennial crop has diverse product outputs as depicted in Figures 2.2(a-c) and 2.3 (a-c).

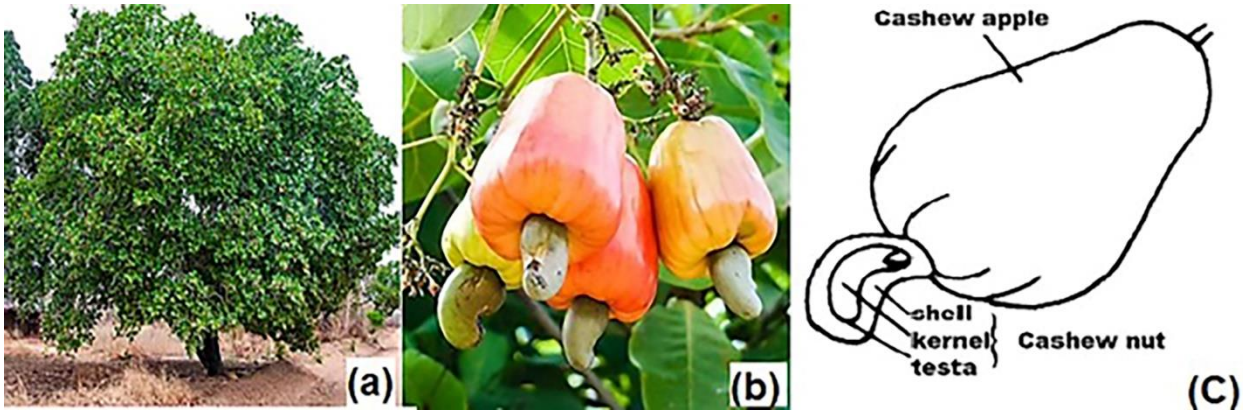

Figure 2.2. (a) Cashew tree canopy, (b) Cashew fruit (cashew apple and nut), (c) Labelled cashew fruit (Taiwo, 2015; Costa and Bocchi, 2017)

As shown in Figure 2.3 (b, c), the cashew fruit has a cashew apple and a nut (kernel), which are edible seeds covered in a honeycomb-like shell, and the most valuable portion of the cashew tree. The cashew plant is a well-known Anacardiaceous plant species that grows between 23° North and 23° South of the Equator.

Figure 2.3. (a) Cashew nut with shell (b) Split cashew nut shell with kernel (c) Labelled cross section cashew nut with shell (Mwangi et al., 2013; Mubofu, 2016; Bastos and Tubino, 2017).

The cashew plant is a drought-resistant, fast-growing tree that can endure a broad range of conditions, including poor soil, although it cannot withstand cold frost. As a tropical plant, it can withstand temperatures as high as 30°C and can thrive in

environments ranging between 20°C and 30°C. It can be cultivated successfully in locations with annual rainfall of 1000-2000mm thanks to its drought-resistant qualities (Taiwo, 2015; Costa and Bocchi, 2017). The cashew tree grows tall between 5 - 10 meters, can develop a canopy diameter of 8 to 12 meters and roots as shown in Figure 2.2(a). It has evergreen leaves that endure almost all year round. It has a characteristic broad root system that allows it to adapt to a wide range of soil types and moisture levels. Cashew trees are ideal for reforestation on a commercial scale, particularly in areas with barren, slash, and extensive burned farmlands. It can also grow on damaged or abandoned coastal sand dunes. The cashew tree is one of the world's most economically viable and profitable tree crops (Mwangi et al., 2013; de Figueirêdo et al., 2016; Mubofu, 2016).

As shown in flow chart Figure 2.4, the cashew plant produces a diverse range of products as a sustainable feedstock for the food industry, chemical and polymer industries, building and construction, as well for energy generation (i.e., biorefinery). The cashew plant has a life range of about 30 to 50 years, during which it can produce four major products: cashew nuts (kernel), cashew apples, CNSL, gum, lumber for construction and firewood (Taiwo, 2015; de Figueirêdo et al., 2016; Mubofu, 2016; Costa and Bocchi, 2017).

One of the most widely consumed edible parts of the cashew tree is the kernel, which is its principal commercial product. Cashew kernels have a high protein content, which accounts for their use as soybean meal substitutes for broiler chicks, while the empty nut shells contain alkenyl phenolic chemicals (de Figueirêdo et al., 2016; Mubofu, 2016).

A cashew apple is used to make juice, jams, jellies and alcoholic beverages, but in other regions, the post-harvest residues are being used to make bioethanol (Berry and Sargent, 2011; de Abreu et al., 2013). After approximately 30 years of cashew fruit harvesting, the wood of the cashew tree can be used as timber for boats and construction materials, activated charcoal, and other items and chemicals are all products from various aspects of the cashew tree (Berry and Sargent, 2011; de Abreu et al., 2013).

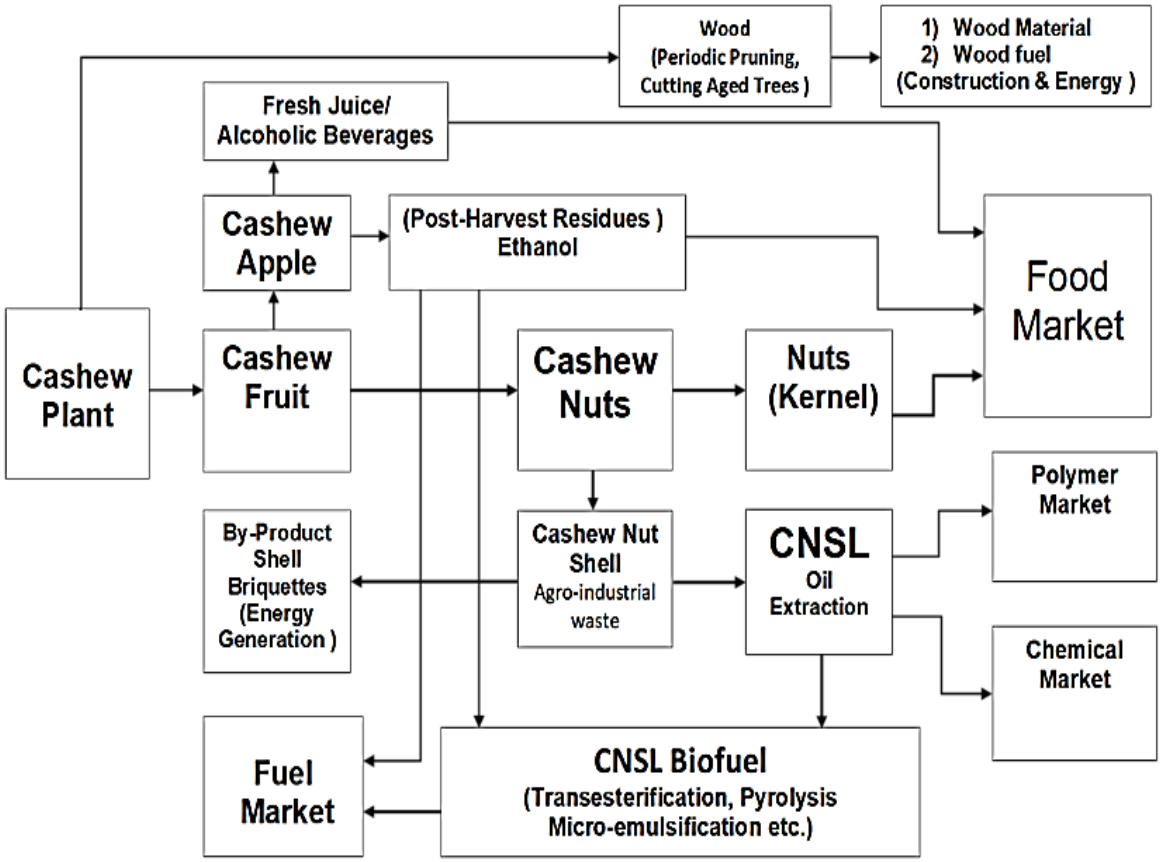

Figure 2.4. Flow chart of cashew nuts and apple processing from plant to food and various markets (Biscoff and Enweremadu, 2023).

A significant amount of trash from the cashew industry can be recycled into fuel briquettes (shell, press cake) (Sawadogo et al., 2017). The CNSL extracted from the shell of the cashew nut can be used to produce a variety of chemicals, including biodiesel (Akinhanmi, Atasie, and Akintokun, 2008; Gui, Lee, and Bhatia, 2008). The produced ethanol from cashew apple post-harvest residues can also be used directly or blended with gasoline in spark ignition engines or in transesterification of CNSL biodiesel (Berry and Sargent, 2011; Mubofu, 2016).

2.3.2. Potential of cashew plants for afforestation and reforestation

The cashew plant is known for its reforestation potential; however, it also helps to regulate climate change by absorbing massive amounts of CO_2 from the atmosphere and acting as carbon sinks, storing carbon in soil and biomass (Rupa, Rejani and Bhat, 2013; Singh, Rao and Shivashankar, 2013). During the latter half of the sixteenth

century, cashew (Anacardium occidentale L.) was first introduced in many tropical regions for the purpose of afforestation schemes and soil conservation in Asia-Pacific and Sub-Saharan Africa (Noiha Noumi et al., 2017). The cashew plant was then purposely planted for afforestation, and cashew trees were utilised to reforest and repair sandbanks on multiple occasions (Rupa, Rejani and Bhat, 2013; Singh, Rao and Shivashankar, 2013).

Cashew farms may be able to mitigate the negative effects of climate change. The carbon potential of this crop opens prospects for cashew plantations to access carbon credit markets through small clean development mechanism (CDM) initiatives (Singh, Rao and Shivashankar, 2013). The cashew tree has greener leaves with exceptional photosynthetic ability, and can be cultivated in highly dense planting systems, and is a good crop for carbon sequestration.

According to studies by Rupa and Sajeev (2015) in research at the Directorate of Cashew Research (DCR), cashew genotype (VTH-174) trees of 7 years old sequestered about 2.2-fold more carbon (C) under high-density planting system (625 trees/ha) as compared to normal-density planting system (156 trees/ha). Under high-density planting, cashew has been projected to store 32.25 and 59.22 tCO_2/ha at the 5th and 7th years of growth, correspondingly. Carbon sequestration is an essential element of emission reduction, therefore crop sequestration potential must be evaluated. The sequestration of cashew plant from biomass into soil organic carbon (SOC) is an important strategy for reducing agricultural gaseous carbon emissions (Noiha Noumi et al., 2017).

2.3.3. Cashew crop year-round harvest

The harvest seasons in producing countries are similar, depending on their proximity to the equator. Figure 2.5 shows that harvesting begins early in the calendar year in Sub-Saharan Africa (SSA) countries north of the equator, especially West Africa and Asia (India and Vietnam), from mid-January to mid-June (Oliveira et al., 2011). Harvesting takes place in the SSA countries that are south of the equator, such as East and Southern African and South America (Brazil) countries, from September or October through the beginning of the following calendar year.

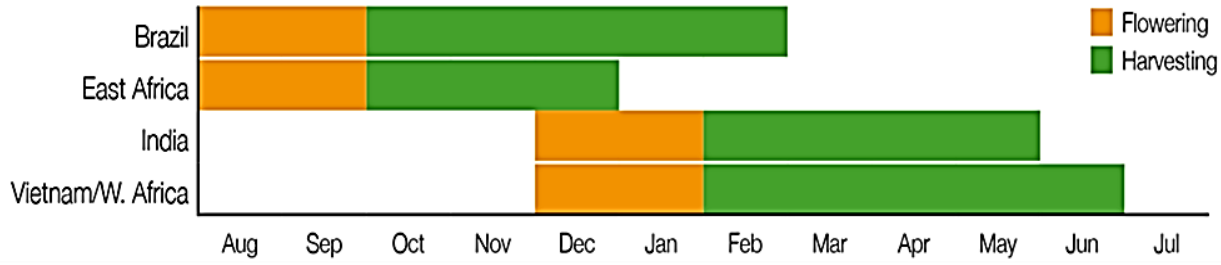

Figure 2.5. The chart illustrates the high concentration months of flowering and harvesting dependent on the tree type and the zone (Oliveira et al., 2011).

This clearly demonstrates that the cashew sector in the SSA region of Africa is capable of producing cashew nuts and apples almost throughout the year (Oliveira et al., 2011). Each year, the average West African farmer household gets 500 - 1200 kg of raw cashew nuts (Costa and Bocchi, 2017).

2.3.4. Cashew apple post-harvest residue

Cashew apple (pseudo-fruit), a by-product of the cashew crop, accounts for approximately 80% of the total weight of the cashew (nut and apple) and is rapidly gaining commercial importance. The greater percentage of cashew apple post-harvest residues are left as waste in the farmlands of almost all cashew fruit-producing countries after the cashew nuts with shells are removed (Berry and Sargent, 2011). This terrible occurrence of cashew apples being thrown away indiscriminately arises because the nut (kernel) is a high-demand product with a cumulative value far greater than the cashew apple juice recovered from the pseudo-fruit (Berry and Sargent, 2011; de Abreu et al., 2013).

According to FAOSTAT data (2020), there is a considerable discrepancy between the global output of cashew nuts with shell and cashew apple, as illustrated in Figure 2.6, and this gap is even greater in SSA countries. The world record shows that within 20 years of the harvest of cashew apple from 2000 to 2019 cumulatively 35,847,169 metric tons of cashew apple was harvested compared to 57,986,773 metric tons of cashew nut with shell. If the weight of cashew apple is 80% of the total weight of the nut and apple combined as indicated by Berry and Sargent, (2011) and de Abreu et al., (2013), then the total presumed cashew apple lost within the years under review was 196,099,923 metric tons.

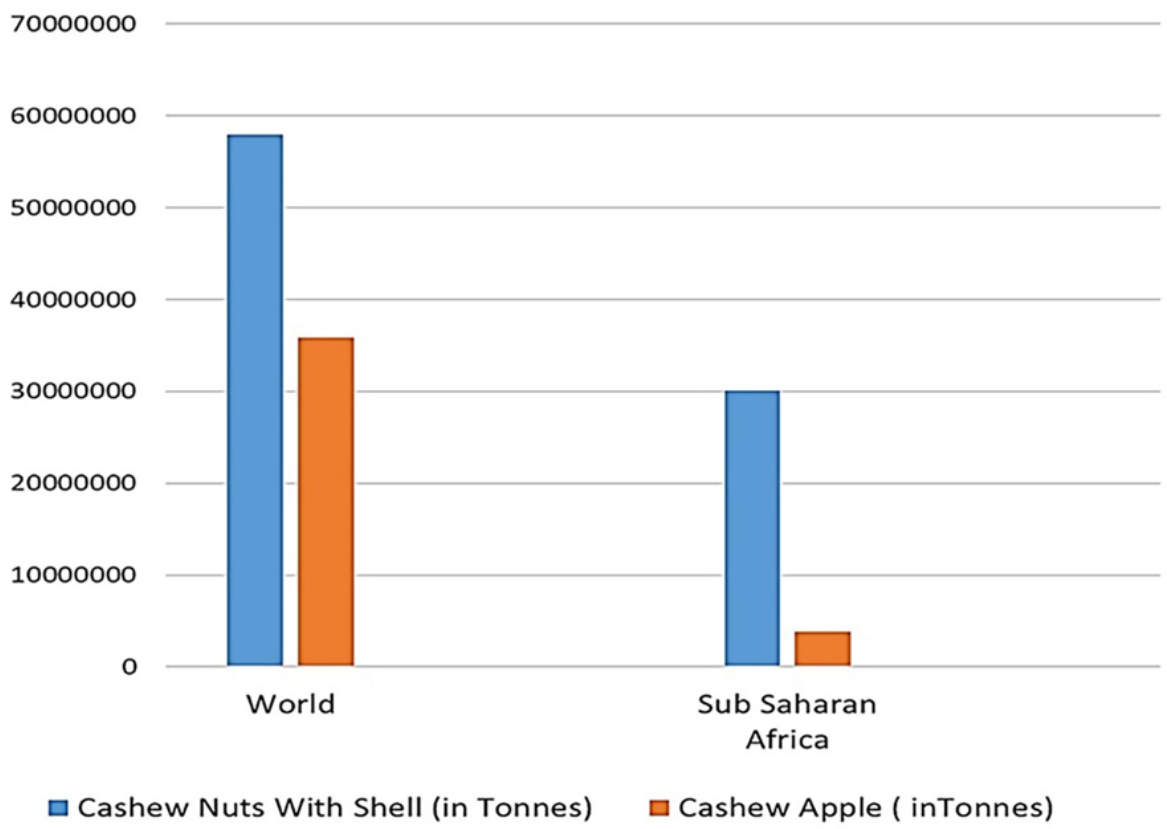

Figure 2.6. Global and SSA cashew nut with shell and cashew apple production compared (2000-2019) (FAOSTAT, 2020).

This quantity was possibly discarded and counted as post-harvest losses. Considering the loss, when approximately 4 tons of cashew apples are wasted for every 1 ton of cashew nut with shell produced (Berry and Sargent, (2011). Between 2000-2019, 3,840,236 cashew apples were harvested in Sub-Saharan Africa, compared to 30,104,678 cashew nuts with shells. As a result, if 30,104,678 tons of cashew nut with shell were produced in the year under consideration, and each ton of cashew nut with shell required 4 tons of cashew apple harvesting, then a total of 120,418,712 metric tons of cashew apples should have probably been harvested. Greater percent (116,578,476 metric tons) was discarded and counted as post-harvest losses (FAOSTAT, 2020.

2.3.5. Cashew apple for ethanol production

Approximately 1.8 million tons of cashew fruit (nut and apple) are processed each year to get the nuts, which are highly valuable products, while over 80% of the cashew apples are discarded as post-harvest trash. Due to their high metabolic activity, ripe cashew apples have long been considered too sensitive and perishable for international trade (Berry and Sargent, 2011). The good news is that this low-cost agricultural waste, the bulk of which is abandoned as post-harvest loss, can be utilised as substrates for industrial and biochemical feedstock, including ethanol production (Berry and Sargent, 2011; de Abreu et al., 2013). Ethanol is seen as a viable alternative fuel for meeting the world's growing energy demands. The ethanol was produced using saccharomyces cerevisiae cell immobilized in silica gel with a cashew apple as the substrate. Berry and Sargent (2011) and de Abreu et al., (2013) refer to cashew apple as a low-priced substrate that has been exploited to produce bioethanol and other value-added manufactured goods.

2.4 Cashew nut shell liquid (CNSL)

The cashew nut shell (CNS), which makes up 20% to 25% of the overall weight of the cashew nut, is commonly discarded and handled as waste in cashew nut processing factories (Akinhanmi, Atasie and Akintokun, 2008; Bello et al., 2013). The use of CNS as a raw material will not compete for land, agricultural resources, or even food production, because the primary goal of a cashew plantation is to acquire the precious cashew kernel (Akinhanmi, Atasie and Akintokun, 2008; Bello et al., 2013). The empty outer shell, inner shell, and edible kernel make up the nut as shown in Figures 2.3 (a-c). The cashew nut empty shell is about 0.32 cm thick. As much as 25% to 35% of the entire nut weight is made up of a dark brown liquid called cashew nut shell liquid (CNSL), which is found in the feathery honeycomb pattern in between outer and the inner layer of the shell (Bastos and Tubino, 2017). As shown in Figure 2.7, the primary constituents of CNSL are cardanol (decarboxylated anacardic acid), a meta-substituted n-long chain (C15) unsaturated alkylphenol, cardol, and methylcardolare. Cardanol is a long meta-position hydrocarbon chain amonohydroxyl phenol (Taiwo, 2015; Kumar, Dinesha and Rosen, 2018).

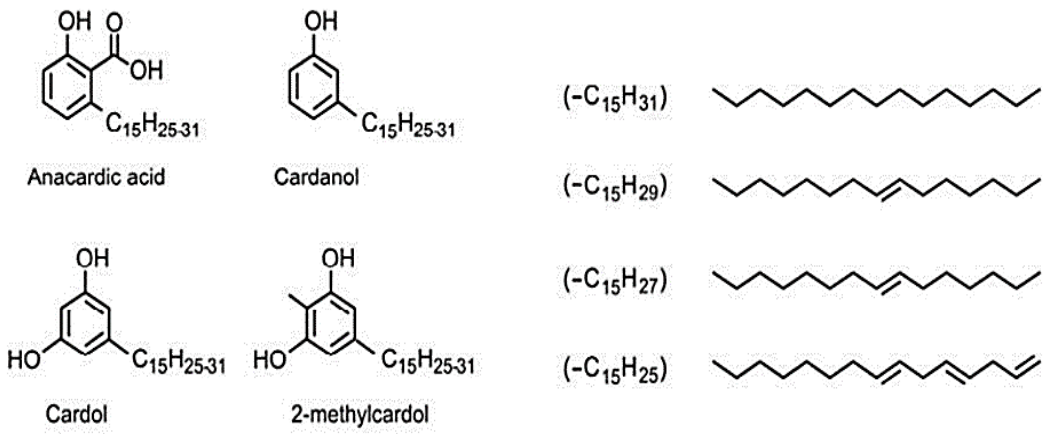

Figure 2.7. Formulas for anacardic acid, cardanol, cardol, and 2-methyl cardol found in CNSL (Kumar, Dinesha and Rosen, 2018).

The CNSL may be extricated from a honeycomb like structure present in the cashew nut shell using a variety of extraction techniques (Bello et al., 2013). The quantity and quality of CNSL is entirely dependent on the extraction method utilised, and the percentage constituent of CNSL changes depending on whether it is a natural or technical CNSL (Patel, Bandyopadhyay and Ganesh, 2006; Bello et al., 2013; Mubofu, 2016). CNSL has a diverse chemical elements and oil composition than traditional vegetable-oil-based fuels, whether edible or inedible (Taiwo, 2015).

The natural CNSL (nCNSL) is extracted at low temperatures, whereas technical CNSL (tCNSL) is extracted at high temperatures (Bello et al., 2013; Raghavendra Prasada, 2014). The primary chemical compounds found in CNSL are anacardic acid, cardanol, cardol, and 2-methylcardol. Anacardic acid accounts for 70% of nCNSL, with cardol accounting for 18%, cardanol accounting for 5%, and the remainder made up of various phenols and less polar compounds. The technical cardanol (tCNSL) contains 83–84 percent; cardanol, 8–11 percent cardol; and a trace of methyl cardol (Risfaheri, Nur and Sailah, 2009; Raghavendra Prasada, 2014; Sanjeeva, et al., 2014). The CNSL has a considerable potential as a future biofuel and trash disposal solution due to its renewability and sustainability (Mubofu, 2016). Recent studies suggest that CNSL is a viable biodiesel feedstock that may be used to augment non-renewable resources (Mubofu, 2016; Fischer et al., 2019). Cashew nut shells (CNS), which make up around a quarter of the total weight of cashew nuts, are typically discarded and disposed of in many cashew nut processing factories (Akinhanmi, Atasie and Akintokun, 2008; Oliveira et al., 2011; Bello et al., 2013).

2.4.1. Cashew nut shell liquid (CNSL) extraction procedures

There are several procedures for extracting CNSL, and other methods are being experimented and developed as shown in Figure 2.8.

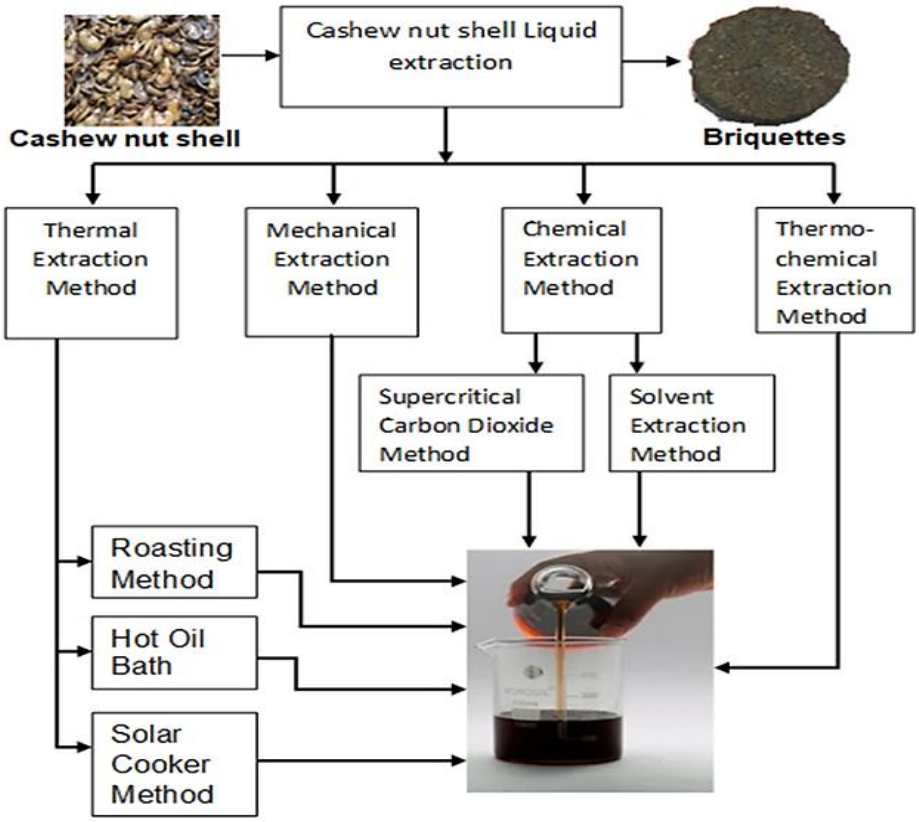

Figure 2.8. Flow chart of Cashew nut shell liquid extraction methods.

The following extracting methods are now prevalent: mechanical, thermal, chemical, and thermochemical (solvent and pyrolysis) extractions (Lubi and Thachil, 2000; Akinhanmi, Atasie and Akintokun, 2008; Kumar, Dinesha and Rosen, 2018).

2.4.1.1 Mechanical method

When cashew nut shells are mechanically pressed, the shell releases the CNSL. The most common mechanical extraction method is the pressure screw press (Akinhanmi, Atasie and Akintokun, 2008; Anilkumar, 2017). An alternative mechanical extraction method utilises a hydraulic press, in which a manual lever operation or a pump controlled by an electrical derivation is used to apply strong hydraulic compression to cashew nut shells (Lubi and Thachil, 2000; Akinhanmi, Atasie and Akintokun, 2008).

In most situations, the mechanical approach is referred to as a cold extraction, and the resulting product is known as natural CNSL (nCNSL), which has a higher percentage of anacardic acid, the only disadvantage with this method is 10 – 15% CNSL remains in the residues (Akinhanmi, Atasie and Akintokun, 2008; Taiwo, 2015; Kumar, Dinesha and Rosen, 2018).

2.4.1.2 Thermal method

Heat is used to extract CNSL from cashew shells in this process. There are numerous thermal extraction processes, including hot oil bath, roasting, and solar cooker method; hot oil bath and the roasting methods are the commonly used methodologies (Patel, Bandyopadhyay and Ganesh, 2006; Raghavendra Prasada 2014; Kumar, Dinesha and Rosen, 2018). In this process, there is massive conversion of anacardic acid to cardanol, the thermal extraction process yields CNSL known as technical CNSL (tCNSL), which includes more cardanol (Lubi and Thachil, 2000; Mubofu, 2016).

2.4.1.3 Roasting method

Roasting the nut shells yields commercially available technical CNSL, which is mostly composed of cardanol and cardol. This typical procedure for extracting CNSL involves roasting shells in a drum. CNSL oozes out of the shells during roasting, making them brittle. In order to recover all the CNSL, the roasted shells are once again put in 180-185 °C bath. The high-temperature bath enables this method to recover 90% CNSL out of the shell (Lubi and Thachil, 2000; Akinhanmi, Atasie and Akintokun, 2008; Mubofu, 2016; Costa and Bocchi, 2017)

2.4.1.4 Hot oil bath method

The hot oil bath, which is widely used in industry, is the most common commercial method for extracting CNSL. Raw nuts are placed in a pool of hot CNSL at 180–200°C. In this process the exterior layer of the shell bursts open, releasing CNSL and about half of the oil will be retrieved. Decorticating nuts with this procedure are straightforward and does not compromise the quality of the kernels. Improvements

over the basic procedure includes preliminary wetting the surface of the shell and immersing it in water at 20–25°C, followed by steam treatment before exposure to the hot CNSL bath. The increased moisture content of 7–10% of the nuts' weight causes the cells to break, allowing oil to escape into the bath (Akinhanmi, Atasie and Akintokun, 2008; Bastos and Tubino, 2017; Costa and Bocchi, 2017)

2.4.1.5 Solar cooker method

In this technique, CNSL was extracted using a concentrated solar stove of 1.4 kW and 1.4m in diameter. The cooker's focal point diameter was 30 cm, and it was utilised to gather the heat generated by the solar rays from the reflector, resulting in a rise in temperature of 225-300 °C, which was then used to extract the CNSL. Figure 2.9 shows the concentrating parabolic solar cooker for CNSL extraction by sunlight. In the process temperature of 320°C was reached inside the extractor with no load, with a thermal profile developed and evaluated. The average oil recovery was 55–70%, according to reports (Mohod, Khandetod and Sengar, 2010; Subbarao, Krishna Prasad and Prasad, 2011). The total energy used for the extraction and production of CNSL biodiesel adds to the overall cost of biodiesel at the pump; therefore, if solar energy can be used, the cost of production will be reduced drastically.

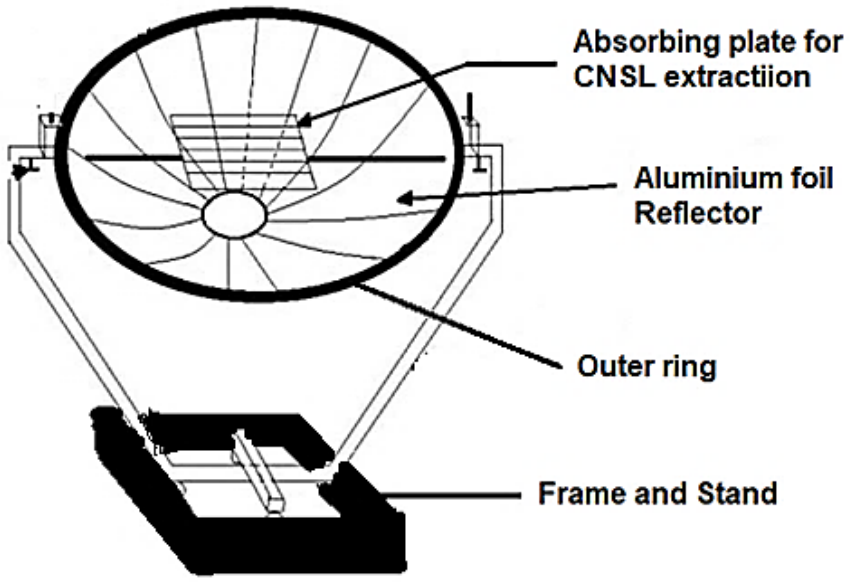

Figure 2.9. The concentrating parabolic solar cooker for CNSL extraction (Mohod, Khandetod and Sengar, 2010)

2.4.1.6 Chemical extraction method

In this category, there are two main procedures: solvent extraction and supercritical carbon dioxide. It is estimated that these techniques can extract 94 percent of CNSL (Kumar, Dinesha and Rosen, 2018).

2.4.1.7 Solvent extraction method

In this process cashew nut shells were cleaned with water and dried at a temperature of 80°C before the oil was extracted. A cross-beater mill was used to grind the shells into fine particles, which were then dissolved in ethanol at a ratio of 150 grams per litre. For 1 hour at room temperature, the solution mixture was constantly mixed. A vacuum filter was used to filter the mixture. In order to remove the ethanol from the filtrate containing isolated chemicals, vacuum evaporation was used. Solvents such as alcohols, benzene, petroleum hydrocarbon solvents or toluene are used to extract the oil (Lubi and Thachil, 2000).

2.4.1.8 The supercritical carbon dioxide method

The Cashew nut shells are sealed in the extractor during this process. To achieve the desired extraction temperature, the extractor is heated. At standard temperature and pressure, a compressed CO_2 is forced throughout the extractor at 0.5-5 L/min flow rate. The CNSL is fetched on a regular basis, about once every hour. This method can produce CNSL at a rate of up to 94%. Supercritical extraction using CO_2 and isopropyl alcohol has also been reported (Lubi and Thachil, 2000; Patel, Bandyopadhyay and Ganesh, 2006; Setianto et al., 2009).

2.4.1.9 Thermal and mechanical method

In this procedure massive amounts of cashew shells are placed in a steel container whiles hot steam is inputted from the bottom during the treatment process. The hot steam is supposed to submerge the shells in a hot surrounding for an extended period, allowing some oil to be recovered. The hot shells are then crushed in a mechanical expeller in order to extract as much CNSL as possible. This method was chosen over

more modern processes such as hot bath and the roasting methods because it allows for mass oil extraction in a single trail, which reduces production costs (Lubi and Thachil, 2000).

2.4.1.10 Thermochemical extraction

Pyrolysis is a thermochemical conversion process that occurs in the presence or absence of a small amount of oxygen, which will be discussed further under the reduction of CNSL viscosity (Bupesh Raja and JayaPrabakar, 2019).

2.5. Industrial applications of CNSL

There are a number of industrial applications for CNSL and it is described as a versatile raw material. CNSL is best known for manufacturing friction-altering materials used in automotive clutch faces, brake linings, and industrial belts (Mwangi et al., 2013; Taiwo, 2015). These are some other industrial applications of CNSL: fungicides, pesticides, insecticides, foundry chemicals, lacquers, flame-resistant materials, CNSL nanoparticles, and special coatings, as well as surfactants, plasticizers, and resin. The impact of CNSL and plant growth, acidity, wood preservation, and pressure control action are being investigated further (Mwangi et al., 2013; Taiwo, 2015). Anacardic acid, a key ingredient in CNSL, has been linked to most of the biological action of the compound, according to research (Oliveira et al., 2011; Sanger et al., 2011; Mwangi et al., 2013; Taiwo, 2015).

2.6. The standard petroleum diesel and biodiesels

2.6.1. The standard petroleum diesel

The major source of diesel fuel is fossil petroleum, but there is an emerging alternative known as biodiesel that is made from bio-resources. In compression ignition engines, diesel fuel is commonly used which require certain characteristics, in reality diesel fuels have a low auto-ignition temperature and a high flashpoint. Diesel fuel has a higher flash point than gasoline, therefore making it harder to ignite (Mollenhauer and Tschoeke, 2010). Diesel fuels are classified according to their types and intended

uses either in buses, trucks, heavy earth moving machines, railroads, marine engines, and stationary engines (Heywood,1988; Stone,1999; Hillier and Coombes, 2004; Nunney, 2007). The ASTM D975 diesel fuel classification specifications are shown in Table 2.2. (Ferguson and Kirkpatrick 2015; Gohrt 2016). The American Society for Testing and Materials classifies diesel fuels according to ASTM D975 categories from 1D to 4D. The 1D diesel fuel is intended for use in cold weather and has a flash point of 38°C, whereas the 2D diesel fuel is less volatile and has a flash point of 52°C, making it suitable for vehicular applications. The 4D diesel engine is commonly used in heavy-duty stationary applications. In the United States, diesel specifications are ASTM D975, while in the European Union, they are EN590.

Table 2.2. Diesel fuel properties as defined in ASTM D975 (Gohrt, 2016).

Property	**ASTM Method**	**#1-D**	**# 2-D**	**# 4-D**
Cetane number, min.	D613	40	40	30
Cetane index, min.	D976	40	45.5	NR
Kinematic viscosity at 40°C (m^2/s), min.	D445	1.3	1.9	5.5
at 40°C (m^2/s), max.		2.4	4.1	24.0
Minimum flash point, ^oC	D 93	38	52	55
High heating value (MJ/Kg)	D 2163	45.6	-	-
Low heating value (MJ/Kg)		42.6		
Cloud point	D2500	local	-	-
Liquid density (Kg/m^3)	D287	820	820	860
Sulphur, wt % max.	D129	0.05	0.05	2.0
Max. copper strip corrosion	D130	No. 3	No. 3	NR
Max. ash, wt %	D482	0.01	0.01	0.1
Max. carbon residue	D524	0.15	0.35	-

NR = Not required

2.6.2. Critical properties of diesel/biodiesel fuels

2.6.2.1. Cetane number (CN)

The cetane number (CN) shows the quality of ignition of the diesel fuel. A higher cetane number means that the fuel will ignite more easily. Once the diesel fuel is delivered into the compressed hot air inside the combustion chamber, it must ignite extemporaneously and with minimal ignition delay. The high cetane number of petroleum diesel, results to a shorter delay of ignition and, as a result, the improved quality of the ignition. This is very essential for easiness of ignition and enhance performance from cold starting hence reduction of noise in the engine while controlling legally mandated emissions. ASTM D613 method is used (Reif 2014; Gohrt, 2016).

2.6.2.2. Cetane index (CI)

Cetane index is used as a substitute for the cetane number of petroleum diesel fuel. The cetane index is calculated based on both density and volatility range. There are two methods used, ASTM D976 and D4737 (Gohrt, 2016).

2.6.2.3. Kinematic viscosity

The kinematic viscosity of the lubricants, i.e., the quotient of dynamic viscosity and oil density, is a function of the temperature. Fuel flow resistance is an important measure of consistency, as it helps injector flow and atomization. ASTM D445 method is used for the measurement (Reif, 2014; Ferguson and Kirkpatrick, 2015; Gohrt, 2016; Munroe, 2016).

2.6.2.4. Flash point

The flash point is the lowest temperature at which it produces enough vapor to create a flammable combination in the air. If an ignition source is present, the lower the flashpoint temperature, the easier it is to ignite the air/fuel mixture. The higher the flashpoint, the safer it is to handle the substance. ASTM D93 method is used (Reif, 2014; Ferguson and Kirkpatrick, 2015; Gohrt, 2016).

2.6.2.5. Calorific value

The calorific value of diesel fuel is an essential property that characterises the quantity of liberated heat energy to the chamber during combustion and denotes the quantity of energy readily available in the fuel (Reif, 2014; Ferguson and Kirkpatrick, 2015; Gohrt, 2016).

2.6.2.6. Cloud point

When cooled under normal test conditions, the temperature at which a diesel or liquid fuels shows a fog or haze of wax crystals at ASTM D2500 standard (Reif, 2014; Ferguson and Kirkpatrick, 2015; Gohrt, 2016).

2.6.2.7. Liquid density

The mass of the material per unit volume, which is vital for consistency and allowing for high fuel efficiency over a long period of time. Two ASTM standards used are ASTM D2622 and ASTM D494 (Reif, 2014; Ferguson and Kirkpatrick, 2015; Gohrt, 2016).

2.6.2.8. Sulphur content (ppm)

It produces acidic chemical products that are detrimental to the atmosphere, and it progressively wears out engine components (SO, SO_2, SO_3). ASTM D2622 and ASTM D494 are two ASTM standards used. This is critical to keep engine wear to a minimum and adhere to legal regulations (Reif, 2014; Ferguson and Kirkpatrick, 2015; Gohrt, 2016).

2.6.2.9. Water and sediment content

ASTM D1796, which determines the quantity of sediment and water in diesel fuel, and ASTM D2709, which determines the amount of sediment. (Reif, 2014; Ferguson and Kirkpatrick, 2015; Gohrt, 2016).

2.6.2.10. Carbon residue

This implies that the fuel has a proclivity for forming carbon deposits in the engine. There are two sorts of test procedures that are widely accepted. ASTM D189 or ASTM D524 standard (Reif, 2014; Ferguson and Kirkpatrick, 2015; Gohrt, 2016).

2.6.2.11. Ash content

A tiny particle of ash-forming elements, such as suspended particles and soluble organometallic compounds, may be present in diesel fuels. This can harm a diesel fuel injection system's tight tolerance, as well as abrasive wear on engine components like piston rings. ASTM D482 standard is used (Reif, 2014; Ferguson and Kirkpatrick, 2015; Gohrt, 2016).

2.6.2.12. Corrosiveness

ASTM D130 is the standard method for the determination of the degree of corrosiveness of petroleum products that exhibit a vapor pressure up to 124 kPa (37.8 °C). D130 therefore can be applied to automotive and aviation gasoline and diesel fuel (Reif, 2014; Gohrt, 2016).

2.6.3. Properties of biodiesel

In order to produce biodiesel that is both effective and efficient, it is important to consider the fatty acid composition of any source. The nature and quality of the source, as well as the geographical conditions in which the plant grows, influence the fatty acid content of biodiesel. In other words, the biodiesel's composition is solely determined by the parent feedstock (Knothe and Razon, 2017). Table 2.3 shows the properties of diesel and biodiesel compared according to ASTM standards.

Table 2.3. According to ASTM, the properties of diesel and biodiesel are compared (Knothe, 2010)

Fuel Property	**Diesel**	**Biodiesel**
Fuel Standard	**ASTM D975**	**ASTM PS121**
Fuel Composition	**C_{10}–C_{21} HC**	**C_{12}–C_{22} FAME**
Kinematic viscosity at 40°C(mm2/s)	1.3–4.1	1.9–6.0
Cetane number	40–45	48–65
Calorific value (MJ/kg)	42-44.5	35–39
Specific gravity kg/l 15°C	0.85	0.88
Flash point (°C)	60 to 80	100 to 170
Pour point (°C)	-35 to -15	-15 to 10
Cloud point (°C)	-15 to 5	-3 to 12
Boiling point (°C)	188 to 343	182 to 338

In Table 2.4, the kinematic viscosities of petroleum diesel and biodiesel were compared according to the United States and European standards.

Table 2.4. Diesel and biodiesel fuel standards for kinematic viscosity. (Knothe and Razon, 2017)

Standard	**ASTM D975**	**ASTM D6751**	**EN 590**	**EN 14214**
Location	United States	United States	Europe	Europe
Fuel	Diesel	Biodiesel	Diesel	Biodiesel
Method	ASTM D445	ASTM D445	ISO 3104	ISO 3104
Kinematic Viscosity (mm^2/s)	1.9—4.1	1.9—6.0	2.0—4.5	3.5—5.0

Transesterification of practically any triglyceride feedstock can be used to make biodiesel fuel, which includes animal fat, oil-bearing crops, and algae lipids. Soybean oil is the leading biodiesel feedstock in the United States, rapeseed oil is the dominant

biodiesel feedstock in Europe, and palm oil is the dominant biodiesel feedstock in Asia Pacific, according to the current global view or trend. There are several countries where biodiesel can be derived from animal fats like beef tallow and frying oil from fast-food joints. Some of the vegetable oils making waves and whipping-up interest in the global biofuel market are canola, coconut, corn camelina, CNSL, jatropha, rapeseed, sunflower and safflower. Recently using algal lipids as a feedstock for biodiesel production is also gaining a lot of attention. (Knothe, 2010; Hoekman et al., 2012; Sadeghinezhad et al., 2013; Datta and Mandal, 2016; Knothe and Razon, 2017; Datta and Mandal, 2016; Knothe and Razon, 2017).

2.7. Utilization of CNSL biodiesel in DICI engines

The CNSL can be utilised in a variety of ways as a liquid biofuel, including direct CNSL blends with diesel or other additives, as well as after pyrolysis and transesterification. CNSL that has not been esterified is referred to as “technical CNSL.” Because of the negative impact of fuel characteristics on fuel spray, mixture formation, and combustion, direct application of CNSL in engines is limited (Kumar, Dinesha and Rosen, 2018). To modify the properties of CNSL, a variety of chemical and thermal methods are applied, including proportional mixing with diesel, microemulsion, transesterification, and pyrolysis (Kumar, Dinesha and Rosen, 2018). The CNSL has a high viscosity when compared to other biodiesels, which is especially visible when used as a fuel in CI engines (Taiwo, 2015; Kumar, Dinesha and Rosen, 2018).

In practice, it has been discovered that previous decarboxylation of the oil is critical, since excessive foaming makes the distillation procedure inefficient and uneconomical (Taiwo, 2015; Kumar, Dinesha and Rosen, 2018). As a result of the heat, anacardic acid is decarboxylated and turned into cardanol. CNSL generated by vacuum pyrolysis has a high cardanol concentration. CNSL biodiesel refers to decarboxylated CNSL that has been converted to cardanol. The technical CNSL is further processed by distillation at reduced pressure to remove the polymeric components. On the other hand, biodiesel made from CNSL has a moderate viscosity, is easily combustible, and has a high miscibility with diesel (Taiwo, 2015; Kumar, Dinesha and Rosen, 2018; Loganathan et al., 2020)

2.7.1. Physicochemical properties of CNSL biodiesel

Various researchers have investigated and reported on the physicochemical features of CNSL, which have discovered feasible qualities that allow it to be considered as a good industrial feedstock for biodiesel production (Dinesha and Mohanan, 2018; Devarajan and Nagappan, 2017; Vedharaj et al., 2016 Shantharaman, Pushparaj and Prabhakar, 2017). Table 2.5 compares the reported properties of CNSL biodiesel to petroleum diesel and biodiesel using the ASTM standards.

Table 2.5. ASTM Specifications for diesel and biodiesel

Fuel Property	**Fuel Standard ASTM**	**Density (kg/m^3) @15 ^oC**	**Viscosity at 40^oC (mm^2/s)**	**Pour Point (°C)**	**Cloud Point (°C)**	**Calorific Value (MJ/kg)**	**Flash Point (°C)**	**Cetane Number**	**Boiling Point (°C)**	**Ref.**
Diesel	**D975**	0.85	1.3 – 4.1	-35 - -15	-15- 5	42-44.5	60 – 80	40–45	188- 343	(a), (b)
Biodiesel	**D6751-08**	0.88	1.9 – 6.0	-15 -10	-3 – 12	35–39	100- 170	48–65	182- 338	(c), (g)
CNSL B100	**CNSLME**	821- 910	4.15 – 6.42	-5 - 1	-8 - 6	38.3 – 42.5	136 -224	45 – 61	368- 374	(f), (c) (h), (h)

(a) Howell, 2007; (b) Knothe, 2009; Knothe, 2010; (c) Raghavendra Prasada 2014; (d) Dinesha and Mohanan, 2015; (c) Vedharaj et al., 2016; (f) Devarajan and Nagappan, 2017; (g) Knothe and Razon, 2017; (h) Shantharaman, Pushparaj and Prabhakar, 2017; (i) Dinesha and Mohanan, 2018.

2.7.2. CNSL biodiesel fatty acid profile

Table 2.6 outlines the fatty acid profiles of CNSL and other biodiesel feedstocks which mostly consist of the following C_{16} and C_{18} fatty acids: palmitic (Hexadecanoic, C16:0), stearic (octadecanoic, C18:0), oleic (9(Z)-octadecenoic, C18:1), linoleic (9(Z),12(Z)-octadecatrienoic, C18:2) and linolenic (9(Z),12(Z),15(Z)-octadecadienoic, C18:3. Modifying the fatty ester composition is a potentially promising route to improving biodiesel fuel properties by enriching it with components possessing more favourable properties (Knothe, 2009; Moser and Vaughn, 2012).

Table 2.6. CNSL Biodiesel fatty acids profiles

Fatty Acid		Formula	Synonyms	(a) **B100**	(b) **B100**	(c) **B100**	(d) **B100**
Palmitic	C16:0	$C_{16}H_{32}O_2$	Hexadecanoic	23.13	10.3	12.5	38.7
Palmitoleic	C16:1	$C_{16}H_{30}O_2$	9-Hexadecenoic acid	5.16	**--**	**--**	--
Stearic	C18:0	$C_{18}H_{36}O_2$	n-Octadecanoic	5.57	8.8	6.6	6.53
Oleic	C18:1	$C_{18}H_{34}O_2$	Cis-9-octadecenoic	31.65	24.7	28.9	42.7
Linoleic	C18:2	$C_{18}H_{32}O_2$	9,12-octadecadienoic	7.62	39.7	35.5	--
Linolenic	C18:3	$C_{18}H_{30}O_2$	Cis-9,cis-15-octadecenoic	20.71	16.5	16.5	12.33

(a) Bello et al., 2013; (b) Devarajan and Nagappan, 2017; (c) Santhanakrishnan and Ramani, 2017; (d) Pandian et al., 2018)

2.7.4. Kinematic viscosity of CNSL biodiesel

The raw CNSL's higher viscosity and lower volatility significantly affect fuel atomization, spray patterns, and mixture formation, causing injector choke, incomplete combustion, carbon deposits, and getting piston rings trapped in grooves. (Taiwo, 2015; Vedharaj et al., 2016). However, there are well-established techniques for reducing the kinematic viscosity of raw CNSL that have been tried and tested. Transesterification, micro-emulsification, pyrolysis, dilution or blending, and preheating are some of them (Taiwo, 2015; Vedharaj et al., 2016; Shantharaman, Pushparaj and Prabhakar, 2017). According to ASTM D6751, biodiesel has kinematic viscosity ranging from 1.9 to 6.0 mm^2/s (Knothe and Razon, 2017)

2.7.5. Transesterification

Transesterification is the process of producing esters and glycerol by mixing a fat or vegetable oil with an alcohol. The reversible nature of the reaction permits extra alcohol to be utilised to move equilibrium to the product side, and a catalyst is employed to boost the reaction rate and yield. Although ethanol and other alcohols can be used, most transesterification are done using methanol, this process generates a plant methyl ester with an identical fatty acid profile as the parent oil. Both acids and bases can be used to catalyse CNSL, but sodium methoxide is used more commonly in industrial processes since it helps to keep the moisture content low (Knothe and Razon, 2017; Pandian et al., 2018).

2.7.6. Micro-emulsification

Solvents such as ethanol, methanol, and 1-butanol are employed to lower the high viscosity of raw CNSL in this method. Emulsification occurs when two normally immiscible liquids spontaneously create a colloidal equilibrium dispersion with optically isotropic fluid microstructure with dimensions in the 1–150 nm range (Raghavendra Prasada 2014; Knothe, 2010).

2.7.7. Pyrolysis

This is a thermochemical process that uses heat and a catalyst to convert one material to another, either in the presence of air or when oxygen levels are decreased to stoichiometric values. It requires heating in the absence of oxygen or air, as well as chemical bond breaking to form small molecules. Pyrolysis of triglycerides has been researched by certain researchers in order to develop chemicals that can be used in diesel engines (Raghavendra Prasada 2014; Knothe, 2010). Risfaheri et al., (2009) describe the CNSL pyrolysis process, which is performed in a reactor at a vacuum pressure of 5 kPa and at temperatures ranging from 400 to 600°C, with each experiment increasing by 50°C. The volatiles extracted during pyrolysis are condensed in a pre-weighed condensing train that proceeds from air condensation to ice bath condensation at 5 to 7°C (Datta and Mandal, 2016). This procedure produces CNSL biodiesel that requires no further processing, such as transesterification, and

has a moderate viscosity, is easily combustible, and has a high miscibility with diesel (Risfaheri et al., 2009; Knothe, 2010).

2.7.8. Preheating

Preheating CNSL biodiesel before injection (at the injector's input side) helps lower viscosity, according to Vedharaj et al., (2015). The viscosity reduces linearly as the temperature rises from 40 to 80°C in 20-degree increments. Because CNSLME is an oxygenated fuel, it is susceptible to substantial vapor production beyond 80°C, hence heating above that temperature will cause air pockets to form in the fuel injection lines (Vedharaj et al., 2015).

2.7.9. CNSLME Diesel blending or additive dilution

To reduce the viscosity and increase the engine performance, biodiesel is blended with diesel or other suitable additives. It has been reported that replacing diesel fuel with 100 % vegetable oil is not feasible (Knothe, 2009; Knothe, 2010; Knothe and Razon, 2017). As a result, combining 10–25% vegetable oil by volume with diesel is considered to provide a favourable outcomes for CI engines without any changes or adjustments to the mechanical components (Knothe, 2010; Mallikappa, Reddy and Murthy 2012; Atabani et al., 2013; Raghavendra Prasada 2014; Atabani et al., 2013) The study by Mallikappa, Reddy and Murthy (2012), investigated volumetric blends of 10%, 15%, B20%, and B25 CNSL biodiesel and diesel, but found that the viscosity exceeded 5 CST when the blend was above 25% (B25). Properties of CNSL biodiesel blend with other additives reported in literature are presented in Table 2.7.

Table 2.7. Properties of CNSL biodiesel and blends to ASTM D6751-08 (Howell, 2007).

CNSL Biodiesel/ Blends	Density @ 40°C ASTM D4052	Kinematic Viscosity 40°C (mm^2/s) ASTM D445	Calorific Value (MJ/kg) ASTM D240	Cetane Index ASTM D976	Flash Points °C ASTM D93	Ref.
Diesel	822	2.5	42.95	46	50	
B5	852	4.82	42.25	49	52	(a)
B10	823-855	2.50-4.99	40.13- 42.1	49	54-53	and
B15	829	3.10	40.2	-	55	(b)
B20	836	3.50	40.261	-	56	
B25	841	4.20	40.33	-	58	
B30	846	5.50	40.392		61	
B10M10	0.836	3.76	39.57	-	52	(c)
B20M10	0.849	4.09	39.29	-	55	
B30M10	0.858	4.41	38.86	-	58	
Cardanol	0.9101	6.42	39.28	-	224	(d)
B20M10	0.849	4.09	39.29	-	55	
CNSOME	0.9064	13.37	38.4	50	66	(c)
CC-CNSL	0.8901	4.101	42.5	48	94	(f)
CNSME100	0.8829	4.30	38.108	52	140	(g)
CNSME90P10	0.8662	3.97	38.56	54	137	
CNSME80P20	0.8482	3.76	38.81	56	136	
CNSBD	0.8833	4.30	38.1	52	140	(h)
CNSBD900H100	0.8541	4.18	38.9	50	120	
CNSBD800H100	0.8210	4.12	38.9	48	111	

(a) Mallikappa, Reddy and Murthy 2012; (b) Senthil Kumar and Thirumalini, 2020; (c) Dinesha and Mohanan, 2015; (d) Dinesha and Mohanan, 2018; (c) Kasiraman, Geo andNagalingam, 2016; (f) Vedharaj et al., 2016; (g) Devarajan and Nagappan, 2017; (h) Pandian et al., 2018.

2.8. Investigation of CNSL biodiesel and blend with diesel and other additives in direct injection compression ignition (DICI) engines

In a single cylinder, 4-stroke cycle direct injection compression ignition (DICI) engine, the performance and emission characteristics of CNSL biodiesel with diesel and other fuel additives blends were tested under various load situations and varied speed ranging from 1200rpm to 1500rpm. Various researchers examined and reported on compression ratios, injection pressure, and injection timing (start of injection) with spontaneous aspiration with oxygen enrichment and exhaust gas recirculation. The performance parameters of CNSL biodiesel in comparison to other fuel blends, such as brake power, torque, brake thermal efficiency (BTE), and brake specific fuel consumption (BSFC), as well as emission characteristics, carbon dioxide (CO_2), unburned hydrocarbons (UHC), carbon monoxide (CO), nitrogen oxides (NOx), and smoke opacity, were reported, and they are extremely encouraging for CNSL use as an alternative fuel in the near future.

In an experiment, Velmurugan, Loganathan, and Gunasekaran (2014) heated cashew nut shell liquid CNSL to various degrees in order to make biodiesel, a process known as thermal cracked cashew nut shell liquid (TC-CNSL). When compared to diesel at 1500 rpm, the DICI engine produced a high braking thermal efficiency. However, even when using lesser mixes, specific fuel consumption increased while CO and HC emissions decreased. When comparing B100 to diesel, the heat release and pressure rise were higher for B100, indicating that the ignition delay and biodiesel resulted in a longer combustion duration. In a related study conducted by Dinesha and Mohanan (2015)**,** performance, combustion, and emission of cardanol derived from CNSL was investigated in a DICI single cylinder engine with injection pressure of 200 bar and at 27.5° start of injection before top dead centre (TDC). Three biodiesel blends of B10M10, B20M10 and B30M10 (10%, 20% and 30% cardanol + 80%, 70%, 60% diesel +10% methanol each) respectively was examined at full load conditions of 25%, 50%, and 75%. When comparing the BTE of B10M10 and B20M10 to that of diesel, the findings were identical. Due to lower HC, CO, and smoke, B20M10 as a better fuel blend for CI engines at 200 bar injection pressure at 27.5° BTDC appears promising. Inedible cashew industrial waste and its low cost are other important elements in the use of cardanol biodiesel.

Vedharaj et al., (2015) also investigated the performance, emissions, and economic feasibility of CNSLME in another study. To lower the CNSLME's high free fatty acid concentration, it was transesterified twice and heated without being blended with diesel. The high viscosity of the fuel was reduced at the inlet side of the injector by preheating the CNSLME at a temperature of 80°C, and the result reveals that brake thermal efficiency (BTE) rose by 20%, and HC and CO emissions were lowered, respectively. Among inedible oil considerations, the economic analysis revealed that the CNSL is a good and low-cost feedstock for biodiesel production. In a further study conducted by Vedharaj et al., (2016), in which another processing approach was used to produce CNSL, steam treatment was followed by mechanical crushing method. A zeolite catalyst was used to further crack the CNSL, resulting in catalytically cracked CNSL (CC-CNSL) with improved viscosity and calorific value. The CC-CNSL was blended with diesel at a ratio of 20% CC-CNSL to 80% diesel and tested in a CI engine at 200, 235, 270, and 300 bar injection pressures. In terms of CO (carbon monoxide), HC (hydrocarbons), NOx (oxide of nitrogen), and smoke emissions, the CC-CNSL 20 outperformed diesel. In addition, CC-CNSL20 outperformed diesel in terms of meeting electric generator regulatory norms.

Kasiraman, Geo and Nagalingam (2016), In a study conducted on engine performance, emission, and combustion characteristics were investigated using neat cashew nut shell oil (CNSO) as a base fuel blended with diesel separately with other fuels such as oxygenates, alcohols, and vegetable oils in various proportions by volume. Results show that when compared to diesel and CNSO methyl ester, the performance of neat CNSO is poor. Among the various oxygenate, alcohol and vegetable oil blends, DEE30 blend (CNSO70% + Diethyl ether30%), BUTANOL30 blend (CNSO70% + Butanol30%) and CMPRO30 (CNSO70% + Camphor Oil 30%) has given better performance. Brake thermal efficiency increases to the maximum of 29.68% with DEE30 followed by CMPRO30 of 29.1% and BUTANOL30 of 28.4%. Smoke emission and BUTANOL30 which is lower compared to neat CNSO and CNSOME.

Devarajan, Munuswamy and Nagappan (2017) looked at the practicality of using plain cashew nut shell methyl ester (CNSME100) and alcohol to power an DICI engine. The emission of CNSME100 was investigated by mixing in two different quantities of pentanol and comparing it to the baseline diesel. Pentanol was chosen as an additive

to alleviate the shortcomings of plain CNSME100 due to its higher intrinsic oxygen content and surface to volume ratio. The results of the research revealed that adding additional alcohol to the methyl ester of cashew nut shells reduces emissions significantly. Emissions from neat methyl ester and pentanol mixtures are similarly shown to be lower than diesel at all loads.

Aruna and Vardhan (2017) tested raw cardanol blended with kerosene by volume, such as BK20 (20 percent kerosene and 80 % cardanol), BK30 (30 % kerosene and 70 % cardanol), and BK40 (40 % kerosene and 40 % cardanol) on a 3.5 kW DICI engine (40% kerosene and 60% cardanol). In comparison to diesel fuel, different compression ratios (16:1, 17:1, and 18:1) were investigated using various fuel blends at varying load circumstances. Increased compression ratio from 16:1 to 18:1 improved brake thermal efficiency from 23.87 to 27.30 % for BK20, 26.83 to 29.87 % for BK30, and 24.28 to 28.62 % for BK40, with lower CO, UHC, and smoke emissions. At the greatest compression ratio, NOx emissions increase by 18.7%, 1.8, and 7.3 percent, respectively, for BK20, BK30, and BK40 mixes compared to diesel. According to this study, cardanol–kerosene mixtures can be used as diesel engine fuel at greater compression ratios.

Pandian et al., (2018) investigated cashew nut shell liquid biodiesel (CNSB) made through traditional transesterification and combined with hexanol as an oxygenated addition in an experimental setting. The performance and emission characteristics of a naturally aspirated DICI with a 17:1 compression ratio was tested at constant speed. CNSBD900H100 is a fuel that contains 10% hexanol by volume and 90% CNSB by volume, whereas CNSBD800H200 is a fuel that contains 20% hexanol by volume and 80% CNSB by volume. According to the findings, adding hexanol to CNSB at a concentration of 10% or 20% (by volume) decreases emissions. There was also a significant improvement in brake thermal efficiency and a reduction in brake-specific fuel consumption. In conclusion, hexanol is a promising add-on which will improve CNSLB downsides when utilised in an unmodified diesel engine.

Dinesha and Mohanan (2018) investigated the combined effect of 7% oxygen enrichment with 10%, 15%, and 20% varied intake charge exhaust gas recirculation (EGR) in a DICI engine at variable load conditions. When comparing B20M10 with 7% oxygen enrichment and 20% EGR to B20M10 without oxygen enrichment and 0%

EGR, it was discovered that B20M10 with 7% oxygen enrichment and 20% EGR produces 11.8 percent less NOx. Increased EGR percentages result in greater CO, unburned hydrocarbon (HC), and smoke emissions, as well as lower brake thermal efficiency. The experiments showed that a B20M10 cardanol blend with 7% intake air oxygen enrichment and 15% EGR reduced NOx emissions more effectively, but the performance and other exhaust characteristics were sacrificed. In another study, Sahoo et al., (2019) examined CNSL biodiesel blended with 5% and 10% of n-pentanol by volume in DICI engine at constant speed. It was found that substantial reduction in viscosity was realised when n-pentanol was added to CNSL biodiesel. Brake thermal efficiency (BTE) increased with an improved atomisation which led to a decrease in brake specific fuel consumption. There was associated reduction of carbon monoxide (CO), nitrogen oxides (NOx), hydrocarbon (HC), and smoke emission.

2.9. Utilisation of simulation and modelling techniques in the combustion and emission of CI engines fuelled with biodiesel

Table 2.8 reviews different scientific publications to ascertain the gaps in the usage of modelling and simulation in the investigation of CNSL biodiesel and other biodiesel for combustion and emission processes in a single cylinder, four-stroke cycle direct injection compression ignition (DICI) engine for engine performance, combustion processes, and emission characteristics.

Table 2.8. Review of experimental, numerical modelling, and simulation techniques for combustion and emission characteristics of dici engines using CNSL biodiesel and other biodiesels

S/No	Work or Studies	References	Gaps identified
1	In this study, hexanol and neat cashew nut shell biodiesel is blended to reduce various emissions and improve direct injection compression ignition (DICI) diesel engine performance.	Pandian et al., (2018)	In this study, experimental investigation is the only method used. This study does not include in-cylinder studies that require modelling or numerical simulation.
2	As CNSL is high in free fatty acids, it is trans-esterified in double stages, and instead of being blended with diesel, its CNSLME is directly used in a single-cylinder DICI diesel engine.	Vedharaj et al., (2015)	In this study, experimental investigation is the only method used. This study does not include in-cylinder studies that require modelling or numerical simulation.
3	An experimental investigation using an inedible plant-based biodiesel cardanol derived from cashew nut shell liquid (CNSL) is conducted to investigate the combustion, performance, and emissions of single-cylinder DICI diesel engines.	Dinesha and Mohanan (2015)	In this study, experimental investigation is the only method used. This study does not include in-cylinder studies that require modelling or numerical simulation.
4	This work involved thermal cracking the CNSL at various temperatures to produce biodiesel. The liquid obtained from this process is called thermal cracked cashew nut shell liquid (TC-CNSL). The performance, emissions, and combustion characteristics of a direct injection DICI diesel engine are studied using blends of biodiesel and diesel.	Velmurugan, Loganathan and Gunasekaran (2014)	In this study, experimental investigation is the only method used. This study does not include in-cylinder studies that require modelling or numerical simulation.

5	In this study, raw cardanol, a renewable biofuel, was blended with kerosene and used as a test fuel in a four-stroke variable compression ratio DICI 3.5-kW diesel engine.	Ravindra, Aruna, and Vardhan (2020).	In this study, experimental investigation is the only method used. This study does not include in-cylinder studies that require modelling or numerical simulation.
6	The DICI diesel engine was operated with CNSL as the base fuel in order to study its performance, emissions, and combustion characteristics. This was blended with diesel and separately with other secondary fuels like oxygenates, alcohols, and vegetable oils in various proportions by volume.	Kasiraman, Geo and Nagalingam (2016)	In this study, experimental investigation is the only method used. This study does not include in-cylinder studies that require modelling or numerical simulation.
7	In this study, oxygen enrichment and exhaust gas recirculation (EGR) are combined to examine the performance and emission characteristics of a B20M10 cardanol biofuel blend (20% cardanol, 70% diesel, and 10% methanol by volume). Testing was conducted under various loading conditions on a four-stroke single-cylinder DICI diesel engine.	Dinesha, and Mohanan (2018)	In this study, experimental investigation is the only method used. This study does not include in-cylinder studies that require modelling or numerical simulation.
8	The present study investigates the emission characteristics of neat cashew nut shell methyl ester (CNSME100) by varying the proportions of pentanol and comparing them to baseline diesel. The work further examines the feasibility of operating a DICI engine powered by neat methyl ester and alcohol blends.	Devarajan, Munuswamy and Nagappan (2017)	In this study, experimental investigation is the only method used. This study does not include in-cylinder studies that require modelling or numerical simulation.
9	In place of directly substituting unprocessed CNSL for diesel in the DICI diesel engine, this study used processed CNSL that had been cracked using a zeolite catalyst. The relevance of the current work is further highlighted by the	Vedharaj et al., (2016)	In this study, experimental investigation is the only method used. This study does not include in-cylinder studies that require modelling or numerical simulation.

	fact that CNSL is extracted from the cashew nut shell differently than it is processed to create CC-CNSL (catalytically cracked CNSL).		
10	The experimental work is done on a single-cylinder DICI diesel engine using cashew nut shell liquid (CNSL) biodiesel blended with petroleum diesel at a constant speed.	Bupesh Raja and JayaPrabakar (2019)	In this study, experimental investigation is the only method used. This study does not include in-cylinder studies that require modelling or numerical simulation.
11	This work investigated the effect of intake air enrichment on the performance, combustion, and emission characteristics of a single-cylinder DICI stationary diesel engine fuelled with an inedible alternative fuel, namely, cardanol — diesel — methanol blend.	Dinesha, Nayak and Mohanan (2014)	In this study, experimental investigation is the only method used. This study does not include in-cylinder studies that require modelling or numerical simulation.
12	In this study, a DICI diesel engine with a single cylinder was simulated using multi-dimensional computational fluid dynamics (CFD) simulations incorporating in-cylinder flow and combustion to determine how soybean methyl ester and piston bowl configuration impact engine performance, combustion, and pollutant emissions. The standard engine design features a hemispherical piston bowl. The investigation has been performed on biodiesel blended with diesel and various piston bowl configurations.	Khan, Panua and Bose (2019)	The AVL FIRE algorithm was used to modelled and simulate the in-cylinder flow and combustion process, and experimental data from a baseline hemispherical bowl was utilised to validate the numerical model. No changes were made to injection timing and spray included angle to determine combustion and emissions characteristics.
13	The current work presents an experimental investigation into the effect of different blends of Jojoba methyl ester (JME) on DICI diesel engine performance, combustion, and emissions characteristics. A numerical	Hawi et al., (2019)	The compression ratio was varied in this study but piston bowl configuration, injection timing and spray included angle were not varied in order to study the combustion and emission characteristics.

	investigation of the effect of compression ratio (CR) using neat JME is also presented. A comprehensive numerical setup using the ANSYS FORTE code is developed and validated against measured data.		
14	In this study, cooled exhaust gas recirculation (EGR) was evaluated experimentally and numerically on fuel consumption and emissions from a single-cylinder DICI diesel engine fuelled with B8 (biodiesel and no. diesel 8:92% by volume).	De Oliveira, Yang and Sodré (2021)	The combustion and emissions of biodiesel were evaluated using an experimental and numerical model, but piston bowl configurations, injection timing, and spray included angle were not varied to determine the effect of combustion.
15	In this work, sub-models are developed for combustion analysis in a single-cylinder DICI diesel engine powered by a biodiesel-diesel blend from Pongamia Pinnata trees. A complex combustion phenomenon was modelled using the Computational Fluid Dynamics (CFD) code FLUENT.	Kolhe, Shelke and Khandare (2015)	The combustion and emissions of biodiesel evaluated using an experimental and numerical model, but piston bowl configurations, injection timing, and spray included angle were not varied to determine the effect of combustion.
16	This study investigates the performance and exhaust emissions of a single-cylinder DICI engine powered by biodiesel produced from Australian beauty leaf tree (BLT) oil. In order to predict the engine performance and emissions of biodiesel and petroleum diesel, a combustion model is developed using computational fluid dynamics (CFD) software, AVL Fire.	Hassan, Rasul and Harch (2015)	The combustion and emissions of biodiesel evaluated using an experimental and numerical model, but piston bowl configurations, injection timing, and spray included angle were not varied to determine their effect on combustion and emissions.
17	In this study, AVL Fire was used to investigate the effect of biodiesel premixing on emissions, combustion characteristics, and engine	Asadi et al., (2019)	In this work piston bowl configurations, injection timing, and spray-included angle were not varied to ascertain combustion and emission characteristics.

	performance. To confirm the validity of the study, combustion inside the chamber was simulated with pure diesel fuel and the results were compared with those reported in other publications. There was a very good agreement between engine performance parameters and emissions reported in other research studies.		
18	The study compares simulations and practical results obtained with mango seed (MSME) biodiesel blended with petroleum diesel in B10, B20, and B30 proportions. The CFD simulation was done using ANSYS Fluent for comparison with practical outcomes.	Srinivas and Posangiri (2018)	In this work piston bowl configurations, injection timing, and spray-included angle were not varied to ascertain combustion and emission characteristics.
19	The goal of this project was to model and simulate the combustion of inedible grade oil from Jatropha plant biodiesel fuel using Ansys Fluent to compare to diesel fuel combustion.	Dixit et al., (2020)	In this work piston bowl configurations, injection timing, and spray-included angle were not varied to ascertain combustion and emission characteristics.
20	In this study, ANSYS Forte software is used to simulate a single-cylinder DICI diesel engine to visualize spray inside the combustion chamber. Results indicate that biodiesel penetrates liquid and vapor better, has larger droplet masses and diameters, and has longer breakup times.	Bari et al., 2022	In this work piston bowl configurations, injection timing, and spray-included angle were not varied to ascertain combustion and emission characteristics

2.9.1. The gaps identified in the review

The following gaps were identified in the investigations summarised in Table 2.8:

i. Detailed studies of in-cylinder phenomena, the spray atomisation, spray propagation, mixture formation and combustion processes of CNSL cardanol biodiesel and associated fuel blend are absent in the works reviewed in table 2.8, although the understanding of in-cylinder combustion processes is significant for optimizing engine performance and pollutant formation. In addition, the engine specifications of the experimental setup utilised in all the studies were almost the same, only a few variations were used.

ii. The geometry of the combustion chamber and swirl ratio were not varied to examine mixture formation, fuel droplet evaporation and combustion process. Jaichandar and Annamalai (2012) and Singh et al., (2017) in examining different open piston bowl geometry reveal that combustion chamber geometry influences the spray propagation, air-fuel mixture formation and subsequent combustion process and pollutant formation in diesel engines. Merker, Schwarz and Teichmann (2011) in their work state that the combustion chamber bowls formed in the crown of the piston geometry have a significant influence on the combustion process.

iii. Injection parameters, i.e., nozzle hole diameter and the number of holes were not varied, because the density and viscosity of biodiesel are high, these parts must be altered to optimize performance. Battistoni and Grimaldi (2012), found that the injection system is altogether influenced by higher density and viscosity of biodiesel since both needle movement and flow attributes are altered.

iv. Injection timing was not varied in almost all the experimental investigations. There is a need to examine early and late injection timing in order to analyse and assess ignition delay and combustion processes hence NOx and soot formation. Raeie et al., (2014), gathered in their studies that the utilization of early injection timing gives minimum soot and higher NOx emission than the late injection. How faster the spray propagation and mixture formation take place is proportional to the amount of heat release rate hence the peak pressure according to Mollenhaur and Tshoeke, (2010).

2.10. Summary

The literature study contains information on cashew nut shell liquid and associated cashew plant products, such as cashew fruits and nuts (kernel), as well as cashew apples. The Cashew nut (Kernel), from which CNSL is extracted and used in a number of chemical applications, including CNSL biodiesel, is the most important and frequently used cashew plant commodity. The inedible cashew nut shell liquid (CNSL) as a biodiesel feedstock is the subject of this study. Cashew apple post-harvest wastes have also been identified as a potential source of bioethanol, which could aid in the transesterification of CNSL methyl ester biodiesel and act as a direct fuel supply for spark ignition engines. According to the evaluation, CNSL biodiesel meets ASTM biodiesel requirements, and standards. With minimal physicochemical alteration, the fuel attributes of CNSL biodiesel are nearly identical to those of diesel, which makes it a viable future biodiesel for compression ignition engines. After the extraction of CNSL, the cashew business commonly uses the empty cashew nut shell waste for inexpensive energy, which is used directly for boiler operations and also as briquettes for other energy purposes. The availability of solar energy in most tropical places where cashew is farmed can also be used to process cashew nuts and extract CNSL, according to this study. Global and SSA cashew nut with shell output increases yearly, according to FAOSTAT statistics (2020), showing the accessibility of cashew nut shell as a resource for CNSL biodiesel production. CNSL has the potential to cut global demand for fossil fuels, lowering carbon footprints and mitigating global warming. The study then goes on to discuss recent trials and studies on the engine performance and exhaust emission outputs of CNSL biodiesel fuelled DICI engines. In the review, it was demonstrated that preheating and blending CNSL biodiesel with diesel fuel and oxygenated fuel additives significantly reduced kinematic viscosity, as well as improved engine performance. The kinematic viscosity of the CNSL biodiesel fuel is the largest hurdle, although it may be reduced using a variety of methods such as thermal cracking, emulsification, pyrolysis, mixing, transesterification, and preheating. According to the review, detailed evaluations of in-cylinder phenomena, spray propagation, spray atomization and mixture formation, and combustion procedures of CNSL cardanol biodiesel and associated fuel blend were lacking from the majority of the experiments and investigations. Understanding in-cylinder combustion processes,

as well as combustion geometry design, are critical for improving engine performance and reducing pollutant production, they are the gaps identified.

CHAPTER 3

Combustion in direct injection compression ignition engines

In direct injection compression ignition (DICI) diesel engines, combustion control is a critical feature for optimum fuel economy, clean emissions, and powerful performance. This chapter discusses combustion and associated end products in the direct injection compression ignition (DICI) engines. These includes, the four phases of combustion process, influencing variables of mixture formation, step by step sub-processes in diesel DICI engine combustion, essential combustion characteristics of DICI diesel engines and finally, pollutant formation.

3.1. Introduction

The compression ignition (CI) engines (diesel engines) of today have evolved from Rudolph Diesel's 3:1 compression ratio engine of 1890 to compression ratios of up to 22:1 with high-pressure fuel injection systems capable of producing 10,000 horsepower. Due to the higher compression ratios, no throttling, lower operating speed than spark ignition (SI) engines, and a lean air/fuel combination, CI engines have high thermal efficiencies (up to 45%) and in most load ranges, CI engines outperform SI engines (McAllister, Chen and Fernandez-Pello, 2011; Mollenhauer and Tschöke, eds., 2010).

The CI engine forms a fusion of air-fuel blend in the combustion chamber when diesel fuel is injected some degrees before top dead centre (BTDC), which then initiates an automatic ignition through a combustion process. The combustion is an unstable process that occurs at numerous points simultaneously in a very non-homogeneous mixture at a rate controlled by fuel injection. The injection continues until the cylinder has received the desired amount of fuel. The rate at which injection takes place and the speed at which mixing develops has a great influence on energy conversion in CI engines (Mollenhauer and Tschoeke, 2010).

Atomization, vaporization, fuel-air mixing, and combustion continue until almost all the fuel has been processed. Moreover, throughout the combustion and expansion processes, the residual air in the cylinder is mixed with burning and already consumed gases. The air intake in CI engine is unrestricted, and the amount of fuel injected per

cycle controls engine torque and power production. It is, therefore, necessary to use a high self-ignitable fuel to initiate ignition within the guaranteed high-temperature environment of the combustion chamber (Pulkrabek, 2007; Ferguso and Kirkpatrick, 2015; Heywood, 2018).

It is critical to reduce heat losses to the combustion chamber walls in order to get the highest possible thermal efficiency from a diesel engine. In fact, the geometrical shapes of combustion chambers must constantly be maintained in such a way that the ratio of total surface area to volume is as little as possible (Heywood, 2018; Hillier and Coombes, 2004; Nunney, 2007). A high compression (compression ratio of 12:1 to 22:1) is used and in some instances, additional heating is used when starting the engine from a cold state. The available pressure and temperature in the combustion chamber should be about 5 MN/m^2 and 800 ^oC simultaneously and getting close to the top dead centre at compression stroke, temperature tends to rise faster before the top dead centre of the compression stroke (Hillier and Coombes, 2004; Nunney, 2007).

3.2. Phases of combustion process

Initial combustion descriptions were based on three phases, but due to increased precision in combustion predictions and new insights, the combustion process in CI engines has been subdivided into four phases (Stone, 1999; Zhao, 2009), as seen in Figure 3.1. The delay period is the first phase AB. It is defined as the interval between the start of injection and the first identifiable increase in pressure in the indicator diagram, which signifies the initiation of fuel injection and the combustion process. The flame spread period is the second phase BC, during which combustion begins and spreads at a faster pace due to the presence of air/fuel that meets during this time. The time period beginning with thermal ignition – which can be viewed as the point shown in the indicator diagram when the pressure increases – and ending when the maximum pressure is attained is referred to as the sudden pressure increase. The third phase CD occurs when the injected diesel burns as soon as it reaches the maximum temperature region in the combustion chamber. This is the time when the highest pressure is reached, and the highest temperature is reached. The final phase D is when the combustion is completely controlled by diffusion until all the air/fuel in

the combustion chamber has been used. This is the delayed post-combustion phase, which can last up to approximately half of the whole combustion period. (Stone, 1999; Hillier and Coombes, 2004; Nunney, 2007; Zhao, 2009).

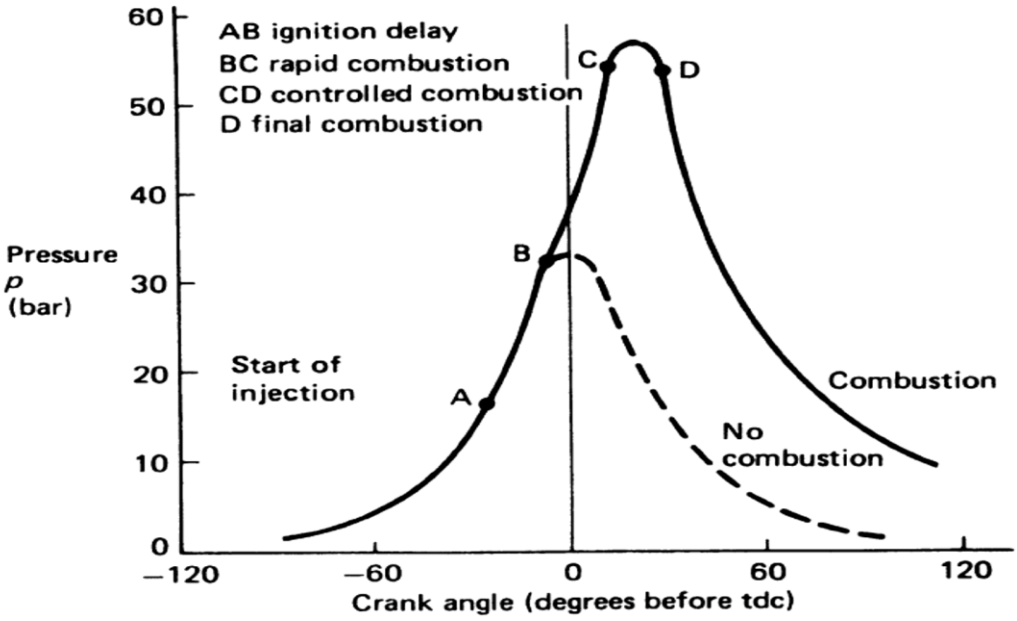

Figure 3.1. Four phases of combustion (Stone, 1999).

3.3. Mixture formation and combustion sequence

In diesel engines, the injection rate and mixture formation speed have an impact on energy conversion. Because the mixture is heterogeneous, there is no flame propagation like in gasoline engines, and there is no risk of “knocking combustion.” Thus, diesel engines can produce high compression ratios and boost pressures. The time required for fuel evaporation and mixture generation restricts the speed of a diesel engine because it is internal (Mollenhauer and Tschöke, 2010).

Nitrogen oxides occur in zones with extra air and high temperatures, as shown in Figure 3.2. The temperature of combustion in the lean outer flame zone is so low that the fuel cannot fully oxidize. The spray core contains air-deficient zones where unburned hydrocarbons get generated, along with soot particles and carbon monoxide precursors.

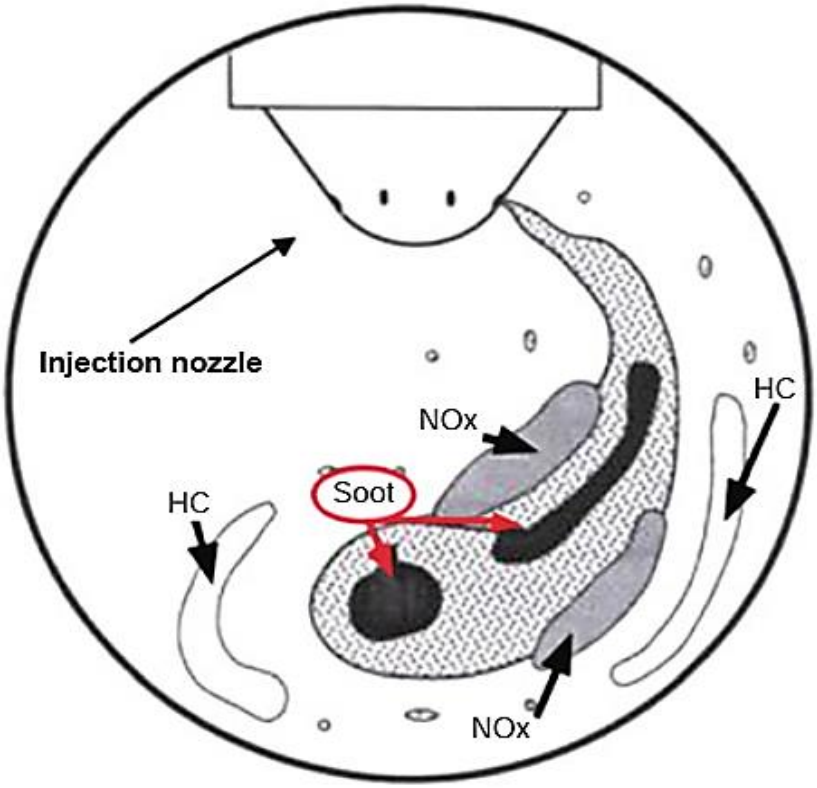

Figure 3.2. Combustion chamber with a heterogeneous mixture and its regions where pollutants are produced (Mollenhauer and Tschöke, 2010).

Modern diesel systems strive to oxidize particles in the engine since the rich mixture area makes it impossible to prevent soot formation in a heterogeneous mixture. This can be significantly enhanced by maintaining or increasing turbulence throughout the expansion stroke. As a result, contemporary diesel engines can burn up to 95% of the particles produced in the engine (Heywood, 1988; Mollenhauer and Tschöke, 2010).

3.3.1. Influencing variables of mixture formation

Aside from the air movement in the combustion chamber (squish or squish flow and air swirl), which can be modified by the architecture of the combustion chamber and the intake port, the injection is largely responsible for internal mixture generation. The following duties must be accomplished by an injection system: provide the requisite injection pressure, meter the fuel, ensure spray propagation, ensure rapid spray breakup, create droplets, and mix the fuel with combustion air (Heywood, 1988; Mollenhauer and Tschöke, 2010).

3.3.2. Air motion in direct injection CI engines

As the fuel is injected into the bulk of the air in open chamber CI engines, the turbulence of the air in the combustion chamber is very important at the time of fuel injection and throughout the combustion process. In the combustion chamber, there are two types of air velocity: (a) air swirl (spiral flow) and (b) air radial flow (squish) (Heywood, 1988).

3.3.3. Air swirl (Spiral flow)

Air swirl is a “rotary flow of solids” around the cylinder axis, the rotational speed of which can be influenced by the intake port design, and which rises with engine speed as the piston velocity increases. The primary role of the air swirl is to break up the dense fuel spray and mix the air sectors between the fuel sprays. Obviously, as the number of nozzle holes grows, the swirl need reduces (Mollenhauer and Tschöke, 2010). When air rushes tangentially into the cylinder, it is very easy to create a swirl. Helical ports, in which the air spirals within the port, are more suited for this as shown in Figure 3.3.

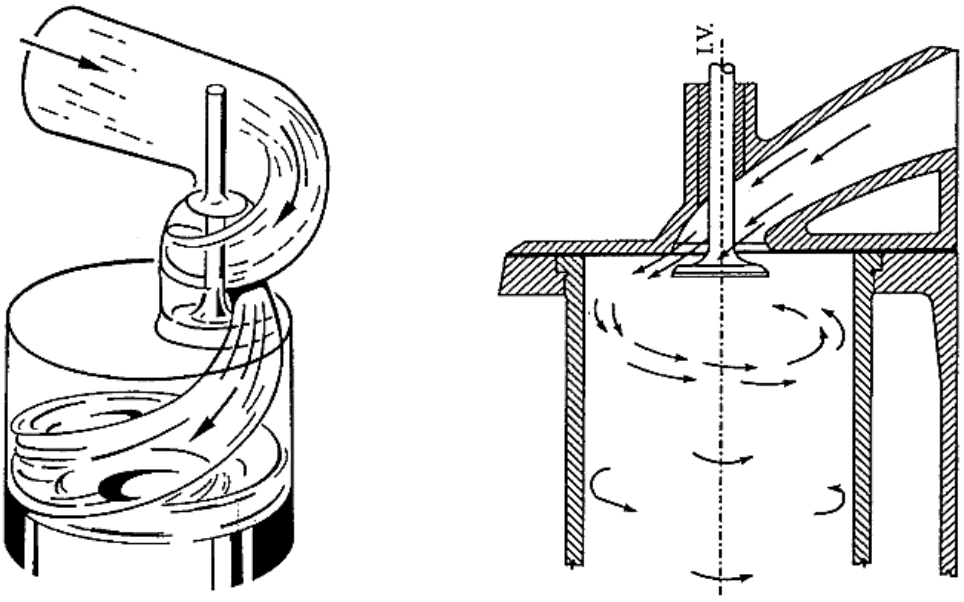

Figure 3.3. Induction induced swirl (Heywood, 1988; Mollenhauer and Tschöke, 2010).

3.3.4. Air radial flow squish

As air is pushed into the piston bowl during the compression stroke, the air swirls more. The small sizes piston bowl gives more swirls. As the piston approaches the top dead centre, a squish flow begins to interfere with the air swirl formed by the intake flow into the cylinder or combustion chamber bowl. The displacement of air between the piston crown and the cylinder head into the piston bowl causes the squish flow. The combustion chamber shown in Figure 3.4 is used in diesel engines which normally houses a bowl within the crown of the piston, significantly affecting the combustion process. The injector nozzle orifices coupled with high injection pressures enables a very fine atomization and mixture formation, supported by the turbulence swirl of combustion chamber gasses (Merker, Schwarz and Teichmann, 2011).

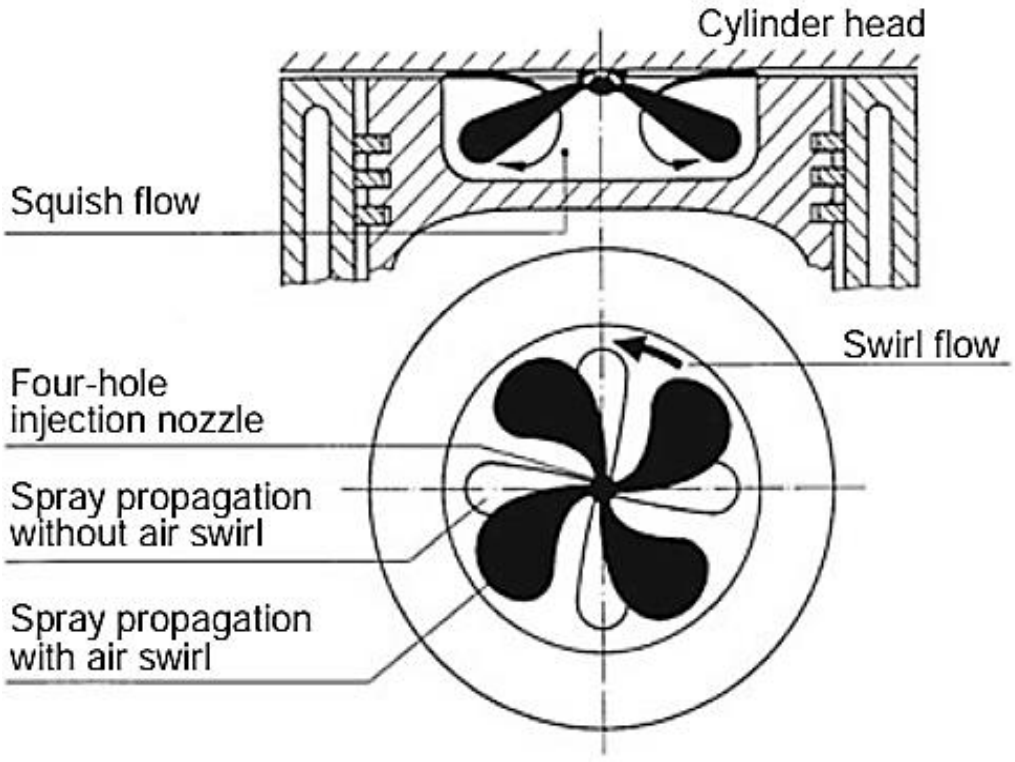

Figure 3.4. The swirl and squish flow structures in a bowl combustion chamber (Mollenhauer and Tschöke, 2010).

The mixture formation is mainly reliant on the diffusion of the diesel fuel sprayed coupled with the in-cylinder air-flow pattern and the interactive energy which is generated by the fuel injected. Figure 3.4 shows a diagrammatic perspective of the two kinds of in-chamber flow structures vital for mixing development in a direct injection compression ignition (DICI) engines, swirl, and squish flow. The squish and

swirl flow are imperative, and it helps in the change of the rate of mixing of air and fuel. (Heywood, 1988; Merker Schwarz and Teichmann, 2011).

3.3.5. The kinetic energy of fuel injection

The fuel metering system and the combustion chamber are linked by the injector nozzle. From vehicles to enormous 2 stroke marine CI engines, the injected fuel is driven via tiny orifices ranging from 0.12 mm to 1.5 mm, and the injection is done at a very high pressure (Merker, Schwarz and Teichmann, 2011). Table 3.1 shows a step-by-step sub-process in diesel (CI) engine combustion. The kinetic energy of the fuel spray is an important factor in mixture formation.

Table 3.1. Step by step sub-processes in diesel (CI) engine combustion

Sub-combustion processes	
Injection atomization	➢ Flow in the nozzle hole ➢ Spray formation ➢ Spray atomization
Spray development	➢ Drop formation ➢ Drop distribution Spectrum ➢ Drop disintegration mechanisms
Mixture formation	➢ Drop evaporation ➢ Drop collision and coalescence ➢ Local air-fuel ratio
Ignition	➢ Low-temperature reaction kinetics ➢ Ignition delay
Combustion	➢ Turbulent transport processes ➢ High-Temperature reaction kinetics ➢ Time and length scales ➢ $C_x H_y$ – Oxidation
Soot and NO formation	➢ OHC- Equilibrium ➢ Zeldovic Mechanism ➢ PAH and Soot formation

In addition to the fuel mass of the injection spray, it is impacted by the pressure gradient at the injector nozzle. The spray cone angle influences the momentum exchange between combustion chamber, air, and fuel spray, as well as the droplet diameter size range. Above all, the spray cone angle is determined by the internal nozzle flow, which is determined by the nozzle design, as well as the nearby pressure and air density. The spray cone angle grows larger as the cavitation in a nozzle hole rises, and the momentum exchange with the air becomes more intense. The injection spray carries the fuel to the outskirts of combustion chamber. This function should not be overlooked because air is highly compressed, heated, and consequently viscous. It is crucial to pay attention to the pressure curve at the nozzle hole. It is preferable to have rising or at least steady pressure as a function of injection time (Heywood, 1988; Mollenhauer and Tschöke, 2010).

3.3.6. Spray breakup

The fuel spray propagation during injection, as depicted in Figure 3.5, can be divided into two primary areas, one with a dense spray close to the injector nozzle and another with a less dense spray further down the stream. Primary spray breakup refers to the strong fuel spray's first disintegration. Secondary spray breakdown occurs when existing droplets break up and become atomized because of streamlining forces created by the relative velocity between the droplet and the combustion chamber surrounds. Furthermore, atomized fuel droplets that collide end up combining. The fuel sprayed energy causes the surrounding combustion chamber air to be enhanced into a fine spray. The momentous heat transfer from the surrounding temperature of the hot chamber walls enables the fine fuel droplets to heat up and the atomized mixed hot fuel/air at this point start to evaporate (Heywood, 1988; Zhao, 2009; Mollenhauer and Tschöke, 2010).

The rate of fuel evaporation is determined by the amount of air that infiltrates into the spray, the droplet size formed on the primary and secondary breakdown, and the available conditions of the combustion. Numerous models are already available in the literature that provide a better understanding of fuel spray propagation and mixture generation, in accordance with the model presented in Figure 3.5. Spray breakup is

subdivided into phases (Baumgarten, 2006; Zhao, 2009; Merker, Schwarz and Teichmann, 2011; Stiesch, 2013).

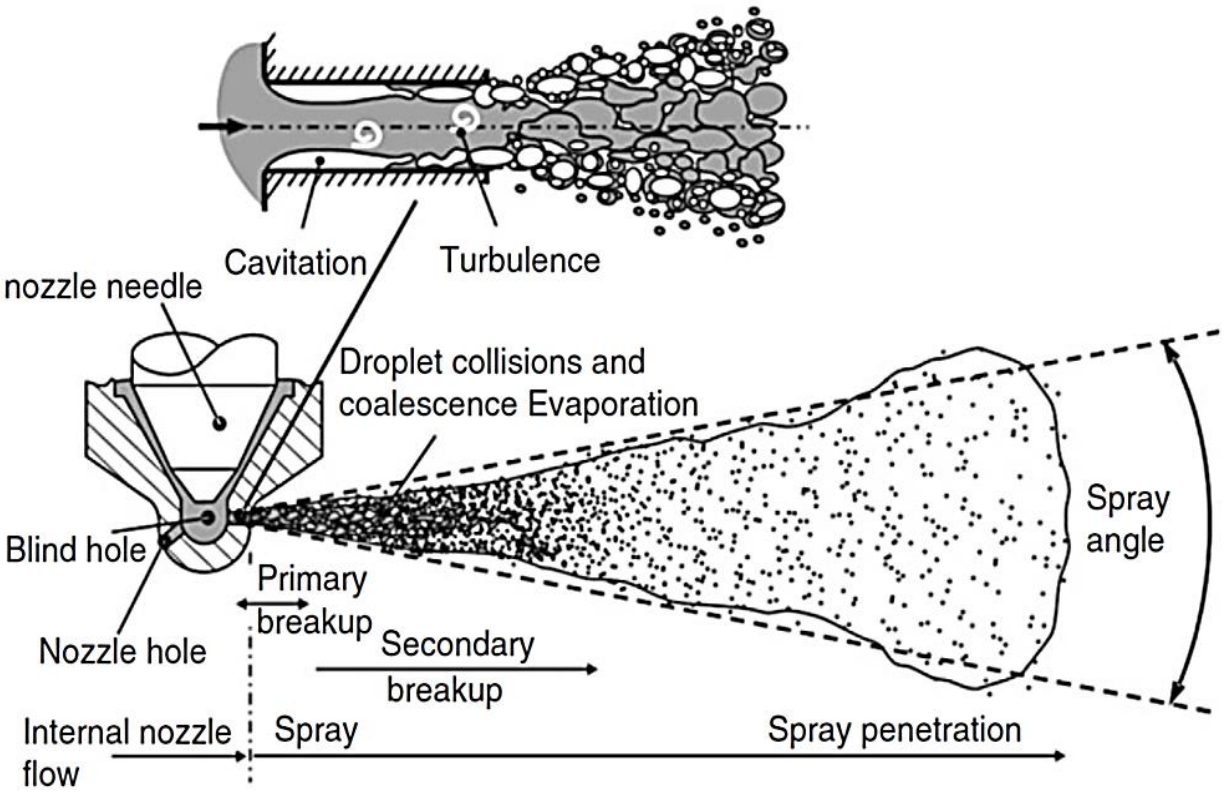

Figure 3.5. The schematic sketch of internal nozzle flow and spray propagation (Baumgarten 2006 as cited in Merker Schwarz and Teichmann, 2011).

3.3.6.1 Primary breakup

In this phase, the turbulent and still compact spray (mostly liquid) is splintered into single droplets through the formation of individual ligaments. Although internal nozzle processes (such as cavitation) play a significant part in this, they are phenomena that cannot be quantified. The redistribution of the velocity profile inside the spray (interaction of different segments in the spray), the surface tension, the aerodynamic forces (exchange of momentum between moving spray and “resting” air), the turbulence (largely induced by the spray momentum), and the cavitation all influence the primary breakup of a fuel spray injected into highly compressed, highly viscous combustion chamber air. Cavitation is caused by the turbulent movement of the fuel in the nozzle. Strong deflections, which are influenced by the ratio of the nozzle curvatures to the hole radius, hydrodynamic flow effects, and hole form and conicity,

all play a role. In nozzle holes, cavitation bubbles influence spray breakup, spray propagation, droplet formation, as well as the formation of deposits in a hole and the durability of a nozzle (Zhao, 2009; Mollenhauer and Tschöke, 2010).

3.3.6.2 Secondary breakup

Secondary breakdown includes: – individual droplet impulse exchange with air – colliding and new formation and/or further breakup of droplets. During secondary breakup, the fuel is evaporating and mixing with the air. The secondary breakage “atomizes” the injectable spray from coarse ligaments into medium and microdroplets through wavy disintegration and atomization. The creation of the latter is required for quick heating and evaporation, and therefore for decreasing the physical ignition delay. Aerodynamic forces play a big role in secondary atomization. Injection pressure, injection pressure curve, spray cone angle, and air density are all significant influencing factors (Heywood, 1988; Zhao, 2009; Mollenhauer and Tschöke, 2010).

It is important to pay attention to two effects that occur simultaneously during secondary breakup: (a) by accelerating the deformation of the primary droplets, frictional forces act on the spray core because it has a greater inertia than the spray edge. (b) Shearing of droplets in the millimetre range caused by disintegration of spray edges caused by wavy disintegration.

3.3.6.3 Spray propagation

The temporal and spatial propagation of fuel in the combustion chamber is referred to as spray propagation. An analytical description of spray propagation is not conceivable, as previously stated. However, to quantify this process, global spray parameters have been established, and empirical models based on experimental data have been developed. Figure 3.6 illustrates the most essential spray parameters – spray angle Θ_0 and spray penetration E_0 (Zhao, 2009).

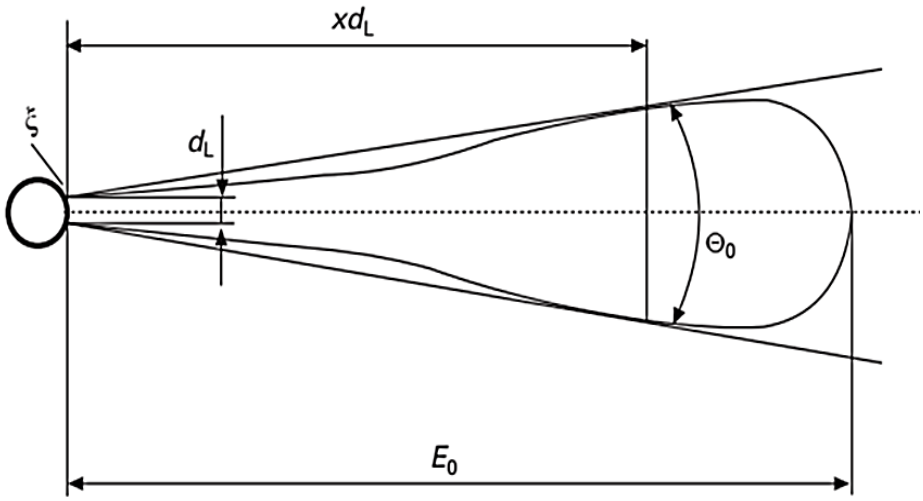

Figure 3.6. The penetration depth and the spray angle without swirling are the spray parameters (Zhao, 2009).

3.3.6.4 Spray angle

An analysis performed by Arai et al., (1984) shows the spray angle Θ_0 (Figure 3.6) as follows:

$$\Theta_0 = 0.05\sqrt{\frac{d_L}{\nu_G \rho_G}}.\sqrt{\rho_G \Delta p_m} \tag{3.1}$$

d_L = nozzle diameter

ν_G = kinematic viscosity of gas (air)

ρ_G = density of gas (air)

Δp_m = average pressure

The shape of the nozzle hole, i.e., the diameter and length of the hole in the nozzle and the diameter of the sac hole:

$$\Theta_0 = 83.5\left(\frac{\rho_G}{\rho_K}\right)^{0.26}\frac{d_L^{0.37}}{d_{SL}^{0.15} l_L^{0.22}} \tag{3.2}$$

where:

$\rho_K = density\ of\ fuel$

$d_{SL} = diameter\ of\ sac\ hole$

$l_L = length\ of\ nozzle\ hole$

Wakuri et al., (1990), on the other hand, claim that just the density ratio of air and fuel determines the opening angle:

$$\Theta_0 = 2\ arctan\left[0.427\left(\frac{\rho_G}{\rho_K}\right)^{0.35}\right] \tag{3.3}$$

3.3.6.5 Spray penetration

In the formulations of Arai et al., (1984), a 'breakup' time t_v is established, which is the time for the spray core to fully develop. After this moment, the spray's behaviour as a function of time changes.

According to this, in the interval $0 < t < \Delta t_E$, the following apply for swirl-free flow in the combustion chamber:

$$t_v = 28.65\frac{\rho_K d_L}{\sqrt{\rho_G \Delta p_m}} \tag{3.4}$$

$$E_0(t) = 0.39 t V_K^0 \tag{3.5}$$

$$E_0(t) = 2.95\sqrt{t d_L \sqrt{\frac{\Delta p_m}{\rho_G}}} \tag{3.6}$$

where:

Δt_E = injection time

E_0 = spray penetration

t = time

V_K^0 = initial velocity of spray

Wakuri et al., (1990) offers an improved formula for penetration that is in good agreement with experimental results from Binder (1992).

$$E_0(t) = \sqrt{\frac{1}{tan(\Theta/2)} t d_L \sqrt{\frac{2\xi\Delta p_m}{\rho_G}}} \tag{3.7}$$

where ξ = flow coefficient.

The cross-sectional area of the spray to be considered for impulse exchange between air and fuel is defined by the spray angle. The flow coefficient ξ identifies the effect of friction during injection (Zhao, 2009).

3.3.6.6 Spray atomization

Fuel drips break down into tiny droplets. Atomization will be faster and more efficient if the injection drop size is smaller (Pulkrabek, 2007). The injection pressure and the injection nozzle influence the atomization quality of the fuel, with several parameters, in addition to the diameter of the nozzle hole, being important in the latter case: (a) The ratio between the diameter and the length of the nozzle hole; (b) the degree of rounding/properties of the injection orifice; (b) the turbulence of the flow inside the nozzle (Zhao, 2009).

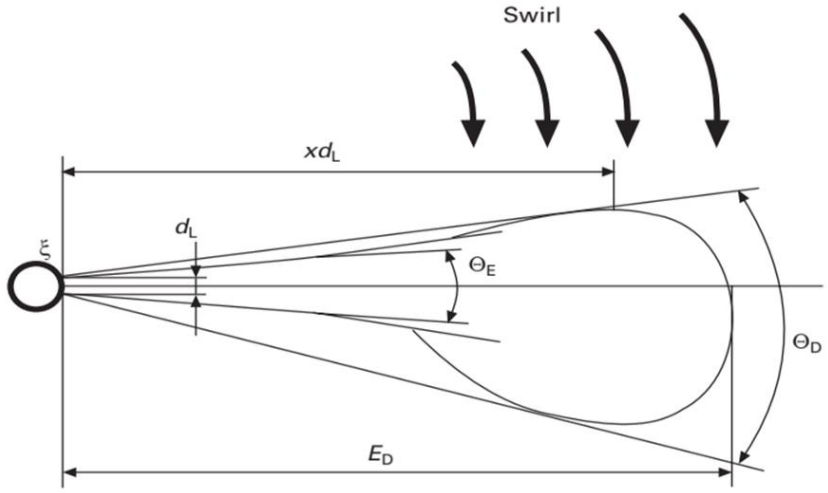

Figure 3.7. Spray parameters: penetration depth and opening angle with swirl.

$$\Theta_D = \Theta_0 \left(1 + \frac{-\omega_D E_0}{V_K^0}\right)^{-1} \quad (3.8)$$

$$E_D = E_0 \left(1 + \frac{\omega_D E_0}{V_K^0}\right)^{-1} \quad (3.9)$$

where:

Θ_D = spray angle with swirl

E_D = spray penetration depth with swirl

ω_D = air angle velocity

The values for cone angle and penetration depth must be adjusted if the flow is subject to swirl. This adjustment is made via the air angle velocity ω_D Figure 3.7 (Zhao, 2009).

3.3.6.7 Fuel vaporization

The liquid fuel vaporizes into microscopic droplets. Due to the heated air temperatures caused by the high compression of CI engines, this happens relatively quickly. The high air temperature required for this vaporization process necessitates a compression ratio of roughly 12:1 in CI engines. Within 0.001 seconds after injection, 90% of the fuel pumped into the cylinder was evaporated. During evaporation, the immediate surroundings are cooled by evaporative cooling. This has a significant impact on later evaporation. The combination of high fuel concentration and evaporative cooling near the fuel jet's centre causes adiabatic fuel saturation. After further mixing and heating, evaporation in this region will cease, and the fuel will only be evaporated after more mixing and heating (Pulkrabek, 2007). Chemical reactions can take place in the resulting heterogeneous combination of air and liquid fuel droplets of different sizes and distribution since the fuel is vaporous. The heat transmission of compressed air to liquid fuel is of critical relevance (Mollenhauer and Tschöke, 2010).

3.3.6.8 Mixing and self-ignition

The fuel vapor must mix with the heated air after vaporization to generate a combustible combination. The high fuel injection velocity, together with the swirl and turbulence in the cylinder and the non-homogeneous distribution of air-fuel ratio that develops around the injected fuel jet, causes this mixing. The air-fuel combination begins to self-ignite at roughly 8° BTDC, 6 – 8° after injection begins. Secondary processes, such as the breakdown of big hydrocarbon molecules into smaller species and partial oxidation, occur before actual combustion. These exothermic reactions, which are produced by the high-temperature air, raise the air temperature in the immediate area. This eventually leads to a long-term combustion process (Pulkrabek, 2007; Zhao, 2009; Mollenhauer and Tschöke, 2010).

The velocity of the process that creates ignition radicals as a result of thermal excitation of the molecules determines the ignition performance of the fuel delivered into the compressed and heated combustion chamber air. The circumstances for auto-ignition are determined by the thermodynamic parameters in the combustion chamber, such as pressure and local temperatures, as well as the local concentration of vapor, which are dependent on the heating and diffusion processes following secondary

breakdown. The fuel itself, of course, has a significant role. Its ignition quality is determined by the cetane number CN. The higher the cetane number, the more easily a fuel can be ignited. For compliance with extremely rigorous exhaust and noise requirements, cetane levels greater than 50 are desirable (Pulkrabek, 2007; Zhao, 2009; Mollenhauer and Tschöke, 2010).

3.4. Combustion phenomenology

Combustion begins with simultaneous self-ignition at a number of sites in the fuel jet's modestly rich zone, where the equivalency ratio is between 1 and 1.5. Approximately 70% to 95% of the fuel in the combustion chamber is in the vapor form at this time. Even where self-ignition did not occur, multiple flame fronts extending from the many self-ignition sites swiftly consume all the gas mixture that is in a correct combustible air-fuel ratio when combustion begins. This causes a rapid rise in temperature and pressure within the cylinder, which reduces the vaporization time and ignition delay time for more fuel particles, resulting in more self-ignition spots and speeding up the combustion process. After the first fuel has burned, liquid fuel is still delivered into the cylinder. After the initial start of combustion, when all the combustible air-fuel mixture is swiftly burned, the pace at which fuel can be injected, atomized, evaporated, and mixed controls the rest of the combustion process. The gradual pressure rise that happens following the initial quick rise shows this rate of combustion, which is now regulated by injection rate. Combustion lasts around 40° to 50° of engine rotation, significantly longer than fuel injection, which lasts only 20° (Pulkrabek, 2007; Zhao, 2009; Mollenhauer and Tschöke, 2010).

Mixture formation cannot be separated from the complete combustion process in diesel (CI) engine combustion operations. The fact that fuel spray propagation, mixture formation, and combustion progress occur in a greater partial simultaneity is an essential distinguishing aspect of the diesel engine combustion process. During ignition delay, only a small portion of the sprayed injected fuel mixes to a near homogenous state with the hot air in the combustion chamber. This hot air fuel mixture combusts almost instantaneously after being ignited. Following that, mixture creation and combustion in the chamber occur simultaneously, with the mixture formation processes controlling combustion. Numerous models currently accessible in the

literature provide a better understanding of fuel spray propagation and mixture generation (Baumgarten, 2006; Merker, Schwarz and Teichmann, 2011; Stiesch, 2013).

A conceptual cross-section model in Figure 3.8 describes a quasi-steady state during main combustion, and it is considered only valid under quiescent conditions. The sprayed fuel enters the combustion chamber, where it reacts with the air and evaporates. The air ratio in the spray then increases with increasing distance from the injection nozzle as well as distance from the spray axis. A rich mixture zone forms as the sprayed fuel goes downstream, allowing partial oxidation of the fuel air mixture and temperatures up to 1600 K. A rich mixing zone forms downstream of the liquid penetration length, resulting in partial oxidation of the fuel and temperatures of up to 1600 K. According to Flynn et al., (1999), as stated in (Merker, Schwarz, and Teichmann, 2011), the air fuel ratio in this zone is in the range of 0.25 < to <0.5, and roughly 15% of heat is emitted.

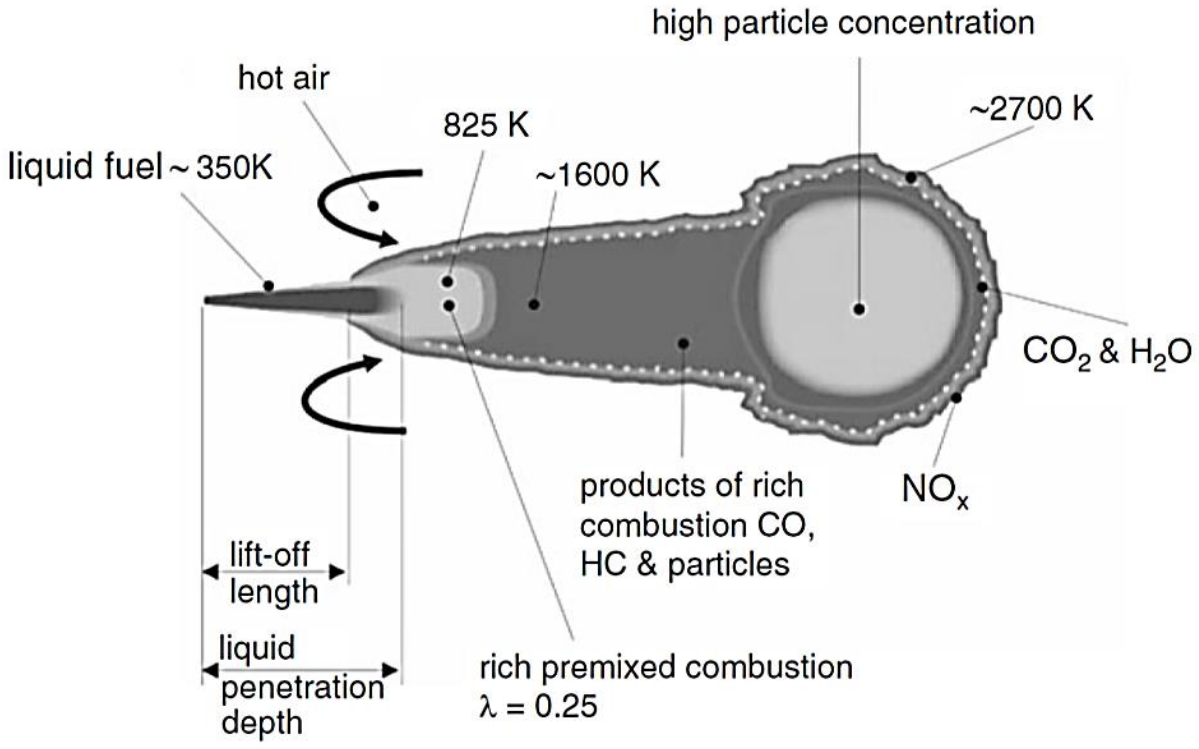

Figure 3.8. The conceptual model of diesel combustion, according to Dec (1997) and Flynn et al., (1999) as cited in Merker, Schwarz and Teichmann, 2011)

Further downstream, the partially oxidized product creates rich premixed combustion particles, which are then delivered into a good diffusion flame, where they are

completely oxidized into carbon dioxide and water. The temperature in this zone can reach 2700K, and because of the high temperatures in this location, nitrogen oxides occur near the lean side of the oxidized diffusive flame. In terms of soot generation, the lift-off length, which is the axial distance from the injector nozzle to the diffusive flame, is a critical feature of a diesel combustion flame. The injection process is completed after the combustion, and the fuel spray receives no further impetus from the injection; however, the flame jet structure transforms into pockets of very fine premixed products surrounded by a diffusive flame (Heywood, 1988; Merker, Schwarz and Teichmann, 2011).

3.5. Essential combustion characteristics of DICI diesel engines

The combustion process depends on the characteristics of the fuel, design of engine combustion chamber and fuel injection system and engine operating conditions. It is an unsteady, heterogeneous, three-dimensional combustion process (Heywood, 1988). The following parameters are crucial to determining the combustion process effectiveness: in-cylinder pressure, ignition delay, combustion duration, rate of heat release, cumulative heat release rate and fuel mass burn fraction. The other combustion parameters can be estimated from the in-cylinder pressure, which can be measured straight from the engine (Heywood, 1988). Using the in-cylinder pressure and the geometry of the crank and connecting rod, the heat release rate is calculated using the first law of thermodynamics. The heat release rate fluctuation over an engine cycle can be used to estimate the other critical combustion characteristics (Tesfa et al., 2013; Rajasekar and Selvi 2014; Kale, 2017).

3.5.1. In-cylinder pressure variations with crank angle

During the development and calibration stages of the engine, the in-cylinder pressure measurement is considered a very significant source of information. The in-cylinder pressure signal can be used to determine peak pressure, pressure and crank angle (P– θ) diagram, estimated mean effective pressure, fuel supply effective pressure, heat release rate, combustion duration, ignition delay, and other parameters (Heywood, 1988; Payri et al., 2010).

The temperature and pressure of the fuel-vapor air mixture are above the ignition point, which prevents fuel oxidation chemistry. As a result, after a little delay, spontaneous igniting (autoignition) of portions of the non-uniform fuel-air mixture within these sprays starts the combustion process, and the cylinder pressure (solid line) as illustrated in Figure 3.9 climbs above the nonfiring engine level as fuel chemical energy is released. The peak cylinder pressure in a CI engine is determined by the burned fuel fraction during the premixed burning phase (Payri et al., 2010; Heywood, 2018).

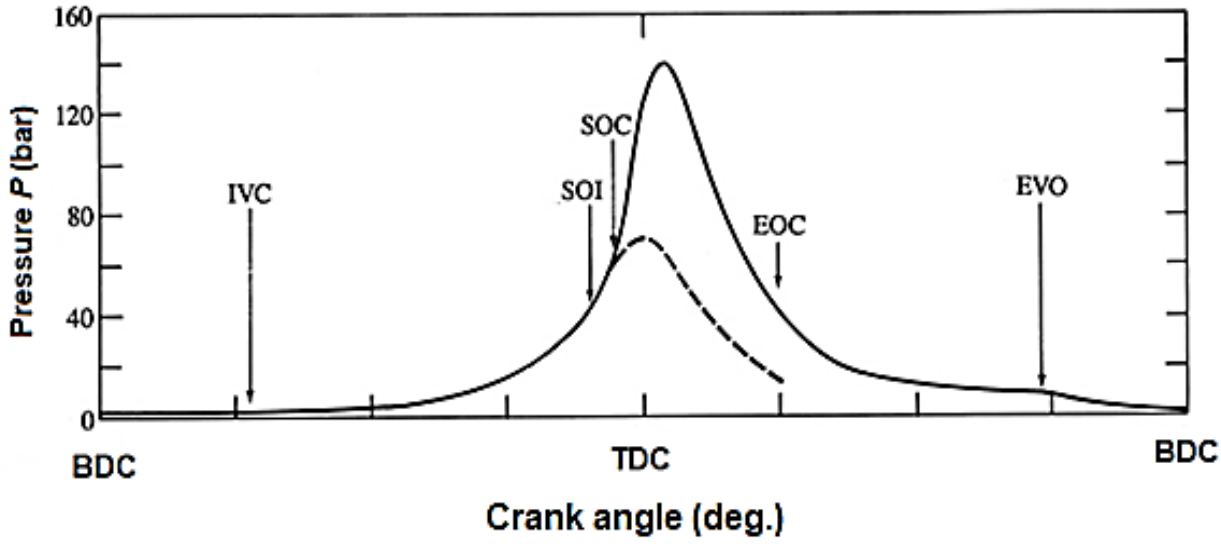

IVE- Inlet valve closed; SOI- Start of injection; SOC-Start of combustion; EOC- End of Combustion; EVO-Exhaust valve closed.

Figure 3.9. Cylinder pressure p – θ diagram (cylinder pressure p – solid line, firing cycle; dashed line – motored cycle) (Heywood, 2018)

3.5.2. Heat release rate (HRR)

The energy release profile in Figures 3.10 has a double peak structure, which is typical of diesel combustion. During the premixed combustion phase, the first peak occurs due to the quick burning of the fraction of the injected fuel that has evaporated and mixed with the air during this time. Because the initial mixing is independent of the injection length, the energy release curve in the premixed combustion phase is relatively independent of the load. The mixing-controlled combustion produces the second peak (Bari, 2013; Heywood, 2018).

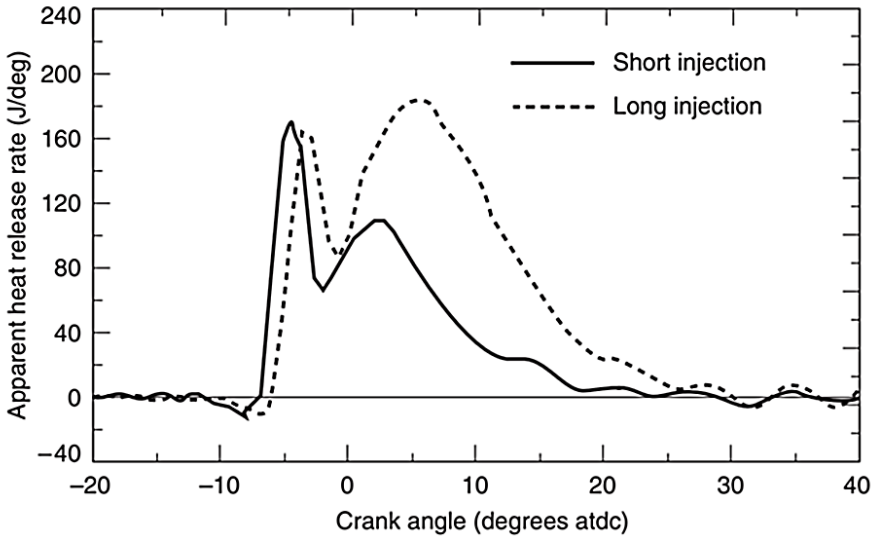

Figure 3.10. An example of a short- and long-term fuel injection energy release profile (Ferguson and Kirkpatrick, 2015).

The amount of energy released during this phase is determined by the injection time. The amount of fuel injected increases as the injection time is raised to match a greater engine load, increasing the amplitude and duration of the mixing-controlled energy release. Following the ignition delay period, the premixed fuel–air mixture burns fast, rapidly releasing heat, followed by diffusion combustion, where the burning rate is governed by the availability of combustible fuel–air mixture (Ferguson and Kirkpatrick, 2015; Kale, 2017; Heywood, 2018). The net heat-release rate, which is the difference between the gross heat-release rate and the heat-transfer rate to the walls, equals the rate at which work is done on the piston plus the rate of change of sensible internal energy of the cylinder contents (Heywood, 2018). The difference between the gross heat-release rate dQ_n/dt and the heat-transfer rate to the walls dQ_{ch}/dt is the net heat-release rate, dQ_{ht}/dt, which equals the rate at which work is done on the piston plus the rate of change of sensible internal energy of the cylinder contents (Heywood, 2018).

$$\frac{dQ}{d\theta} = \frac{1}{\gamma - 1}\left(\gamma p \frac{dV}{d\theta} + V \frac{dp}{d\theta}\right) \tag{3.10}$$

The first law of thermodynamics is used to model the heat release rate. Equation 3.10 depicts the simplified model. The cylinder content is a homogeneous mixture of air

and combustion products in Equation 3.10, where $\frac{dQ}{d\theta}$ is rate of heat release (kJ/deg), P is the in-cylinder gas pressure, V is in-cylinder pressure, and γ is the ratio of specific heats. It is also always believed that during the combustion process, a constant temperature and pressure exist.

The engine geometry specification and the cylinder pressure recorded during the testing were utilised to calculate the heat release rate (HRR) of the internal combustion engine using Equation 3.8 (Kale, 2017; Heywood, 2018). Figure 3.11 shows the various succession processes during heat release.

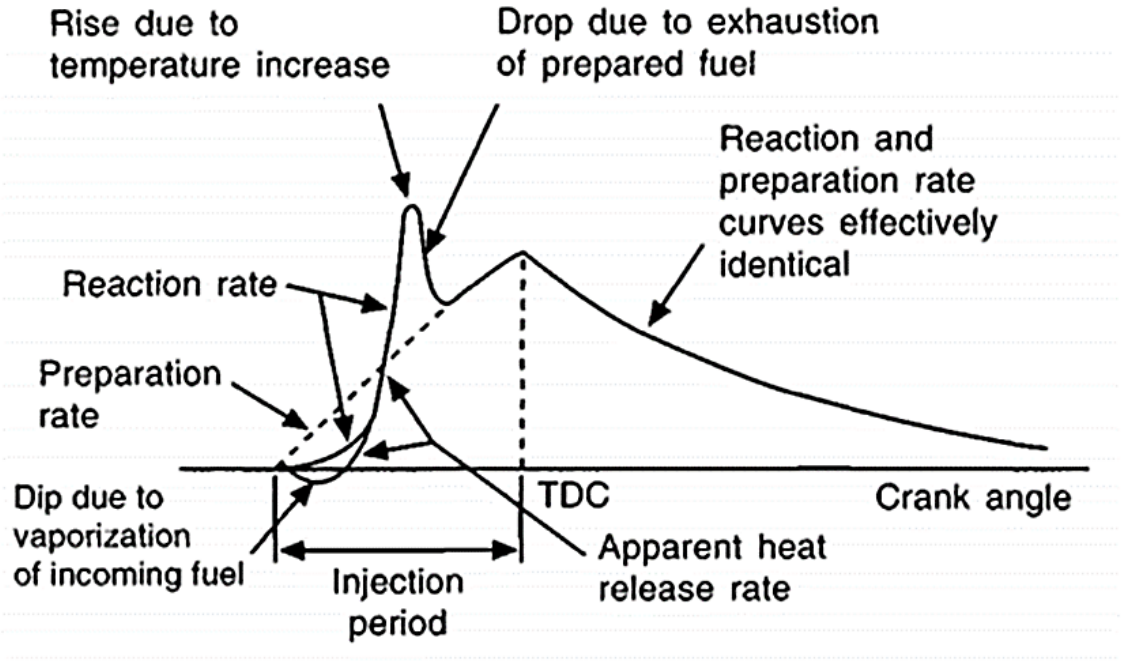

Figure 3.11. Heat release rates (HRR) (Challen and Baranescu, 1999)

3.5.3. Cumulative heat release rate

The cumulative heat release rate graph is shown in Figure 3.12 as a function of crank angle. The cumulative heat release curve can be used to estimate combustion. Combustion is defined as the time interval between the commencement of combustion and the angle at which 90% of the heat is discharged (Çelik et al., 2017). The cumulative heat release is a crucial measure for determining the combustion process' efficiency.

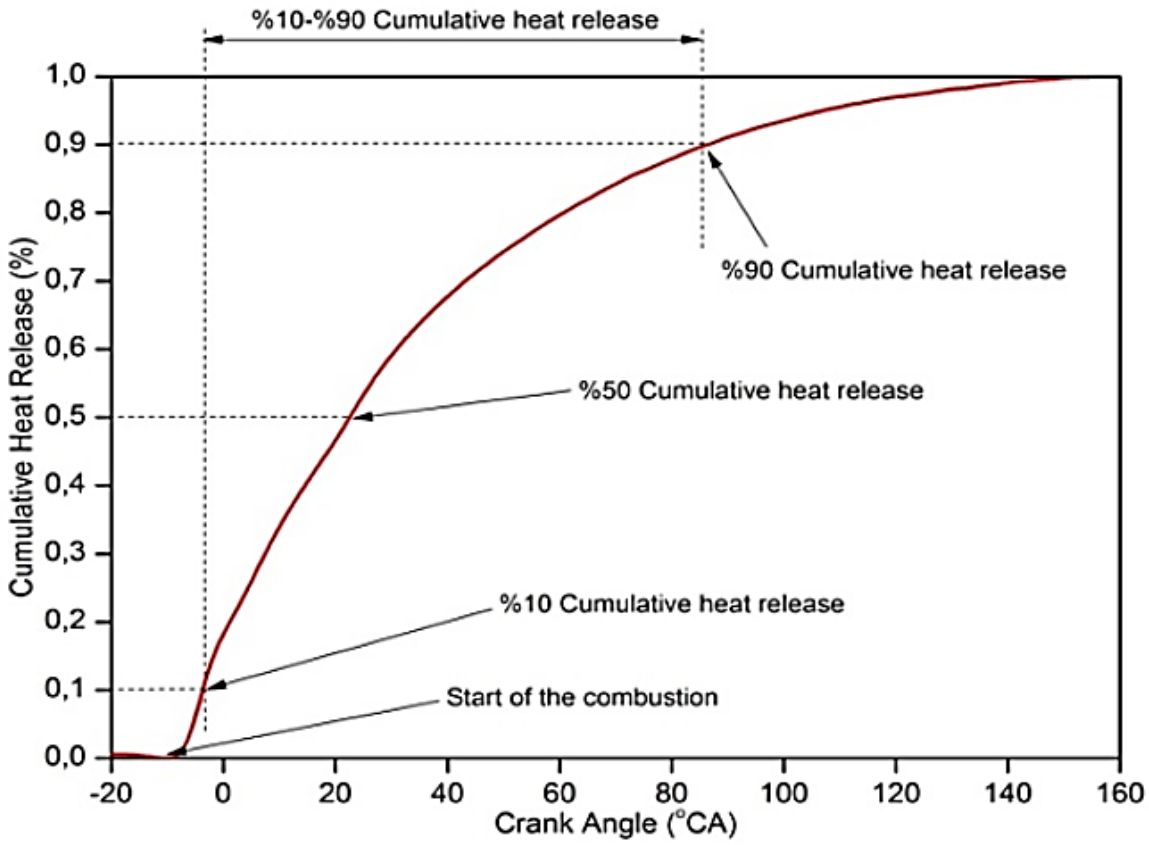

Figure 3.12. Cumulative heat release with crank angle (Çelik et al., 2017).

Equation 3.11 is used to calculate the cumulative heat release (Q_{ac}) in a combustion cylinder.

$$Q_{ac} = \int dQ = \int \frac{\gamma}{\gamma-1}(PdV + VdP) \qquad (3.11)$$

In comparison to diesel, biodiesel has a tendency for late heat release in the early stages of combustion, as shown in the graph (Kale, 2017).

However, at a later stage of burning, the CHR value of diesel fuel quickly exceeds that of biodiesel. The lower heating value (LHV) of biodiesel relative to diesel fuel is the fundamental reason for the drop in CHR. Due to an increase in the amount of gasoline injected into the cylinder, CHR rose as the engine load increased. (Shahabuddin et al., 2013; Xue, 2013; Kale, 2017)

3.5.4. Fuel mass burning rate

The actual fuel burn rate is unknown since not all the fuel is burned with sufficient air to produce the products of complete combustion. In the first one-third of the whole combustion period, about 60% of the fuel has burned. The total fuel mass burned should be equal to the integral of the fuel mass burning rate over the combustion process; in this case, it is 3 % less than the total fuel mass injected. It is worth noting that chemical energy is released far into the expansion process. However, the accuracy of this form of calculation suffers as a result of mistakes in estimating heat transfer, which have a considerable impact on the apparent fuel-burning rate (Ferguson and Kirkpatrick, 2015; Heywood, 2018).

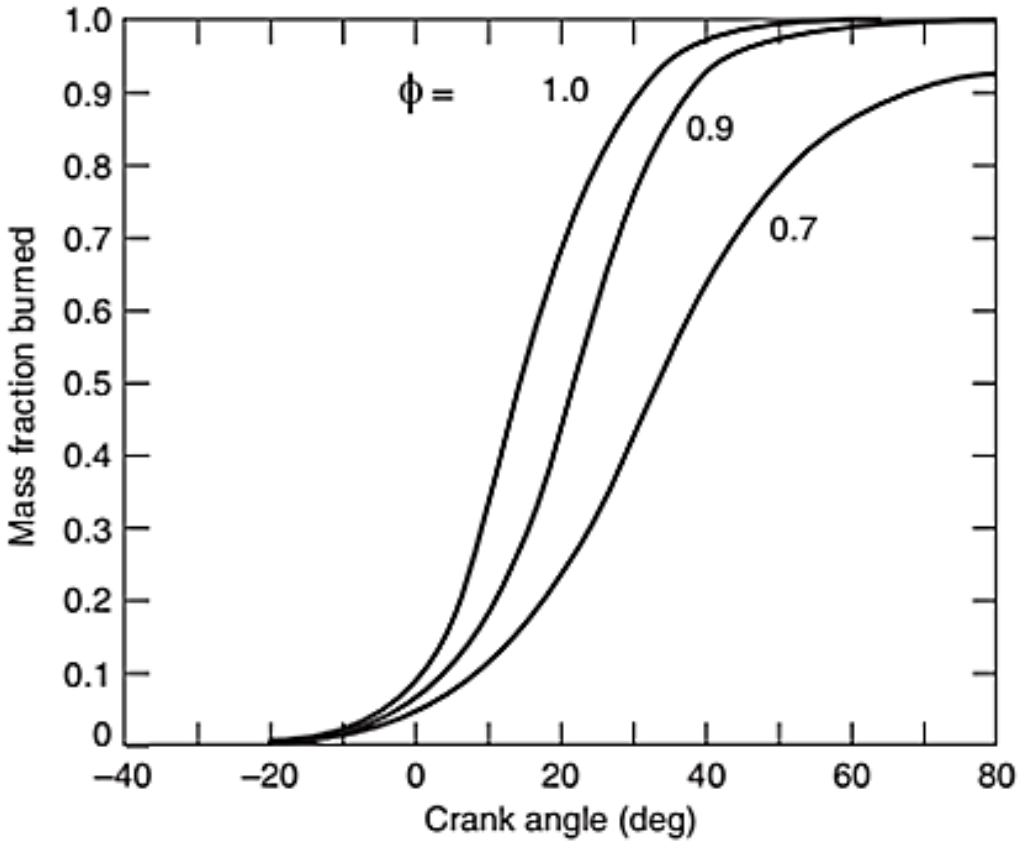

Figure 3.13. Mass-fraction burned curves for varying equivalence ratios (Ferguson and Kirkpatrick, 2015)

An apparent fuel mass burning rate is the end outcome. It’s better to think of it as the fuel chemical-energy or heat-release rate after multiplying by the heating value of the fuel. The mass of fuel burned increased by around 5% as a result of the heat-transfer changes of 50%. The phasing of the pressure data changed more dramatically.

It should be emphasized that precise pressure data (in magnitude and phasing) is a prerequisite for useful heat-release or fuel-mass-burning rate analysis (Ferguson and Kirkpatrick, 2015; Heywood, 2018). Figure 3.13 shows representative results, with the ignition delay and combustion duration parts of the mass-fraction burned curve increasing as the equivalence ratio is reduced (Ferguson and Kirkpatrick, 2015; Heywood, 2018).

3.5.4. Ignition delay (ID) and combustion duration (CD)

The velocity of the process that creates ignition radicals because of thermal excitation of the molecules determines the ignition performance of the fuel delivered into the compressed and so heated combustion chamber air. One of the most important aspects of the combustion process is the ignition delay (ID). The first stage of heat release, also known as the ignition delay, is a charge preparation stage in which injected liquid fuel is atomized, mixed, and disseminated in hot compressed air. Liquid fuel vaporization and a chemical kinetics stage precede the start of fuel pyrolysis reactions during this delay interval. There is a period of unburned fuel accumulation and apparent inactivity within the cylinder during this part of the overall burn (Keating, 2007; Mollenhauer and Tschöke, 2010; Heywood, 2018).

The start of fuel injection (SOI) represents a point on the needle-lift signal that is just beginning to increase from zero. The second derivation of in-cylinder pressure, in which the crank angle point passes through zero before increasing to the maximum value of slope, was used to estimate the start of combustion (SOC). The ignition delay for any fuel can be calculated using the time between the start of fuel injection and the start of combustion i.e., the crank angle between the SOI and SOC is the ignition delay (ID) (Keating, 2007; Heywood, 2018). There are a few factors that can affect how long the delay period occurs before ignition and rapid pressure rise, which includes: Fuel cetane number, compression ratio, injection pressure, fuel injection rate, inlet air temperature, coolant temperature, piston speed, fuel droplet size and fuel latent heat of vaporization (Heywood, 1988; Keating, 2007).

3.5.4.1. Ignition quality of fuel

The physical and chemical qualities of the fuels will influence the ignition delay time, with chemical properties being significantly more important than physical properties, according to researchers (Singh et al., 2020). With diesel and biodiesel, the cetane number is utilised to determines the ignition quality. A greater cetane number means a shorter igniting delay in general. Singh and colleagues (Singh et al., 2020). It is critical to utilise the correct cetane number of fuels for a given engine. The cetane number is a measurement of ignition delay that must be matched to a certain engine cycle and injection method. Ignition delay, given as a cetane number, can be referred to as fuel quality if specific requirements are met. Figure 3.14 depicts these interactions graphically.

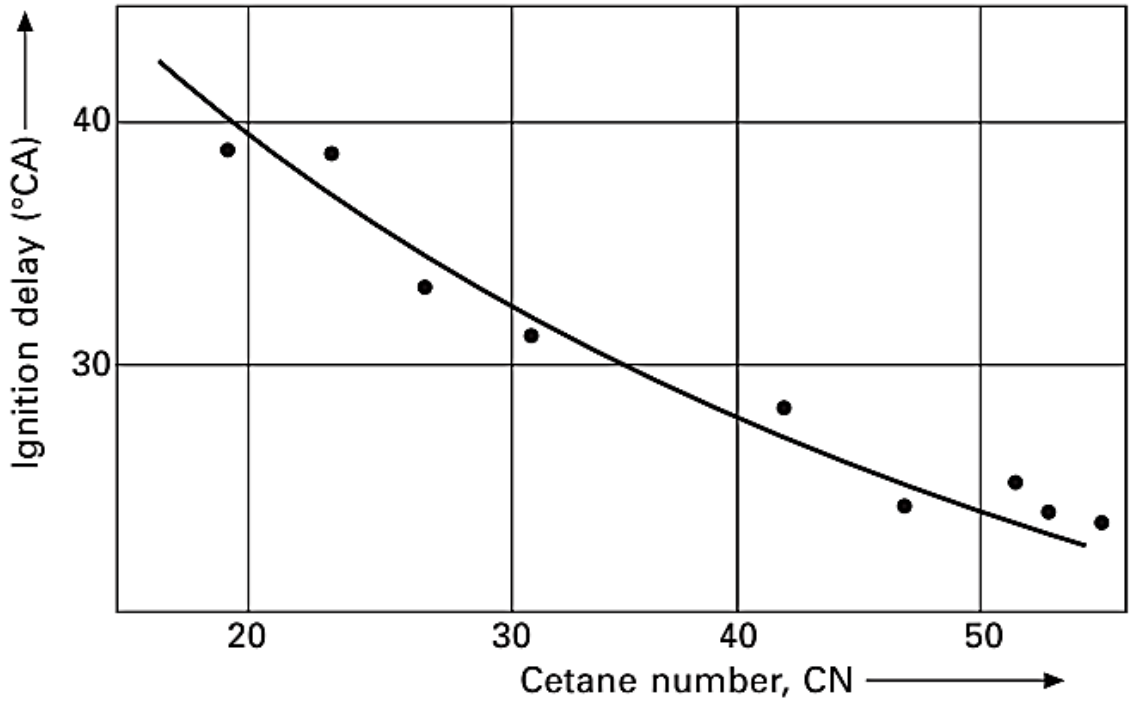

Figure 3.14. Ignition delay of fuels with varying ignition quality versus cetane number (Zhao, 2009)

As illustrated in Figure 3.15, if the cetane number is low, the ignition delay is too long, and more fuel is delivered into the cylinder than is desirable before combustion begins. When the cetane number is excessively high, combustion begins too soon before TDC, resulting in a loss of engine output. Commonly used fuels have cetane values in the range of 40-60 (Keating, 2007; Heywood, 1988). Small amounts of specific

additives can be blended with the fuel to modify the cetane number. Nitrites, nitrates, organic peroxides, and certain sulphur compounds are among the additives that enhance ignition (Pulkrabek, 2007).

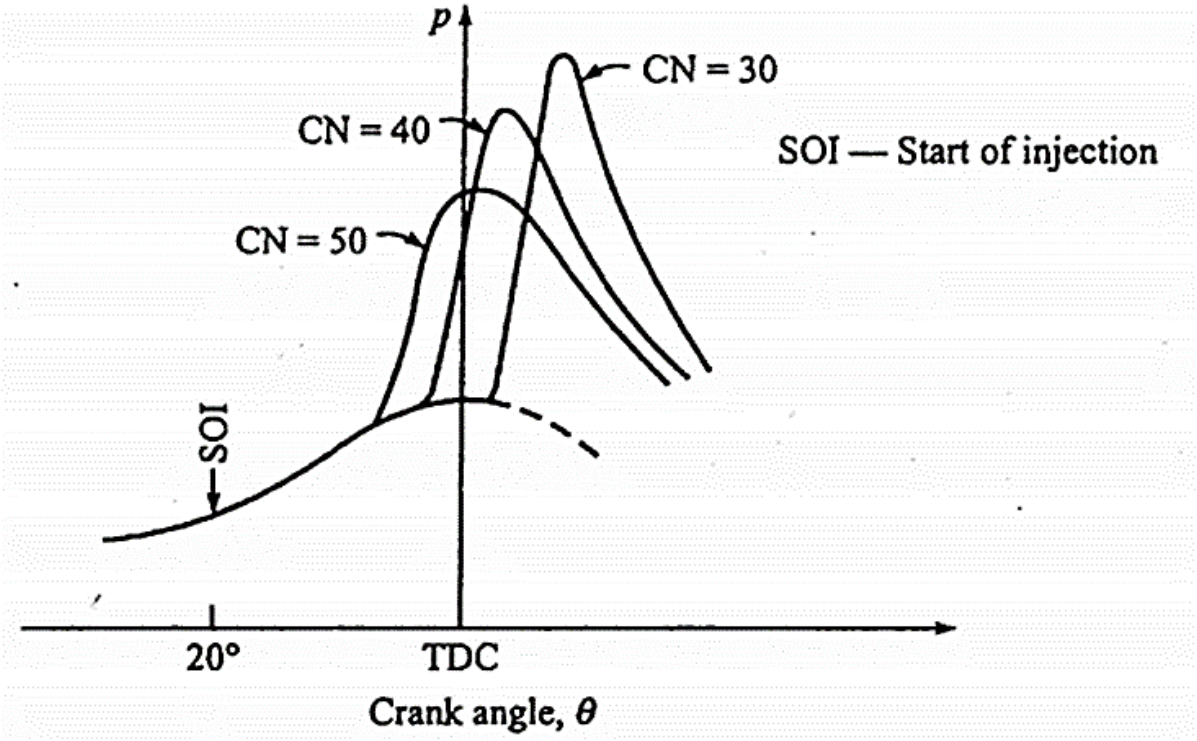

Figure 3.15. Effect of Cetane number (CN) on the *p*-*θ* diagram. (Heywood, 1988)

3.5.4.2. Compression ratio

Increasing the compression ratio will raise the initial charge reaction air temperature, i.e., molecular collisions, and chemical kinetic rates at TDC and shorten the delay. Increasing inlet air temperature for a specified compression ratio may also shorten this delay (Keating, 2007). At the start of injection, a higher compression ratio raises the temperature and pressure of the air. This shortens the delay period and makes the engine run more smoothly. As shown in Figure 3.16, variation in compression ratio will have a typical effect on the p-θ diagram when injection timing, speed and fuel quality are held constant. As the compression ratio increases, the delay period decreases (Heywood, 1988; Keating, 2007).

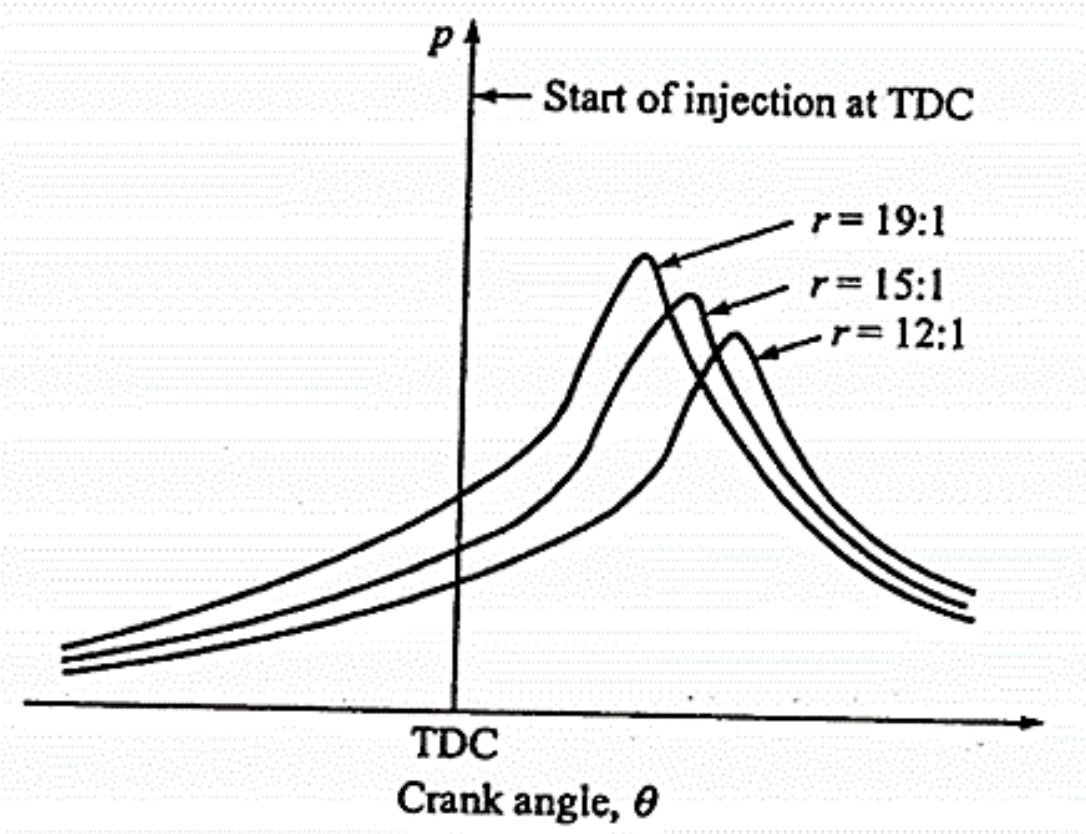

Figure 3.16. Effect of compression ratio on the p-θ diagram (Heywood, 1988).

3.5.4.3. Injection timing

The minimum delay occurs with the initiation of injection at roughly 10° BTDC under normal engine circumstances (low to medium speed, fully warmed engine). When the injection timing is earlier or later, the temperature and pressure of the air change, increasing the delay. If injection begins earlier, the delay will be longer as the temperature and pressure are lower at the start. When injection begins later (near to TDC), temperature and pressure are slightly higher at first, but gradually decrease as the delay progresses. The best conditions for ignition are found in the middle (Heywood, 2018).

If injection is too early, ignition delay time will increase because temperature and pressure will be lower. If injection is late, the piston will move past TDC, pressure and temperature will decrease, and again ignition delay time will increase (Keating, 2007; Heywood, 1988). Figure 3.17 shows the indicator diagrams obtained at various angles of injection, i.e., 10°, 20° and 30° advance at a constant time of injection, with the most

beneficial angle being about 20° before TDC. The ideal injection advance angle is determined by a few factors, including the compression ratio, air pressure and temperature at the cylinder inlet, injection characteristics, load, and engine speed, and so on. (Heywood, 1988; Keating, 2007; Pulkrabek, 2007)

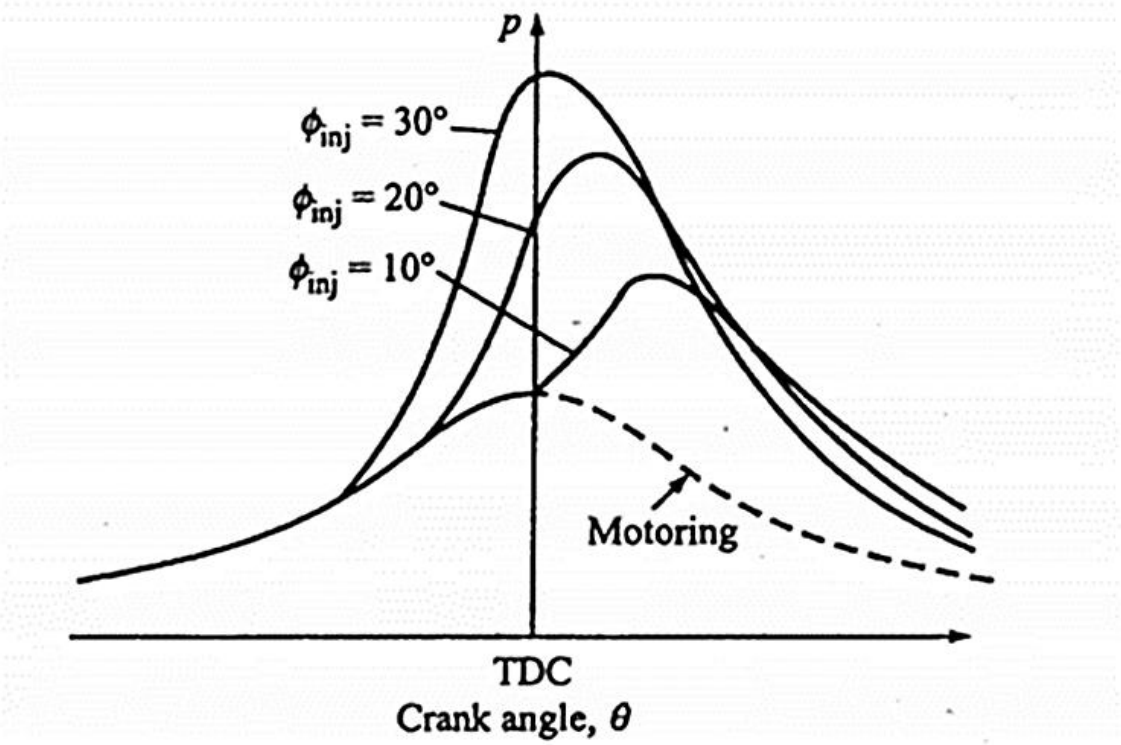

Figure 3.17. Indicator diagrams at various injection advance angles,ϕ_{inj} (Heywood, 1988).

3.5.4.4. Injection pressure

High injection pressures, in general, should shorten delay period by influencing the size, velocity, and dispersion of fuel droplets. The size of the fuel droplet will affect the delay period; larger droplets will cause longer delays, whilst small droplets may not have enough momentum to provide effective fuel dispersion. Because initial injection happens in a high-oxygen environment with low reaction rates, but the end of fuel injection occurs in a lower-oxygen environment with greater temperatures and response rates, fuel injection rate is also a role in delay (Heywood, 2018).

3.5.4.5. Engine speed

When measured in milliseconds, increases in engine speed at constant load result in a modest reduction in ignition delay; when measured in crank-angle degrees, the delay grows virtually linearly. The temperature/time and pressure/time correlations alter as engine speed changes. In addition, as the speed of the engine increases, so does the injection pressure. Because there is less heat loss during the compression stroke, the peak compression air temperature rises with increasing speed (Heywood, 2018).

3.5.4.6. Air/fuel ratio

The cylinder wall temperature and combustion temperatures are dropped as the air/fuel ratio is increased, resulting in an extended delay period. Except at very high air/fuel ratios, there is very little reduction in the maximum rate of pressure rise.

3.5.4.7. Load on engine

The residual gas temperature and the wall temperature both rise as the engine's load rises. As a result, the charge temperature upon injection is higher, which reduces the delay time.

3.6. Pollutant formation

The exhaust gas would only contain the chemical species carbon dioxide (CO_2), water (H_2O), and molecular nitrogen (N_2) in the ideal scenario of full burning of a hydrocarbon fuel with stoichiometric air. In the case of lean equivalence ratios, molecular oxygen (0_2) was equally found in the products. However, there are two factors that prevent complete combustion in an actual combustion system: (i) chemical processes in general never go totally in one direction, but they always approach a state of equilibrium between products and reactants. As a result, at least some reactants will remain. (ii) non-ideal local boundary conditions include mixture distribution, temperature, and turbulence level. As a result, flame extinction may occur, along with the development of wholly new products, such as soot or nitrogen oxides, or the formation of unburned or partially burned species. As a result, extra components are

present in combustion engine exhaust gases. Carbon monoxide (CO), unburned hydrocarbons (HC), nitrogen oxides (NO_X), and particulate matter, which is commonly referred to as soot, are among these components. There may also be traces of sulphur oxides (SO_X) in the exhaust gas, depending on the quality of the fuel (Heywood, 2018; Stiesch, 2003).

Combustion end products cause harm at a wide range of scales. Carbon monoxide, soot, oxides of nitrogen, and unburned hydrocarbons directly harm the health of organisms that inhale the emissions. Nitrogen oxides, unburned hydrocarbons, and sulphur oxides negatively affect the environment of cities and counties. On a global scale, increased atmospheric carbon dioxide concentrations contribute to global warming through enhancement of the greenhouse effect. Unburned hydrocarbons and soot are known to be carcinogenic and cause respiratory issues. Carbon monoxide binds to haemoglobin in the blood, preventing the blood from carrying oxygen. The combined content of NO and NO_2 is referred to as NO_x. The nitrogen in the air is largely used to make these nitrogen oxides. NO, like CO, binds to haemoglobin in the blood and can be fatal if inhaled in large amounts. Above all, NOx is the primary contributor to smog and acid rain. Smog is formed by photochemical reactions caused by the ultraviolet light of the sun irradiating NOx. Photochemical smog is made up of a variety of toxic chemicals that induce respiratory issues and allergies (Correa,1993; McAllister, Chen and Fernandez-Pello, 2011).

For a variety of fuels, global characteristics such as gaseous mixture ignition delay time, flame velocities, and the strain rate required to extinguish diffusion flames may be estimated in reasonable agreement with experiments. The concentration profiles of fuel, oxidizer, intermediate products, and major products (CO_2, N_2, and H_2O) of combustion processes may also be predicted with fair accuracy. The most essential chemical routes that lead to the creation of air pollutants, such as CO, NOx, soot, and dioxins, are well understood today (Heywood, 1988; McAllister, Chen and Fernandez-Pello, 2011; Heywood, 2018).

The pollutant production processes are greatly influenced by the fuel distribution and how it varies over time as a result of mixing with hot air. An illustration of how certain parts of the fuel spray and diffusion flame can affect the formation of NO, unburned

HC, and soot (or particulates) during the “premixed” and “mixing controlled” phases of diesel combustion in a direct injection engine with swirl is shown in Figure 3.18.

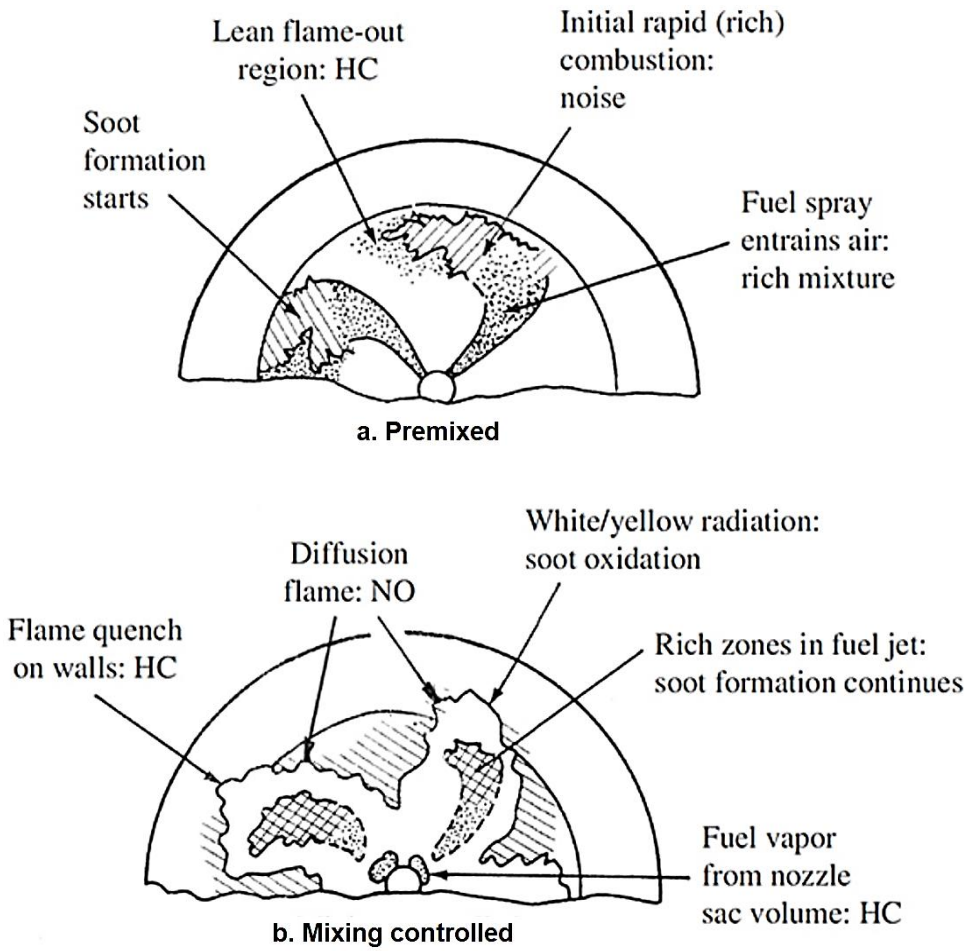

Figure 3.18. The summary of pollutant generation mechanisms in a direct-injection diesel engine during (a) “premixed” and (b) “mixing-controlled” combustion phases (Heywood, 2018).

Although nitric oxide is still produced in high-temperature burned gas regions, temperature and fuel/air ratio distributions within the burned gases are now nonuniform, and production rates are highest in the close-to-stoichiometric diffusion flame reaction zone. Soot formed in the rich unburned-fuel-carrying core of fuel spray when the fuel evaporates due to mixing with hot entrained air. When soot in the diffusion zone flame comes into contact with oxygen, it oxidizes, giving the flame its golden glow spectacle. In locations where the flame is quenched both on the walls and where the combustion process is stopped from starting or concluding due to excessive dilution with air, hydrocarbons and aldehydes are formed. HC is also created during the later stages of combustion as fuel vaporizes from the nozzle sac volume. The initial

quick heat release following the ignition delay, which occurs early in the premixed (rich) combustion process, limits combustion-generated noise (McAllister, Chen and Fernandez-Pello, 2011; Ferguson and Kirkpatrick, 2015; Heywood, 2018). There are various types of pollutants produced by engine combustion depending on the cause: incomplete combustion produces pollutants like (carbon monoxide, hydrocarbons, and soot); secondary pollutants resulting from undesirable reactions (NOx); those pollutants created as a result of reactions with impurities in the fuel (SO_2) (Zhao, 2009).

3.6.1. Particulate emissions (PM)

In the exhaust gases, a high concentration of particulate matter (PM) manifests as visible smoke or soot. The inhalation of microscopic particulate matter can cause respiratory difficulties; hence engine emissions are restricted. Particulates are a significant source of emissions from diesel engines, whose performance is hampered by smoke. A particle is defined by the US Environmental Protection Agency as any substance other than water that can be recovered by filtering diluted exhaust at or below 325 K. The particulate matter collected on a filter can be divided into two categories (Heywood, 2018; Stiesch, 2003). The organic fraction consists of hydrocarbons and their partial oxidation products that have been condensed onto the filter or adsorbed to the soot. One component is a solid carbon material or soot, and the other is an organic fraction consisting of hydrocarbons and their partial oxidation products that have been condensed onto the filter or adsorbed to the soot. The mechanisms that dilute the exhaust with air as it exits the engine have an impact on the organic fraction. “Fine” particles are those with a diameter of less than 2.5 microns (PM2.5) and are thought to offer the greatest health hazards. The term “coarse” refers to particles with a diameter of 2.5 to 10 microns (Zhao, 2009). Particulates contain more than simply dry soot; they are the soot particles on which the other compounds, often the polycyclic aromatic hydrocarbons (PAH), have condensed. The level of particulates increases with the sulphur content in the fuel. Particulates are made up of more than just dry soot; they are the soot particles that other substances, such as polycyclic aromatic hydrocarbons (PAH), adhere to. The number of particles in the fuel rises with the proportionate sulphur concentration (Heywood, 1988; Zhao, 2009; Ferguson and Kirkpatrick, 2015).

3.6.2. Carbon monoxide (CO) formation

In rich-running engines, carbon monoxide (CO) occurs in the exhaust because there is insufficient oxygen to convert all the carbon in the fuel to carbon dioxide. The dissociation of CO_2 at high combustion temperatures is another source of CO. The creation and destruction of CO is a key chemical pathway in hydrocarbon combustion, which entails breaking down the hydrocarbon fuel into carbon monoxide and then oxidizing the carbon monoxide to produce carbon dioxide. Majority of the combustion heat is released in the CO oxidation, which involves the following reaction (Ferguson and Kirkpatrick, 2015)

$$CO + OH \leftrightarrow CO_2 + H \tag{3.12}$$

Fuel-air equivalence ratio is the most important engine parameter that affects carbon monoxide levels. In other words, the results obtained when varying the fuel-air ratio are generally the same. Fuel-air equivalence ratio is the most important engine parameter that affects carbon monoxide levels. In other words, the results obtained when varying the fuel-air ratio are generally the same (Heywood, 1988; Zhao, 2009; Ferguson and Kirkpatrick, 2015).

3.6.3. Hydrocarbons (HC) formation

There are nearly identical sources of unburned hydrocarbon emissions and the polluting component carbon monoxide. At high temperatures in the combustion chamber, the molecular bonds of heavy fuel components break down, creating a range of hydrocarbons with shorter C-atom chains (thermal cracking). During subsequent combustion, they are engulfed by the flame. However, because the requisite preconditions (oxygen concentration and temperature) are not present in some portions of the spray, the flame cannot spread further (quenching effect). Hydrocarbons cannot be oxidized any more in these locations and will remain unburned until the conclusion of combustion unless they are transported to areas with better oxidation conditions through appropriate flow characteristics. The spray core and perimeter, as well as the zones adjacent to walls, are crucial in this regard (Heywood, 1988; Zhao, 2009; Ferguson and Kirkpatrick, 2015).

3.6.4. Oxides of nitrogen (NO_X) formation

NO_X refers to a group of nitrogen and oxygen-based chemical compounds with various atom-to-atom interactions. NO is the most common component of NO_X (>90%). During combustion processes, nitrogen monoxide (NO) is created primarily from molecular nitrogen in the combustion air, 'thermal NO' is generated at high temperatures (T > 2200 K) in the burnt component of the working medium (post-flame range). Oxygen radicals start the process, which is aided by OH radicals. As with 'fuel NO', it is also formed by an oxidation of the nitrogen chemically bonded within the fuel (Zhao, 2009; Heywood, 2018). The expanded 'Zeldovich mechanism' can be used to describe the reaction kinetics that underpin 'thermal NO production' (Heywood, 1988; Zhao, 2009).

To date, investigations of removal of exhaust gas from the combustion chamber and/or exhaust-gas testing at the end of combustion combined with simulation calculations, have revealed that NO is primarily formed in diesel engine combustion processes, similar to combustion in natural gas or light oil operated industrial firing systems. The 'thermal NO creation' is based on the extended 'Zeldovich mechanism,' which includes the following reactions (Heywood, 1988; Zhao, 2009):

$$N_2 + O \longrightarrow NO + N \quad (a)$$
$$O_2 + N \longrightarrow NO + O \quad (b) \qquad (3.13)$$
$$OH + N \longrightarrow NO + H \quad (c)$$

There is significance in the reactions 3.13(a) and 3.13(b) with 'lean' mixtures ($\lambda \geq 1$), as well as reactions 3.13(c) with stoichiometric and 'rich' mixtures ($\lambda \leq 1$). Diesel engines with localized air–fuel ratios have kinetically controlled reaction mechanisms, so at the local prevailing temperatures, chemical equilibrium is not reached when the gas mixture is housed in a combustion chamber for the given residence time. In consequence, the NO concentration measured in the exhaust gas of the diesel engine is a lot higher than the equilibrium concentration for the temperature and air–fuel ratio of the exhaust gas. NO formation and breakup reaction takes place in this way when temperatures drop below roughly 2200 K, also known as the 'freeze effect' (Heywood, 1988; Zhao, 2009; Ferguson and Kirkpatrick, 2015).

3.6.5. Soot formation

When insufficient oxygen is present at sufficiently high temperatures, flame soot is a potential intermediate product of combustion processes that happens directly in the flame or combustion chamber. At temperatures exceeding 1000 K, fuel molecules decompose to generate unsaturated intermediate products like acetylene, which starts the process (if sufficient oxygen is available, it is possible to fully oxidise the small hydrocarbon compounds). Large unsaturated hydrocarbons are created when there is a lack of oxygen owing to agglomeration and dehydration processes that comprise mostly carbon and, to a lesser extent, hydrogen. The first soot particles form at this stage (Heywood, 1988; Zhao, 2009).

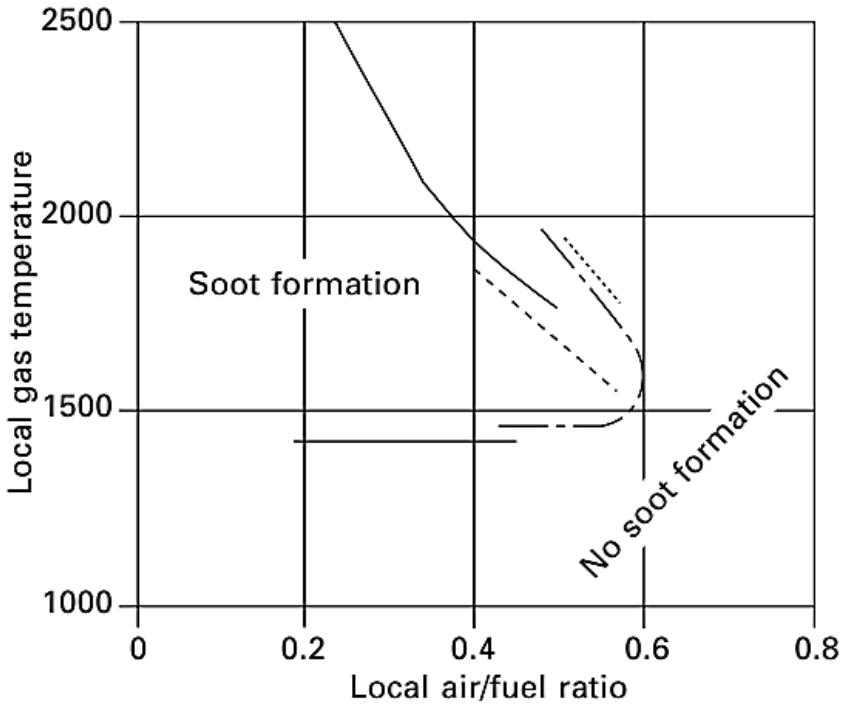

Figure 3.19. Limits of soot generation as a function of localized temperature and air–fuel ratio (Pischinger et al., 1988)

Carbon-rich and unsaturated starting components aids the creation of soot. Furthermore, cyclical hydrocarbons emit more soot than chain hydrocarbons. Figure 3.19 shows the soot generation limitations determined by fundamental analyses in flame and shock-wave discharge tubes in terms of localized air–fuel ratio and localized temperature (Pischinger et al., 1988; Zhao, 2009)

3.6.6. Sulphur dioxide (SO_2) formation

Sulphur dioxide is generated in the flame front and 'post-flame' area when sulphur in the fuel is directly oxidized with molecular oxygen. Almost all the sulphur in the fuel (in the form of organic sulphide, for example) is transformed to SO_2 during this process. As a result, the sulphur content of the fuels utilised can be used to quantify SO_2 emissions (Zhao, 2009; Heywood, 2018).

3.7. Summary

This chapter has provided details about the combustion processes in direct injection compression ignition DICI diesel engine. Mixture formation which is the essential feature in combustion has been thoroughly discussed with other influencing variables such as, air motion in the cylinder swirl and radial flow squish. The kinetic energy of the fuel injected with the accompanying sequences starting from the spray breakups, primary breakup, secondary breakup, spray propagation, spray penetration, spray atomization, fuel vaporization was all detailed. The essential combustion characteristics of DICI diesel engine performance were considered and reviewed, the in-cylinder pressure variations with crank angle, heat release rate, cumulative heat release rate, fuel mass burning rate and ignition delay. There are a number of factors that can influence and affect how long the delay period occurs before ignition and rapid pressure rise were also discussed, which includes: ignition quality of fuel, compression ratio, injection timing, injection pressure, engine speed, air/fuel ratio, load on engine. In addition, pollutant formation was reviewed considering, particulate emissions, carbon monoxide, hydrocarbons, oxides of nitrogen, soot formation and sulphur dioxide. These are important features that affect directly and indirectly the combustion, performance, and emission characteristic of DICI diesel engines.

CHAPTER 4

Piston bowl design and injection spray parameters optimisation

The chapter discusses many influencing design factors, such as the combustion chamber (CC) piston bowl geometry, injection spray angle, and injection timing, that affect air fuel mixing quality, combustion, and emissions. Furthermore, the chapter examines the different designs of piston bowls currently used in direct injection compression ignition (DICI) diesel engines and how they affect combustion processes and emissions characteristics. In the conclusion of this chapter, five (5) piston bowls were designed from the baseline piston bowl geometry and four injection timings, and four spray-included angles were chosen for optimisation in order to find the highest possible performance.

4.1. Introduction

In the heavy duty (HD) direct injection compression ignition (DICI) diesel engines, the fuel/air mixture is the main propelling factor that controls the combustion processes, engine performance and emission characteristics, in these processes within milliseconds, injected fuel must mix with intake air and combust (Debnath, Saha and Sahoo, 2013; Hellier and Ladommatos, 2015; Yousefi, Birouk and Guo, 2017). The start of injection (SOI) and the start of combustion (SOC) in which there is the delay period is crucial during the combustion process of the DICI diesel engines. In order to initiate a start of combustion rapid mixing and/or long ignition delay the air fuel mixture need a very good homogenization (Hellier and Ladommatos, 2015; Yousefi, Birouk and Guo, 2017).

The CC piston bowl geometry, ignition timing, and injection included angle have a direct relationship with combustion, performance, and emission formation processes in DICI diesel engines, all of which can have a significant impact on air-fuel mixing before combustion begins (Shi and Reitz, 2008; Dolak and Reitz, 2011; Jaichandar, Kumar and Annamalai, 2012). The combustion mechanism, which is strongly reliant on air-fuel mixing phenomenology, will require a full investigation to meet impending emission requirements. Understanding the air-fuel mixture, which has a significant impact on the combustion and emission processes in diesel engines, is aided by liquid

fuel spray characteristics. Engine variables such as the compression ratio (CR) and injection timing have a considerable impact on the combustion processes and emissions of a DICI diesel fuelled CI engines (Shi, Y. and Reitz, R.D., 2008; Dolak and Reitz, 2011; Jaichandar, Kumar and Annamalai, 2012).

In order to obtain a better understanding of the spray atomization processes inside the combustion chamber, researchers have spent the last two decades investigating a range of fuel spray circumstances in the combustion chamber (Shi, and Reitz, 2008; Dolak and Reitz, 2011; Jaichandar, Kumar and Annamalai, 2012; Dakhore et al., 2015; Tay et al., 2017; Ganji et al., 2018; Şener, Özdemir and Yangaz, 2019; Channappagoudra, Ramesh and Manavendra, 2020). In accordance with some studies, modification in the combustion chamber for biodiesel engines has a favourable impact on the combustion process hence engine performance and emission characteristics since it impacts the air/fuel mixture formation (Jaichandar, Kumar and Annamalai, 2012; Dakhore et al., 2015; Tay et al., 2017; Ganji et al., 2018). The piston bowl, on the other hand, is a key component of the combustion chamber because of its significant contribution to the combustion processes and emission parameters (Dolak and Reitz, 2011; Jaichandar, Kumar and Annamalai, 2012).

In recent years, a number of experimental and numerical CFD studies have been carried out to investigate the impact of various piston bowl shapes coupled with injection strategies on the combustion and emission characteristics of DICI engines; however, it is necessary to conduct additional research to modify and optimize the piston bowl and injection spray strategy for DICI biodiesel engines. Jaichandar and Annamalai (2012) experimentally studied the influences of re-entrant combustion chamber geometry on DICI diesel engine emission, performance and on the combustion using pongamia oil methyl ester (POME). The toroidal re-entrant combustion chamber (TRCC) and shallow depth re-entrant combustion chamber (SRCC) were compared to the baseline hemispherical open type combustion chamber (HCC). When compared to a baseline HCC engine fuelled with 20% POME, the test findings showed that TRCC had significantly higher brake thermal efficiency and reduced specific fuel consumption. TRCC had a significant reduction in particles, CO, and UBHC when compared to the other two. TRCC, on the other hand, has greater nitrogen oxides (NOx). The combustion analysis reveals that the ignition delay for

TRCC is shorter than the baseline engine, and the peak pressure at full load is also higher.

In a study, Jaichandar, Kumar and Annamalai (2012) in an attempt to optimize the combined effect of injection timing and combustion chamber geometry, experimentally examined hemispherical (HCC) and toroidal re-entrant combustion chamber (TRCC) of a single cylinder DICI diesel engine using a blend of 20% pongamia oil methyl ester (POME) by volume in ULSD (B20). The results revealed improved air-fuel mixing with retarded injection timing, TRCC demonstrated a 5.64% gain in brake thermal efficiency, a 4.6% drop in brake specific fuel consumption, and an 11% rise in oxides of nitrogen (NOx) level when compared to a baseline engine run with ULSD.

In a study Dakhore et al., (2015) used numerical CFD simulations to investigate the piston cavity geometry, such as torus radius, pip region, cavity lip area, and impingement area, to understand the trade-off between NOx, PM, and fuel consumption of a medium-duty diesel engine at constant speed. It was discovered that a bigger toroidal radius improves engine performance by improving mixing, and that these qualities help to reduce both soot and NO without sacrificing fuel economy. Simulation results demonstrate that optimizing the combustion chamber geometry reduces emissions while also increasing efficiency. Simulation results show that optimum shape of the combustion chamber helps to simultaneously reduce emissions.

The effects of piston bowl shape on Reactivity Controlled Compression Ignition (RCCI) performance and emissions at low, medium, and high engine loads was also investigated by Benajes et al., (2015) in which a study was carried out at 1200rev/min and with a compression ratio (CR) of 14.4:1. With single and double injection techniques, three distinct piston bowl geometries: stock, stepped, and bathtub were investigated. It was discovered that piston geometry has a significant impact on combustion development at low load settings, especially when single injection strategies were used. When using multiple injection techniques, the three geometries offer ultra-low NOx and soot emissions at low and medium loads. The stepped piston geometry, which has a modified transition from the centre to the squish zone and a smaller piston surface area than the stock geometry, is better for RCCI operation, however unacceptable emissions were measured at high load.

In a related study, Singh et al., (2017) review and studied various combustion geometries of the DICI diesel engines, comparing performance parameters, combustion processes, and emission characteristics obtained through experimental and numerical analysis, and concluded that any minor change in the combustion chamber leads to biodiesel suitability for the DICI engine.

Tay et al., (2017) studied the combustion and emission of DICI engine fuelled with kerosene-diesel mix and examined the shallow-depth combustion chamber (SCC), shallow-depth re-entrant combustion chamber (SRCC) and omega combustion chamber (OCC), in combination with six different ramp injection rate-shapes. It was clear SRCC geometry, which has the shortest throat length, gives the highest turbulence kinetic energy (TKE) and this amounts to two peak heat-releases, in addition, the SCC geometry gives rather distinct premixed combustion and mixing-controlled combustion. It is interesting to note that the effect of injection rate-shaping on the heat-release rate is more obvious for bowl geometries that generate less TKE. Additionally, bowl geometries with greater TKEs, as well as fuels with lower viscosities, produce lower carbon monoxide (CO) and higher nitrogen oxide (NO) emissions. More crucially, by using the proper bowl geometry, injection rate-shape, and fuel, minimal NO and CO emissions can be achieved simultaneously, but a minor reduction in power is unavoidable.

Ganji et al., (2018) used the CONVERGETM CFD code in conjunction with the SAGE combustion model to analyse the performance and emissions of a 17.5 compression ratio DICI diesel engine with three different piston bowls: hemispherical combustion chamber (HCC), shallow depth combustion chamber (SCC), and toroidal combustion chamber (TCC). According to the research, TCC piston bowls allow improved air/fuel mixing in the cylinder, resulting in a more homogeneous charge. Further research found that lowering the bowl depth by 1.26 mm from the baseline resulted in enhanced engine performance and emission characteristics with the TCC design.

Leach et al., (2018) also investigated experimentally and numerically two piston bowl shapes, a standard re-entrant bowl and a bowl with a stepped lip, at two part-load operating points. The results show that the stepped lip design consistently increases the 50–90% mass fraction burned duration across all operating conditions due to the trapping of the flame in the region of the stepped lip. The use of the stepped bowl

allowed injection timing to be advanced at full load and minor penalty in NOx emissions reported for the stepped bowl design at full load points.

In another study, Şener, Özdemir and Yangaz (2019) also investigated six different piston bowl geometries by utilizing numerical approach to examine the effect of the bowl shape of the piston on the performance behaviour, emission rates and combustion characteristics in DICI engine at 1750 rev/min constant speed with n-heptane (C_7H_{16}) as fuel. The findings reveal that the piston bowl geometry has a considerable impact on the engine's heat release rate, in-cylinder pressure, in-cylinder temperature, and emission trends. Among the six piston bowl geometries investigated, re-entrant alike single swirl combustion designs, showed better combustion characteristics and lower emission trends than other designs. These two geometries have larger rates of heat release, in-cylinder pressure, and in-cylinder temperature magnitudes than other geometries.

Gugulothu et al., (2019) investigated three split injection geometries, swirl ratios and four piston bowl geometries of DICI diesel engine numerically by CFD model in ANSYS FLUENT. The results show that, pilot injection generates favourable situation for the impending main fuel injection in the case of multiple injection. Meanwhile, there is a significant reduction in NO generation due to the multiple injections. The study concluded that the final NO produced is 24% lower than that produced by normal injection and 22% lower than that produced by delayed injection. Split injection combined with a proper combustion chamber arrangement would considerably improve engine performance while also lowering emissions to a larger extent.

In another study, Channappagoudra et al., (2020) modified hemispherical piston bowl geometry (HPBG) into toroidal piston bowl geometry (TPBG) to examine the DICI engine performance fuelled with 20% dairy scum biodiesel (B20). The result shows the modified engine TPBG operation has increased brake thermal efficiency, increased heat release rate, raised cylinder pressure. When compared to a 20% dairy biodiesel operated standard engine with piston HPBG there was a reduction in brake-specific fuel consumption, reduction in HC emissions, reduction in ignition delay, and reduction in combustion duration.

4.2. Factors considered in combustion chamber piston bowl design

The combustion chamber piston bowl design, more than any other component of the engine, has a significant impact on emissions, performance, and knocking features. Type of piston bowl wall material, valve placement, varied volume of air in different portions of the combustion chamber such piston bowl, clearance between cylinder head and piston, valve recess, and so on are all parts to be considered in the design.

4.2.1. Heat loss from combustion chamber wall

In diesel engines, heat losses are defined as a reduction in energy available to the engine, which has a direct impact on volumetric efficiency and cold starting. The pressure and temperature within the cylinder fall as a result of increased heat transfer from the combustion chamber wall, thus reducing the work per cycle transfer to the piston. Convective heat transfer is primarily influenced by the heat transfer coefficient and gas temperature, both of which are influenced by the geometry of the combustion chamber hence the piston bowl. According to Yamada et al., (2002), the reduction in heat loss from combustion chamber is due to deposition adhesion determinant of heat flux and surface temperature (Sugihara et al., 2007; Singh et al., 2017)

4.2.2. Injection nozzle design configuration

The fuel injector nozzle is critical for DICI engines to optimize emissions and performance. It features essential parameters that can change in design, such as the layout, quantity, and size of holes. Higher moment was created by the nozzle, which improved mixing conditions. Spray breakup, droplet formation, and injection spray coverage of combustion air are all influenced by the injection nozzle (Mollenhauer and Tschöke, 2010; Singh et al., 2017).

Four-valve technology in recent designs allows centring the nozzle relative to the cylinder, facilitating symmetrical conditions for fuel sprays. This improves mixture formation and, as a result, the typical engine parameters of consumption, combustion noise, and emissions, as well as allowing for the optimization of partially opposing forces. The point of impact of the fuel sprays on the bowl rim is determined by nozzle

projection and nozzle hole cone angle, in addition to injection timing and spray velocity as shown in Figure 4.1. The impact point should be as high as possible. Design work must account for the influence of a potentially existing squish flow on the site of impact as a function of speed, as well as the interference with spray propagation caused by increased air density (Mollenhauer and Tschöke, 2010; Singh et al., 2017).

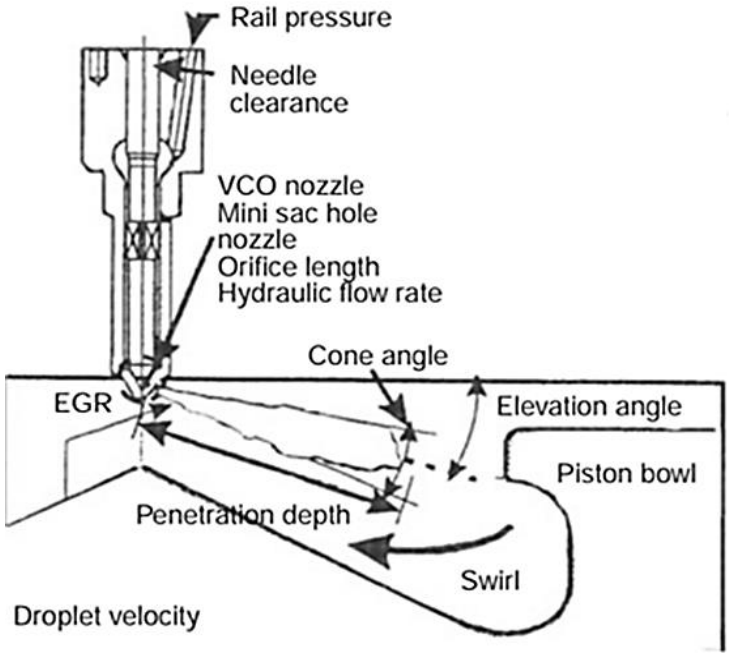

Figure 4.1. Spray propagation and its influencing factors (Mollenhauer and Tschöke, 2010).

4.2.3. Degree of air turbulence required

Air turbulence and better mixing of air-fuel in diesel engines are greatly influenced by the form of the CC geometry, which improves whirling and squish action within the CC. The velocity of air allows for greater atomization, dispersion, and mixing of fuel, resulting in less afterburning and a shorter delay period, as well as better air utilisation in the cylinder. It works in conjunction with other mass motions within the cylinder to mix the air and fuel and spread the flame front quickly. Squish velocity reaches its peak about 10° BTDC. Squish action provides a secondary rotational flow called tumble when the piston approaches TDC as depicted in Figure 4.2. This rotation occurs around a circumferential axis near the piston bowl's outside edge (Pulkrabek, 2007; Singh et al., 2017).

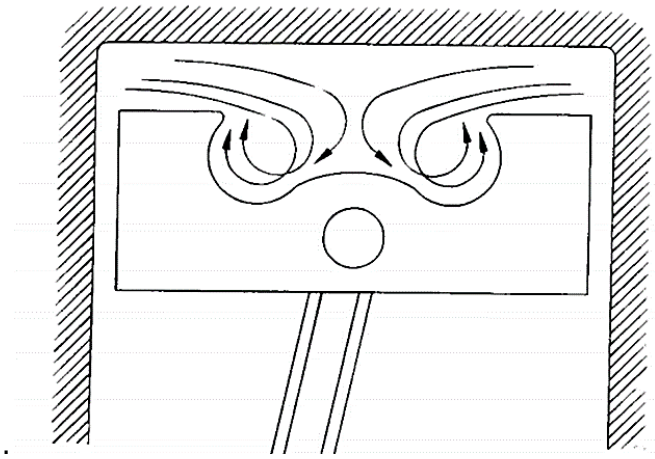

Figure 4.2. Tumble action caused by piston bowl as it approaches TDC (Pulkrabek, 2007).

4.2.4. The shape of the combustion chamber

The primary function of the piston head is to create turbulence, which leads to improved combustion and reduced knocking and enhance ignition delay period. The shape of the combustion chamber varies depending on the engine type. Different piston bowl geometry is necessary for certain cases, such as single curve (cylindrical, hemispherical, and trapezoidal), double curve (toroidal, omega, and shallow depth), and triple curve (toroidal, omega, and shallow depth). The quiescent direct injection systems combustion chamber, for example, is commonly shaped like a shallow bowl in the piston crown, with a central multi-hole injector and used in heavy duty engines (Pulkrabek, 2007; Singh et al., 2017). In a study conducted by Sakthisaravanasenthil, Senthilkumar and Sivakumar (2017) it was discovered that changing the geometry of the re-entrance combustion chamber lowered HC and CO by 20% and 24%, respectively. In another study, Bawankar and Gupta (2016) compared an omega-shaped combustion chamber to a hemispherical type, where the soot particles were reduced by 19% and NOx was increased by 12%.

4.3. Combustion chamber geometries for DICI diesel engines

A wide variety of geometries of combustion chamber (CC) piston bowls have been studied through experiments and numerical modelling using different types of

biodiesel fuels. Low-speed (less than 1500 rpm) and medium-speed (1500–3000 rpm) direct injection combustion chambers are designed. The high swirl design and the low swirl design are two design ideas for direct injection combustion chambers. In the first situation, the injector has fewer holes, and the piston has a deep bowl, but in the second case, the injector has more holes, and the piston has a shallow bowl (Amate and Khairnar, 2015; Singh et al., 2017). The following are some of the most commonly used geometries: (Amate and Khairnar, 2015; Singh et al., 2017)

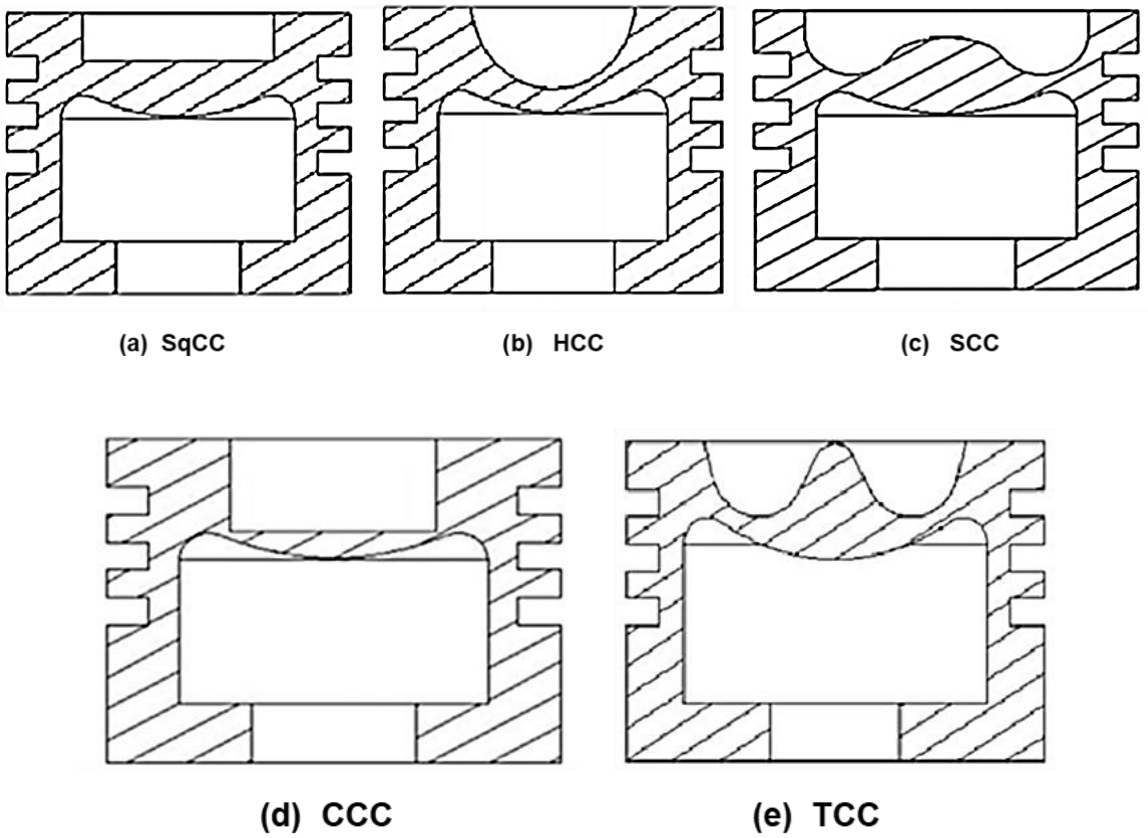

Figure 4.3. Common direct injection combustion chambers are shown in a schematic diagram. (a) SqCC (b) HCC (c) SCC (d) CCC (e) TCC (Singh et al., 2017).

4.3.1. Square combustion chamber (SqCC)

A powerful squish motion forces the swirling motion into the bowl during the compression stroke when utilising a square bowl combustion chamber Figure 4.3 (a). with a limited squish region, providing a turbulent environment, especially in the corner sections (Singh et al., 2017).

4.3.2. Hemi-spherical combustion chamber (HCC)

This is the standard CC for diesel fuelled engines, Figure 4.3 (b). The depth to diameter ratio in this combustion chamber can be adjusted to get any desired squish for improved performance. However, it is ineffective when using biodiesel as a fuel. Because biodiesel has a higher viscosity than diesel, proper atomization and burning of biodiesel is not possible in this CC (Singh et al., 2017).

4.3.3. Shallow depth combustion chamber [SCC]

A little cavity depth is supplied in SCC shown in Figure 4.3 (c). The cavity diameter is also enormous, resulting in little squish and swirl motion. However, it produces better biodiesel atomization than HCC. This is primarily employed at low speeds in large engines (Singh et al., 2017).

4.3.4. Cylindrical combustion chamber (CCC)

The CCC is formed by a cylindrical chamber Figure 4.3 (d). This is a conical chamber modification that looks like a truncated cone with a 90° base angle. The swirl is created by turning the entire circumference 180 degrees. Squish may be altered by adjusting the depth (Singh et al., 2017).

4.3.5. Toroidal combustion chamber [TCC]

The squish motion is better in TCC 4.3 (e) than in other geometries, better air movement in the CC results in greater combustion. TCC has a cone angle ranging from 150 to 160 degrees (Singh et al., 2017).

4.3.6. Quiescent combustion chamber for heavy duty diesel engines

The quiescent direct injection combustion chamber systems are shown in Figure 4.4. This type of combustion chambers is utilised in the larger engines, where mixing rate requirements are the least rigorous. The momentum and energy of the fuel jets ensure adequate distribution of fuel and mixing with air. There is no need for additional planned air movement. The combustion chamber is commonly shaped like a shallow bowl in the crown of the piston, with a central multi-hole injector (Heywood, 2018).

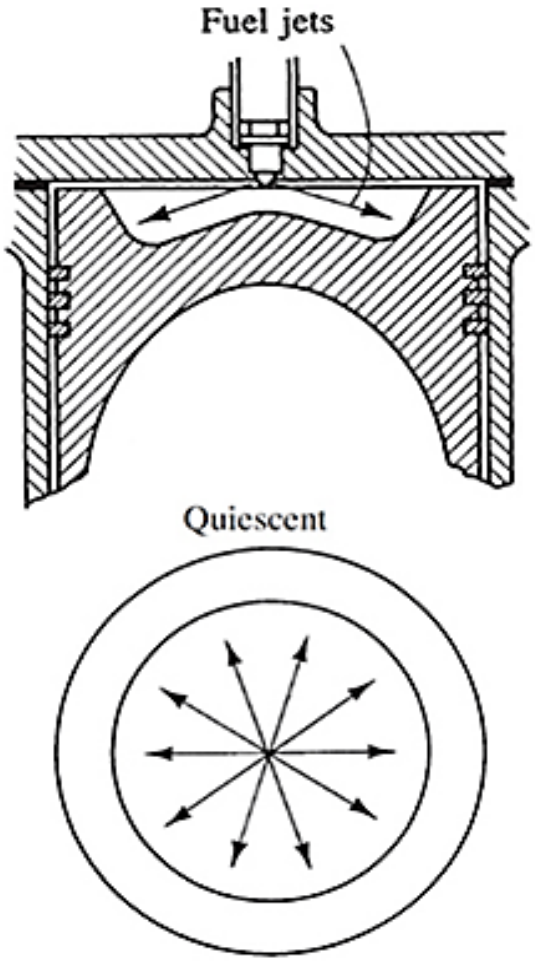

Figure 4.4. Quiescent chamber with multi-hole nozzle typical of larger engines (Heywood, 2018).

4.4. Piston bowl designation

The piston bowl design is one of the main engine design elements that affects air/fuel mixing and subsequent combustion and pollutant generation processes. The pip region, bowl lip area, and toroidal radius, among other bowl geometries and dimensions as shown in Figure 4.5 have a significant impact on in-cylinder mixing, combustion, and engine out emissions. The approach of speeding fuel/air mixing to increase combustion in the cylinder and minimize combustion duration is widely utilised and proven effective in DICI diesel engines to achieve a better combustion with less pollutant emissions. By delaying injection timing, NOx emissions can be minimized without a significant increase in exhaust pollutants or fuel consumption. The

air movement in the chamber is stronger with a tight throat than without one (Amate and Khairnar, 2015; Singh et al., 2017; Sreedharan and Krishnan, 2018).

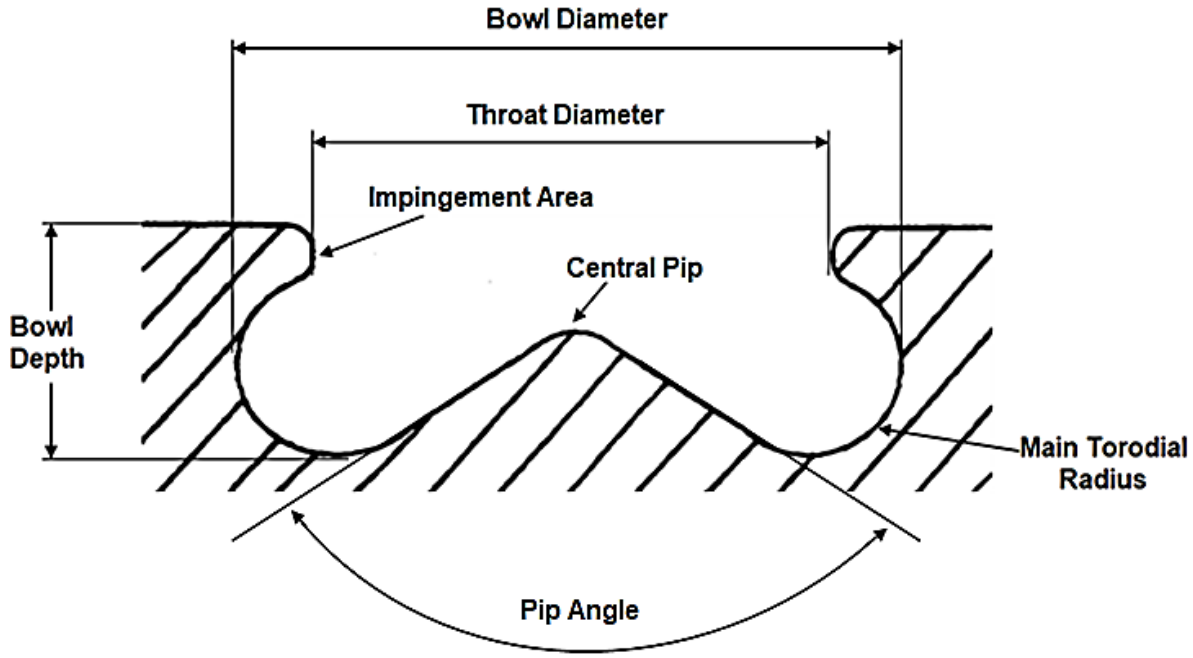

Figure 4.5. Piston bowl configuration (Amate and Khairnar, 2015)

4.4.1 Throat diameter of the piston bowl

The minimum diameter between the piston bowl edges, near the piston top face, is specified as the throat diameter. The quantity of re-entrancy in a piston bowl design was determined by the ratio of the throat diameter to the maximum bowl diameter. Large temperature gradients and high heat transfer rates to the piston bowl top surfaces are created by high velocity airflow into the bowl and combustion gas out of the bowl. The piston bowl lip is frequently the hottest component of the inside surface of the piston bowl (Amate and Khairnar, 2015; Balasubramanian et al., 2018). Smoke can be reduced without increasing NOx emissions by using a sharp squish lip design. However, its capacity to reduce smoke is dependent on how it interacts with other bowl shape characteristics. It was discovered that bowls with a broader neck diameter and a limited pip height mix air and fuel better than bowls with a narrow throat (Sreedharan and Krishnan, 2018).

4.4.2. Bowl diameter

The biggest diameter parallel to the piston face at any point through a section of the piston bowl is described as the maximum bowl diameter as in Eq. (4.1). The piston bowl aspect ratio is defined as the ratio of the maximum bowl diameter to the bowl depth as in Eq. (4.1). The maximum bowl diameter determines the overall volume of the piston bowl and hence the compression ratio. When creating a new piston bowl form, this is one of the initial factors to be set (Amate and Khairnar, 2015; Balasubramanian et al., 2018).

$$Aspect\ Ratio = \frac{Maximum\ Bowl\ Depth}{Bowl\ Diameter} \tag{4.1}$$

$$Re - entrancy\ Ratio = \frac{Throat\ Diameter}{Bowl\ Diameter} \tag{4.2}$$

$$Bore\ to\ Bowl\ Ratio = \frac{Bowl\ Depth}{Bore\ Diameter} \tag{4.3}$$

4.4.3. Central pip

During periods of low air velocity, the central pip is used to fill a space in the centre of the piston bowl. The swirling flow-field results in poor mixing of air and fuel due to low air velocity in the centre. As a result of the central pip, this volume was redistributed further from the centre of rotation, which resulted in a higher mean airflow velocity and more efficient air/fuel mixing (Amate and Khairnar, 2015; Balasubramanian et al., 2018).

4.4.4. Impingement area

The impingement region is the area on the side of the piston bowl where high-velocity fuel impinges during fuel injection. In the early stages of fuel injection and combustion, the impingement area is particularly important. Controlling the volume and composition of the fuel air mixture prepared for initial combustion can alter the ignition delay and initial rate of pressure rise (Amate and Khairnar, 2015; Sreedharan and Krishnan, 2018)

4.5. Effect on emissions due to bowl parameters

In-cylinder air and fuel mixing, combustion process, and engine emissions are all influenced by the shape and dimensions of the bowl, including the pip radius, bowl lip area, and toroidal radius as shown in Figure 4.6 (Amate and Khairnar, 2015; Sreedharan and Krishnan, 2018)

4.5.1. Effect of toroidal radius

The following are the effects of toroidal radius and lip shape on diesel engine performance and emissions. The author discovered that a bigger toroidal radius in the cavity improves engine performance by improving fuel air mixing. Less soot emission is also caused by higher peak cylinder temperatures and a lack of fuel-rich zones, resulting in a reduction in soot emission (Amate and Khairnar, 2015; Sreedharan and Krishnan, 2018).

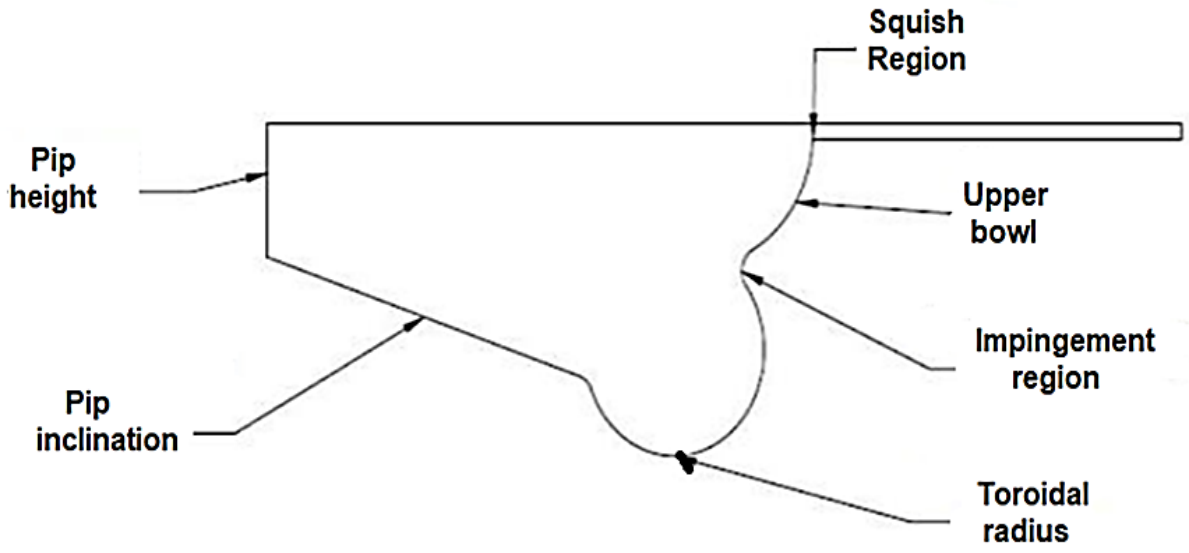

Figure 4.6. Piston cavity geometrical parameters (Amate and Khairnar, 2015)

4.5.2. Effect of lip shape

In a combustion study to investigate the influence of lip form, it was discovered that the lip splits the fuel into upper and lower bowls on purpose. The first stage of combustion occurs in the higher bowl, followed by the lower bowl, which aids in moving

gases with lower oxygen concentrations farther up into the bowl. However, in a traditional single bowl cavity, combustion begins in a single bowl, and any fuel injected later is forced to mingle with the hot, lower oxygen-concentrated gases from the first injection, resulting in the formation of extra soot. The amount of oxygen exposed to the injected fuel is limited by this traditional bowl. On the other hand, in a stepped bowl, the fuel is injected at an angle that allows oxygen to be injected on either side of it. The result is better air entrainment (Amate and Khairnar, 2015; Sreedharan and Krishnan, 2018)

4.5.3. Effect of pip inclination

The swirl and vortex that is the flow in the combustion space are activated by the pip form, and the mixing of the fuel and air flowing into the combustion space is improved, and the mixing ratio can be considerably raised in the exemplary embodiment (Amate and Khairnar, 2015).

4.5.4. Effect of impingement position

The following is the influence of impingement point and lip shape on combustion: The wall jet in a hollow with a lip is separated into two regions: one above and one below the lip. The spray is semi-circular rather than circular below the lip. The main spray runs smoothly down the concave surface of the lip with the round lip, and the kinetic energy loss is minimal, as shown in Figure 4.6. Because of the reduced energy loss, the spray volume at the bottom is bigger. In compared to a cavity without a round lip, the unburned HC emission in a re-entrant cavity with a round lip improves at high loads. The fuel distribution and combustion are significantly influenced by the impinging position on the cavity wall (Amate and Khairnar, 2015; Balasubramanian et al., 2018; Sreedharan and Krishnan, 2018).

4.5.5. Effect of cavity size

When the cavity wall distance is adjusted for the same volume, the spray spreading regions do not differ significantly. A shallow bowl, on the other hand, will result in a lengthy floor jet, which is undesirable, and too deep bowls with smaller diameters will result in a lot of fuel moving to the hollow outside. Furthermore, sprays injected from two successive holes in the hollow wall will interfere if the distance between them is too short. A large gap between two consecutive sprays is created by a large wall distance. The increased radius of the bottom corner reduces the volume of air near the side wall, causing the air distribution in the chamber to shift, resulting in a poor air-fuel balance (Amate and Khairnar, 2015; Balasubramanian et al., 2018; Sreedharan and Krishnan, 2018).

4.5.6. Effect of lip shape

The lip corner and the cavity entrance are often avoided because sharp edges can cause heat stress. The spray impinges and then follows smoothly along the lip in the cavity with the round lip, resulting in minimal energy loss owing to impingement. The combustion pressure and temperature are slightly higher, and the combustion rate is slightly faster when impingement occurs on the lip corner than at other impingement locations. With a modest penalty in NOx emissions, this helped to reduce HC and smoke emissions. Strong swirl and a restricted number of nozzle openings improve emissions in a deep bowl combustion chamber, according to the review. A large number of nozzles opening gives better emissions in the shallow dish chamber, but huge strong swirl creates over-swirl phenomena, leading in inferior emissions and fuel consumption (Amate and Khairnar, 2015; Sreedharan and Krishnan, 2018).

4.5.7. Effect of cavity depth

The shallow piston bowl geometry for small engines results in lower efficiency because fuel reaches the cylinder liner at all values of the spray angle (α) as shown in Figure 4.7. Fuel reaches the cylinder liner in such zones. The use of shallow piston bowls is advantageous only in large engines with a large distance between the sprayer and the cylinder liner as well as in engines with a high boosting pressure since the high density

of air reduces the spray penetration distance, as a result of which fuel does not reach the cylinder liner (Amate and Khairnar, 2015).

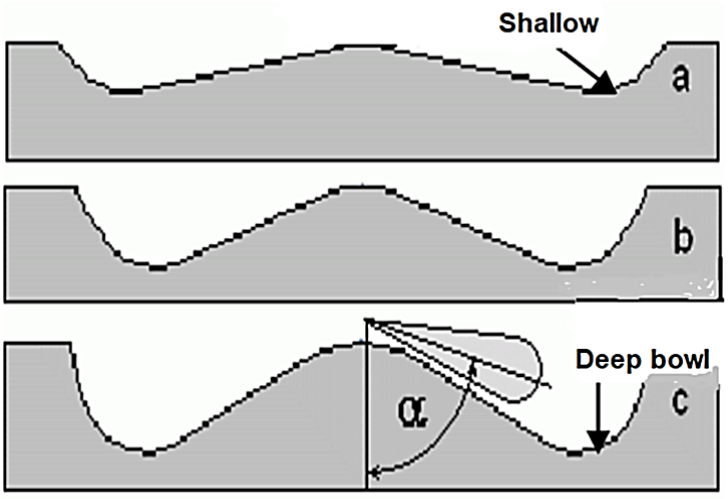

Figure 4.7. Bowl Depth (Amate and Khairnar, 2015).

Deep piston bowls are advantageous when the engine has a low boosting pressure, and the fuel sprays have a deep penetration length due to the low air density and long injection duration. Strong swirl and a restricted number of nozzle openings improve emissions in a deep bowl combustion chamber, according to literature (Amate and Khairnar, 2015; Balasubramanian et al., 2018; Sreedharan and Krishnan, 2018). A large number of nozzle apertures gives better emissions in the shallow dish Chamber, but huge strong swirl creates over-swirl phenomena, leading in inferior emissions and fuel consumption (Amate and Khairnar, 2015; Singh et al., 2017; Sreedharan and Krishnan, 2018)

4.5.8. Effect of bottom corner radius

Due to the huge change in direction, energy loss is particularly considerable with a sharp bottom corner. This results in a decreased wall jet diameter, which has an impact on the fuel-air mix. However, a large bottom corner diameter reduces the volume of air along the side wall, causing air distribution to alter and a poor air-fuel balance. To improve fuel dispersion and air-fuel distribution, a suitable value for the bottom corner radius is preferred (Amate and Khairnar, 2015; Sreedharan and Krishnan, 2018).

4.6. Impact of injection spray included angle and timing on combustion

A key characteristic of combustion is the atomization characteristics of fuel sprays because the mixture formed between the atomized spray and the entrained air directly impacts emission formation and combustion efficiency. In addition, spray formation and injection process are the two important mechanisms for in-cylinder air/fuel mixing, which controls the combustion and emissions. The injection timing and spray angle coupled with the piston bowl interaction determine the targeting points at the surface of the piston bowl on the DICI diesel engine (Kim et al., 2016; Singh et al., 2017; Zhou et al., 2020).

4.6.1. Injection spray included angle

Several studies investigated injection timing and spray angle for optimizing engine performance and emission characteristics of direct injection compression ignition (DICI) engines. In an experimental study, Yoon et al., (2010) investigated the effects of spray angles and injection strategies on combustion characteristics, exhaust emission concentrations, and particle size distribution in a direct injection compression ignition (DICI) diesel engine powered by dimethyl ether (DME). The geometry of the combustion chamber and test injectors are shown in Figure 4.8 in which three types of injectors were tested, two kinds of narrow spray angle injectors at 60° and 70° and a conventional degree injector of 156° were examined. The early injection timing of 40° Before Top Dead Centre (BTDC) resulted in a spray angle of 156° onto the cylinder liner or wall, which led to a higher PM, HC, and CO emission.

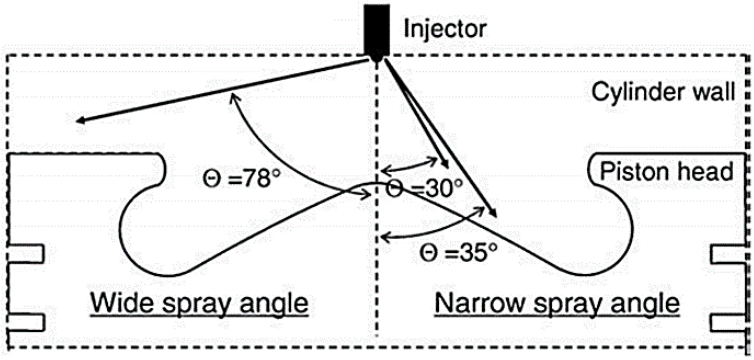

Figure 4.8. Illustration of a combustion chamber with fuel spray at 40° BTDC (Yoon et al., 2010).

The results of this investigation were compared to those of a typical conventional spray angle of 156° and two types of narrow spray angle injectors with spray angles of 70° and 60°, respectively. Early single-injection and multiple-injection timing tactics were employed to limit injected fuels' cylinder wall-wetting to further examine the ideal operating conditions. When compared to the findings of the wide-angle injector spray = 156° with advanced injection timing of BTDC 35°, the combustion pressure from single combustion for narrow-angle injectors spray = 70° and 60° is increased. The NOx emissions from narrow-angle injectors grew in proportion to the advance in injection timing up to BTDC 25°, whereas the wide-angle injector's emissions increased in proportion to the advance in injection timing up to BTDC 20°.

When using narrow-angle injectors for repeated injections, the combustion pressure is higher, and the ignition delay of the second injected fuel is less than when using a wide-angle injector. Kim, Park, and Lee (2016) evaluated the effects of fuel spray angles such as narrow (60°) and conventional (156°) on spray behaviour, combustion, and emissions characteristics in a study. Two injectors were studied as a function of injection timing and injection pressure at spray angles of 60° and 156°.

The impacts of spray angle on combustion and emission characteristics, as well as engine performance in DICI engine, were investigated. It was revealed that the 60° injectors had a higher maximum combustion pressure, a faster maximum heat release rate, and a shorter ignition delay than the 156° injector, according to the findings. In terms of emission characteristics, using a narrow spray angle injector with an early injection combustion strategy is advantageous since it produces low indicated specific hydrocarbon (ISHC), indicated specific carbon monoxide (ISCO), and indicated specific nitrogen oxides (ISNOx) emissions. An injector with a narrow spray angle has a higher indicated mean effective pressure (IMEP) as well. In another study, Shu et al., (2019) investigated the effect of different injection spray included angles 60°, 80°, 100°, 120°, 140°, and 160° on the combustion process in DICI engine utilising validated (Computational fluid dynamics) CFD as shown in Figure 4.9.

The results showed that the peak cylinder pressure increases as the spray angle increases from 60° to 140°, but slightly decreases if the spray angle continues to increase to 160° as shown in Figure 4.10. Further it was discovered that the NOx emissions ascend when the spray angle increases from 60° to 140° and changes little

if it continues to increase from 140° to 160°. When the spray angle ranges between 120° and 160°, the CO emissions keeps at a lower level.

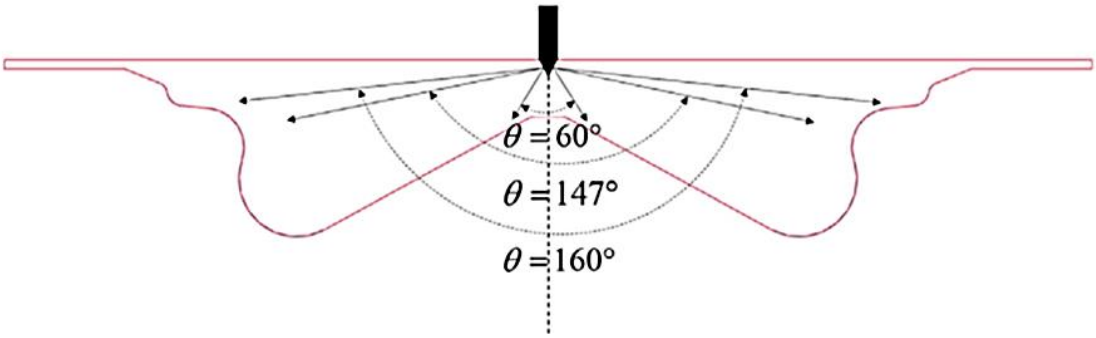

Figure 4.9. The schematic diagram of different injector spray angles in a combustion chamber (Shu et al., 2019).

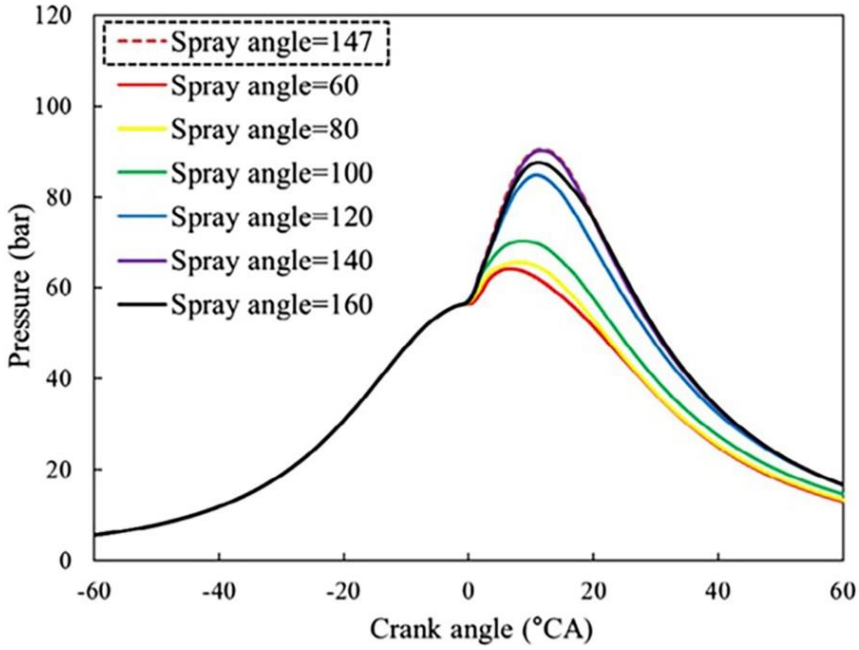

Figure 4.10. The in-cylinder pressure with different spray angles at 1000 rpm, 50% load (Shu et al., 2019).

4.8. Engine description and operating conditions

The computational results will be validated using measured data from the Cummins N series 4 stroke direct injection compression ignition (DICI) diesel heavy-duty engine with a 2.34 L displacement (Singh, Reitz and Musculus, 2006). Table 4.1 contains a summary of the major engine specifications.

Table 4.1. Engine Specification of modelled DICI diesel Engine (Singh, Reitz and Musculus, 2006)

Engine Details	Specifications
Engine base type	**Cummins N series**
Number of Cylinders	1
Inlet Valves	2
Exhaust Valve	1
Combustion Chamber	Quiescent, direct injection
Bore x Stroke (cm)	13.97 x 15.24
Bowl width x depth (cm)	9.78 x 1.55
Displacement, L	2.34
Swirl ratio	0.5
Connecting rod length (cm)	30.48
Geometric Compression ratio	11.2:1
Spray included angles	(126° ,136° 146° and156°)
Start of Injection (^{0}BTDC)	(-25.5°, -22.5° -18.5° and -15.5°)
Fuel injector type	Common rail, pilot valve actuated
Number of holes	8, equally spaced
O2 Concentration (Vol %)	12.6 to 21
Intake valve closing, IVC (CAD)	-165° BTDC
Exhaust valve open, EVO (CAD)	125° ATDC

4.7. Piston bowl designs

This investigation utilises five different combustion chamber piston bowl designs by altering the pip heights, pip inclination and the bowl toroidal radii from the base design shown in Figure 4.11. The cylinder piston bowl configuration of the Cummins N series single cylinder DICI four-stroke diesel engine with 2.34 L displacement will be used as a base reference design, the engine specification is in Table 4.1 (Singh, Reitz and Musculus, 2006). The effects of these eight distinct piston bowl profiles on the combustion, performance and emissions characteristics of DICI heavy-duty diesel engines for biodiesel fuelled investigations in this study.

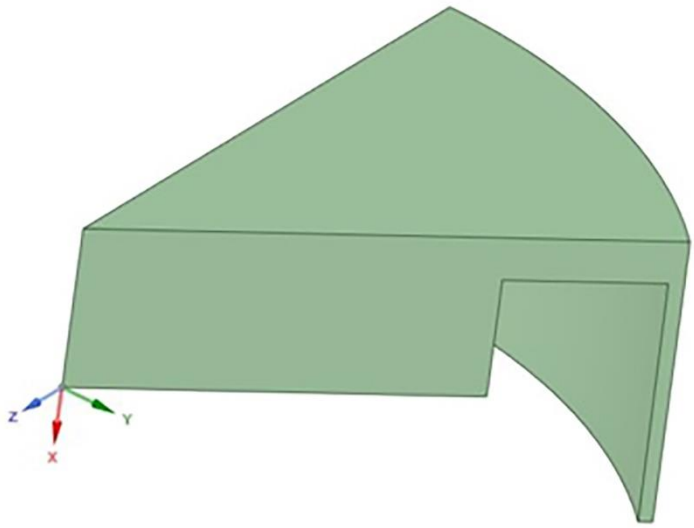

Figure 4.11 Baseline design of cylindrical piston bowl 45° sector geometry

4.7.1. Piston bowl designs geometries

Figure 4.12 (a) to (f) shows the geometry of the five (5) combustion chamber piston bowls, which were designed in accordance with the baseline design. Table 4.2 shows the detailed features of the various piston bowl designs: the outer bowl diameter, upper bowl, impingement region, upper lip radius, lower lip radius, bowl depth, bowl radius, pip height, pip angle, and toroidal radius.

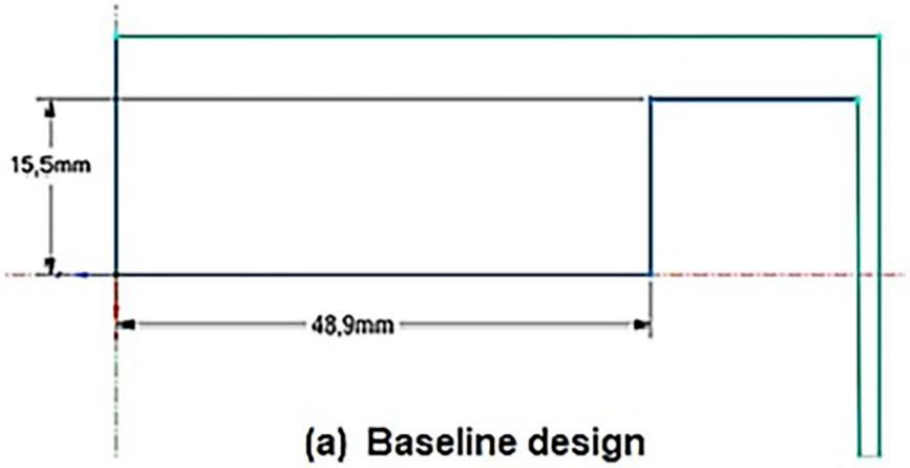

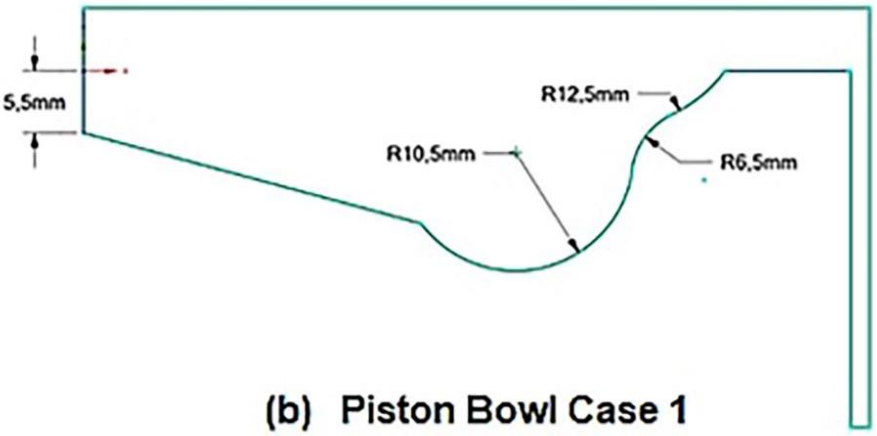

(b) Piston Bowl Case 1

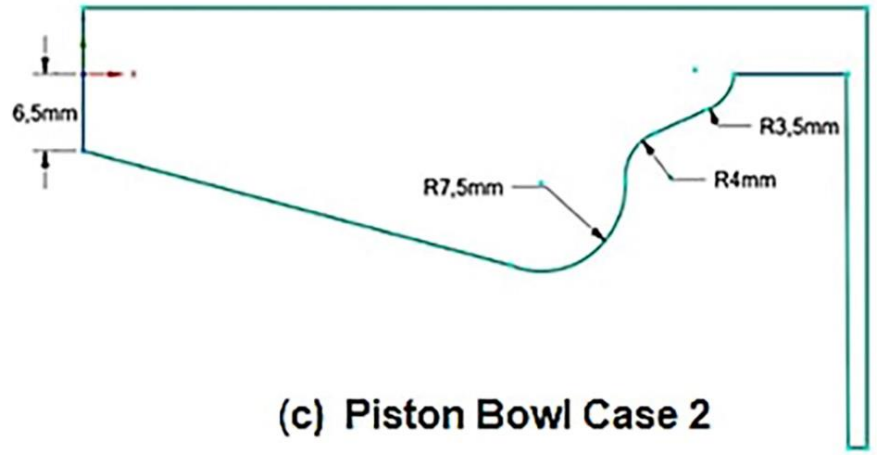

(c) Piston Bowl Case 2

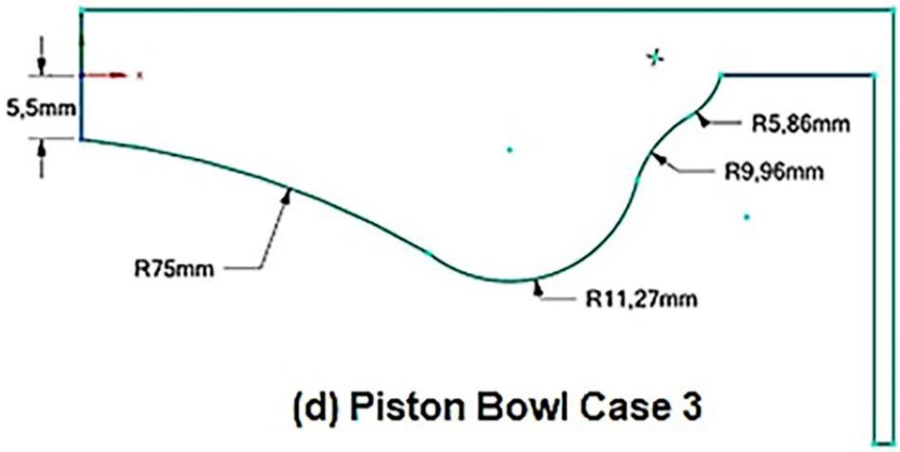

(d) Piston Bowl Case 3

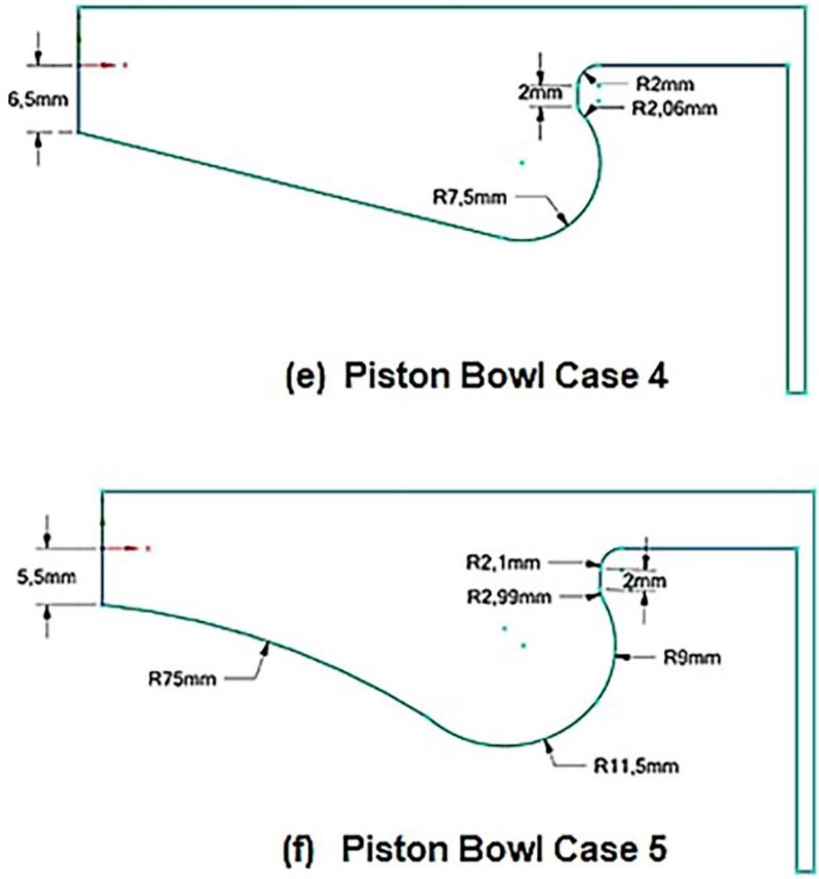

Figure 4.12. (a) to (f) Baseline piston bowl and five piston bowl design cases.

Table 4.2. Parameters of the Piston Bowl Designs: Baseline Design and Cases 1 to 5

Piston Bowls Profile Dimension (mm)	**(a) Baseline**	**(b) Case 1**	**(c) Case 2**	**(d) Case 3**	**(e) Cas 4**	**(f) Case 5**
Outer Bowl Diameter	97.8	114	116	110	100	102
Upper Bowl		R 12.5	R3.5	R5.86	--	--
Impingement Region		R 6.5	R4	R9.96	2	2
Upper lip Radius	--	--	--	--	R2	R2.1
Lower lip Radius	--	--	--	--	R2.06	R2.99
Bowl depth	15.5	17.73	16.7	17.7	16.92	19.34
Bowl Radius	--	R10.5	R7.5	R11.27	R7.5	11.5
Pip height	15.5	5.5	6.5	5.5	6.5	5.5
Pip Angle	--	150°	150°	R 75	150°	R75
Toroidal radius	--	--		--	R7.5	R9

4.8. Injection spray parameters

The start of injection and spray included angle are injection parametric factors which influences combustion, and emissions characteristics. In this study, four (4) different start of injection (SOI) and four (4) spray included angles (SIA) were used as indicated in Table 4.3. The four different spray included angles were aimed at four separate areas in the piston bowl to focus the main fuel spray propagation and penetration. The two injection characteristics will optimize the air-fuel mixture, enhance combustion, and improve emissions.

Table 4.3. Spray included angle (SIA_θ°) and start of injection (SOI_CA BTDC)

Spray Included Angle (SIA_θ°)	
Parameter 1	126°
Parameter 2	136°
Parameter 3	146°
Parameter 4	156°
Start of Ignition (SOI) (CA BTDC)	
Parameter1	-25.5°
Parameter 2	-22.5°
Parameter 3	-18.5°
Parameter 4	-15.5°

4.9. Summary

In this chapter, different combustion chamber geometries from various scientific sources were examined, and the results of experimental and numerical analysis were taken into consideration. The key findings are that enhanced combustion chamber flow behaviour is affected by bowl construction, squish, tumble, and turbulence. The findings demonstrate that toroidal (TCC) and toroidal re-entrant (TRCC) combustion chambers offer superior air motion, which raises combustion parameters including cylinder pressure, heat release rate, and peak pressure. Five (5) piston bowl profiles were designed out of the baseline features which would then be modelled in accordance with the base piston bowl design profile. These designs were considered

after a thorough consideration of various combustion chamber piston bowl profiles and other influencing related factors, such as the start of injection (SOI) and spray included angle (SIA), which are parameters that directly impact combustion and pollutant generation in both petroleum diesel and biodiesel fuelled engines. The chapter also selected four parameters of SOI (-15.5°, -18.5°, -22.5° and -25.5° BTDC) and four SIA (126°, 136°, 146° and 156°), both of which have significant impact on DICI diesel engine operations. In order to examine injection spray propagation, spray penetration, and mixture formation, the four different SOI and SIA will be used to run the DICI engine in different scenarios. The numerical CFD model in this work will be validated using measurement data from a single-cylinder, four-stroke Cummins N-series diesel engine with a displacement of 2.34 L (Singh, Reitz and Musculus, 2006).

CHAPTER 5

Combustion model description and validation

This chapter presents several computational fluid dynamics (CFD) numerical sub-models that were used in the ANSYS Forte package for simulating internal combustion engines. Direct injection compression ignition (DICI) combustion and emission characteristics, as well as in-cylinder physical and chemical kinetic models, were considered. Numerical models are used to describe the in-cylinder flow fields, heat release rate and transfer, combustion characteristics, and pollutant formation processes. Additionally, the chapter includes computational grid independence sensitivity study, details of the engine specifications and operating conditions as described in chapter 4 as well as combustion and engine performance data from the validated model of the Cummins N series engine with a displacement of 2.34 L, which was used in this study as the base bowl design of the DICI engine.

5.1. Introduction

The 3-D fluid flows, spray dynamics, and combustion behaviour of the ANSYS Forte programme are represented theoretically in well-established ways. The dynamics of spray combustion in diesel engines is influenced by the turbulent mixing dynamics and fuel combustion kinetics. Spray dynamics and fuel vaporisation are often the key contributors to the development of stratified fuel/air mixtures. The chemical kinetics of ignition and combustion are controlled under these stratified conditions by a sophisticated network of interactions between fuel and air species. Spray dynamics and chemical kinetics are the two different types of source terms included in the equations describing reacting-flow transport (Pérez de Albéniz Azqueta, 2020; ANSYS Forte, 2020). Both turbulence mixing dynamics and fuel combustion kinetics govern the dynamics of spray combustion in diesel engines. Usually, the main factors that contribute to the formation of stratified fuel/air mixes are spray dynamics and fuel vaporisation. Additionally, ANSYS Forte establishes new benchmarks for direct-injection engine droplet breakage and vaporisation representation. For instance, multi-component chemical models and true multi-component fuel vaporisation models can now coexist. The ANSYS Forte CFD programme is built on numerical models and sub-

models that engine simulation experts thoroughly tested with experimental data using a variety of settings over an extended period.

5.2. Basic governing equations

5.2.1. Conservation equations for turbulent reacting flow

The working fluids in internal combustion engines are the fuel-air combination prior to combustion and the burnt by-products following combustion. Fluxes of reactive, multi-phase, and turbulent fluids are all considered. The fundamental fluid dynamics in ANSYS Forte, which use a turbulent reactive flow description, are governed by the Navier-Stokes equations. Model transport equations comprising mass, momentum, and energy conservation rules are developed for compressible, gas-phase flows to depict the flows' turbulent nature. The usage of the gas-phase thermodynamics equation of state, Fick's law for mass diffusion, the assumption of a Newtonian fluid, and Fourier's law for thermal diffusion are the key presumptions utilised in the construction of the governing equations. The governing equations for the gas phase of the engines' operating fluids are presented in this section (ANSYS Forte Theory, 2020).

5.2.2. Species conservation equation

The internal combustion engine working gas is modelled as a combination of discrete gas species, or components, whose composition changes over time due to flow convection, turbulent transport, interactions with fuel sprays, combustion, and molecular diffusion. The conservation equation (Eq. 5.1) for the total number of species is:

$$\frac{\partial \bar{\rho}_k}{\partial t} + \nabla.(\bar{\rho}_k \tilde{u}) = \nabla.[\bar{\rho} D \nabla \bar{y}_k] + \nabla.\Phi + \dot{\bar{\rho}}_k^c + \dot{\bar{\rho}}_k^s (k = 1, \dots, K) \quad (5.1)$$

in which: ρ = the density

k = the species index

K = the total number of species

$\tilde{u}$ = the flow velocity vector

$y_k = \rho_k/\rho$ = the mass fraction of species k

A mixture-averaged molecular diffusion coefficient, D, is produced by the application of Fick's Law of Diffusion.

The Φ term is responsible for the results of ensemble-averaging or sorting of the convection term, such as, $\Phi = \bar{\rho}_k\tilde{u} - \overline{\rho_k u}$, that should be modelled. The source terms $\dot{\bar{\rho}}_k^c$ and $\dot{\bar{\rho}}_k^s$ are caused by spray evaporation and chemical reactions, correspondingly (ANSYS Forte Theory, 2020).

5.2.3. Fluid continuity equation

The continuity equation for the entire gas-phase fluid is obtained by the summing of equation (Eq. 5.1) for all species:

$$\frac{\partial\bar{\rho}}{\partial t} + \nabla.(\bar{\rho}\tilde{u}) = \dot{\bar{\rho}}^s \tag{5.2}$$

5.2.4. Momentum conservation equation

The convection, pressure force, viscous stress, turbulent transport, liquid sprays, and body force are all considered by momentum equation (Eq. 5.3) of the fluid:

$$\frac{\partial\bar{\rho}\tilde{u}}{\partial t} + \nabla.(\bar{\rho}\tilde{u}\tilde{u}) = -\nabla\bar{p} + \nabla.\bar{\sigma} - \nabla.\Gamma + \bar{F}^s + \bar{\rho}\bar{g} \tag{5.3}$$

where g is the specific body force, p is the pressure, F^s is the rate of momentum gain per unit volume owing to the spray $\bar{\sigma}$ is the viscous shear stress determined by (Eq. 5.4):

$$\bar{\sigma} = \bar{\rho}\nu\left[\nabla\tilde{u} + (\nabla\tilde{u})^T - \frac{2}{3}(\nabla.\tilde{u})I\right] \tag{5.4}$$

where I**,** is the identity tensor, ν is the laminar kinematic viscosity, and superscript T denotes tensor transposition. The stress considers the nonlinear convection term effects from ensemble averaging or filtering, such as, $\Gamma = \bar{\rho}(\widetilde{\tilde{u}\tilde{u}} - \tilde{u}\tilde{u})$.

It is referred to as the Reynolds stress when using the Reynolds-Averaged-Navier-Stokes (RANS) method and as the Sub-grid scale (SGS stress when using the Large-Eddy Simulation (LES) methodology. Turbulence models are necessary in both cases to provide closure.

5.2.5. Energy conservation equation

The First Law of Thermodynamics states that pressure work and heat transfer must balance the change in internal energy. When resolving flow problems of internal combustion engines, turbulent transport, chemical reactions, convection, sprays, turbulent dissipation, and enthalpy diffusion of a multi-component flow should be considered. The following is Eq. (5.5), the internal energy transmission equation:

$$\frac{\partial \bar{\rho}\tilde{I}}{\partial t} + \nabla.(\bar{\rho}\tilde{u}\tilde{I}) = -\bar{p}\nabla.\tilde{u} - \nabla.\bar{J} - \nabla.H + \bar{\rho}\tilde{\varepsilon} + \dot{\bar{Q}}^{c} - \dot{\bar{Q}}_{rad} \qquad (5.5)$$

where J is the heat flux vector which accounts for the contribution of enthalpy diffusion and heat conduction, and I is (Eq. 5.6) the specific internal energy:

$$\bar{J} = -\lambda\nabla\bar{T} - \bar{\rho}D\sum_{k}\tilde{h}_{k}\nabla\bar{y}_{k} \qquad (5.6)$$

λ = the thermal conductivity, is in relation with the thermal diffusivity α and heat capacity by $\lambda = \bar{\rho}c_{p}\alpha$, T = the fluid temperature, and h_k = the specific enthalpy of species k. $\tilde{\varepsilon}$ = the dissipation rate of the turbulent kinetic energy, where the definition is in turbulence models. The source terms $\dot{Q}^{c}$ and $\dot{Q}^{s}$ are because of spray and interactions chemical heat release, concurrently. The letter H account for the impacts of ensemble-averaging or sorting of the convection term, that is, $H = \bar{\rho}\left(\widetilde{uI} - \tilde{u}\tilde{I}\right)$. In furtherance, there is a need to appropriately modelled it from the turbulence approach. $\dot{\bar{Q}}_{rad}$, is the radiative heat loss, whose modelling is introduced in radiation heat transfer model.

5.2.6. Gas-phase mixture equation of state

In addition to providing relationships for the internal energy, the equation of state relates the thermodynamic parameters of temperature, pressure, and density for the gas-phase mixture. The ideal gas law is the most fundamental and widely used equation of state (Eq. 5.7). The mixing of gas components is meant to follow the ideal gas law, according to the Dalton model, which stipulates that each component behaves as an ideal gas as if it were alone at the temperature and volume of the mixture.

$$\bar{p} = R_u \bar{T} \sum_k \left(\frac{\bar{\rho}_k}{W_k}\right) \tag{5.7}$$

in which

R_u = the universal gas constant, and

W_k = the molecular weight of species k.

The internal energy of an ideal gas depends exclusively on temperature. The specific internal energy of the gas constituent ($\tilde{I}$) is a mass-average of the specific internal energy of elements ($\bar{I}_k$), that are being formulated by Eq. (5.8) with reference to temperature:

$$\tilde{I}(\bar{T}) = \sum_k \bar{y}_k \bar{I}_k (\bar{T}) \tag{5.8}$$

At a significantly larger range of pressures and temperatures, the real-gas model can predict thermodynamic property relations with greater accuracy.

The pressure-temperature-volume relation is written as follows by the Peng-Robinson equation of state (Eq. 5.9), which is implemented by ANSYS Forte:

$$\bar{p} = \frac{R_u \bar{T}}{\bar{v}_{molar} - b} - \frac{a}{\bar{v}_{molar}^2 + 2b\bar{v}_{molar} - b^2} \tag{5.9}$$

whereby $\bar{v}_{molar}$ is the molar specific volume of the mixture ($\bar{v}_{molar} = \sum_k (\bar{\rho}_k / W_k)$).

The Van der Waals mixing rule is used Eq. (5.10) to calculate the parameters a and b:

$$a = \sum_i \sum_j x_i x_j \left(a_i a_j\right)^{1/2} \left(1 - k_{ij}\right)$$

(5.10)

$$b = \sum_i x_i b_i$$

whereby the parameters for constituent a_i, and b_i are calculated as in Eq. (5.11):

$$a_i = 0.45724 \frac{R_u^2 T_{c,i}^2}{p_{c,i}} x \left[1 + f(\omega_i)\left(1 - T_{r,i}^{1/2}\right)\right]^2$$

(5.11)

$$b_i = 0.07780 \frac{R_u T_{c,i}}{p_{c,i}}$$

5.3. Turbulence models

5.3.1. Reynolds-Averaged-Navier-Stokes (RANS) approach

As it was indicated at the commencement of this section, the ensemble-averaged fluid flow is attempted to be replicated by the RANS technique. A most common method which is utilised is the gradient-diffusion assumptions to describe turbulent transport processes. The mean deviatoric rate of strain in the momentum equation is thought to be proportional to the deviatoric components of the Reynolds stress.

The Reynolds stress tensor Γ in Eq. (5.12), is defined as:

$$\Gamma = -\bar{\rho} v_T \left[\nabla \tilde{u} + (\nabla \tilde{u})^T - \frac{2}{3}(\nabla . \tilde{u}) I\right] + \frac{2}{3}\bar{\rho}\tilde{k} I \quad (5.12)$$

where the turbulent kinematic viscosity v_T, and $\tilde{k}$ is the turbulent kinetic energy, well-defined in Eq. (5.13) by:

$$\tilde{k} = \frac{1}{2\bar{\rho}} trace(\Gamma) = \frac{1}{2}\widetilde{u''.u''} \quad (5.13)$$

The turbulent viscosity v_T is associated to the turbulent kinetic energy $\tilde{k}$ and its dissipation rate $\tilde{\varepsilon}$ by in Eq. (5.14) as:

$$v_T = C_\mu \frac{\tilde{k}^2}{\tilde{\varepsilon}} \quad (5.14)$$

In which C_μ is a model constant that differs in various turbulence model formulations, as outlined in (Table 5.1: constant in the Re-Normalisation Group turbulent kinetic energy (k) and the rate of dissipation of the turbulent kinetic energy (ε) (RNG k–ε) models (Tan, 2003).

Table 5.1. The RNG k – ε models constants (Han and Reitz 1995).

RNG	C_μ	$C_{\varepsilon 1}$	$C_{\varepsilon 2}$	$C_{\varepsilon 3}$	$1/Pr_k$	$1/Pr_\varepsilon$	η_0	β
k- ε	0.0845	1.68	1.42	-1.0	1.39	1.39	4.38	0.012

The turbulent flux term in the species transport equation (5.1) is modelled in Eq. (5.15) as:

$$\Phi = \bar{\rho} D_T \nabla \bar{y}_k \tag{5.15}$$

where D_T is the turbulent diffusivity. Comparably, the turbulent flux term H in the energy equation (5.5) is modelled in Eq. (5.16) as:

$$H = -\lambda_T \nabla \bar{T} - \bar{\rho} D_T \sum_k \tilde{h}_k \nabla \bar{y}_k \tag{5.16}$$

in which λ_T represents the turbulent thermal conductivity which is relates to the turbulent thermal diffusivity α_T and heat capacity c_p by $\lambda_T = \bar{\rho} c_p \alpha_T$.

The turbulent viscosity is correlated with the turbulent mass and thermal diffusivity by Eqs. (5.17) and (5.18):

$$D_T = \frac{\nu_T}{Sc_T} \tag{5.17}$$

$$\alpha_T = \frac{\nu_T}{Pr_T} \tag{5.18}$$

in which respectively Sc_T and Pr_T are the turbulent Schmidt and Prandtl numbers.

As shown in the Eq. (5.12), to calculate turbulent viscosity there is a need for the turbulent kinetic energy $\tilde{k}$ and its dissipation rate $\tilde{\varepsilon}$ are being modelled. In ANSYS Forte, both the standard and the advanced (based on Re-Normalized Group Theory) k-ε model formulation are accessible. In this, consideration is given to velocity

dilatation in the ε- equation and spray-induced source terms for both k and ε equations (Han and Reitz 1995).

The standard Favre-averaged equations for k and ε are given in Eq. (5.19) and Eq. (5.20):

$$\frac{\partial \bar{\rho}\tilde{k}}{\partial t} + \nabla.\left(\bar{\rho}\tilde{u}\tilde{k}\right) = -\frac{2}{3}\bar{\rho}\tilde{k}\nabla.\tilde{u} + (\bar{\sigma} - \Gamma):\nabla\tilde{u} + \nabla.\left[\frac{(\mu+\mu_T)}{Pr_k}\nabla\tilde{k}\right] - \bar{\rho}\tilde{\varepsilon} + \dot{\bar{W}}^s \tag{5.19}$$

$$\frac{\partial \bar{\rho}\tilde{\varepsilon}}{\partial t} + \nabla.(\bar{\rho}\tilde{u}\tilde{\varepsilon}) = -\left(\frac{2}{3}C_{\varepsilon 1} - C_{\varepsilon 3}\right)\bar{\rho}\tilde{\varepsilon}\nabla.\tilde{u} + \nabla.\left[\frac{(\nu+\nu_T)}{Pr_\varepsilon}\nabla\tilde{\varepsilon}\right] + \frac{\tilde{\varepsilon}}{\tilde{k}}(C_{\varepsilon 1}(\sigma - \Gamma):\nabla\tilde{u} - C_{\varepsilon 2}\bar{\rho}\tilde{\varepsilon} + C_s\dot{\bar{W}}^s) \tag{5.20}$$

In the equations above, Pr_k, Pr_ε, $C_{\varepsilon 1}$, $C_{\varepsilon 2}$ and $C_{\varepsilon 3}$ considered model constants and are outlined and detailed in Table 5.1: Constants in the standard and RNG k – ε models (Tan, 2003).

Based on the droplet probability distribution function, the source terms for $\dot{\bar{W}}^s$ are computed (Amsden, 1997).

In physical terms, $\dot{\bar{W}}^s$ is the opposite of the speed at which the turbulent eddies are redistributing the spray droplets. Using the assumption that spray/turbulence interactions preserve length scale, Amsden (1997) proposed the equation $C_s = 1.5$.

The more advanced (and the more recommended) version of the k – ε model is derived from Re-Normalized Group (RNG) theory, as first proposed by Yakhot and Orszag (1986). The conventional form of the k equation model is the same for the RNG version, but the ε equation is based on a laborious mathematical calculation rather than on constants that were determined empirically.

The RNG ε equation is written as (Eq. (5.21)):

$$\frac{\partial \bar{\rho}\tilde{\varepsilon}}{\partial t} + \nabla.(\bar{\rho}\tilde{u}\tilde{\varepsilon}) = -\left(\frac{2}{3}C_{\varepsilon 1} - C_{\varepsilon 3}\right)\bar{\rho}\tilde{\varepsilon}\nabla.\tilde{u} + \nabla.\left[\frac{(\nu+\nu_T)}{Pr_\varepsilon}\nabla\tilde{\varepsilon}\right] + \frac{\tilde{\varepsilon}}{\tilde{k}}\left[C_{\varepsilon 1}(\sigma - \Gamma):\nabla\tilde{u} - C_{\varepsilon 2}\bar{\rho}\tilde{\varepsilon} + C_s\dot{\bar{W}}^s\right] - \bar{\rho}R \tag{5.21}$$

in which the later part on the right-hand side of the equation has the following definition (Eqs. (5.22) and (5.23)):

$$R = \frac{C_\mu \eta^3 (1-\eta/\eta_0)}{1+\beta\eta^3} \frac{\tilde{\varepsilon}^2}{\tilde{k}} \tag{5.22}$$

$$\eta = S \frac{\tilde{k}}{\tilde{\varepsilon}} \tag{5.23}$$

where: $$S = (2\bar{S}:\bar{S})^{1/2} \tag{5.24}$$

and $\bar{S}$ is the mean strain rate tensor,

$$\bar{S} = \frac{1}{2}(\nabla\tilde{u} + (\nabla\tilde{u})^T) \tag{5.25}$$

In relation with standard ε equation, the RNG model has an extra term, accounting for non-isotropic turbulence, as described by Yakhot and Orszag (1986).

The various model constants $Pr_k, Pr_\varepsilon, C_{\varepsilon 1}, C_{\varepsilon 2}$ and $C_{\varepsilon 3}$ which are utilised in the RNG version are also listed in Table 5.1: RNG k – ε models (Tan, 2003).

In the Forte implementation, the RNG value for the variable is based on the work of Han and Reitz (1995), who modified the constant to take the compressibility effect into account.

According to Han and Reitz (1995),

$$C_{\varepsilon 3} = \frac{-1+2C_{\varepsilon 2}-3m(n-1)+(-1)^\delta \sqrt{6} C_\mu C_\eta \eta}{3} \tag{5.26}$$

in which ideal gas is n =1.4, m = 0.5, and

$$C_\eta = \frac{\eta(1-\eta/\eta_0)}{1+\beta\eta^3} \tag{5.27}$$

with

$$\delta = \begin{cases} 1, if\ \nabla.\tilde{u} < 0; \\ 0, if\ \nabla.\tilde{u} > 0. \end{cases} \tag{5.28}$$

In utilising this method, the notation $C_{\varepsilon 3}$ differs in the range of -0.9 to 1.726 (Han and Reitz,1995), and in Forte is automatically determined, depending on the flow circumstances and other model constants, η_0 and β descriptions. Han and Reitz (1995)

utilised their edition of the RNG k- ε model for the simulation of engine and notice good improvement in the result comparative to the standard k- ε model.

Therefore, for this purpose, the recommended and default model in Forte is RNG k- ε model.

5.4. Chemical kinetics formulation

In combustion simulations, the pathways and rates of reactions defined by chemical kinetic mechanism can be used to describe chemical reactions. Reversible (or irreversible) reactions involving K chemical species can be expressed in the general form in detailed chemical kinetic mechanisms (CHEMIKIN-Pro, 2008).

$$\sum_{k=1}^{K} v'_{ki}\chi_k \Leftrightarrow \sum_{k=1}^{K} v''_{ki}\chi_k \ (i = 1, \dots, I) \tag{5.29}$$

The formation level of the kth species in the ith reaction could be formulated as

$$\dot{\omega}_{ki} = (v''_{ki} - v'_{ki}) q_i (k, \dots, K) \tag{5.30}$$

where q_i is the rate of progress of reaction i.

The summation of over all the reactions gives the chemical source term in the species continuity Eq. (5.1) as:

$$\dot{\rho}_k^c = W_k \sum_{i=1}^{I} \dot{\omega}_{ki} \tag{5.31}$$

Consequently, the energy equation of chemical heat release term is given by:

$$\dot{Q}_c = -\sum_{i=1}^{I} Q_i q_i = \sum_{i=1}^{I} \sum_{k=1}^{K} (v''_{ki} - v'_{ki}) \left(\Delta h_f^0\right)_k q_i \tag{5.32}$$

In which Q_i is the heat of reaction at absolute zero,

$$Q_i = \sum_{k=1}^{K} (v''_{ki} - v'_{ki}) \left(\Delta h_f^0\right)_k \tag{5.33}$$

and $\left(\Delta h_f^0\right)_k$ is the heat of formation of species *k* at absolute zero.

5.5. Spray models

Advanced models for multi-component fuel-spray dynamics and spray interactions with flowing multi-component gases are included in ANSYS Forte. Nozzle flow, spray atomization, droplet disintegration, droplet collision and coalescence, droplet vaporization, and wall impingement are among the sub-processes that have been modelled. To simulate the spray atomization and droplet breakage processes of solid-cone and hollow-cone sprays, different sub-models are used. In solid-cone sprays, discharge coefficients or nozzle-flow models are used to determine initial spray conditions, and the Kelvin-Helmholtz / Raymond Taylor (KH/RT) model are being utilised for droplet breakup (Beale and Reitz, 1999). The spray-atomization, droplet-breakup, and droplet-collision models in Forte employ several cutting-edge strategies to lessen the dependence of outcomes on mesh size and time-step size. For solid-cone sprays, a steady gas-jet breakup model is commonly used. For both solid-cone and hollow cone models, additional options include a radius-of-influence (ROI) collision model and a collision mesh approach. The purpose of this chapter is to go over the major spray alternative sub-models. Spray injection of diesel is most frequently carried out using solid-cone spray models.

5.5.1. Solid-cone spray models

For solid-cone injections, there are two alternatives for initializing the spray: employing a nozzle-flow model or an empirically examined nozzle discharge coefficient to calculate nozzle discharge characteristics. The subsequent sections discuss the detailed Kelvin-Helmholtz/Rayleigh-Taylor break-up models.

5.5.2. Nozzle flow model

Models of nozzle-flow describe the flow conditions inside the nozzle at any given moment in time. Initially, the spray model is based on the nozzle-flow model. Nozzle-flow model input parameters include:

i. ambient gas pressure
ii. physical properties of the liquid fuel

iii. mass flow rate
iv. geometrical hole diameter
v. The R/D ratio (see Figure 5.1: Flow through nozzle passage), where R is the radius of curvature of the injector entrance region.
vi. L/D ratio (Figure 5.1: Flow through nozzle passage)

The instantaneous discharge coefficient (Cd), spray angle, effective injection velocity, and effective flow exit area are calculated by the nozzle-flow model using these inputs. The flow exit area is then used to calculate the size of the initially injected liquid droplet.

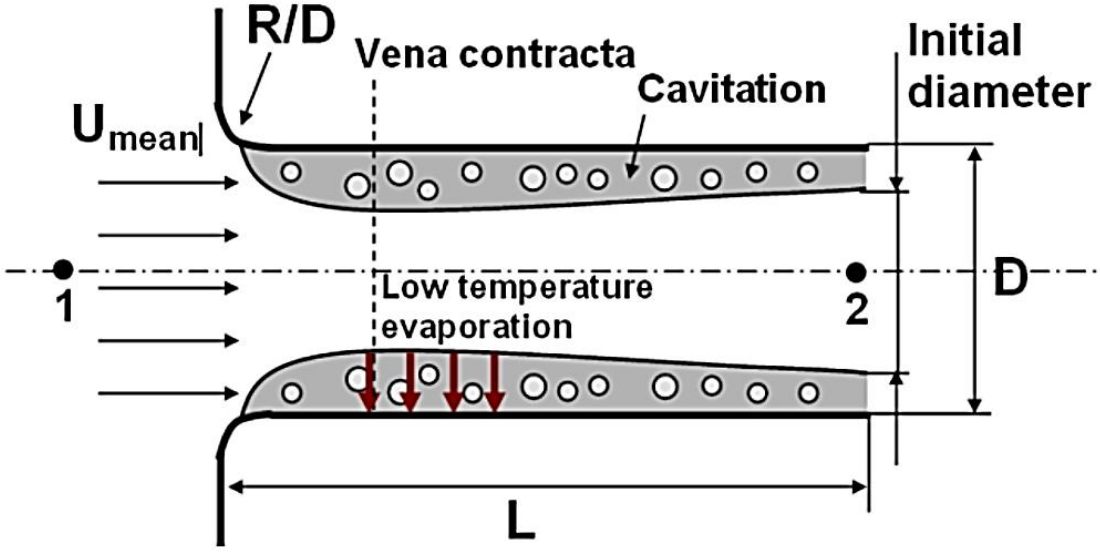

Figure 5.1. Flow through nozzle passage (ANSYS Forte Theory, 2020).

5.5.3. Discharge coefficient

The formula for calculating the volumetric mean flow rate of liquid fuel at the nozzle passage U_{mean} inlet is:

$$U_{mean} = \frac{\dot{m}}{\rho_l A} = \frac{4\dot{m}}{\rho_l \pi D^2} \tag{5.34}$$

in which ρ_l is liquid fuel density, $\dot{m}$ is fuel mass flow rate, and D is nozzle diameter and A is nozzle cross-sectional area.

The mean mass flow through the nozzle exit is never as high as the Bernoulli equation predicts due to flow losses. The expansion after the vena contracta, the velocity

profile's formation at the intake, and wall friction are all factors in the losses. The discharge coefficient, C_d, is used to quantify this difference and is defined as follows:

$$C_d = \frac{U_{mean}}{\sqrt{2.(p_1 - p_2)/\rho_1}} \tag{5.35}$$

where p_1 and p_2 are pressures at position 1 and 2, correspondingly, flow through nozzle passage as shown figure 5.1.

The discharge coefficient is calculated by utilising the Blasius or laminar equation for wall friction along with tabularized inlet loss coefficients (K_{inlet}), as specified in Eq. (5.36):

$$C_d = \frac{1}{\sqrt{K_{inlet} + f.{}^{L}/_{D} + 1}} \tag{5.36}$$

in which f well-defined as:

$$f = Max\left(0.316.Re^{-0.25}, {}^{64}/_{Re_D}\right) \tag{5.37}$$

and Re_D is the Reynolds number founded on nozzle diameter.

A first estimation of the inlet pressure, p_1, for a turbulent flow yields:

$$p_1 = p_2 + \frac{\rho_1}{2}\left(\frac{U_{mean}}{C_d}\right)^2 \tag{5.38}$$

5.5.4. Spray angle

The spray angle in the nozzle flow model is predicted using an aerodynamic model. This approach is based on Taylor's investigation of unstable surface wave formation and mass shedding-induced high-speed liquid breakup. The spray angle, θ, is expressed as follows in this method:

$$tan\left(\frac{\theta}{2}\right) = \frac{4.\pi}{A}.\sqrt{\frac{\rho_g}{\rho_l}}.f(T) \tag{5.39}$$

In which L/D is the length-to-diameter ratio of the nozzle in a formula: A = 3 + 0.28(L/D).

As an approximate expression for the function f(T), is tabulated as:

$$f(T) = \frac{\sqrt{3}}{6}.\left(1 - exp(-10.T)\right) \tag{5.40}$$

$$T = \left(\frac{Re}{We}\right)^2.\frac{\rho_l}{\rho_g} \tag{5.41}$$

5.5.5. Kelvin-Helmholtz/Rayleigh-Taylor breakup model

The Kelvin-Helmholtz/Rayleigh-Taylor (KH/RT) hybrid breakup model is used to simulate the spray atomization and droplet breakup of solid-cone sprays (Beale and Reitz, 1999; Su et al., 1996). The application of the KH/RT breakdown models is shown in Figure 5.2: KH/RT breakup model for solid-cone sprays.

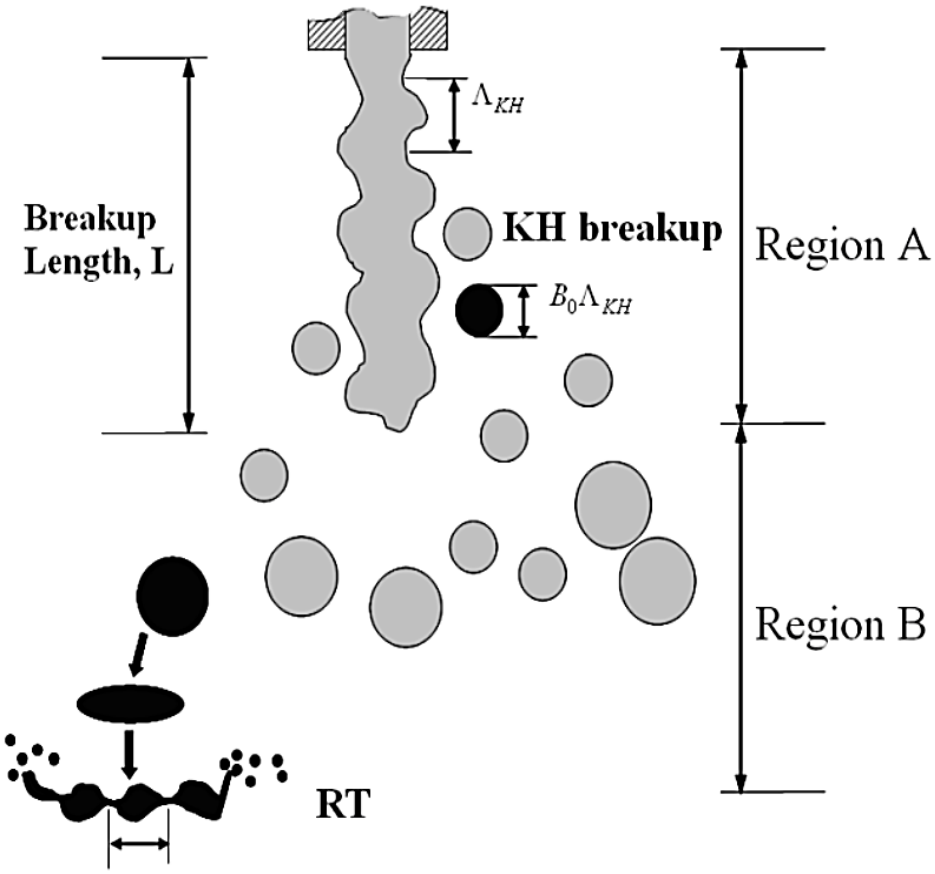

Figure 5.2. Solid-cone sprays for KH/RT breakup model (ANSYS Forte Theory, 2020)

Inside a predetermined breakup length, L, measured from the nozzle exit, the KH breakup model has been used (region A). It removes tiny droplets from the jet (represented by parent parcels, or “blobs”) while leaving the core of the jet, which is a thick liquid, intact.

The RT model is combined with the KH model to estimate secondary break-up beyond the Breakup Length (region B) (Beale and Reitz, 1999; Wang, Ge and Reitz, 2010).

5.5.6. Kelvin-Helmholtz breakup

The main region of the breakup of the jet is represented by the Kelvin-Helmholtz (KH) model, which is dependent on the liquid jet of linear stability analysis (Habchi et al., 1997; Beale and Reitz, 1999; Angeli and Hewitt, 2000). Any perturbation applied to a liquid-gas interface can be extended using the linear stability analysis as a Fourier series, with the fastest growing mode contributing to the final breakup and production of new droplets.

Fastest growing mode with a growth rate and wavelength were calculated numerically by Beale and Reitz, 1999 and that is:

$$\frac{\Lambda_{KH}}{r_p} = 9.02\,\frac{(1+0.45Z^{0.5})(1+0.4T^{0.7})}{(1+0.87We_g^{1.67})^{0.6}} \tag{5.42}$$

$$\Omega_{KH}\left[\frac{\rho_l r_p^3}{\sigma}\right]^{0.5} = \frac{(0.34+0.38We_g^{1.5})}{(1+Z)(1+1.4T^{0.6})} \tag{5.43}$$

In which Λ_{KH} is the wavelength of the fastest growing wave, Ω_{KH} is its growth rate, r_p is the jet radius, σ is surface tension, the dimensionless gas Weber number We_g is defined as:

$$We_g = \frac{\rho_g U_{rel}^2 r_p}{\sigma} \tag{5.44}$$

with U_{rel} being the magnitude of the liquid-gas relative velocity:

$$U_{rel} = \left|\vec{V}_{gas} + \vec{V}_{turb} - \vec{u}_d\right| \tag{5.45}$$

With this $\vec{V}_{gas}$ as gas-phase velocity of the CFD, $\vec{V}_{turb}$ is the local gas-phase turbulent fluctuating velocity vector, and$\vec{u}_d$ is the droplet velocity vector.

Correspondingly, the liquid Weber number can be defined as:

$$We_l = \frac{\rho_l U_{rel}^2 r_p}{\sigma} \tag{5.46}$$

and the dimensionless Ohnesorge number is:

$$Z = \frac{\sqrt{We_l}}{Re_l} \tag{5.47}$$

The Reynolds number is defined as:

$$Re_l = \frac{\rho_l U_{rel} r_p}{\mu_l} \tag{5.48}$$

In which μ_l is the dynamic viscosity of the liquid. The last dimensionless number is the Taylor number:

$$T = Z\sqrt{We_g} \tag{5.49}$$

The primary breakdown mechanism produces new droplets with a radius (designated as r_c) that are correlated with the wavelength Λ_{KH} as follows:

$$r_c = B_{kH}\Lambda_{KH} \tag{5.50}$$

in which B_{KH} of the KH breakup model is the size constant.

The rate equation describes how the parent droplet's radius changes as a result of mass being transferred to its "child" droplets (Reitz and Diwakar, 1986):

$$\frac{dr_p}{dt} = -\frac{r_p - r_c}{\tau_{KH}} \tag{5.51}$$

in which r_c is less than or equal to r_p . Here, the breakup time scale τ_{KH} is calculated as:

$$\tau_{KH} = \frac{3.726 C_{KH} r_p}{\Lambda_{KH}\Omega_{KH}} \tag{5.52}$$

In Eq. (5.52), C_{KH} is the Time Constant of KH breakup. This is a user-controlled input for which a general-purpose default value is provided in ANSYS Forte (ANSYS Forte Theory, 2020).

As shown in Figure 5.3, the KH breakup model involves two steps: the KH breakdown model is implemented in two steps: in the first phase, the parent droplet size (r_p) is gradually decreased by the rate Eq. (5.51); in the subsequent step, a fresh droplet parcel is created from the original, and the child droplet size (r_c) is predicted by Eq. (5.56).

It is presumed that the droplets in the parent count is constant both before and after the breakup (that is: $n_p^{new} = n_p$).

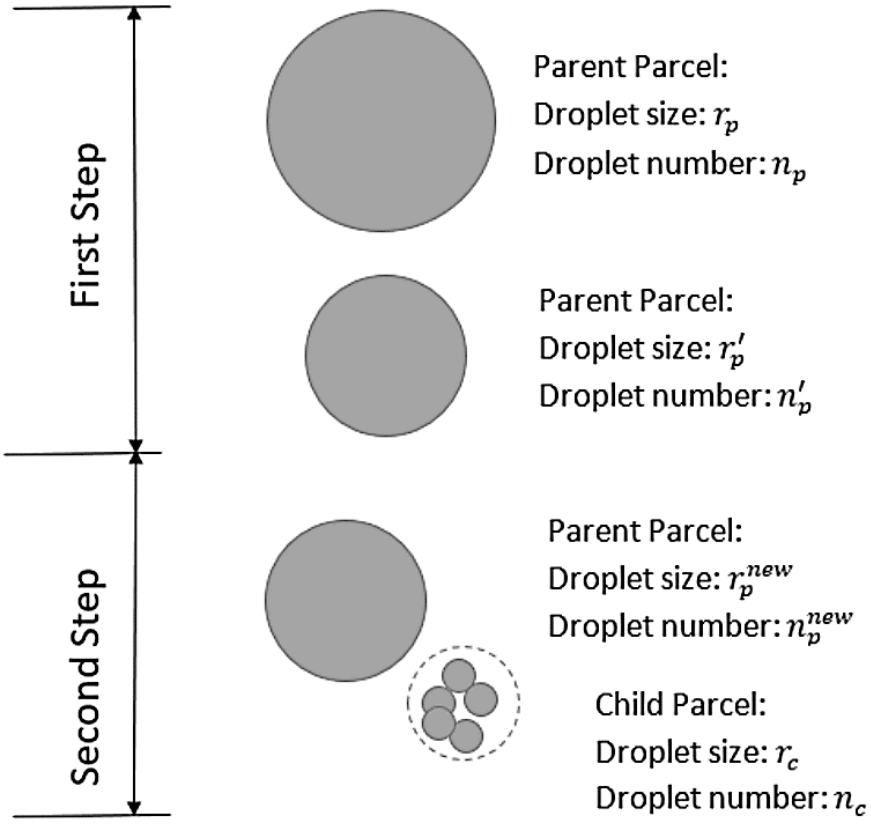

Figure 5.3. KH breakup model implementation in two steps (ANSYS Forte Theory, 2020).

5.5.7. Rayleigh-Taylor breakup

The Rayleigh-Taylor (RT) model and the KH model are used to estimate secondary breakup of spray droplets further than the Breakup Length emanating from the nozzle outlet (Su et al., 1996; Beale and Reitz, 1999).

According to Levich's theory (Levich, 1962), the "breakup length" is defined as:

$$L_{brk} = C_b D \sqrt{\frac{\rho_l}{\rho_g}} \tag{5.53}$$

where C_b is a constant notation of 10.29. In ANSYS Forte, the breakup length is applied as follows:

$$L_{brk} = D_{RT} C_b \sqrt{A_{noz} \frac{\rho_l}{\rho_g}} = D_{RT} \sqrt{\frac{\pi}{4}} C_b d_{noz} \sqrt{\frac{\rho_l}{\rho_g}} \tag{5.54}$$

where A_{noz} as nozzle cross-section area, d_{noz} as diameter of nozzle and C_b stated as 10.29, and D_{RT} as distance constant expressed in the ANSYS Forte interface. When compared with Levich's original definition Eq. (5.53), D_{RT} in Eq. (5.54), two purposes are served two: in one the conversion factor commencing from d_{noz} to A_{noz}; the other one serves as model calibration knob. The commended amount for D_{RT} is about 1.9. It is used beyond the breakup length from the nozzle outlet when the RT model is used. The RT model considers the instability that develops when two fluids with different densities are accelerated in a direction perpendicular to their interface.

According to Bellman, the wavelength and frequency of the wave with the fastest growth rate (Bellman and Pennington, 1954) are:

$$\Omega_{RT} = \sqrt{\frac{2}{3\sqrt{3\sigma}} \frac{\left[-a(\rho_l - \rho_g)\right]^{3/2}}{\rho_l + \rho_g}} \tag{5.55}$$

$$\lambda_{RT} = 2\pi \sqrt{\frac{3\sigma}{-a(\rho_l - \rho_g)}} \tag{5.56}$$

The notation a is the retardation brought on by drag while a high-speed droplet is travelling through the air. Like the KH model, this fastest-growing wave is predicted to break into droplets. Predictions for the freshly created radius of droplets and its disintegration time are as follows:

$$r_c = B_{RT} \Lambda_{RT} \tag{5.57}$$

$$\tau_{RT} = \frac{C_{RT}}{\Omega_{RT}} \tag{5.58}$$

where B_{RT} and C_{RT} are constants. B_{RT} is the size constant of RT breakup and C_{RT} is the time constant of RT breakup. The KH model separates little droplets from their parent droplets, and the liquid column eventually disintegrates and disperses into the

surrounding gas, in contrast to the common use of the RT model which predicts a catastrophic breaking of the parent droplet into mini droplets.

To decrease the time step dependence of the RT model, a rate equation is like the one used in the KH model to describe the RT breakup process, Eq. (5.51):

$$\frac{dr_p}{dt} = -\frac{r_p - r_c}{\tau_{RT}} \tag{5.59}$$

in which r_c is predicted by Eq. (5.57). The parent droplet breaks up continuously at each time step, and the time-step dependency is avoided.

Assuming r_c and does not change with time, Eq. (5.59) can be solved analytically as:

$$r_p = r_c + \left(r_{p,0} - r_c\right) exp^{\frac{t}{\tau_{RT}}} \tag{5.60}$$

Here $r_{p,0}$ is the radius of parent droplet at the start of break-up. Thus, is the characteristic time required to break the parent droplet.

5.6. Droplet collision model

In order to estimate the number of droplet collisions and their outcomes in a computationally efficient manner, the droplet collision model integrates droplet tracking. The model is based on O'Rourke's technique, which posits that collisions are approximated stochastically (Basha, Prasad and Rajagopal, 2009; Tatschl and Priesching, 2009; Kongre, and Sunnapwar, 2010; Belal et al., 2013). When two droplet packages collide, an algorithm determines the sort of collision. Only the outcomes of coalescence and bouncing are measured. The collision Weber number was used to compute the likelihood of each outcome, which was then fitted to experimental data.

The Weber number was given as:

$$We = \frac{\rho V_r^2 l}{\sigma} \tag{5.61}$$

where V_r is the relative velocity between two parcels and l is the arithmetic mean diameter of the two parcels. In the event of a collision, the state of the colliding parcels is modified.

5.7. Wall film model

In diesel engines, spray wall interaction is a key part of the mixture generation process. Fuel was pumped directly into the combustion chamber of a DICI engine, where the spray could impinge on the piston. The presence of carbon deposits on the combustion chamber surfaces complicated the modelling of the wall film within a DICI diesel engine. The liquid layer is absorbed by the carbon deposit. The carbon deposits were thought to absorb the fuel later in the cycle. A single ingredient liquid drop can impinge on a boundary surface and generate a thin film using the wall film model in ANSYS Forte. The impact energy and the boiling temperature of the liquid determine the interactions during impact with a boundary, as well as the criteria by which the regimes are separated (Basha, Prasad and Rajagopal, 2009; Tatschl and Priesching, 2009; Kongre, and Sunnapwar, 2010; Som and Longman, 2011; Belal et al., 2013). The impact energy is calculated as follows:

$$E^2 = \frac{\rho V_r^2 D}{\sigma}\left(\frac{1}{min(h_0/D,1)+\delta_{bl}/D}\right) \tag{5.62}$$

where ρ is the liquid density, V_r is the relative velocity of the particle in the frame of the wall, D is the diameter of the droplet, σ is the surface tension of the liquid and δ_{bl} is a boundary layer thickness.

5.8. NOx formation modelling

At high temperatures, the mechanism for NOx formation is well understood. Under high-temperature, oxygen-rich circumstances, NOx forms very quickly. As a result, NOx is usually rather predictable, particularly when the combustion temperature is predictable. The expanded Zeldovich model mechanism (Heywood, 1988; Zhong and Roslyakov, 1996) is the most often utilised mechanism to characterize NO formation:

$$N_2 + O \leftrightarrow NO + N \quad (a)$$
$$O_2 + N \leftrightarrow NO + O \quad (b) \tag{5.63}$$
$$OH + N \leftrightarrow NO + H \quad (c)$$

To comply with ASTM requirements, a factor of 1.533 (the molecular weight ratio of NO_2 to NO) is employed to convert NO to NO_X.

It is worth noting that the Zeldovich technique solely considers the thermal NO. Under different engine operating circumstances, a variety of distinct NO_X processes are thought to be important.

When a detailed fuel chemistry kinetics mechanism is used in combustion calculations, a detailed NO mechanism can be incorporated into the fuel mechanism to better estimate NOx emissions. NOx is equal to the NO_2 and NO product in this instance.

$$k_1[N][O_2] \leftrightarrow k_2[NO][O] \tag{5.64}$$

$$k_3[O][N] \leftrightarrow k_4[NO][N] \tag{5.65}$$

The assumption that the reaction rates of the forward and reverse processes are equivalent is used to calculate the concentrations of radicals. This assumption has been demonstrated experimentally at high temperatures exceeding 1600 K. Thermal NO production can be described by the reactions outlined in Eqs. (5.64) and (5.65) using this partial equilibrium. This premise, however, only yields satisfactory outcomes at high temperatures where partial equilibrium is already achieved.

5.9. Semi-empirical soot modelling

In the two-step soot model that is utilised in ANSYS Forte, it is composed of competing production and oxidation phases. Particle nucleation, surface growth, surface oxidation, particle coagulation, and other physical and chemical processes are all involved in the creation of soot in engines. The use of empirical soot models in multi-dimensional engine simulations has grown significantly. Two-step soot models have gained wide popularity due to their simplicity and moderate accuracy (ANSYS Forte Theory, 2020).

In these models, soot oxidation and soot production are two competing processes:

$$\frac{dM_s}{dt} = \frac{dM_{sf}}{dt} - \frac{dM_{so}}{dt} \tag{5.66}$$

in which M_{sf}, M_{so} and M_s are the formed, oxidised, and net soot mass in each computational cell at time t (Patterson et al., 1994; Kitamura et al., 2002)

$$\frac{dM_{sf}}{dt} = K_f M_{pre} \tag{5.67}$$

$$K_f = A_{sf} p^n exp\left(-E_f/RT\right) \tag{5.68}$$

$$\frac{dM_{so}}{dt} = \frac{6MW_c}{\rho_s D_s} M_s R_{total} \tag{5.69}$$

in which n is a constant, p is pressure, Ms is soot mass, with f for "formation" or o for "oxidation" as an extra subscript. K_f represents soot formation rate, M_{pre} also represents mass of the soot precursor, E_f is the activation energy for soot formation, A_{sf} is the pre-exponential factor for the global soot-formation reaction, MWC is the molecular weight of carbon, D_s is the presumed soot particle diameter, ρ_s is soot density, and R_{total} is the Nagle and Strickland-Constable oxidation rate (Vishwanathan and Reitz, 2008).

5.10. Computational grid independence and sensitivity

A mesh independence test was performed for the geometry configuration of the base piston bowl. The computational domain is formed from a 45° sector of the engine, corresponding to one injector nozzle hole. Figure 5.4 shows the computational grid at start of compression stroke. This computational domain represents the area between the intake valve closure (IVC) and exhaust valve opening (EVO) in the simulated engine cylinder. As a result, the model only computes the closed volume phase of the engine cycle of the IVC to EVO. The models are often calibrated for a specific mesh size. It is necessary to minimise the interference of grid-dependent models from the present CFD engine scaling study to enable the achievement of comparable results.

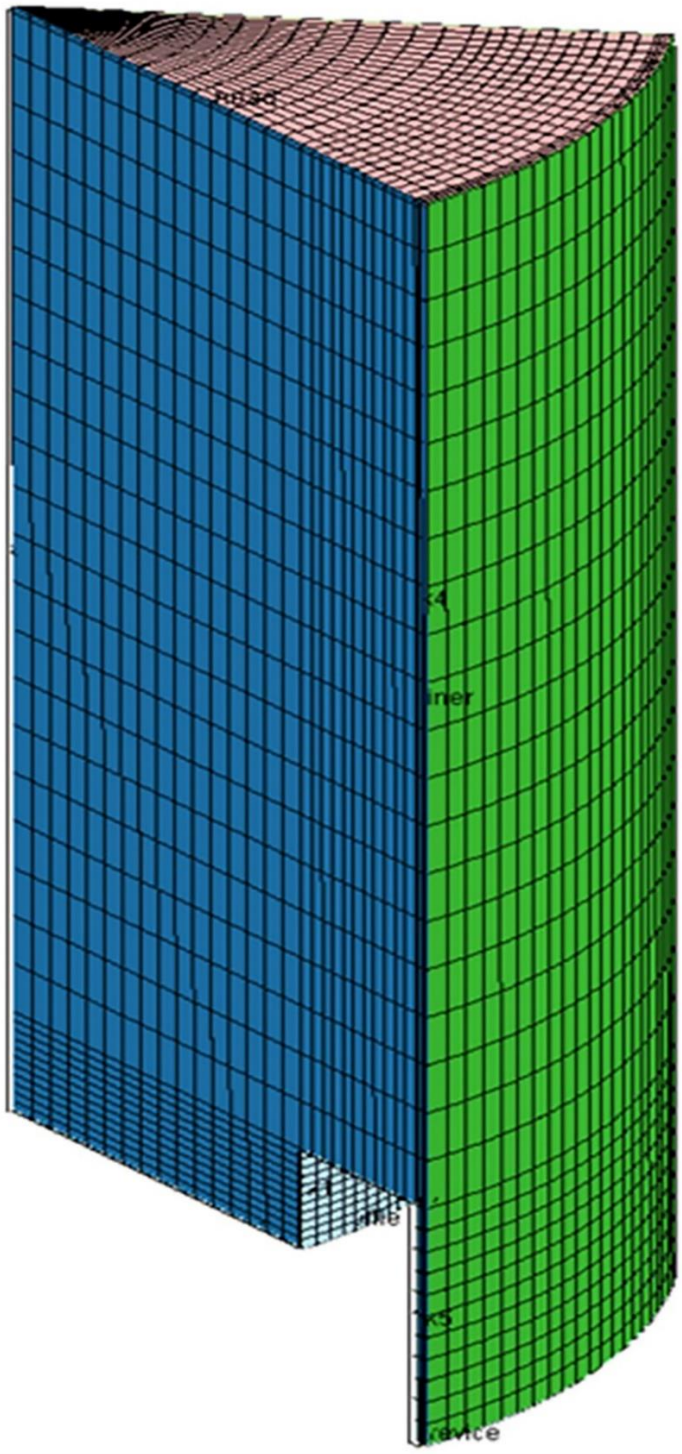

Figure 5.4. Computational grid of the base bowl medium mesh.

In the grid independence study, three mesh resolutions are evaluated, namely coarse mesh, medium mesh, and fine mesh. Figure 5.5 shows a graph of the three mesh types and their associated computational runtimes as numerated in Table 5.2.

Table 5.2. Computational mesh details

	Mesh type	Number of cells	Runtime (hours)
1	Coarse mesh	2339	0.5
2	Medium mesh	11,844	1.2
3	Fine mesh	106,807	12

The in-cylinder pressure trends for the three meshes in the preliminary simulation shows that there is no significant difference between the fine mesh and the medium mesh, but rather that the fine mesh required more runtime for analysis because it has more cells than the medium mesh. Consequently, in this study the medium mesh was chosen to reduce computation runtime.

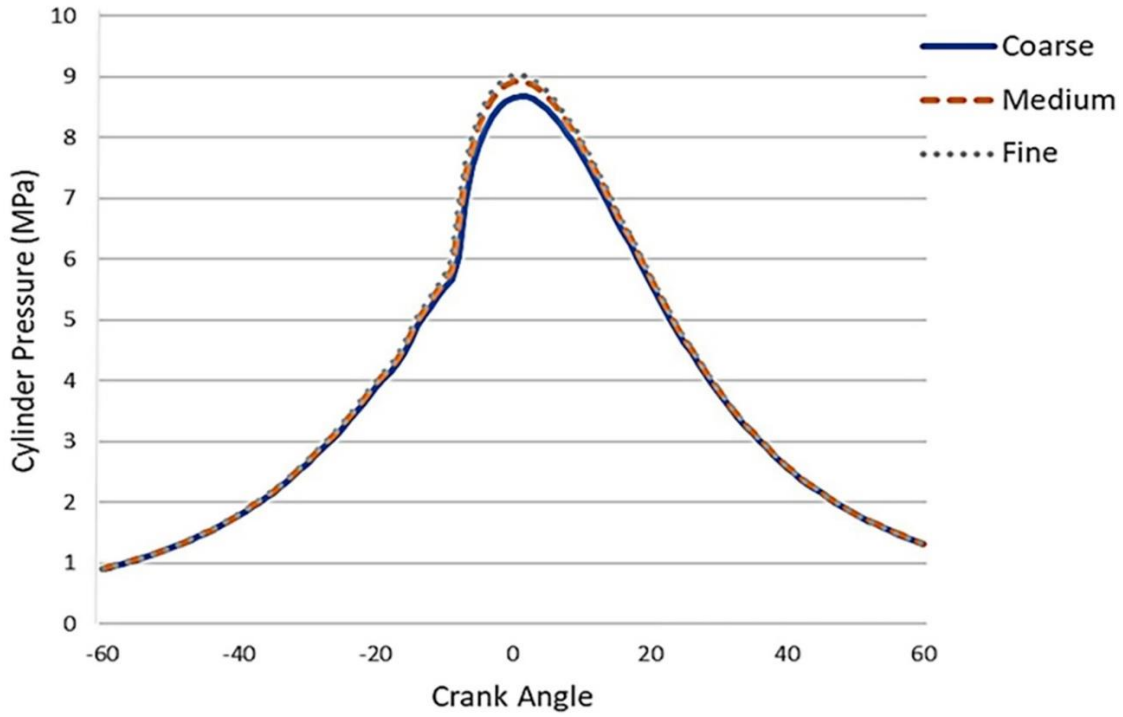

Figure 5.5. In-cylinder pressure plots for coarse, medium, and fine mesh.

5.11. Model validation

The combustion and emission measurements from a single cylinder direct injection 4 stroke heavy duty diesel engine, Cummins N series with a displacement of 2.34 L were used to validate the computational results of the Base Bowl and five different modified Bowls (Singh, Reitz and Musculus, 2006). The peak in-cylinder pressure, the

combustion efficiency and thermal efficiency were used as a validation criterion. The CFD simulation trend for the peak in-cylinder pressure seems to be reasonably close for all the bowls profiles in the simulated engine performance. The peak pressure of the five different bowl designs varies by +2° at TDC which is less than 3% deviation from the validated base bowl design outlined in Table 5.3 and shown in Figure 5.6 graph.

Table 5.3. Peak pressure profile at various crank angles of base bowl and five modified bowl designs

Bowl profile	Peak in-cylinder pressure (MPa)	Crank angle (degree)
Base bowl	8,539	1° ATDC
Case 1	8,604	2° ATDC
Case 2	8,674	1° ATDC
Case 3	8,931	1° ATDC
Case 4	8,334	1° ATDC
Case 5	8,467	2° ATDC

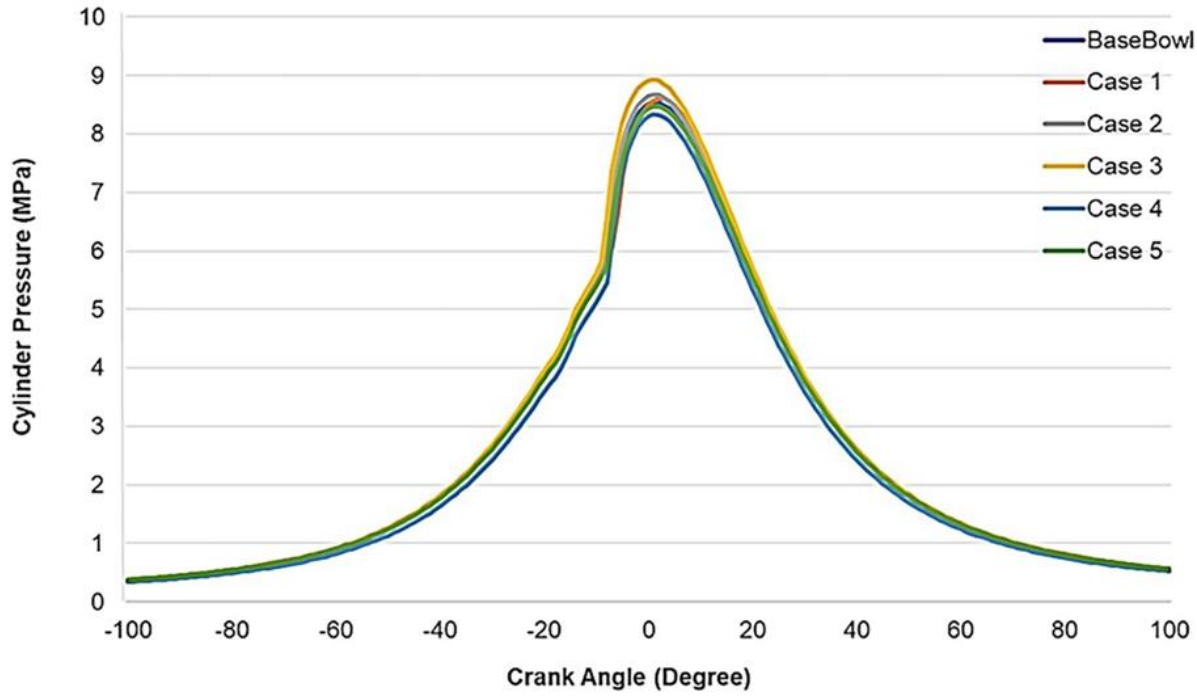

Figure 5.6. In-cylinder pressure plot of the validated base bowl and five bowl designs cases.

The combustion efficiency and thermal efficiency outline in Table 5.4, indicates a good corelation between the base bowl and the five modified bowl designs. The combustion efficiency and thermal efficiency of the five modified bowls deviates from the base bowl design model by less than the average amounts of 0.2% and 0.3%, respectively.

Table 5.4. Combustion efficiency and thermal efficiency of the base bowl and five bowl designs.

Bowl profile designs	**Combustion efficiency (CE)**	**CE deviation Base bowl**	**Thermal efficiency (TE)**	**TE deviation Base bowl**
Base bowl	0,99376	± 0.2%	0,404	± 0.3%
Case 1	0,98236	0,0057	0,413	0,00484
Case 2	0,99385	0.00045	0,4101	0,002975
Case 3	0,99705	0,001645	0,4088	0,002295
Case 4	0,99758	0,00191	0,41	0,002425
Case 5	0,98949	0,002135	0,41	0,000435

The fuel vapor mass fraction contour plots in Figure 5.7 were drawn at -17° BTDC with a spray included angle of 152° and injection timing of -22.5° with 7.75° duration. At this stage, more than 50% of the fuel has been injected into the combustion chamber. Within the combustion chambers, the in-cylinder contour plots of the fuel vapour mass fraction distribution in Figure 5.7 shows a similar pattern for the base bowl and the cases 1–5 piston bowl designs.

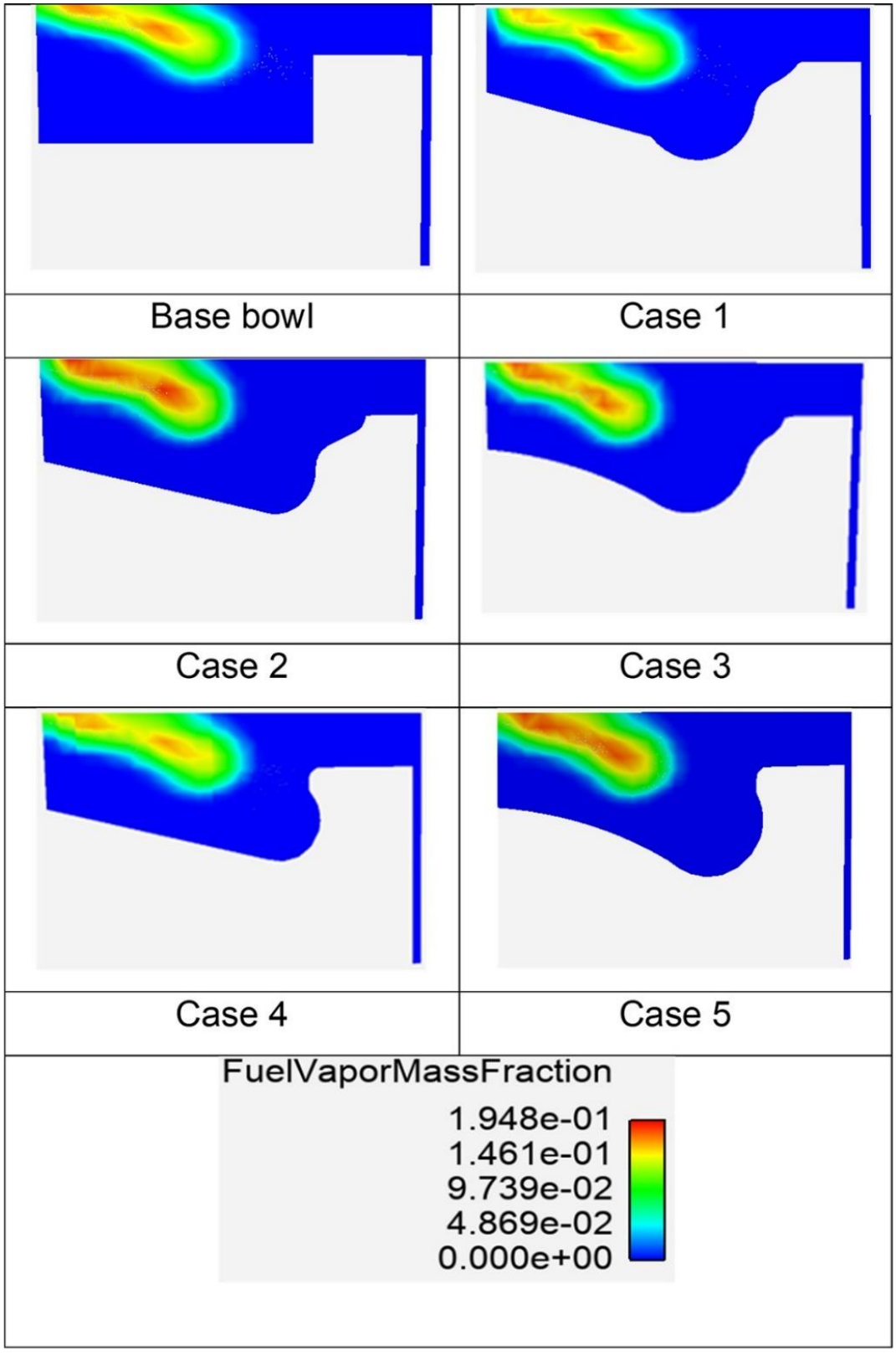

Figure 5.7. Contours of in-cylinder fuel vapor mass fraction distribution on a cut-plane along the axis of the injection nozzle hole at -17° crank angle BTDC, of the base bowl and the five different bowl design.

5.12. Summary

This chapter describes various numerical equations and the sub-models employed in the ANSYS Forte package of the CFD software used for simulating internal combustion diesel engines. The in-cylinder physical and chemical kinetic models, as well as the processes that determine the combustion and emission characteristics of direct injection diesel compression ignition engine with required governing equation was discussed. The chapter also included the computational grid independence sensitivity study. In conclusion, measurement data from a single-cylinder direct injection four-stroke heavy-duty diesel engine, the Cummins N series, with a displacement of 2.34 L was used to validate the computational results of the base bowl and five different piston bowl designs as described in Chapter 4.

CHAPTER 6

Result and discussion of combustion simulation of DICI engine

In this chapter a reduced normal heptane (n-heptane) kinetic mechanism is used to represent petroleum diesel as fuel surrogate to simulate combustion process and emission characteristics of base bowl and five modified piston bowl designs in low-temperature combustion direct injection compression ignition (DICI) engine. It further conducted a parametric study on injection spray phenomena, i.e., start of injection (SOI) and spray included angle (SIA) in tandem with the five piston bowl geometry designs to ascertain the optimum bowl designs and operating conditions. The chapter discusses the result of combustion processes, and emission characteristics. It concludes taking into consideration the trade-offs between gross indicated specific fuel consumption (GISFC), soot and nitrogen oxide (NOx) formation.

6.1. Introduction

The study used ANSYS FORTE, version 2020 R2, to simulate the combustion processes, and emission characteristics of a low-temperature, heavy-duty DICI diesel engine with five different piston bowl combustion chamber designs and further conducted a parametric study utilising the start of injection (SOI) and spray included angle (SIA). This is a computational fluid dynamics (CFD) programme that focuses on simulating combustion processes in internal combustion engines using a highly efficient connection of detailed chemical kinetics, liquid fuel spray, and turbulent gas dynamics. The petroleum diesel fuel in this study was represented by a reduced normal heptane (n-heptane) kinetic mechanism. For simulations of diesel engine combustion, normal heptane (n-heptane) is frequently used as a substitute fuel for diesel, due to its identical cetane number to petroleum diesel (Meloni and Naso, 2013; Wang and Liu, 2015). The importance of the cetane number as it relates to the auto-ignition of diesel makes it a crucial fuel attribute to be considered. The mechanism used in this study contains 35 species, which are taken from the ANSYS Forte library (ANSYS Forte, 2020). To simulate the combustion of diesel fuel, a reduced n-heptane mechanism is introduced to the chemistry model in the CFD simulation code.

6.1.2. CFD sub-models used

The computations were performed utilising ANSYS Forte and several physical and chemical sub-models. The essential CFD sub-models used in the simulations of the DICI engine are listed in Table 6.1, and all the equations were resolved in Chapter 5. Re-normalisation group (RNG) k-ε model is applied to model in-cylinder turbulence and liquid-phase turbulence, and the Diesel Unsteady Laminar-flamelet model is employed to model the interaction between turbulence and chemistry. The RNG k-ε turbulence model is used to simulate in-cylinder turbulent flow because it takes high swirling flows into account and can quantitatively enhance NOx emission prediction for single-injection combustion cases. To analyse the physical processes underlying the change in kinetic energy, the RNG k-ε model was chosen as the turbulence model.

Table 6.1. CFD sub-models used in the simulation and the equations Chapter 5.

Sub-models used	
Turbulence model	RNG k-ε model
Combustion model	Mixing controlled combustion (MCC)
Fuel chemistry model	Skeletal n-heptane reduced mechanism
Droplet breakup model	KH- RT model
NOx mechanism	Extended Zeldovich mechanism
Soot model	Two-step semi-empirical soot model

6.1.3. Geometry and mesh generation

In the case of a diesel engine with a multi-hole injector that has equally spaced holes, properties such as injection pressure, temperature, air-fuel mixture homogeneity or mixture concentration, combustion process, and so on are considered identical. As a result, the combustion chamber within the engine cylinder is assumed to be symmetrical in relation to each injector nozzle hole. As a result, rather than considering the entire engine geometry for calculation, an advantage can be easily acquired by simulating a specific piece of geometry. An eight-hole injector, for example, can simulate a 45° sector (360°/8). Instead of employing the entire geometry of the engine, a 45° angle sector with periodic boundary conditions applied at the periodic faces of the sector is examined in the current study for computational domain and mesh creation to reduce computational cost and time without compromising accuracy.

Table 6.2. Engine specifications and operating conditions

Engine base type	**Cummins N-14, DI diesel**
Number of cylinders	1
Cycle	4-stroke
Number of intake valves	2
Number of exhaust valves	1
Combustion chamber	Quiescent, direct injection
Bore	13.97cm
Stroke	15.24 cm
Compression ratio	11:2,
Bowl width x depth (base bowl)	9.79 x 1.55 cm
Connecting rod length	30.2 cm
Engine speed	1200 rpm
Fuel injector type	Common rail, pilot valve actuated
Number of holes	8, equally spaced
Nozzle orifice area	$3.02x10^{-4}$ cm^2
Spray included angle (varied)	(Base 152°) 126°, 136°, 146° and 156°
Start of injection (SOI) (varied)	-15.5, 18.5, -22.5 and 25.5 [Before TDC]
Discharge coefficient	0.7

The base bowl and five bowl profile geometry were created in ANSYS Space-Claim and exported to Forte Sector Mesh Generator, which was used to refine the geometry and create the mesh before being imported into Forte Simulate (ANSYS simulation interfaces are shown in appendix 1). A single cylinder DI diesel engine based on a Cummins N-series production engine has been modelled as the base engine using ANSYS Forte CFD simulation software (Musculus, 2004). The engine specifications and operating conditions are listed in Table 6.1, Table 6.2. Figure 6.1 shows the 3D CFD 45° sector mesh of the base bowl and five modified bowl profile geometries of spatial distribution of turbulence velocity at -10° crank angle (CA) BTDC under engine speed of 1200 rpm.

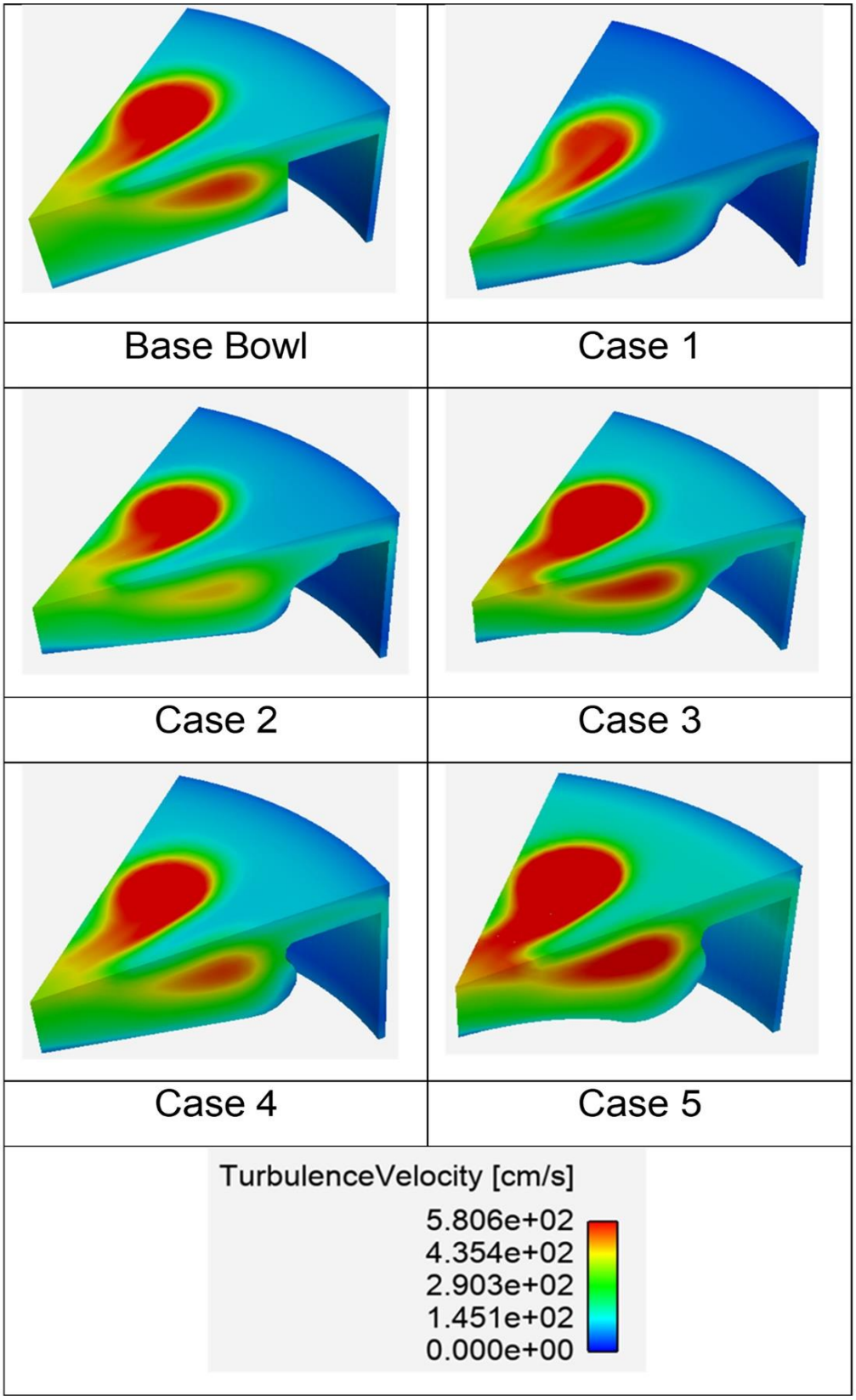

Figure 6.1. The 3D spatial plots of turbulence velocity at -10° crank angle (CA) BTDC under engine speed of 1200 rpm, a 45°-sector mesh of the base bowl and five modified bowl profile geometries.

6.1.4. Initial and boundary conditions

In Table 6.3, the initial and boundary conditions for engine simulations are presented. In cases with different diesel injection timings and diesel ratios, these values will apply. To capture wall boundary layer effects more accurately, pistons, heads, and liners are specified with the Law of the Wall model. Turbulent law-of-the-wall velocity conditions and fixed temperature walls are commonly used in simulations of in-cylinder engines.

Table 6.3. Initial and boundary conditions

Parameters	**Value**
Intake valve closing	-165° before TDC
Exhaust valve open	125° after TDC
Temperature at inlet valve closing	362 K
Pressure at inlet valve closing	2.215 bar
Turbulent kinetic energy	10,000 cm^2/sec^2
Turbulent length scale (cm)	1.0
Initial swirl ratio	0.5
Initial swirl profile factor	3.11
Boundary conditions	
Periodicity	45 degrees
Wall model	Law of the wall
Piston temperature	500 K
Head temperature	470 K
Line temperature	420 K

In diesel engines, the combustion process is often simulated from intake valve closure to exhaust valve opening, rather than modelling the full intake and exhaust flow processes involving the intake and exhaust ports. This is usually a reasonable approximation since the gas in the cylinder at IVC is a relatively homogeneous mixture of air and exhaust gas (due to internal residuals or exhaust-gas recycling), prior to fuel injection (Heywood, 2018). In this study, only a part of the engine operation cycle from inlet valve closing (IVC) before top dead centre (-165° CA BTDC) to exhaust valve opening (EVO) after top dead centre (125° CA ATDC) is simulated for the desired investigations.

6.2. Results and discussions

6.2.1. Turbulence velocity and turbulence kinetic energy analysis

Figure 6.1 shows the 3D spatial distribution of turbulence velocity, and Figure 6.2 presents the velocity vector flow field of the cut-plane in the axis of the injection nozzle in the cylinders at -10° crank angle (CA) before top dead centre for the six bowl profiles. The piston bowl geometry has a significant impact on the squish formation, which in turn affects the evaporation and mixing processes. Therefore, before analysing the engine performance, combustion process, and emissions characteristics in relation to various bowl profile geometries with other changing injection parameters, it is necessary to first take a closer look at the respective velocity vector flow fields, turbulence velocities (TVs), as well as the turbulence kinetic energies (TKEs), for all the bowl geometries.

The main toroidal section in the piston bowl profile enables a stronger vortex around that region when the piston is getting to the end of the compression stroke at TDC, this enhances good fuel-air mixture for complete combustion. Compared to the base bowl design, case 1, case 2, case 4 and case 5 had improved velocity vector magnitudes, hence increasing the turbulence velocities, as indicated in Table 6.4 and in Figure 6.3. The reason for this trend can be attributed to higher squish generation by these bowl profile designs. The larger toroidal radius in the piston cavity improves engine performance by enhancing fuel-air mixing, and the tighter throat of cases 4 and case 5, gives a forceful airflow in the chamber in agreement with results of Sreedharan and Krishnan (2018).

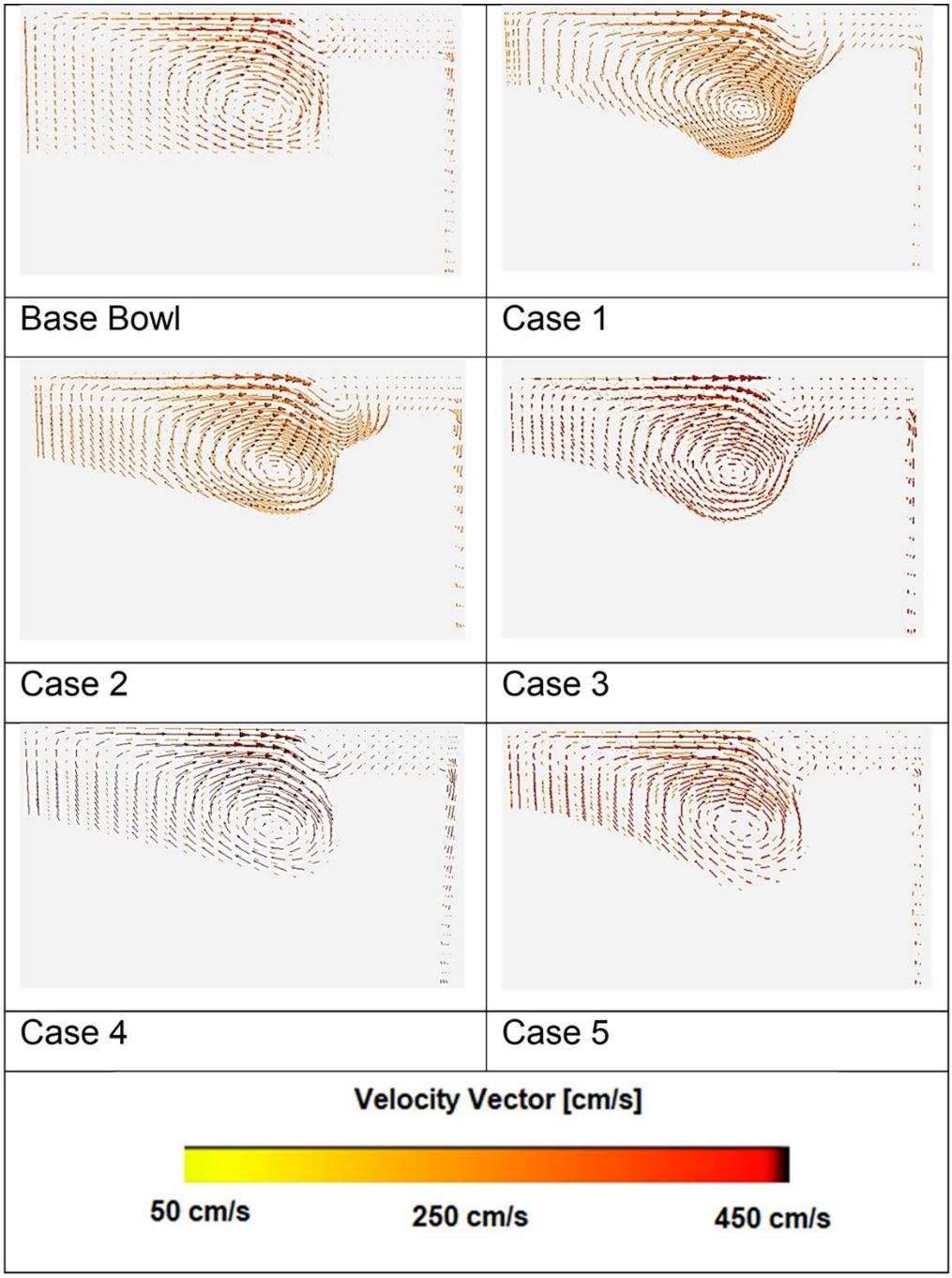

Figure 6.2. Velocity vector flow fields of cut-plane in the axis of the injection nozzle at -10° CA BTDC of the base bowl and five bowl design geometries

Table 6.4. Turbulence velocity and turbulence kinetic energy

Property	Base bowl	Case 1	Case 2	Case 3	Case 4	Case 5
TV (cm/s)	376.05	382.39	376.47	371.53	375.01	374.65
TKE (cm^2/s^2)	$6.2x10^5$	$6.3x10^5$	$6.4 x10^5$	$6.3 x10^5$	$6.7 x10^5$	$6.4 x10^5$

*TV -Turbulence velocity; TKE - Turbulence kinetic energy.

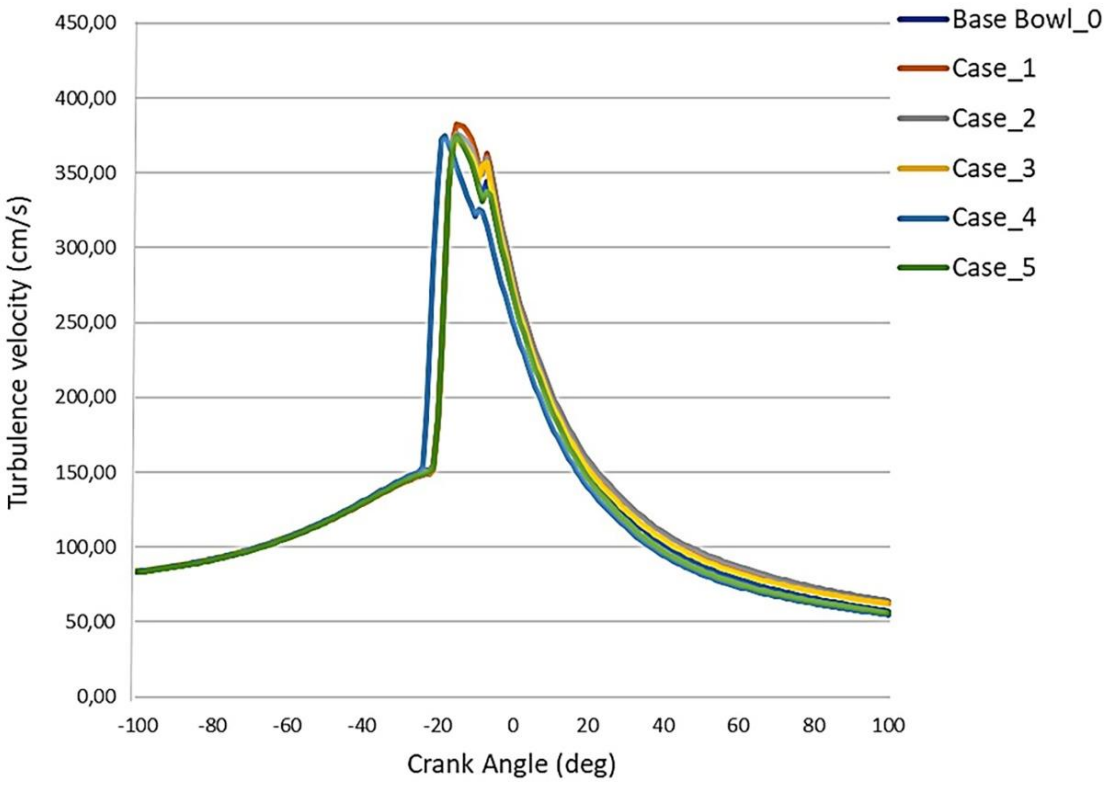

Figure 6.3. Turbulence velocity plot for the base bowl and five bowl design cases.

The complete amount of air is compressed into a compact toroidal volume at the end of the compression stroke, dissipating a higher TKE. The flow during compression was from the squish to the bowl. The rate at which turbulence kinetic energy is converted to thermal internal energy is known as turbulence dissipation. The turbulence dissipation describes the rate of turbulence kinetic energy converted into thermal internal energy.

Figure 6.4 compares the spatial plot distribution of turbulent kinetic energy for six distinct piston bowl configurations of combustion chamber getting to the end of the compression stroke: -10° CA BTDC (350°), 0° CA TDC (360°), and 10° CA ATDC (370°). For all the configurations of the combustion chamber piston bowls, it was found that the turbulent kinetic energy (TKE) is spread out across all the combustion chamber bowls, and this TKE dissipates more at the end of the compression stroke. The peak value of TKE recorded during the end of the compression stroke for base bowl design is 6.2 x 10^5 (cm^2/s^2), and Table 6.2 lists the various peak values of both TVs and TKEs. The upward movement of the piston enhances the flame propagation creating high turbulence in the area close to the re-entrant walls of cases 4 and 5 bowl design. The high turbulence created by the squish volume improved

flame propagation inside the piston bowls and the spatially averaged TKE of cases 1, 2, 3, 4 and 5 were higher than the base bowl design, because of its toroidal cavity in their piston bowls as shown in Table 6.2.

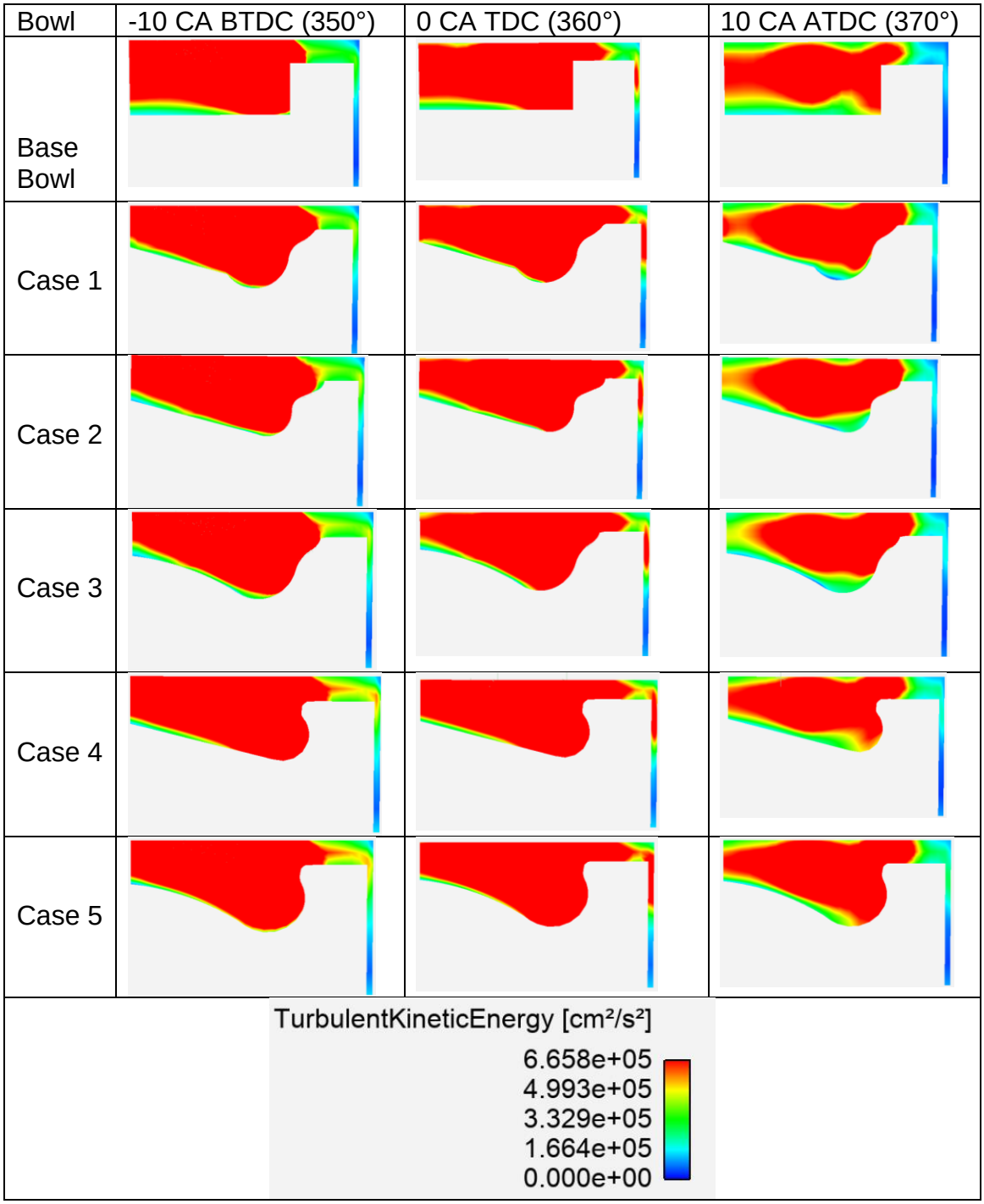

Figure 6.4. The spatial plot distribution of a cut-plane of TKE at -10 CA BTDC (350°), 0° CA TDC (360°), 10 CA ATDC (370°).

The base bowl had the lowest due to its design, and a slower flame propagation. As a result of the toroidal cavity, the spatially averaged TKE of case 4 during the operation was higher than cases 1, 2, 3, and 5 due to the significant turbulence produced by the high squish volume. Due to the bowl design and possibly a slower rate of flame propagation, the base bowl had the lowest TKE. The little variations in TKE across these five bowl scenarios showed, however, that the choice of adopting a toroidal cavity region can considerably alter the turbulence. The spatially resolved turbulence kinetic energy distribution is depicted in Figure 6.4. The flame front advanced the gas toward the edge of the bowl once the flame had erupted.

As the gas descended during the expansion stoke, the flame advanced the unburned gas in the direction of the cylinder lining. Small variations in TKE distribution at TDC and 10° CA ATDC (red region) were mostly caused by various flame propagation effects, as illustrated by the corresponding variations at the same place in the spatial plot distribution. The findings imply that the in-cylinder turbulence was significantly influenced by the toroidal cavity in the bowl.

6.2.2. The engine in-cylinder pressures and apparent heat release rates

In Figure 6.5, all six bowl profile designs are compared in terms of pressure profiles over a range of 100° CA BTDC to 100° CA ATDC. The change of in-cylinder pressure levels inside the piston bowl for six bowl types helped to better understand the combustion process. There is a greater pressure in cases 1, 2, 3 and 4 than in the base bowl and case 5, especially at the top dead centre. Increased pressure causes temperatures to rise due to enhanced particle motion inside the combustion chamber. According to the study conducted by Yao et al., (2018), this trend is quite related to the efficiency of the combustion process and how well the fuel is burned.

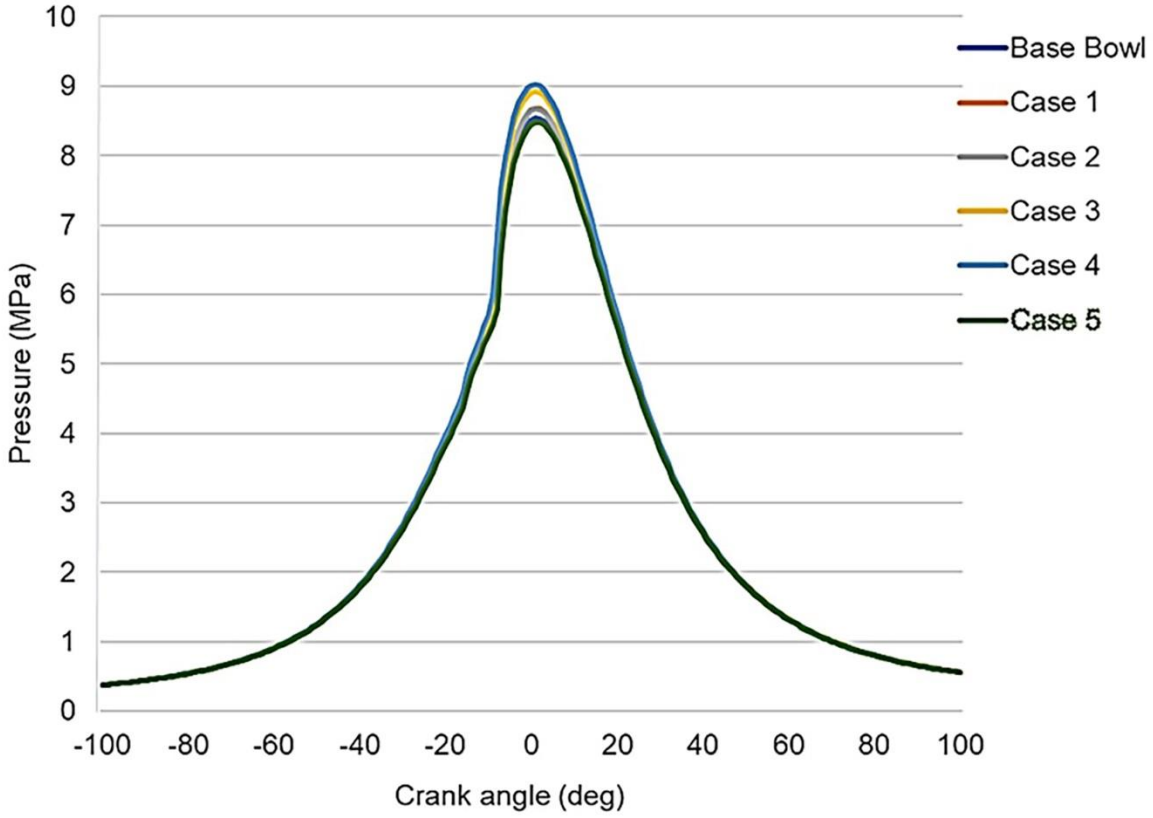

Figure 6.5. The in-cylinder pressures of the six different piston bowl designs.

Two possible explanations for this outcome are the toroidal cavity structure of the piston bowls and the fact that the mixing ratios differ depending on the bowl shapes. All geometries should theoretically have the same compression ratio, hence readings of the in-cylinder pressure should be same across all geometries. The local pressures and, consequently, the in-cylinder pressure measurements differ, though, because each design has a distinct piston bowl curvature and various mixing ratios that lead to either greater or lower in-cylinder pressure hence different combustion efficiency.

The apparent heat release rate plotted over crank angles (CA) from 100 degrees CA BTDC to 100 degrees CA ATDC are shown in Figure 6.6 of base bowl and the five various bowl cases are. The ignition delay is essentially unaffected by changes in bowl parameters, although the first peak of the heat release rate is significantly affected. The influence of piston bowl shape on heat release rate is caused by its impact on the fuel-air mixing process when the injection and intake system parameters are the same.

The bowl design in case 1 has the highest peak heat release rate, followed by cases 2 and 4. This is because the piston bowl diameter of cases 1, 2, 3 and 4 are larger, which has a significant impact on the peak heat release rate. The first and second

peak heat release rates appeared around the same position at -7° CA BTDC, being cases 1 and 2, and this leads to good efficient combustion. For bowl design cases 1, 2, and 4 BTDC, which correlate to high peak pressure and temperature under the same circumstances, more heat is released. As a result of the higher heat release from bowl design cases 1, 2, and 4, the in-cylinder mean temperature of the combustion chamber is higher.

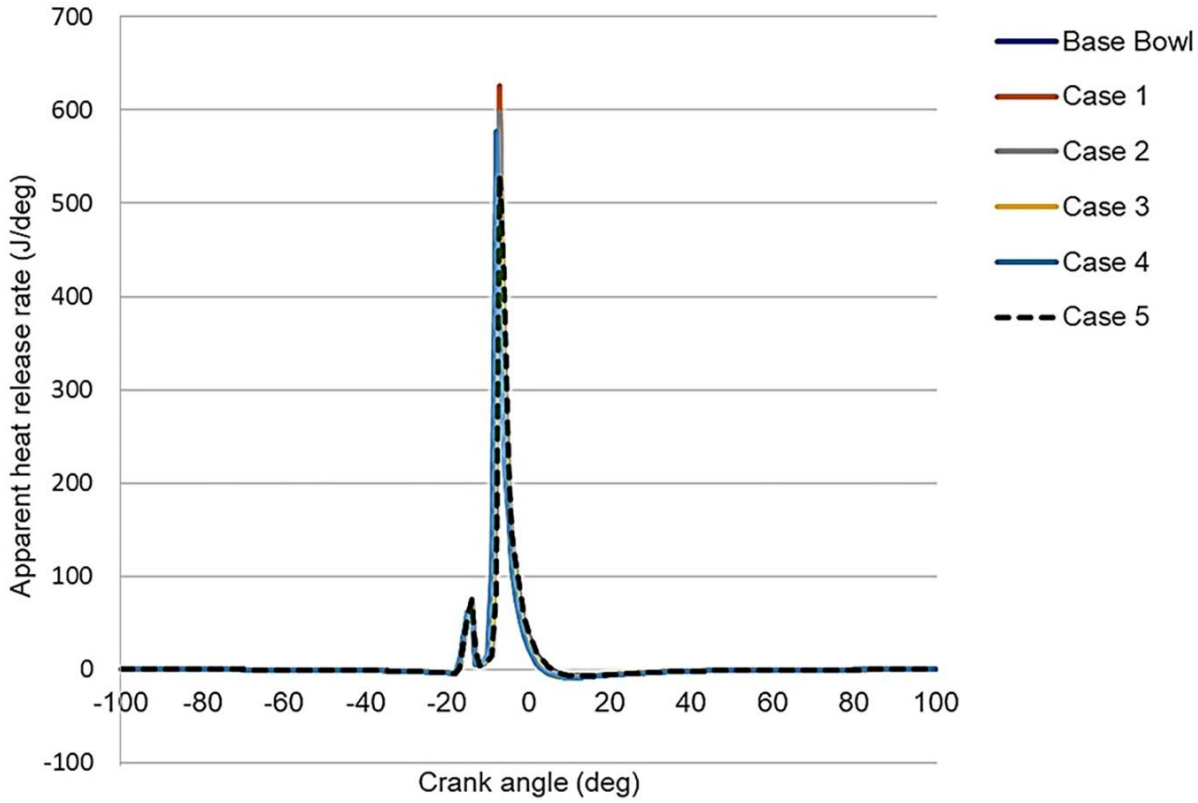

Figure 6.6. Apparent heat release rates for the six different piston bowl designs.

6.2.3. In-cylinder temperature among the piston bowls

The temperature distribution in the six bowl shapes at -10° CA BTDC, 0° CA TDC, and 10° CA ATDC is shown in Figure 6.7. The temperature is higher for bowl design cases 2, 3, and 4 than it is for other designs, as can be seen from Figure 6.7.

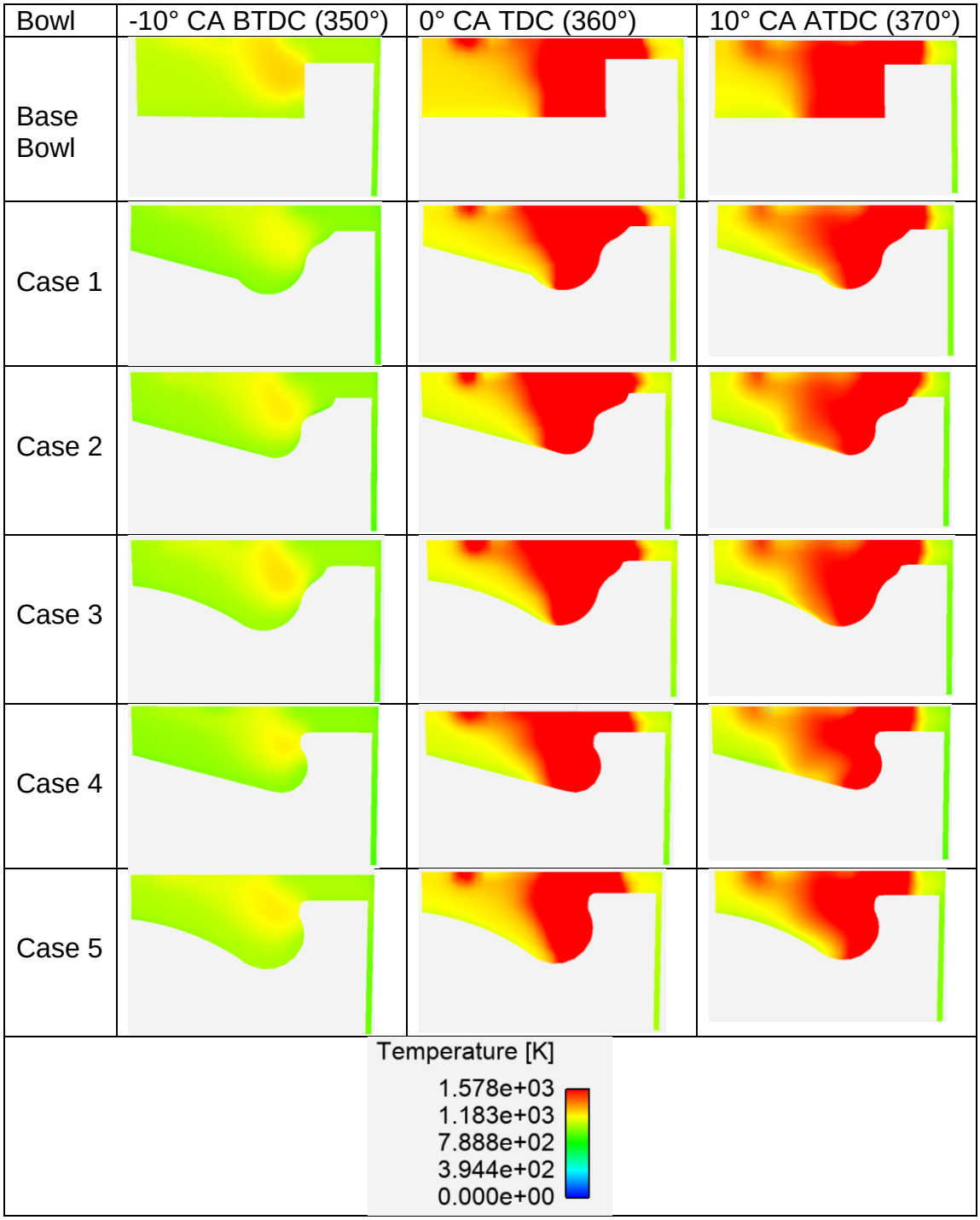

Figure 6.7. Spatial plots for in-cylinder temperature distribution of a cut-plane of at -10° CA BTDC (350°), 0° CA TDC (360°), 10° CA ATDC (370°)

These findings validate the information provided by the graphs of turbulence velocity and in-cylinder pressure as shown in Figure 6.3 and 6.5. A larger pressure is exerted by a higher temperature value. Therefore, it is not unexpected that the pressure and temperature graphs for the various designs produced comparable results. For designs

cases 1, 2, 3, 4 and 5, the temperature distribution is also more uniform as shown in the spatial distribution view in Figure 6.7, with a higher overall average temperature.

6.2.4. Emission characteristics of the base bowl and five piston bowl designs

As shown in Figures 6.8 (a) to (d), base bowl and five different piston bowl designs are compared in terms of their emission characteristics. As air pollution problem is of global importance, the emission characteristics deserve special attention.

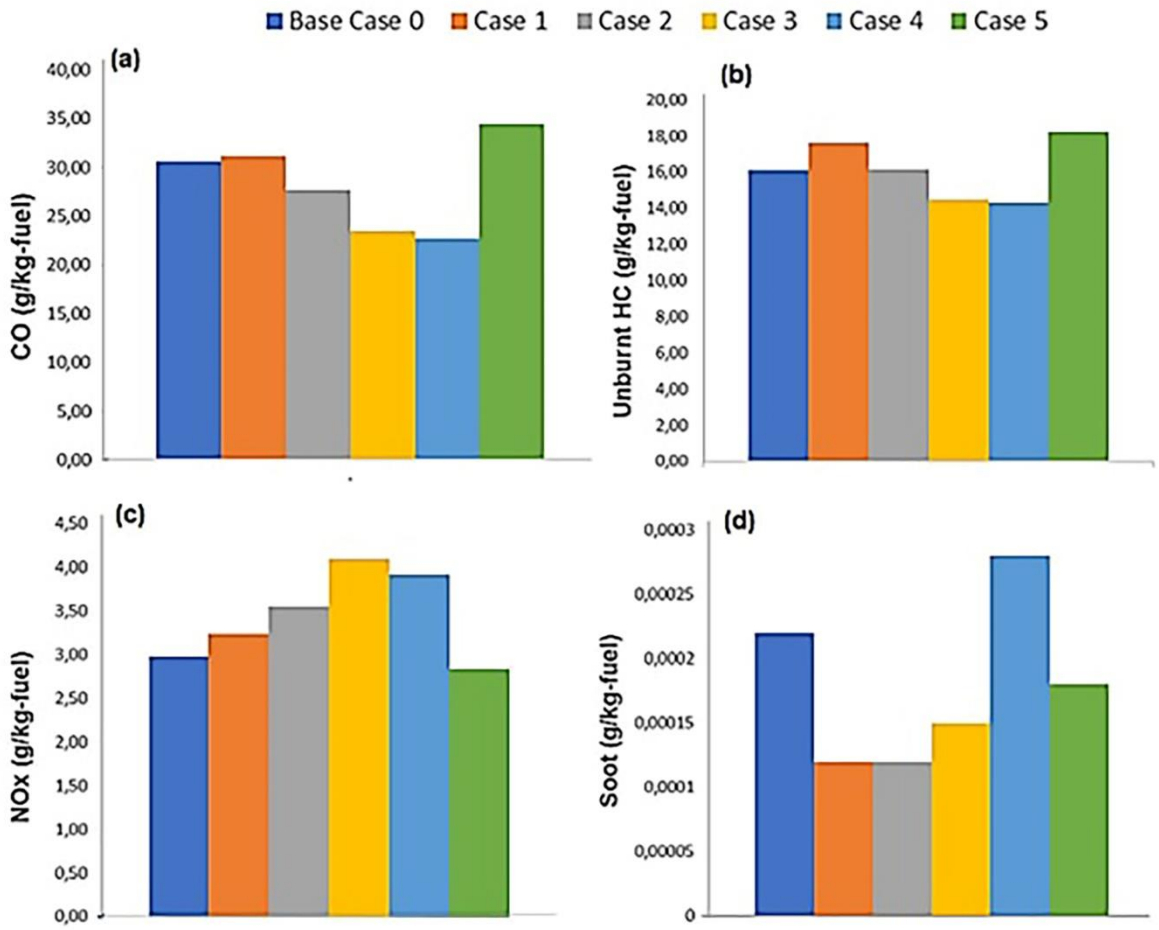

Figure 6.8. Comparison of emission characteristics for the base bowl and the five bowl designs: (a) CO emission, (b) unburnt hydrocarbon emission, (c) NOx emissions, and (d) Soot emission.

In this study, the graphical representations of CO, unburnt hydrocarbon (UHC), NOx, and soot emissions from several designs are presented. More importantly, NOx and

soot emissions require more focus since it is of a great concern in diesel engines operations.

The correlation between combustion efficiency and CO and UHC emissions is also significant. The bowl design cases 2, 3 and 4 demonstrate greater combustion efficiency compared to other designs. Therefore, it is projected that these three designs will release less CO and UHC than the other designs, as shown in Figures 6.8 (a) and (b). An intermediate combustion product called carbon monoxide (CO) is created when there is insufficient oxygen or incomplete fuel combustion. Low gas temperature or a lack of air can both lead to the formation of CO. Higher CO_2 and reactive HC from effective combustion led to decreased CO and UHC emissions. The ratio of the air to fuel mixture is yet another cause for this trend to exist. Better air/fuel mixture was given by design cases 2, 3 and 4. The higher CO mass fraction percent caused the insufficient combustion process in the other designs. According to bowl design case 5, the highest CO emission value is 34.44 g/kg-fuel, and the lowest CO emission value is 23.45 g/kg-fuel. Unburned HC emission ranged from a maximum of 18.21 g/kg-fuel in bowl design case 5 to a minimum of 14.28 g/kg-fuel in bowl design case 4.

As established in diesel engine operations, the process of NOx formation inside the combustion chamber is highly temperature dependent. The fact that a lean burn strategy in a diesel engine result in significant NOx emissions is also widely known. The volume and duration of the hottest region of the flame, which is directly related to the thermal NOx process, determines how much nitrogen oxides (NOx) are generated. However, in a cylinder of an engine, other processes, such as fuel NOx, can also be effective at a certain range of crank angles during a complete cycle. The bowl design cases 5, base bowl, and case 1 release very little nitrogen oxide (NOx) emissions (3.24, 2.98, and 2.84 g/kg-fuel, respectively), although the design cases 3, 4 and 2 more NOx are released than the other designs (4.09, 3.92 and 3.55 g/kg-fuel, respectively) as shown in Figure 6.8 (c) and Figure 6.9 (a).

Higher temperature and pressure values are mostly connected to the formation of NOx gases. The fact that the greater in-cylinder temperature of bowl design case 3, 4 and 2 are at TDC may be the cause of this trend. As a result, the higher temperature value at TDC increases the amount of N_2 that reacts, which causes more NOx to develop.

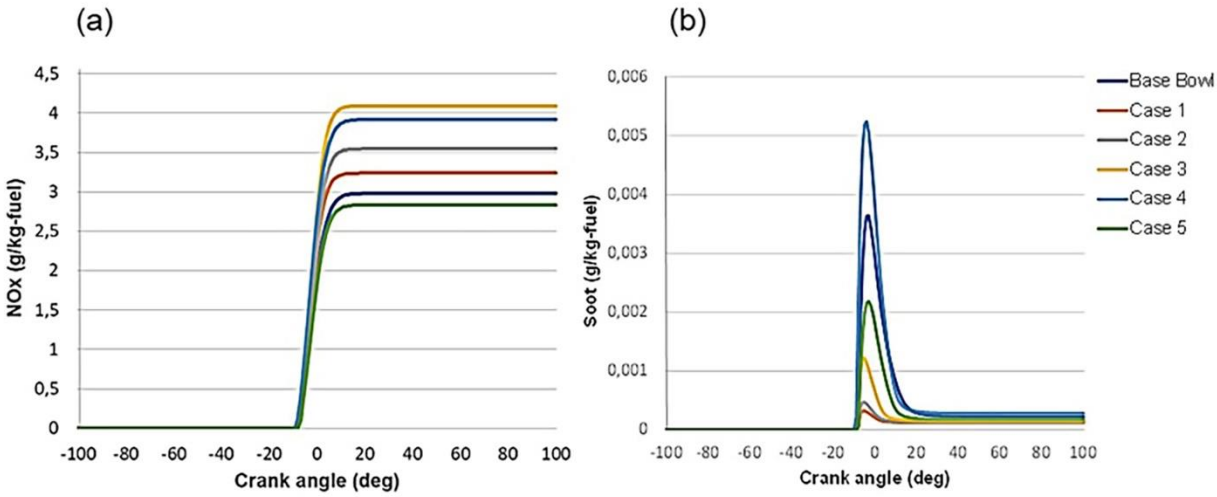

Figure 6.9. Emission of NOx and soot vs crank angle of the base bowl and the five different designs

As shown in Figure 6.10, the spatial plot of the in-cylinder gas, NO, and NO_2 mass fraction for the test engine at 0° TDC and 10° ATDC is displayed. The crank angles 0° TDC and 10° ATDC are selected to represent NO and NO_2 mass fractions, respectively; these represent the period in which the average in-cylinder gas temperatures peak and drop. There is an increase in NO_2 with a drop in NO, indicating that some of the NO generated is oxidized into NO_2, resulting in an increase in NO_2 with a decrease in in-cylinder NO concentration. On the other hand, at maximum in-cylinder temperature, NO formation is highest (Heywood, 2018).

These results support conclusions drawn by Koten (2018). Similarly in Figure 6.8 (a) and Figure 6.9 (b) shows the graph of soot emission for the base bowl and the five different piston bowl designs. High temperature and high pressure in the fuel-rich zone leads to soot production and high-temperature decomposition was used to create the combination which agrees with the study conducted by Kumar et al., (2018) and Leach et al., (2018). Bowl design cases 1, 2, 3 and 5 emit the least soot, with 0.12, 0.12, 0.15 and 0.18 g/kg-fuel, respectively, because of the improved air-fuel combination in the cylinder. It is the base bowl and case 4 that emit the worst value in this instance, 0.22 and 0.28 g/kg-fuel, respectively. The emission of soot shows an improved performance compared to NOx emission.

	Nitrogen monoxide (NO)		Nitrogen dioxide (NO_2)	
Piston Bowl	0° CA TDC	+10° CA ATDC	0° TDC CA ATDC	+10° CA ATDC
Base bowl	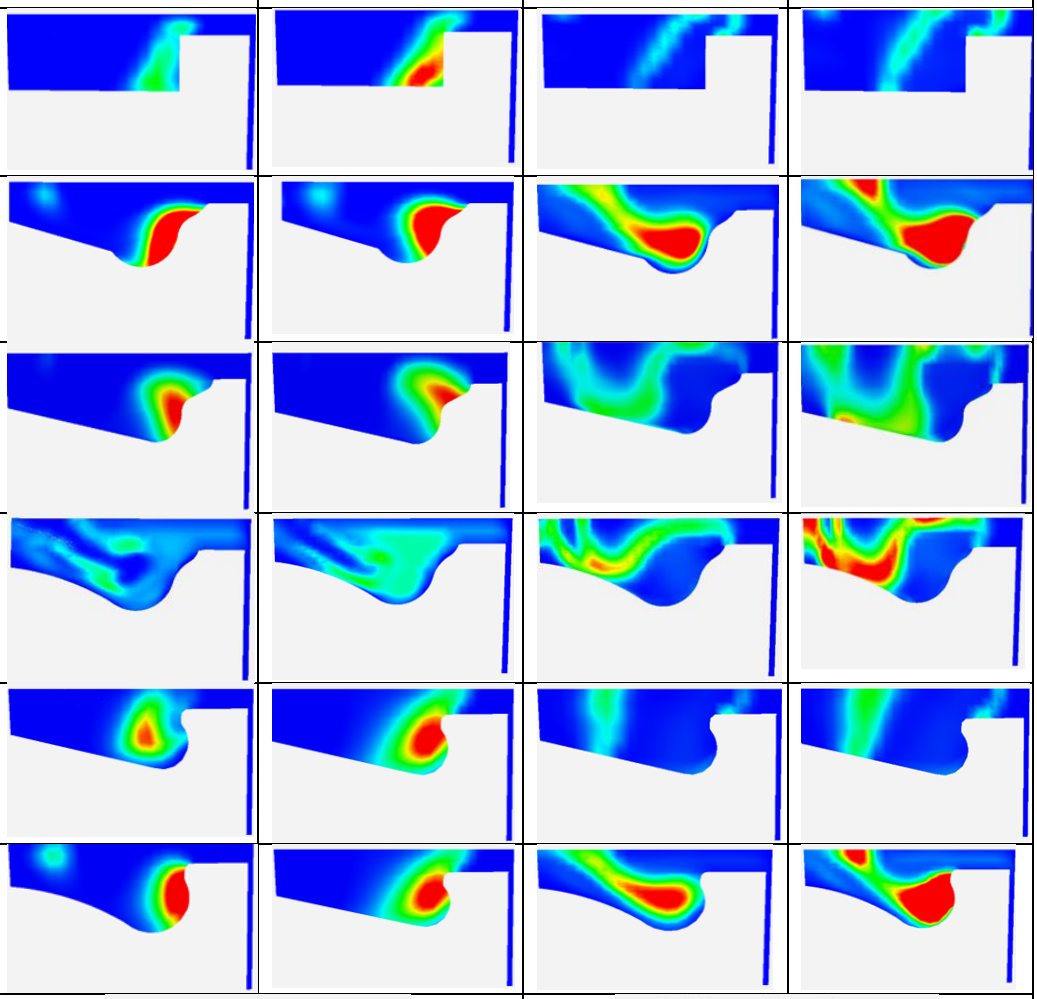			
Case 1				
Case 2				
Case 3				
Case 4				
Case 5				
	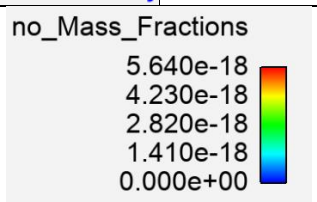		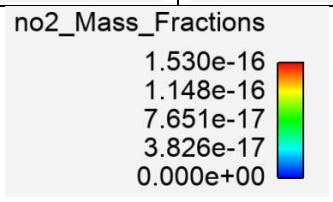	

Figure 6.10. Spatial plot of in-cylinder cut plane at 0° TDC and 10° ATDC of NO, and NO_2 mass fraction

6.2.5. Comparison of performance and emission characteristics of the base bowl and five bowl designs

The engine performance and emissions of the base bowl design and the five different bowls are compared, considering the gross indicated power (GIP), gross indicated specific fuel consumption (GISFC), CO, UHC, SOOT, and NOx. A list of the results for

the base bowl design and cases 1 to 5 at 1200 rpm is shown in Table 6.5. This numerical analysis demonstrates that these design cases simultaneously and considerably increased engine performance and emission as compared to the base bowl design, for instance, cases 1, 2, and 3 show improvements of 1.34%, 2.1%, and 1.6% of the gross indicated power, respectively.

Table 6.5. Comparison of the performance and emissions of Base Bowl and five bowl design cases

Bowl design	**Base bowl**	**Case 1**	**Case 2**	**Case 3**	**Case 4**	**Case 5**
GIP (kW)	**9.58**	**9.71** (1.34%↑)	**9.78** (2.1%↑)	**9.73** (1.6%↑)	**9.58** (0%↔)	**9.64** (0.62%↑)
GISFC (g/kW-h)	**201.02**	**198.28** (1.4%↓)	**196.94** (2.1%↓)	**197.90** (1.6%↓)	**200.94** (0.04%↓)	**199.85** (0.6%↓)
CO (g/kgf)	**30.62**	**31.21** (1.9%↑)	**27.75** (9.8%↓)	**23.45** (26.5 %↓)	**22.71** (29.7%↓)	**34.44** (11.7%↑)
UHC (g/kgf)	**16.09**	**17.64** (9.2%↑)	**16,16** (0.4%↑)	**14.47** (10.6%↓)	**14.28** (11.9%↓)	**18.21** (12.4%↑)
NOx (g/kgf)	**2.98**	**3.24** (8.4%↑)	**3.55** (17.5%↑)	**4.09** (31.4%↑)	**3.92** (27.2%↑)	**2.84** (4.8%↓)
Soot (g/kgf)	**0.00022**	**0.00012** (58.8%↓)	**0.00013** (51.4%↓)	**0.00015** (37.8%↓)	**0.00028** (24%↑)	**0.00018** (20%↓)

GIP-Gross indicated power; GISFC- Gross indicated specific fuel consumption

Up - ↑ Down - ↓ Equal - ↔

Due to lower heat losses, the base bowl engine produced low NOx but had slightly high fuel consumption due to the lower in-cylinder averaged temperature. Compared with the base bowl design, cases 2, 3 and 4 have lower CO levels, and additionally design cases 3 and 4 also show lower UHC. The improvement of premixed combustion, which favours a decrease in soot emissions and fuel efficiency but leads to increased NOx emissions, is made possible by an increase in the swirl ratio. The bowl design cases 1, 2, 3 and 4 had increased NOx compared to the base bowl design at 8.4%, 17.5%, 31.4% and 27.2% respectively, the bowl design case 5 shows lower NOx and this is due to the less temperature generated in the combustion chamber. In

a similar manner, the low combustion temperature suppresses soot formation without adversely affecting its oxidation. When the surrounding air is utilised during combustion, more NOx emissions are produced, and fuel consumption is reduced. The soot formation of the bowl design cases 1, 2, 3 and 5 showed lower soot compared to the base bowl design; this is due to enhanced homogeneous air fuel. Bowl design cases 1 and 2 showed the lowest soot which is due to the high turbulence velocity which assisted complete combustion hence less soot.

With a 2.1% improvement in GISFC over the base bowl design, bowl design case 2 is the best fuel consumption design. In comparison to the base bowl design, the bowl design case 5 has a good GISFC reduction of 0.6%, with decrease NOx of 4.8%, and low soot emission of 20%. The bowl design case 5 therefore shows good trade-off between NOx, soot, and GISFC. In comparison to other bowl designs, design case 1 exhibits the lowest soot reduction of 58.8% and a comparably low rise of NOx emission. The bowl design cases 1 and 5 prove to be the optimal performing engines when it comes to NOx, soot, and GISFC. It is essential and worth noting to emphasise the influence of swirl ratio on the trade-off between NOx, soot, and GISFC.

6.3. The Effect of injection timing on combustion, and emission

A major parameter affecting engine combustion is the fuel injection timing in diesel engines (Heywood, 2018). This section presents results on the effect of injection timing for the base bowl and the five different bowl designs, including in-cylinder pressure profiles, apparent heat release rates, in-cylinder temperatures, GISFC, CO, UHC NOx, and soot emissions. The in-cylinder pressure, temperature, heat release rate, and emissions are plotted against crank angle and range from 100°-to-100° ATDC.

6.3.1. Effect of injection timing on in-cylinder pressure

In theory, all piston bowl geometries with the combustion chamber at the TDC should have the same compression ratio, which in turn should correspond to the same in-cylinder pressure readings. Each design, however, has unique piston bowl corners and varying mixing ratios that result in better or worse combustion efficiency, which may significantly change the local pressures and, as a result, lead to various in-cylinder pressure readings. The compared in-cylinder pressure graphs for the base bowl and the five different bowl designs with the associated injection timing SOI -15.5°

CA, SOI -18.5° CA, SOI -22.5° CA, and -25.5° CA BTDC values are presented in Figure 6.11. The peak in-cylinder pressure at the start of injection of injection (SOI) -25.5° CA BTDC is higher for the base bowl and five bowl designs, as shown in graphs in Figure 6.11 and Table 6.6 respectively. The value of the peak in-cylinder pressure is increased at the commencement of the injection for the base bowl and the five bowl designs, as can be seen from the graphs in Figure 6.11 and supported in Table 6.6. Due to the lower temperature and pressure of the air/fuel combination in the combustion chamber at the beginning of injection, the ignition delay increases when the injection advance is raised. As a result, more fuel accumulates during the ignition delay interval, increasing the peak in-cylinder pressure and heat release rate during the quick or uncontrolled combustion stage (Gupta, 2009; Heywood, 2018).

Table 6.6. In-cylinder pressure (MPa) of the Bowl designs and injection timings

SOI	Base Bowl	Case 1	Case 2	Case 3	Case 4	Case 5
15.5 $\boldsymbol{inj\Theta}$	8.25	8.39	8.41	8.69	8.80	8.19
18.5 $\boldsymbol{inj\Theta}$	8.38	8.53	8.54	8.80	8.90	8.33
22.5 $\boldsymbol{inj\Theta}$	8.54	8.68	8.68	8.93	9.02	8.48
25.5 $\boldsymbol{inj\Theta}$	8.59	8.70	8.72	8.98	9.08	8.51

SOI – Start of injection

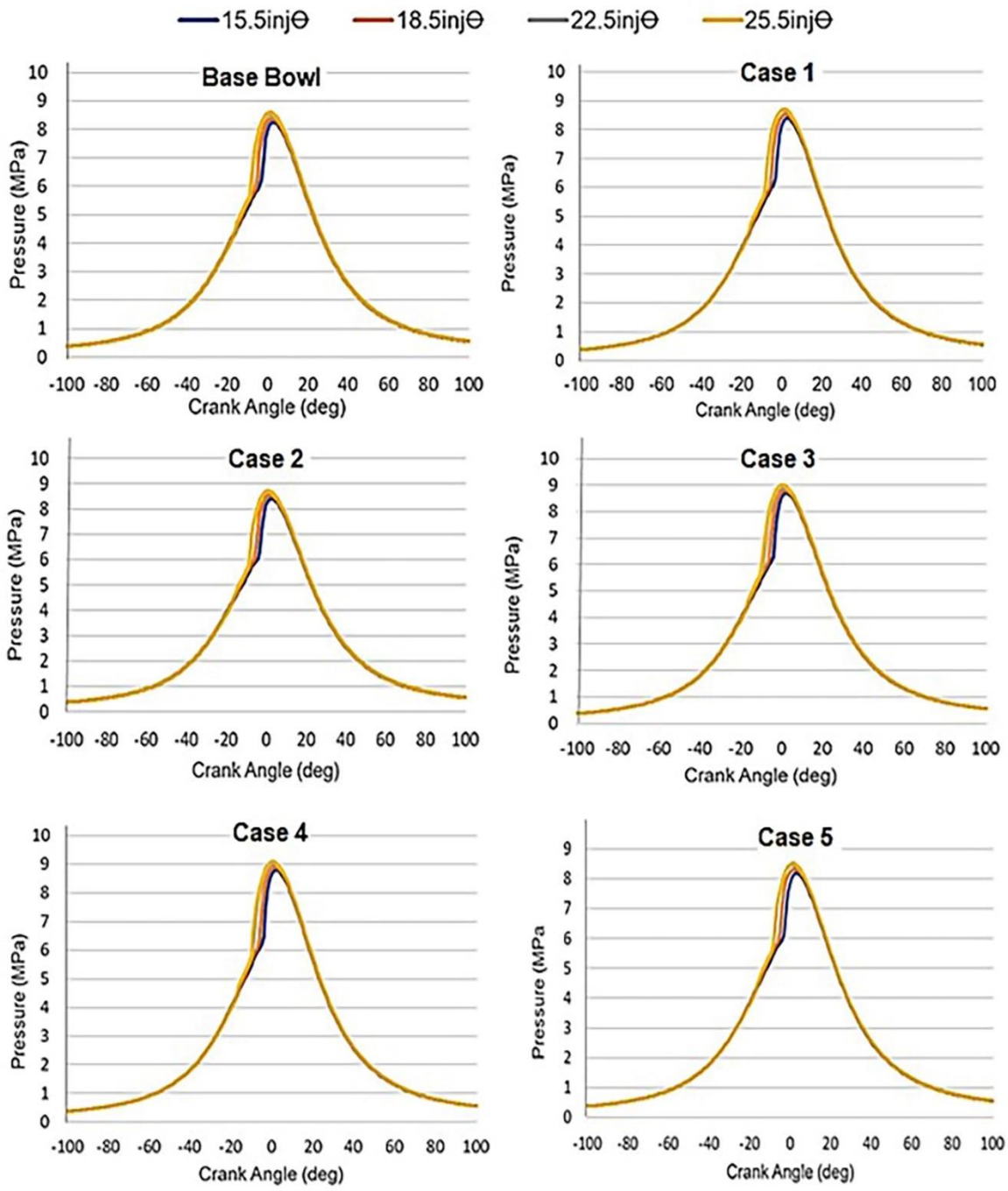

Figure 6.11. Effect of injection timing on in-cylinder pressure for the base bowl and the five bowl designs.

The lowest peak in-cylinder pressure for each bowl design occurred at SOI -15.5° CA BTDC. In the combustion process, when the injection timing is too far retarded as at -15.5° CA BTDC, the combustion process is delayed, the peak in-cylinder pressure occurs later in the expansion stroke, and its magnitude is reduced. The advanced injection timing of -25.5° CA BTDC causes bowl design cases 3 and 4 to exert higher pressures at 3° CA ATDC of 8.98 and 9.08 MPa compared to other bowl designs since

higher pressures increase particle motion inside combustion chambers, which leads to higher temperatures.

At retarded timing SOI -15.5° CA BTDC, the bowl design case 5 and base bowl show the lowest in-cylinder pressures of 8.19 and 8.25 MPa respectively, and give the lowest temperature and shorter delay period, thus reducing proper fuel-air mixing before TDC. These results have shown reasonable agreement with a study conducted by Rostami, Ghobadian and Kiani (2014) and Sathiyamoorthi and Sankaranarayanan, (2015).

6.3.2. Effect of injection timing on in-cylinder temperature

In the combustion chamber, the increase or decrease in temperature is caused by the advanced or retarded ignition timing (start of ignition), which makes it easier for the fuel to atomise, vaporise, and mix with the surrounding air, and reduces or prolongs ignition delay depending on earlier or later injection (Heywood, 2018).

High temperatures, however, accelerate pre-flame reactions and prepare the air-fuel mixture for autoignition, thus shortening the chemical delay. The Figure 6.12 shows the comparisons of temperature profile against crank angle between the injection timing SOI -25.5° CA, SOI -22.5° CA, SOI -18.5° CA, and SOI -15.5° CA BTDC. Advance injection timing improves the combustion rate in the combustion chamber piston bowls, and this would cause a rise in temperature and the peak pressure. It was noticed that there is a continuous drop in temperature for the SOI -25.5° CA to SOI -15.5° CA BTDC for the base bowl and the bowl design cases 1, 2, 3, 4, and 5. Early injection and longer ignition delay gives scope to accumulate more evaporated fuel to before start of combustion. From the observations, the low temperature was recorded for each bowl at ignition timing SOI -15.50° CA. However, the lowest at this retarded SOI were piston bowl design case 5 and the base bowl with 1220 K and 1222 K respectively. In the case of SOI -25.50° CA the increased ignition delay improves air fuel mixture formation hence quick rise in temperature. The high temperature corresponds with the peak pressure as shown in Table 6.6 and Table 6.7, in which bowl design cases 3 and 4 show higher temperatures of 1278 K and 1278 K simultaneously for ignition timing SOI -25.50° CA.

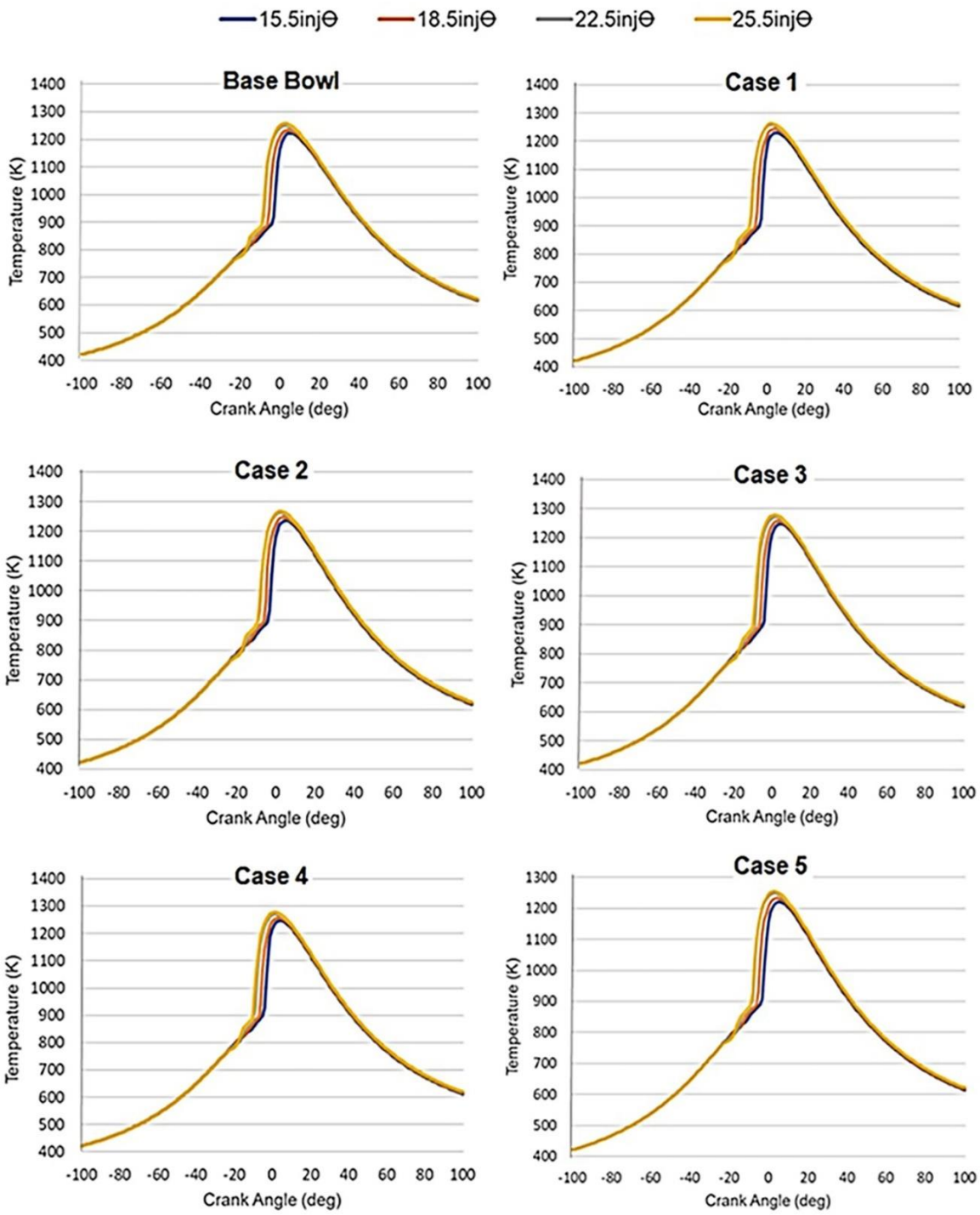

Figure 6.12. Effect of injection timing on in-cylinder temperature for the base bowl and five bowl designs.

Table 6.7. Effect of injection timings on in-cylinder temperature (K) for base bowl and the five bowl designs.

Maximum temperature (K)						
SOI	**Base bowl**	**Case 1**	**Case 2**	**Case 3**	**Case 4**	**Case 5**
15.5 $inj\Theta$	1222.00	1230.09	1236.12	1247.98	1246.79	1220.13
18.5 $inj\Theta$	1233.31	1243.46	1247.00	1257.40	1256.52	1232.31
22.5 $inj\Theta$	1249.91	1258.52	1261.56	1270.84	1270.03	1248.81
25.5 $inj\Theta$	1257.95	1262.84	1267.18	1278.13	1277.68	1254.63

SOI – Start of Injection

6.3.3. Effect of injection timing on apparent heat release rate

The amplitude and duration of the mixing-controlled energy release increase when the injection time is increased to correspond to a higher engine load. The premixed fuel-air mixture burns quickly after the ignition delay phase, releasing heat quickly and this is aided by retarded or advanced injection timing. This is followed by diffusion combustion, where the burning rate is controlled by the availability of combustible fuel-air mixture (Ferguson and Kirkpatrick, 2015; Heywood, 2018). The apparent heat release rate profiles against the crank angle of the base bowl and the five different bowl designs were compared at injection timings SOI -15.5° CA, SOI -18.5° CA, SOI -22.5° CA, and SOI -25.5° CA BTDC as shown in Figure 6.13. As the fuel was injected at the early stage of compression, a longer ignition delay was observed. In contrast, SOI -15.50° CA BTDC was the retarded ignition timing, where fuel injection was delayed, resulting in a shorter ignition delay.

When combustion starts, the rate of heat release increases in the premixed or rapid combustion phase of the combustion process; and this is due to the suitability of the mixture of air and fuel (Heywood, 2018). Chemical reactions may intensify due to the close mixing of fuel and air during compression, increasing turbulence, and completing the burning of the weak charge, resulting in enhanced heat release and heat transfer to the cylinder wall. For bowl design cases 1, 2, and 4, the maximum heat release rate recorded at injection timing SOI -15.50° CA are 616.5 J/deg, 616.2 J/deg, and 639.8 J/deg, and occurring at -2°, -2°, and -3° CA BTDC, respectively. The highest heat

release rate for SOI -18.5° CA, SOI -22.5° CA, and -25.5° CA were recorded for bowl design cases 4, 1 and 5 at 654.95 J/deg @ -5°, CA BTDC, 626.51 J/deg @ -7° and 551.56 J/deg @ -7°CA BTDC respectively.

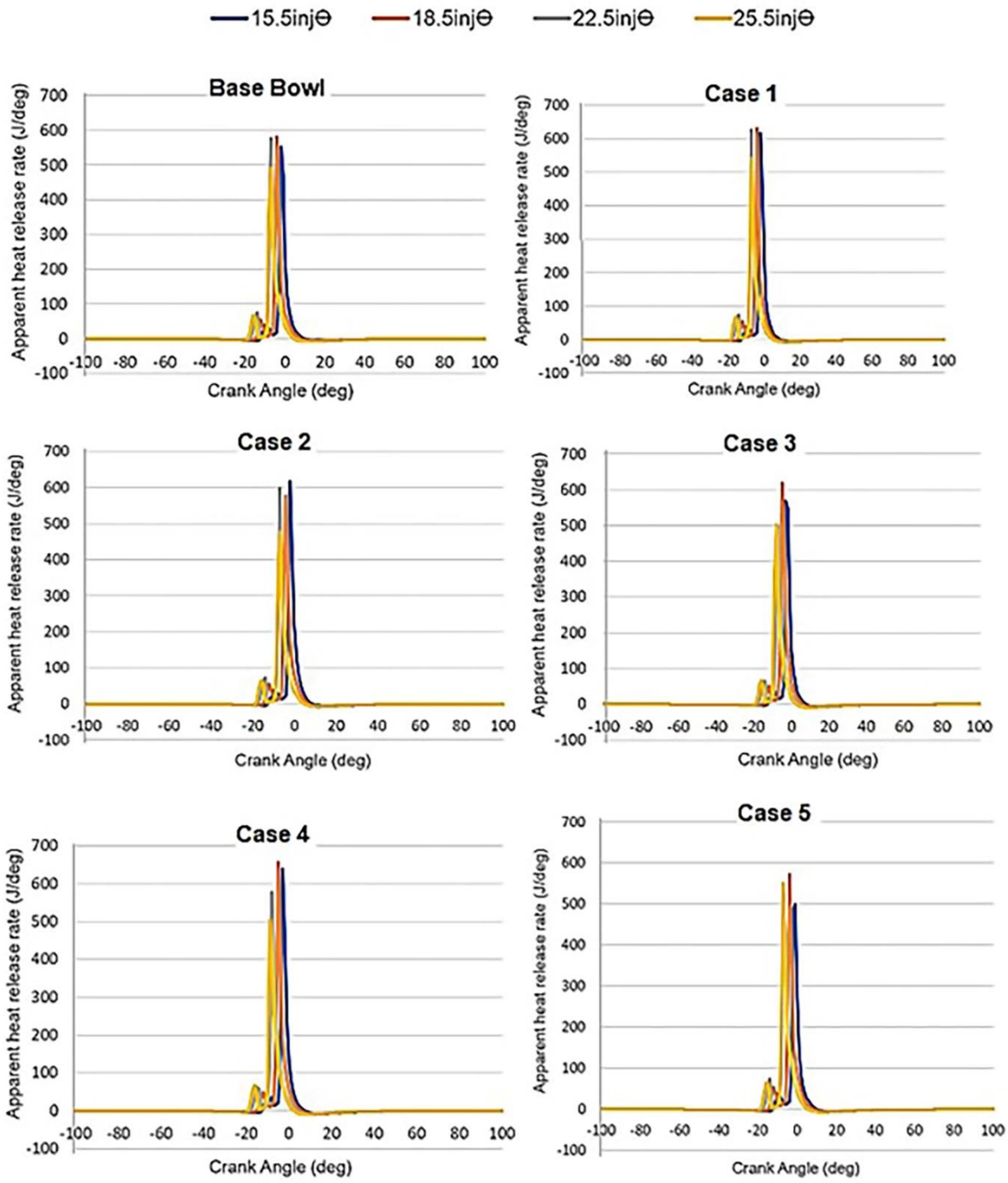

Figure 6.13. Effect of injection timing on apparent heat release rate for the base bowl and the five bowl designs.

6.3.4. Effect of injection timing on carbon monoxide (CO) formation.

In diesel engine combustion, carbon monoxide (CO) occurs in the exhaust because there is insufficient oxygen to convert all the carbon in the fuel to carbon dioxide. The amount of CO emissions increases or decreases depending on whether the injection timing is advanced or retarded (Zhao, 2009; Ferguson and Kirkpatrick, 2015). Figure 6.14 the compares the changes in peak CO emission for the base bowl and five different bowl designs at various injection timings at SOI -15.5° CA, SOI -18.5° CA, SOI -22.5° CA, and SOI -25.5° CA BTDC. At injection timing SOI -15.5° CA, where the timing is retarded, the ignition delay becomes short, thereby giving a low temperature, which is due to poor oxidation between the oxygen and carbon atoms (Heywood, 2018). The CO is higher for all bowl design cases at SOI 15.5° CA, with bowl design cases 1 and 5 exhibiting the highest CO values of 62.44 and 66.38 g/kg-fuel, respectively. The CO at 39.92 and 37.99 g/kg-fuel were low simultaneously in cases 3 and 4 at the same SOI of -15.5°; this could be due to bowl formation, which facilitates mixture formation and improves combustion. The bowl design cases 3 and 4 show the lowest CO mass fractions of 21.30 and 20.71 g/kg fuel, respectively, at SOI -25.5° CA BTDC. This is due to the bowl design coupled with a longer ignition delay, which allows sufficient oxygen to convert all the carbon in the fuel to carbon dioxide (Ferguson and Kirkpatrick, 2015).

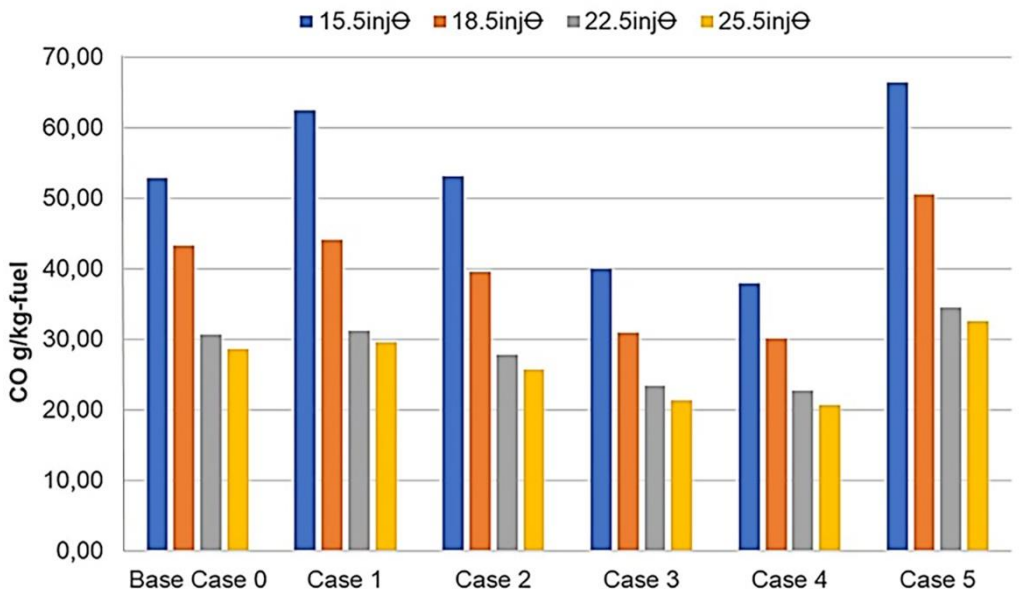

Figure 6.14. Maximum carbon monoxide (CO) for the base bowl design and five bowls cases

6.3.5. Effect of injection timing on unburnt hydrocarbon (UHC) formation

As diesel injection timing is advanced, HC emissions increase significantly because the longer delay period, which is longer than the optimal value, results in over-leaning (over-mixing). On the other hand, delayed timing results in a shorter delay period, which is less than the optimal value, and leads to under-mixing (over-rich mixture), which increases HC emissions (Heywood, 2018). Figure 6.15 shows a comparison of maximum unburned hydrocarbon (UHC) in the base bowl and the five different bowl designs at injection timings SOI -15.5° CA, SOI -18.5° CA, SOI -22.5° CA, and SOI -25.5° CA BTDC. The UHC is high for each of the bowl at SOI -15.5° CA BTDC, which is attributed to shorter delay period over rich mixture in the combustion chamber. In addition, the graph illustrates that injection timing has a significant impact on UHC emissions. As depicted in Figure 6.15 compared to all other combustion chamber designs, that bowl design cases 3 and 4 have lower UHC values of 13.55 and 13.39 g/kg-fuel at SOI -25.5° CA, and bowl design cases 1 and 5 show higher UHC values of 28.64 and 29.77 g/kg-fuel at SOI -15.5° CA, respectively.

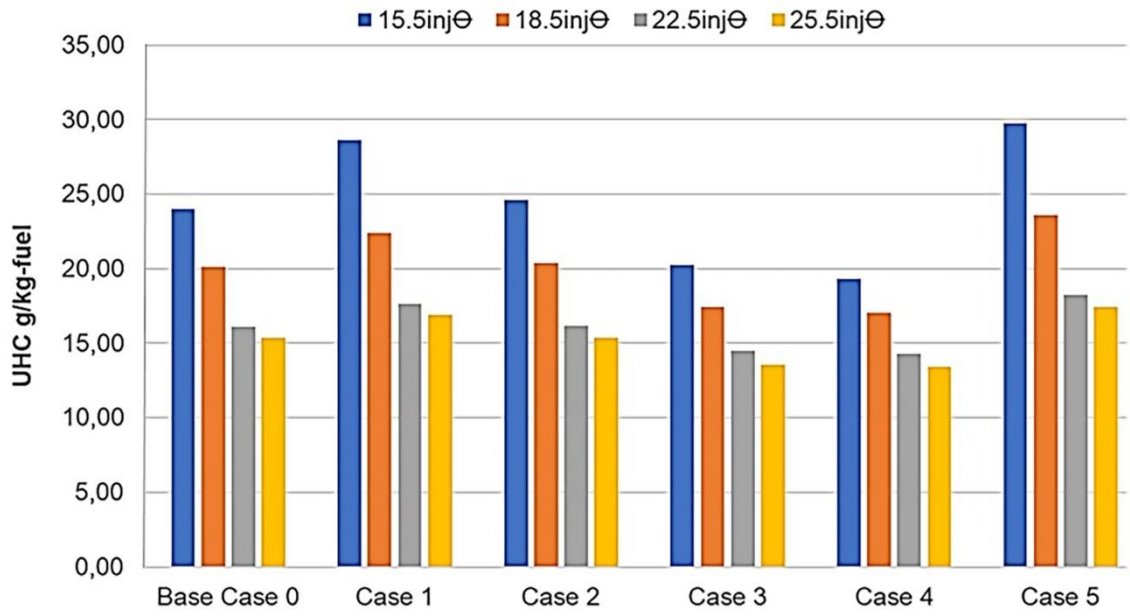

Figure 6.15. The effect of injection timing on unburnt hydrocarbons (UHC) for the base bowl design and five bowls cases

This is because of better burning due to improved swirl and squish air movement in the bowl design cases 3 and 4 during the compression stroke. When injection timing is advanced, UHC emissions are reduced. When injection timing is advanced before

TDC, combustion occurs earlier. This results in a relatively higher temperature in the air-fuel mixture as the piston moves toward TDC, thereby lowering UHC emissions (Abd Alla et al., 2002).

6.3.6. Effect of injection timing on NOx formation

The formation of NOx is highly dependent on the maximum temperature of the burning gases, oxygen content, and the amount of time available for the reactions to take place under these extreme conditions. The NOx emissions from diesel engines increase dramatically with advanced injection time due to greater temperatures brought on by more fuel-air mixture burning in the premixed combustion phase because of increased delay period (Heywood 1988; Sayin, et al., 2009). As shown in Figure 6.16 maximum nitrogen oxide (NOx) formation in a base bowl and five different bowl designs was compared at varying injection timings of SOI -15.5° CA, SOI -18.5° CA, SOI -22.5° CA, and SOI -25.5° CA BTDC. In Figure 6.16 maximum nitrogen oxides (NOx) in the base bowl and five different bowl designs are compared at injection timings of SOI -15.5° CA, SOI -18.5° CA, SOI -22.5° CA, and SOI -25.5° CA BTDC.

The retarded injection timing SOI -15.5° CA gave low NOx emissions and increased progressively for SOI -18.5° CA and SOI -22.5° CA but decreased sharply at injection SOI -25.5° CA for all the bowl design cases. This may be due to sufficient time in the delay period that enables the excess temperature to be absorbed by the surrounding hydrocarbons, thereby reducing the NOx level (Heywood, 2018). As compared to the base bowl design with NOx of 2.14 g/kg-fuel at SOI -15.5° CA, cases 1 and 5 showed low NOx levels of 2.49 g/kg-fuel and 2.16 g/kg-fuel. In bowl design cases 3 and 4, the highest NOx levels were observed at SOI -22.5° CA, respectively, 4.09 and 3.92 g/kg-fuel, which can be attributed to the high in-cylinder pressure and temperature generated by turbulence kinetic energy in these combustion chambers (Ferguson and Kirkpatrick, 2015).

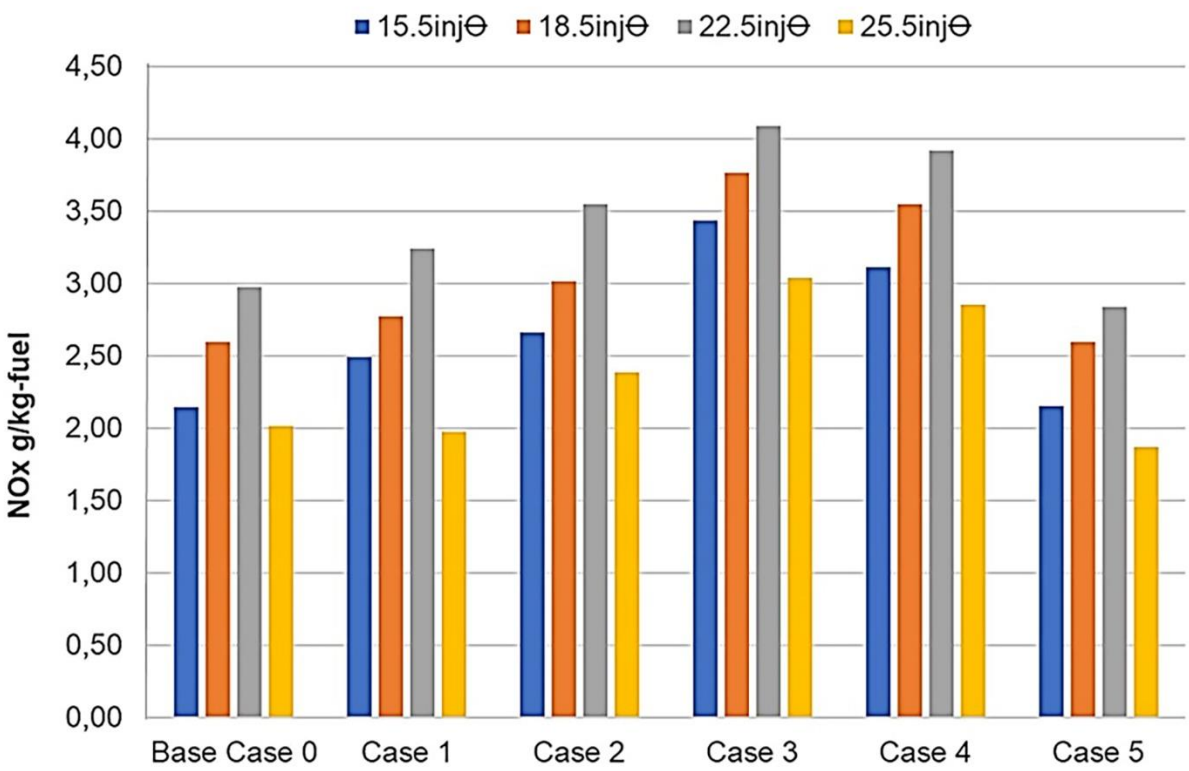

Figure 6.16. The effect of injection timing on nitrogen oxides (NOx) for the base bowl design and five bowls cases.

6.3.7. Effect of injection timing on soot formation

When oxygen is insufficient at high enough temperatures, flame soot is a potential intermediate by-product of the combustion processes. During the mixed and late combustion phases, there is less oxidation, which results in more soot production. As a result of agglomeration and dehydration processes involving mostly carbon and hydrogen, large unsaturated hydrocarbons are formed; therefore, the first soot particles form in this stage (Zhao, 2009). Figure 6.17 shows the peak soot that is generated in the base bowl, and five different bowl designs that are compared at injection timings of SOI -15.5° CA, SOI -18.5° CA, SOI -22.5° CA, and SOI -25.5° CA before the top dead centre (BTDC). Maximum soot is produced at SOI -15.5° CA for all bowl designs, with case 4 producing the highest of 0.00087 g/kg-fuel, followed by case 5, which produces 0.00058 g/kg-fuel. It has been found that the lowest soot generation occurs at SOI -25.5° CA, between 0.00011 and 0.00013 g/kg-fuel, which

is highly significant and supports the idea that injection timing at this stage can significantly improve combustion and reduce soot production.

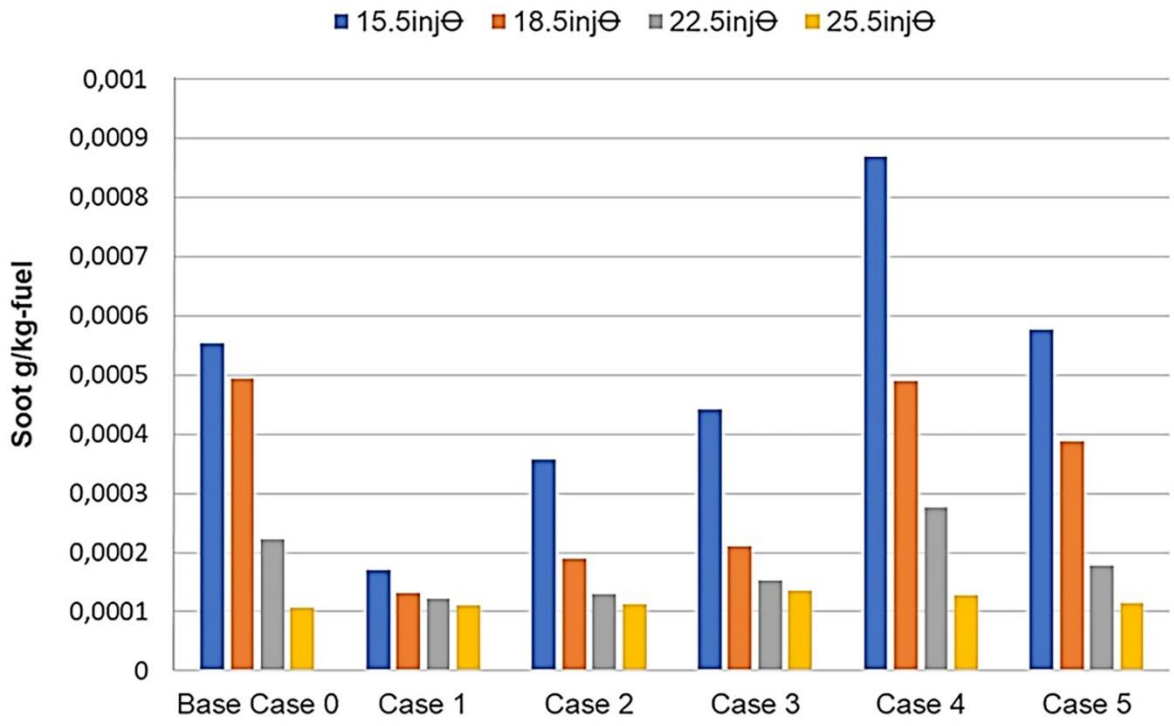

Figure 6.17. The effect of injection timing on Soot emission for the base bowl design and five bowls cases

6.4 The effects of injection spray included angle on combustion process and emissions in the base bowl and five bowl designs

To illustrate the effects of spray included angle (SIA) on combustion processes and emissions characteristics, the base bowl design and the five different bowl designs were simulated with diesel fuel injection timing kept constant; while spray angles varied at 126°, 136°, 146°, and 156° with the same speed. The in-cylinder fuel vapour mass fraction distribution along the axis of the injection nozzle hole at -16° crank angle before the top dead centre (BTDC) of the base bowl and the five different bowl designs at spray angles of 126°, 136°, 146°, and 156° are shown in Figure 6.18. The sprayed fuel will collide with the chamber floor at a lesser spray angle (i.e., below 126°).

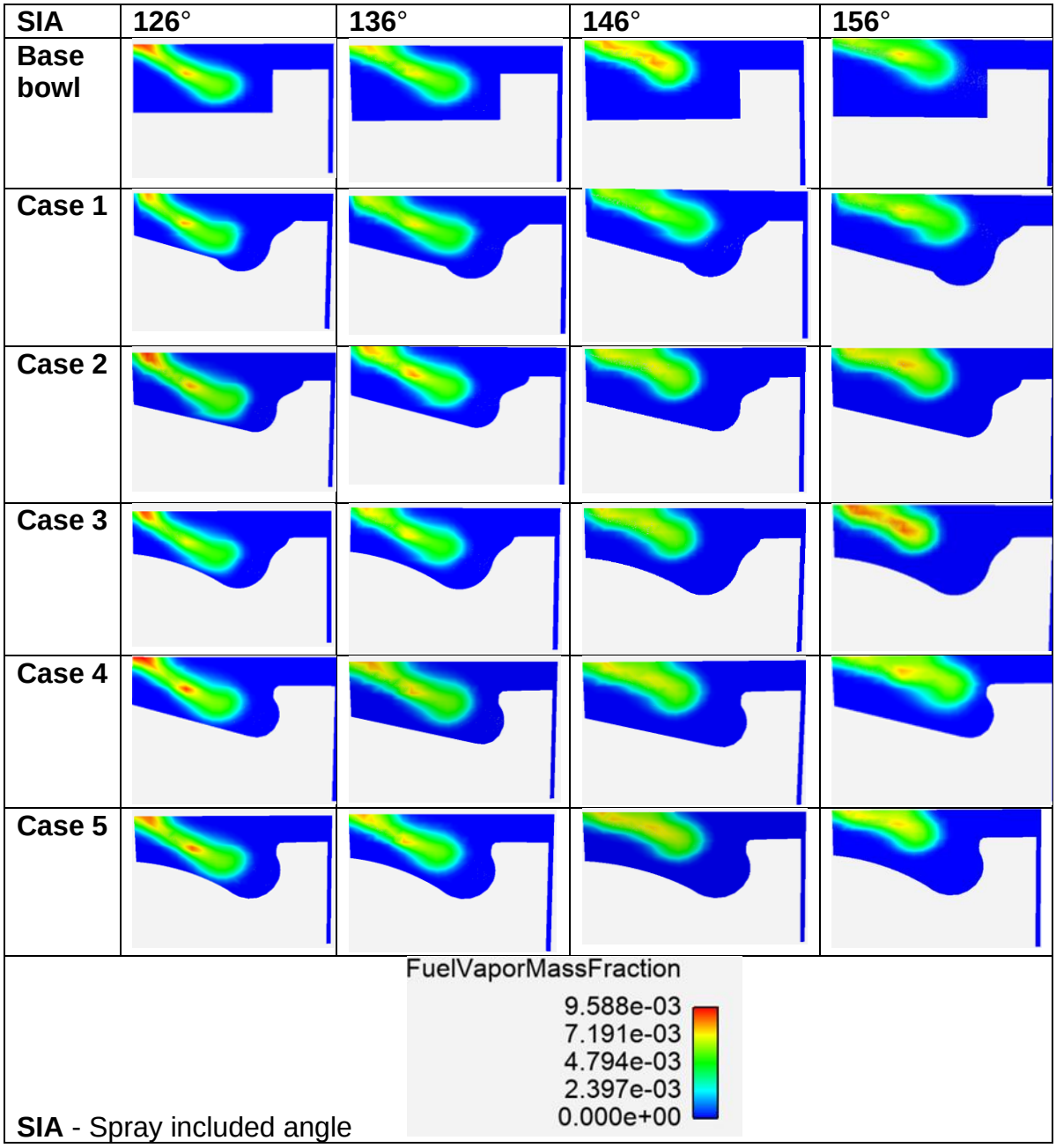

Figure 6.18. Fuel vapor mass fraction distribution on a cut-plane along the axis of the injection nozzle hole at -16° CA BTDC, for SIA 126°, 136°, 146°, and 156°.

Additionally, it has been discovered that most of the spray fuel will collect on the surface of the chamber wall when the spray angle is less than 126°, and to a large extent, the advancement of the injection timing BTDC prevents this impingement thereby allowing the fuel to be sprayed into the bowl cavity. When the sprayed fuel impinges on the floor wall of the piston bowls, it slows the pace at which most of the spray fuel evaporates. And when the piston moves to TDC, it is easy to observe that there is a higher molecular concentration of spray fuel on the surface of the chamber

wall at a small spray angle (less than 126°), indicating that the primary cause of the decline in indicated work is the collision of diesel with the combustion chamber walls.

6.4.1. Impact of spray included angle on in-cylinder pressure

Figure 6.19 and Table 6.8 shows the instances of in-cylinder pressure for varying spray angles of the base bowl design and five different bowl design cases. The in-cylinder pressure for the base bowl design increased marginally from 126°, 136°, and 146° to 8.70, 8.76, and 8.79 (MPa) and dropped at 156° to 8.51 MPa. The same trend followed for bowl design case 1, case 3, case 4, and case 5, and the overall highest pressure occurred at 136° for bowl design case 4 at 9.16 MPa.

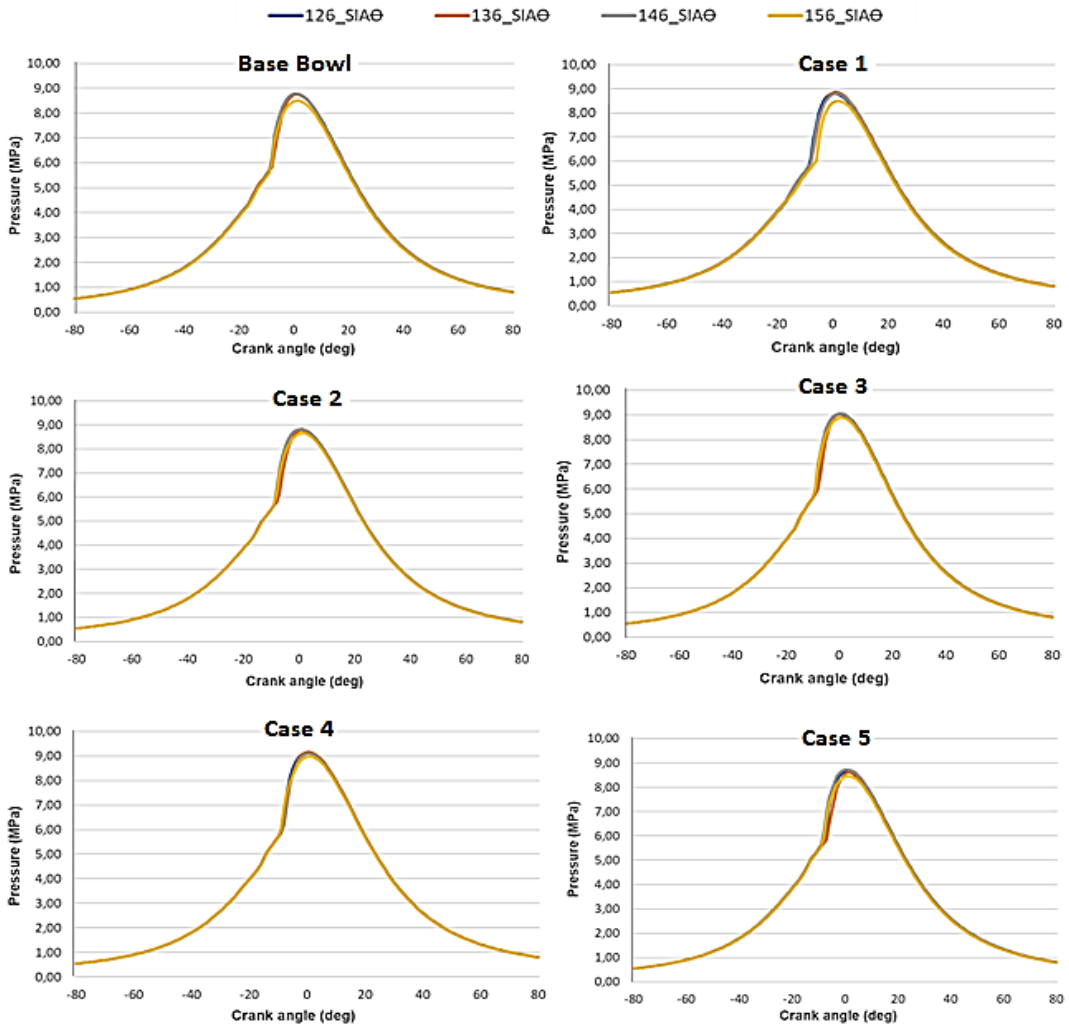

Figure 6.19. The effect of spray included angle on in-cylinder pressure for the base bowl design and five bowls cases

The spray included angle at 156° experienced pressure drop for all bowl design cases due to spray wall-wetting at compression strokes a few degrees to top dead centre (TDC). For all bowl case designs, it is shown that the highest in-cylinder pressure occurs between 136° and 146° spray angles and increases with increasing spray angles, but it somewhat decreases at 156°, which implies that the power performance is very close in this spray angle range (between 136° and 146°).

Table 6.8. Peak in-cylinder pressure at varied included angle for base bowl and five bowl designs

Max pressure [MPa]						
SIA	**Base bowl**	**Case 1**	**Case 2**	**Case 3**	**Case 4**	**Case 5**
126°	8.70	8.80	8.80	9.02	9.13	8.63
136°	8.76	8.87	8.79	9.05	9.16	8.61
146°	8.79	8.81	8.83	9.05	9.09	8.74
156°	8.50	8.64	8.65	8.89	8.97	8.46

SIA- spray included angle

6.4.2. Impact of spray included angle on apparent heat release rate

In Figure 6.20, graphs of apparent heat release rates (AHRR) for the base bowl design and five different bowl designs are shown for different spray angles of 126°, 136°, 146°, and 156°. It was observed that the combustion rate or AHRR has some changes as the spray angle is less than 146°; while the effect of the spray angle on the AHRR of diesel engines becomes weak when the spray angle is above 156° (Zhou et al., 2020). On the other hand, the sprayed fuel does not collide with the chamber wall when the spray angle is above 126°, during the upward movement of the piston toward TDC; this enables the fuel droplets to flow into the squish area of the bowl cavity, which is beneficial for the diffusion and evaporation of pilot fuel due to the larger space and higher temperature, as demonstrated in a study by Zhao, Gutmark, and de Goey (2018).

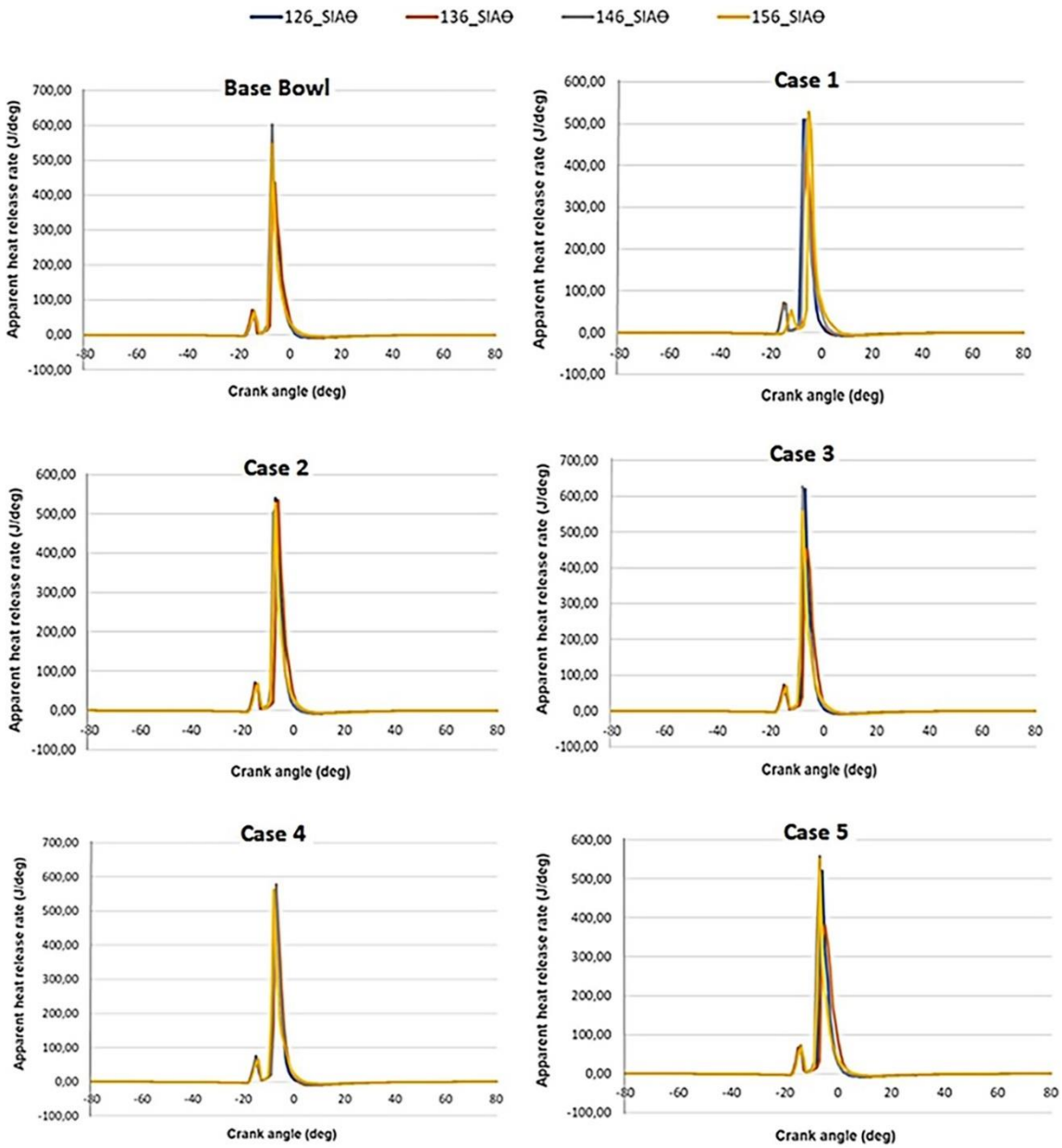

Figure 6.20. Effect of spray included angle on apparent heat release rate (AHRR) for the base bowl design and five bowls cases

The highest AHRR occurred with bowl design case 3 at 126°, which was 620.35 J/deg at -7° CA BTDC, and the lowest AHRR occurred with the base bowl design at 474 J/deg on -7° CA BTDC at this spray angle. The peak AHRR occurred at 146° for the base bowl, bowl design case 1, and case 5 at 603.12 J/deg, 627.53 J/deg, and 557.18 J/deg, respectively; however, the peak AHRR dropped marginally for these bowl designs to 546.06 J/deg, 556.74 J/deg, and 552.21 J/deg at SIA 156° concurrently. Additionally, because the sprayed fuel enters the combustion chamber's centre at a

wider spray angle (bigger than 126°), additional ignition sources are created in the bowl cavity's larger size (Fang et al., 2008). The adjacent fuel is then virtually instantaneously ignited by these sources of ignition, accelerating combustion and heat release to a maximum AHRR of 627.53 J/deg.

6.4.3 Impact of spray angle on engine performance

For comparison of performance, Figure 6.21 (a) and (b) shows the effect of spray angle on gross indicated power and gross indicated specific fuel consumption (GISFC). When the gross indicated power was 10.17 and 10.18 kW for bowl design case 2 and case 3 at a spray angle of 146°, these cases experienced the lowest GISFC at 189.34 g/kW-h and 189.12 g/kW-h respectively.

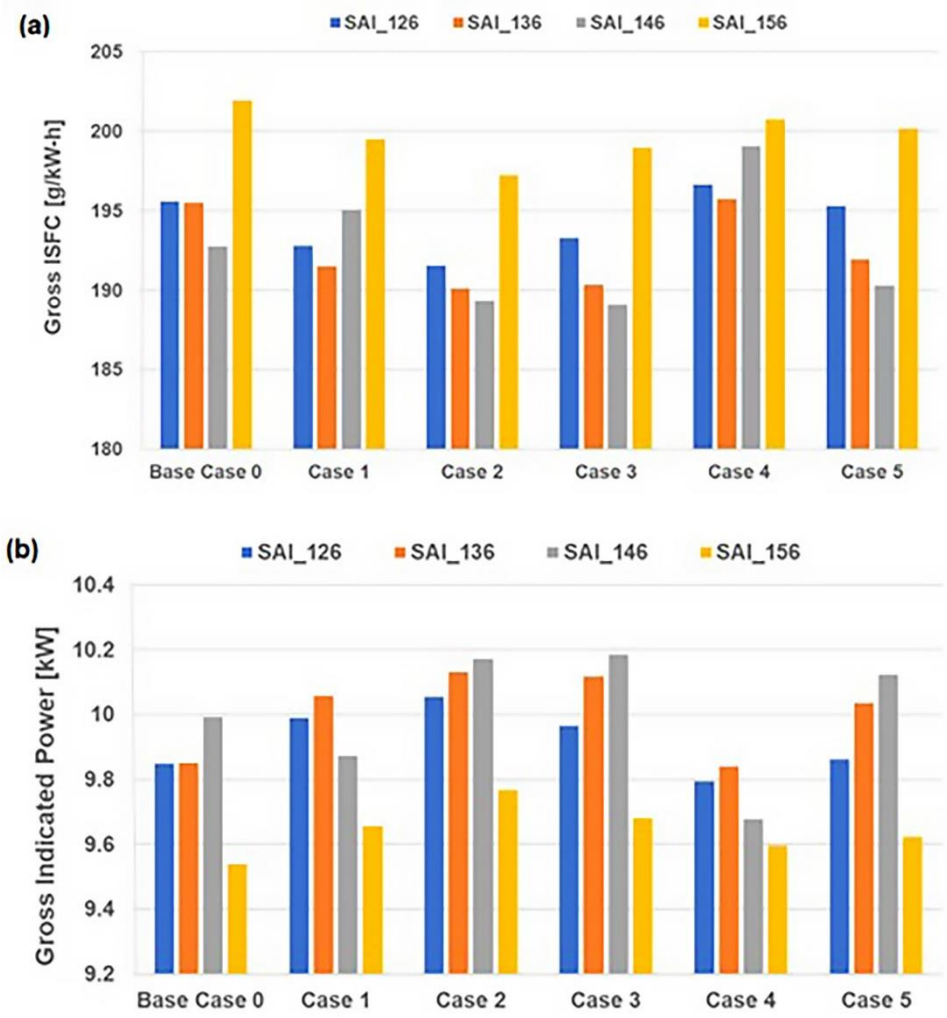

Figure 6.21. The effect of spray angle on (a) Gross indicated power and (b) Gross indicated specific fuel consumption

It was observed that minimum indicated power occurs at 156° for all the piston bowl designs with a high GISFC respectively. This is due to the wall impingement that occurs at this spray angle, and it slows the pace at which most of the sprayed fuel evaporates leading to low leading to low indicated power and high fuel consumption due to waste (Shu et al., 2019).

6.4.4. Impact of spray angle on engine performance exhaust emissions

The way in which exhaust emissions is created are complicated in the combustion processes of compression ignition engines; it depends a lot on the chemical and physical properties of the fuel, the fuel spray parameters, and the way atomization and combustion work. It has been demonstrated that limiting the injection angle is an effective strategy for lessening the wall-wetting phenomena (Liang et al., 2019). The distance between the nozzle and the cylinder wall increased substantially with the early injection timing and lowered injection angle strategy, and more fuel was atomised before reaching the cylinder, resulting in less fuel mass that wetted the walls of the cylinder. Target impingement has a significant impact on emissions (Mobasheri and Peng, 2012). Figure 6.22 (a) and (b) show CO and UHC emissions for the base bowl and the five different bowl designs. The spray angle 156° recorded the highest CO and UHC emissions for all the bowl designs, and case 5 recorded a peak level of 36.49 and 18.07 g/kg-fuel, respectively. The spray angles of 126°, 136°, and 146° show averagely low CO and UHC for all the bowl designs, while bowl designs case 2, case 3, and case 4 recorded the lowest CO and UHC between 136° and 146°. Accordingly, spray impingement was reduced for spray targeting closer to the bowl surface, and HC and CO concentrations in the spray were also reduced as compared to higher values of 156° injection angles (Liang et al., 2019). Numerous studies have demonstrated that the fuel-air mixing is improved when the spray impinges on the bottom edge of the bowl lip (Mobasheri and Peng, 2012; Shu et al., 2019; Liang et al., 2019). Furthermore, the restricted injection angle caused more fuel film to build up, resulting in more soot, and the fuel was not completely burned (Yoon et al., 2010; Mobasheri and Peng, 2012; Shu et al., 2019).

Figure 6.22 (c) and (d) show NOx and soot emissions plotted at spray angles of 126°, 136°, 146°, and 156° for the base bowl and the five different bowl designs. The highest

NOx was produced at spray angle 146° for the base bowl designs, cases 2, case 3, and case 5, with the peak of all being 8.32 g/kg-fuel for case 5. All bowl designs had lower NOx emissions when the spray angle was set to 136°, with bowl design case 5 having the lowest NOx emissions of 0.68 g/kg-fuel and the lowest soot emissions occurring at the same spray angle across all the bowl designs. Likewise, the highest soot emissions occurred at 156° spray angles with bowl design case 4, with correspondingly high CO and UHC for the same bowl design; however, soot emissions for case 5 dropped marginally at this spray angle. The NOx concentration significantly increased with the narrow injection angle with the advancement of early injection timing. With a reduced injection angle came a decrease in NOx emissions.

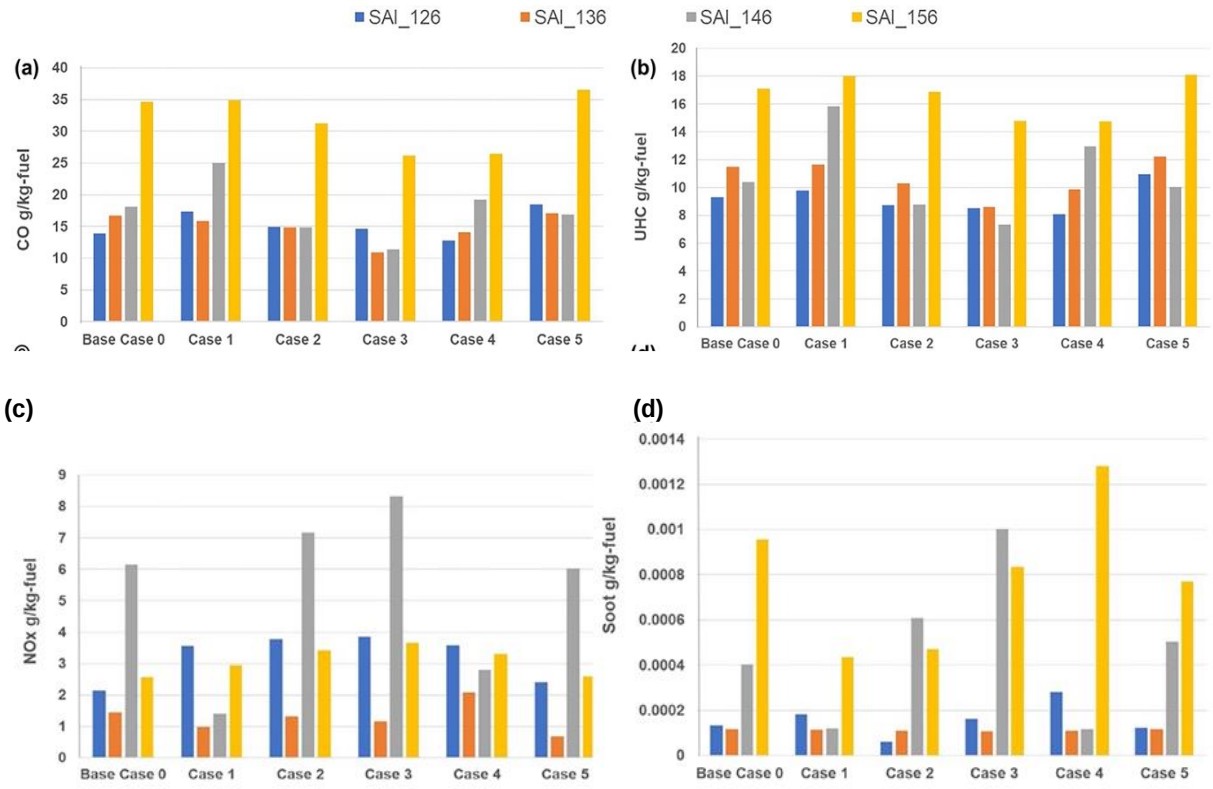

Figure 6.22. The effect of spray angle on (a) carbon monoxide (CO) (b) unburnt hydrocarbons (UHC) (c) nitrogen oxide (NOx)(d) soot emissions for the base bowl and five bowl design cases

As the injection angle decreased, so did the soot emissions. There was an optimal injection angle for soot emissions, which most likely depended on the interaction of the spray and the piston bowl, but as the injection angle fell, soot emissions initially

decreased and then increased (Shu et al., 2019). Figures 6.21 (c) and (d) depict the NOx and soot trade-offs, with NOx and soot emissions at their lowest levels for all bowl designs at 136° spray angles. At this spray angle of 136°, the NOx and soot mass fractions are lower in all piston bowl configurations compared to the conventional spray angle of 156°. Due to fuel impingement and film deposition at the 136° included spray angle, a quite rich region is formed in the near wall region, due to the lack of available air for mixing. Therefore, NOx and soot formation are significantly reduced because the injected fuel is rapidly consumed by combustion before a rich soot region can accumulate.

6.5. Evaluation of regression optimisation

The parameters were varied in the simulation runs and the results were subjected to hierarchical regression analysis to optimize the results. The individual and interaction effect of piston bowl design (PBD), start of injection (SOI) and spray included angle (SIA) on the response parameter such as gross indicated specific fuel consumption (GISFC), nitrogen oxide (NOx), soot, gross indicated power (GIP), carbon monoxide (CO) and unburnt hydrocarbons (UHC) were used to calculate the regression coefficients and the t value for different response parameters of the model. These t values show how a particular parameter significantly affects the output responses. The model is significant as the t value is more than 1.96 (Shi and Reitz, 2008).

Results in Table 6.9 shows that PBD has negative significant linear effect ($p<0.05$) on soot emission. This explains that a poor piston bowl designs leads to a poor mixture of fuel and oxygen in the tangential direction, and eventually deteriorates combustion efficiency (Shi and Reitz, 2008). On the other hand, appropriate bowl design reduces soot. The linear effect of individual parameters, SOI and SIA on GISFC, CO and UHC was positively significant. On the contrary, the linear effect of SIO and SIA on soot emission and GIP showed negative significance respectively. This implies that injection timing and spray angle improve fuel consumption and pollutant emissions (Shi and Reitz, 2008).

The interaction of SOI and SIA (SOI.SIA) showed negative significant effects on GISFC, CO and UHC. However, it shows a positive significant effect on soot emission. This implies that the mutual effect of advanced injection timing and wider spray angles reduces specific fuel consumption, carbon monoxide and unburnt hydrocarbon as the

wider spray delivers more fuel into the squish region where turbulence velocity is high, and concentration is more oxygen. But these interactive parameters are likely to increase soot emission.

Likewise, the combined effect of piston bowl design with start of injection (PBD.SOI) showed significant positive effect on soot emission, explaining that the interaction of these parameters contributes more to soot emission. Some parameters have no significant effect on the response variables for instance NOx and GIP. Thus, it is concluded that the insignificant effects of parameters on some response variables can be neglected. It should be noted, however, that the interaction effects that are significant are only plotted and discussed in the next section.

Table 6.9 (a). Regression analyses for parameters: Gross indicated power (GIP) and Gross indicated specific fuel consumption (GISFC)

Parameters	GIP (kW)			GISFC (kW-h [g])		
	Stand. coefficient	**t value**	**F value**	**Stand. coefficient**	**t value**	**F value**
PBD	-1.06	-0.96	7.66**	0.97	.885	7.64*
SOI	-1.32	-1.28	4.02*	1.29*	2.26	4.01*
SIA	-1.22*	-2.57	26.88***	1.19*	2.54	27.49***
PBD.SOI	0.31	0.65	20.12***	-0.31	-0.66	20.57***
PBD.SIA	0.49	0.47	15.97***	-0.40	-0.39	16.30***
SOI.SIA	1.24	1.12	13.57***	-1.21*	-2.10	13.82***

Table 6.9 (b). Regression analyses for parameters: Carbon monoxide (CO) and Unburnt Hydrocarbons (UHC)

Parameters	CO (g/kg-fuel)			UHC (g/kg-fuel)		
	Stand. coefficient	t value	F-value	Stand. coefficient	t value	F-value
PBD	-0.282	-0.33	0.08	0.071	0.065	0.067
SOI	2.34**	2.95	12.89	4.59***	4.53	7.78***
SIA	1.89***	5.23	50.58	2.66***	5.72	15.82***
PBD.SOI	0.26	0.72	37.77	0.13	0.27	11.73***
PBD.SIA	0.01	0.01	29.82	-0.22	-0.22	9.27***
SOI.SIA	-3.19***	-3.77	31.64	-5.50***	-5.07	14.57***

Table 6.9 (c). Regression analyses for parameters: Nitrogen oxide (NOx) and Soot emissions

Parameters	NOx (kg-fuel [g])			Soot (kg-fuel [g]		
	Stand. coefficient	t value	F-value	Stand. coefficient	t value	F-value
PBD	-1.16	-0.76	0. .158	-2.64*	-2.16	0.166
SOI	-2.06	-1.44	2.764	-5.17***	-4.55	8.58***
SIA	-0.85	-1.29	1.834	-2.62***	-5.02	8.68***
PBD.SOI	0.29	0.44	1.409	0.38	0.73	6.57***
PBD.SIA	0.87	0.61	1.191	2.28*	2.01	6.08***
SOI.SIA	1.85	1.21	1.242	5.03***	4.12	8.99***

6.5.1 Model fitting

The R-squared (R^2) is a statistical measure that represents the proportion of variance in the response variable (the variable the model is trying to predict) that is explained by the parameters (the factors the model considers). In this case, the result in Table 6.10 indicates that the model tested is statistically significant and the variance explained in the response variables spans from 59.7% to 84.7%, which suggests that the model's performance varies across different response variables (Ulfarsson, Kim and Booth, 2010; Raihan et al., 2022). The result in Table 6.10 shows that the model is statistically significant and explained a variance (R^2) of 74.1%, 59.7%, 66.5%, 73.2% and 84.7 % and 74.6% in gross indicated specific fuel consumption, NOx, soot, gross indicated power, carbon monoxide and unburnt hydrocarbons respectively.

Table 6.10. Model fitting

Model	**GISFC (kW-h [g])**	**NOx (kg-fuel [g])**	**Soot (kg-fuel [g])**	**GIP (kW)**	**CO (g/kg-fuel)**	**UHC (g/kg-fuel)**
R^2	0.741	0.597	0.665	0.732	0.847	0.746
Adjusted R^2	0.682	0.515	0.581	0.689	0.795	0.718
Predicted R^2	0.819	0.801	0.753	0.846	0.912	0.863

6.5.2. Interaction effect on GISFC

Figure 6.23 shows the interactive effects of injection timing and spray angle on GISFC. As the start of injection is advanced from 14° to 22.2° ATDC, GISFC is decreased. Also, as the spray included angle is increased from 150° to 160°, GISFC increased. However, GISFC is observed to be low from 140° to 120° at spray angle. Specifically, the combination of a bit early injection timing and narrow spray angle resulted in reduction of specific fuel consumption. Similar trend was reported by (Shi, and Reitz, 2008) who found that fuel consumption reduces with a combination of either wider spray angle and early injection or a narrow spray angle and a bit later injection. Another study also found that if a large spray angle is employed, the effect of SOI on GISFC weakens (Ganji, Raju, and Rao, 2017).

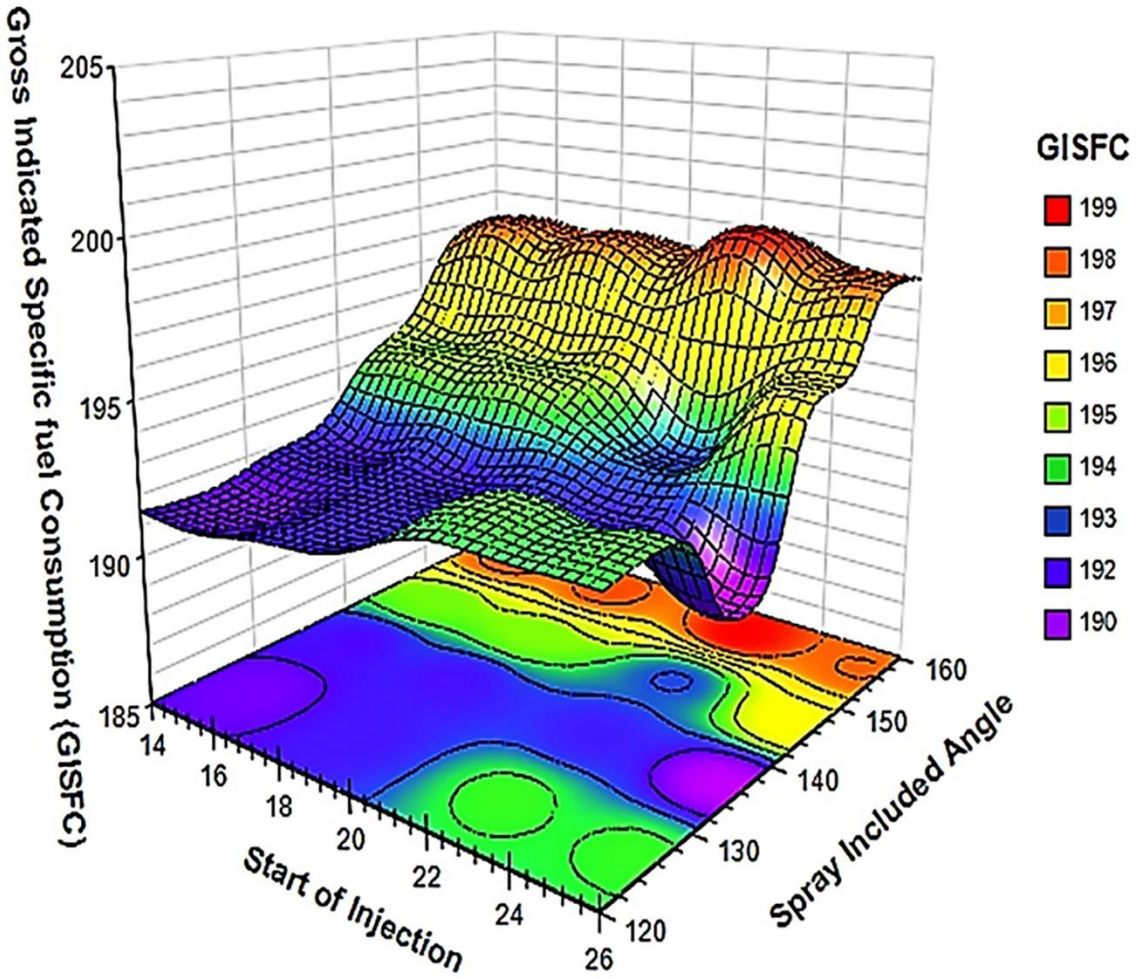

Figure 6.23. GISFC variations against SOI and SIA

6.5.3. Interaction effect on soot

It can be observed from Figure 6.24 that increase bowl design and wider spray included angle reduces the soot emission significantly. This explains that the combined effect of piston bowl geometry parameters and spray parameters have a significant influence on the soot emissions. In other words, a big bowl throat radius with a wide spray angle works well to reduce soot emission.

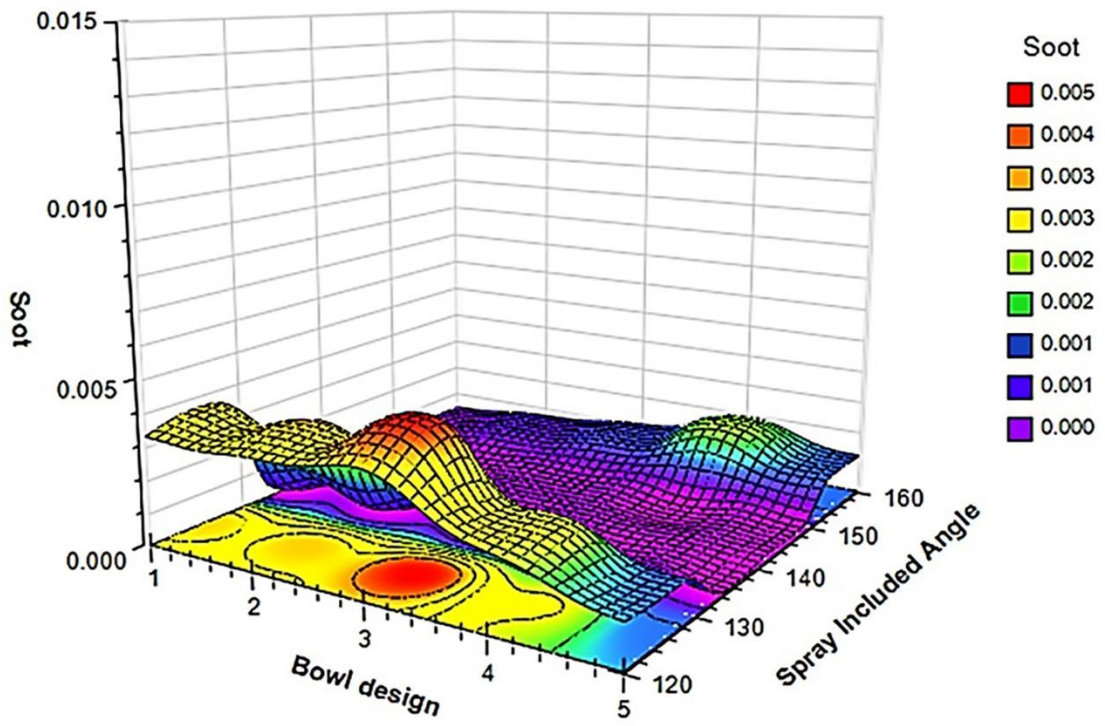

Figure 6.24. Soot variations against bowl design and SIA

A study also revealed that an improve piston bowl design and wider spray angle can generate a strong tumble flow component, which can significantly reduce soot emissions (Shi and Reitz, 2008)

In accordance with previous findings (Ganji et al., 2017)**,** Figure 6.25 explains that retarding the injection timing resulted in high soot emission. At the same time, the combination of advanced injection timing and both narrow and wide spray angle reduced the soot. This is due to increased wall impingement, which enhances mixture formation and piston bowl interaction of injected fuel. This causes a dilution effect and lower in-cylinder temperature during combustion, resulting in lower soot emissions due to efficient combustion (Yoon et al., 2010; Shu et al., 2019).

6.5.4. Interaction effect on carbon monoxide

The result in Figure 6.26 shows the mutual effect injection timing and spray angle on carbon monoxide. It is found that retarding the injection timing and wider spray angle reduce the carbon monoxide. Specifically, carbon monoxide is reduced as the injection timing is retarded from 26° to 14° BTDC and remain constant as the spray included angle is widen from 120° to 152°. In accordance with related studies, this is due to

the fact that the in-cylinder local temperature increases sharply as the spray angle becomes larger; however, carbon monoxide increases at late injection and a wider spray angle beyond 152° (Yoon et al., 2010; Shu et al., 2019).

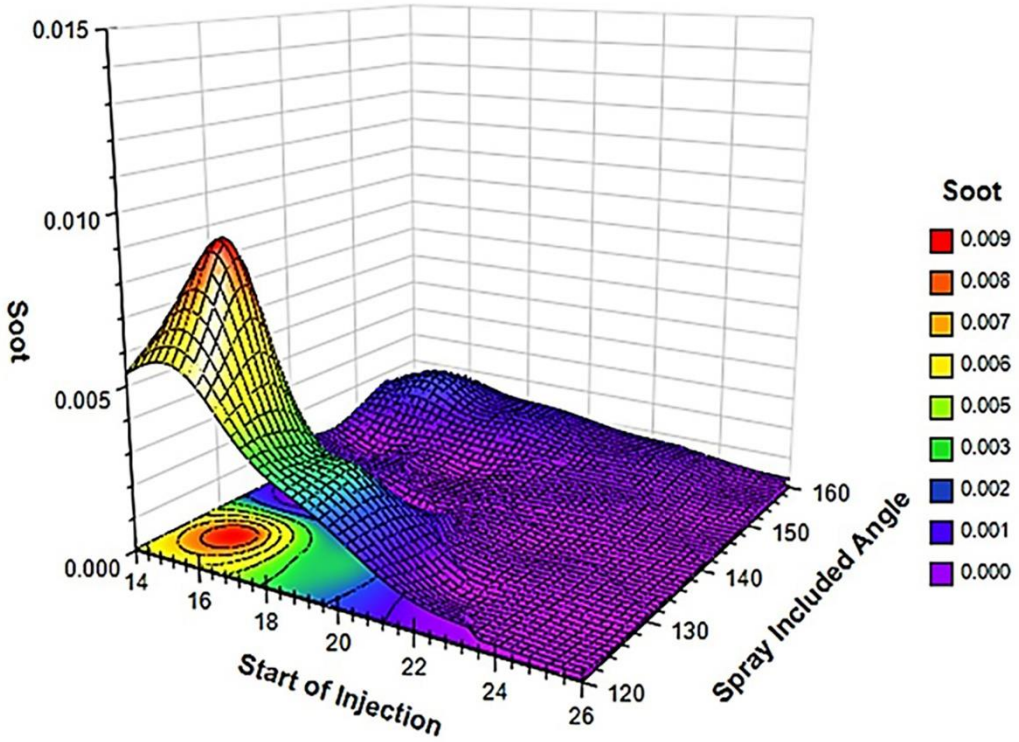

Figure 6.25. Soot variations against SOI and SIA

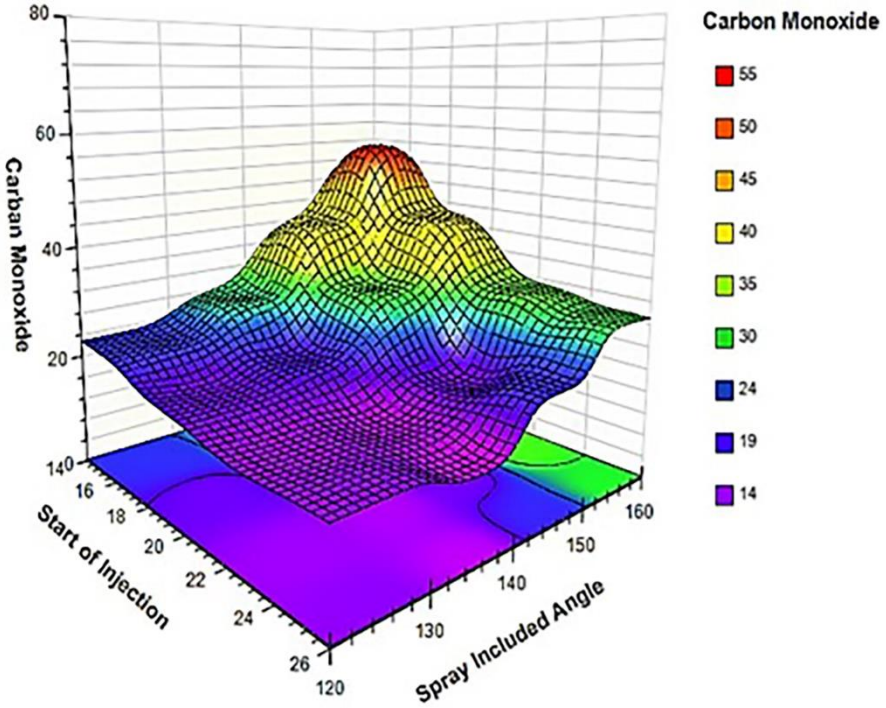

Figure 6.26. Carbon monoxide variations against SOI and SIA

6.5.5. Interaction effect on unburnt hydrocarbon

The result on the combined effect of injection timing and spray angle on unburnt hydrocarbons is demonstrated in Figure 6.27. It was found that the interaction effect of retard injection and wider spray angle reduced unburnt hydrocarbon. Emphatically, it is observed that as the start of injection is retarded to from 21° to 14° BTDC and spray angle is widened from 130° to 152°, the unburnt hydrocarbon becomes very low. The results imply that in order to attain both emissions reduction and improve fuel economy, a combination of large spray angle and late injection is required.

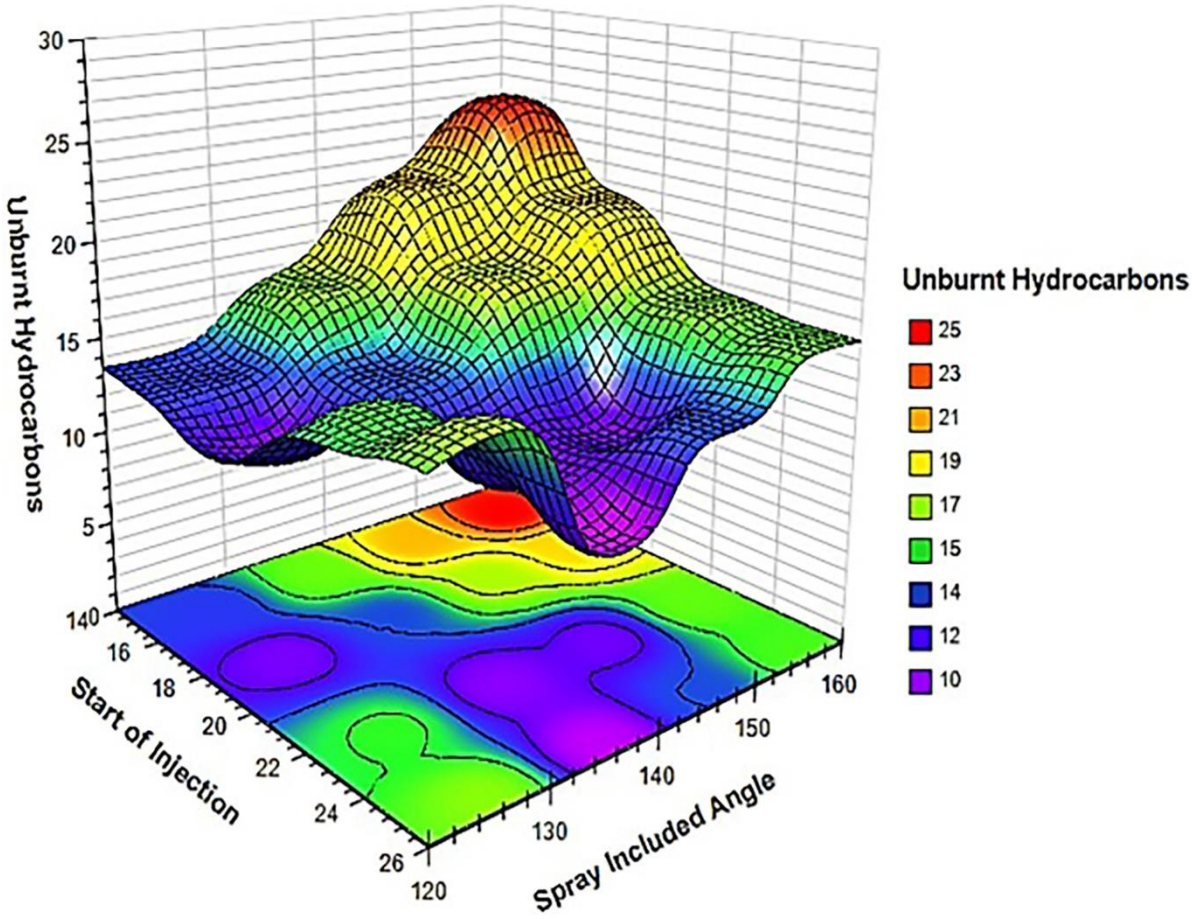

Figure 6.27. Unburnt hydrocarbon variations against SOI and SIA

6.6. Model validation

The Table 6.11 explains the comparison of standards with respect to baseline configuration and optimized model. The comparison was performed to check the accuracy of the results. It was observed that significant reduction between baseline

engine performance and optimized case was found to be 15%, 3%, 14% and 16%, respectively in GISFC, CO, UHC, NOx and SOOT with 3% improvement in GIP. These results explained that the standard engine performance configurations had a good agreement with the optimized or simulated results.

Table 6.11. Comparison of optimized and baseline cases

Parameters and responses	Baseline case	Optimized case	t value	Signf. (2-tailed)
Gross indicated power (GIP)	9.58 kW	9.92	16.67	<0.000
Gross indicated specific fuel consumption (GISFC)	30.62 g/kg-fuel	26.05	-3.23	0.002
Carbon monoxide (CO)	16.09 g/kg-fuel	15.52	-2.067	0.008
Unburnt hydrocarbons (UHC)	201.02 g/KW-h	194.27	-16.97	<0.000
Nitrogen oxide (NOx)	2.98 g/kg-fuel	2.49	-2.78	0.007
Soot	0.00022 g/Kg-fuel	0.00012	-3.44	0.001

6.7. Summary

In this study, the combustion, performance, and emission characteristics of the base bowl and five modified piston bowl designs in low-temperature combustion direct injection compression ignition (DICI) heavy-duty engines are simulated using a reduced normal heptane (n-heptane) kinetic mechanism as a fuel surrogate. The numerical CFD model developed in this study has been validated with the measured data from the base bowl design and in-cylinder pressure was compared to ensure accuracy. The measured data demonstrated a significant and reasonable agreement with the modified bowl design cases 1, 2, 3, 4, and 5, which were used to investigate combustion, performance, and emission characteristics. The following are the summary of the observations:

i. In cases 1, 3, 4, and 5, the piston bowl design has a high TKE due to the throat diameter and toroidal radius of the piston cavity, which enhances fuel-air mixing and concentrates airflow in the combustion chamber. As a result of TKE-

generating bowl geometries, CO emissions are typically lower and NOx emissions are increased. When the right bowl geometry is used, NOx emissions can be reduced simultaneously, and CO emissions can be reduced as well. The combustion process requires good turbulence velocity and a high TKE at the end of the compression stroke. In case 1, turbulence velocity was 382.39 cm/s; in cases 2, 4, and 5, TKE was higher, resulting in better combustion. In addition, this study has shown that in-cylinder pressures, temperatures, and heat release values are directly affected by rapid turbulence and squish.

ii. The results showed that out of the bowl designs, cases 3, case 4 and 5, with piston curved toroidal inside shape, produced better combustion and emissions performance when compared to other designs. The results led to the conclusion that these bowl designs are effective. Several essential features such as the impingement region, pip curves, and pip heights, as well as the provision for a homogeneous mixture, which directly affects performance, are incorporated into them.

iii. According to the results, the gross indicated power (GIP) for bowl design cases 1, 2, 3, and 5 is marginally high compared to the base bowl design. In contrast, the gross indicated specific fuel consumption (GISFC) for these bowl design cases is marginally lower than for the base bowl design.

iv. With a favourable air-fuel mixture, due to the internal design features of bowl cases 2, 3, and 4, the record showed less than 22% CO compared to the base bowl design. However, bowl design cases 3 and 4 recorded 10% less UHC compared to the base bowl design. The other bowl designs had marginally higher CO and unburned hydrocarbons (UHC) due to incomplete combustion that may be present in the bowl cavity at the end of the compression stroke.

v. The base bowl and the five bowl design cases were compared for emissions of NOx and SOOT, and the trade-offs between NOx and SOOT have been looked at. The bowl design cases 3, 4, and 2 each emit more NOx than the base bowl design (4.09, 3.92, and 3.55 g/kg-fuel, respectively). The generation of NOx gases is primarily associated with higher temperatures and pressures. While the base bowl design has low NOx but high SOOT, cases 1, 2, 3, and 5 have comparatively low SOOT. As a result, bowl design case 5, which produces low

SOOT and NOx emissions, is the optimal bowl design for reducing SOOT and NOx emissions.

vi. The study shows that when injection timing is retarded, the delay period becomes short, and there is a lack of sufficient time for the air-fuel mixture to have complete combustion, resulting in higher CO and UHC. It became evident with SOI 15.5° CA BTDC and 18.5° CA BTDC, which recorded higher CO and UHC for all the bowl designs.

vii. The study shows that when the start of injection is advanced, the in-cylinder peak pressure increases, and when the timing is retarded, it decreases. A longer ignition delay interval is achievable with improved injection timing; and as a result, more fuel accumulates inside the cylinder, hastening the release of heat and increasing temperature and pressure during the premixed combustion stage. The ideal injection timing is when in-cylinder peak pressure is the highest, NOx and soot emissions are the lowest. Therefore, SOI -22.5° CA BTDC showed improved performance and was tipped as the optimum injection timing for the bowl designs in this study. Maximum pressure is reached at SOI -25.5° CA BTDC, but substantial high quantities of NOx and SOOT are generated, so it is not recommended.

viii. The piston bowl cavity design, spray angle, and injection timing all have a significant impact on the impingement target. In the study, injection included angle 136° and 146° showed improved indicated power for bowl design cases 2, 3 and 5, and in the same vein, engine performance recorded slightly reduced gross indicated specific fuel consumption (GISFC) for the same bowl design cases 2, 3 and 5. When the spray angle got wider to 156° there is more wall impingement; this results to low work done therefore the indicated power for all bowl designs became low and the GISFC become high for all the bowl designs.

ix. According to the findings, when the spray impinged on the bowl lip bottom edge at the 146° spray angle, atomization was enhanced in the bowl cavity of the combustion chamber and resulted in a drop in emissions of UHC and CO. However, CO emissions increase as the spray angle decreases below 136° but remain low when the spray angle ranges between 146° and 156°. Therefore, to balance the emissions of NOx, unburned hydrocarbons (UHC), and CO, the optimal spray angle should range between 136° and 146°.

CHAPTER 7

Results and discussion of CNSL biodiesel simulation in DICI engine

In this chapter, combustion and emission characteristics of cashew nut shell liquid (CNSL) biodiesel blended with petroleum diesel (B10, B20, B30, and B50) are discussed. Results of modelling and simulation are also discussed. The study utilised the same single-cylinder low-temperature combustion (LTC) direct injection compression ignition (DICI) based on a Cummins N-series production engine's measured data as a baseline for the modelling and simulation (Musculus, 2004). This engine specification, which was utilised in Chapter 6, was modelled with two cases of optimized piston bowl designs (Cases 1 and 2). Statistically significant results were determined for combustion, including in-cylinder peak pressure, temperature, and apparent heat release rate of B10, B20, B30, and B50 compared to baseline data. The results of emission characteristics including carbon monoxide (CO), carbon dioxide (CO_2), hydrocarbons (HC), and oxides of nitrogen (NOx) are also studied. The study also discussed engine performance parameters, gross indicated power, gross indicated specific fuel consumption (GISFC), and thermal efficiency.

7.1. Introduction

In order to model and simulate biodiesel combustion and emissions characteristics of a compression ignition engine in this study, the ANSYS CHEMKIN-PRO and ANSYS Forte programmes were used. A mixture of CNSL biodiesel is modelled using the programme ANSYS CHEMKIN-PRO, which enables specification and simulation of scenarios for chemical processes prior to the simulation of combustion. CHEMKIN-PRO, which solves problems through kinetic analysis, is principally employed in this study to assess the impacts of biodiesel combustion in CI engines. In chemical and combustion engineering, CHEMKIN-PRO is essential because it accurately solves complex chemical and gas reaction models and flows quickly and thoroughly.

In contrast to conventional fuels, biodiesel has a complicated structure and long carbon chains, making it more difficult to numerically analyse its full chemical kinetic reaction mechanism. It takes too long to simulate the combustion phenomena of biodiesel using numerical analytical techniques like three-dimensional (3-D)

computational fluid dynamics (CFD) due to the high number of species and reactions involved in the complex biodiesel mechanism (Li et al., 2019). The reduction mechanism process was used in simulating CNSL biodiesel combustion and emission characteristics in this study.

The automatic mechanism reduction process of ANSYS Reaction Workbench was used in this study (ANSYS CHEMKIN-PRO 2020). The modelled in ANSYS FORTE, version 2020 and simulation conducted in order to examine their impact on combustion and emission characteristics. Various mechanism reduction methods have been implemented in ANSYS Reaction Workbench to reduce mechanisms. Among these methods, are the directed relation graph (DRG)–based methods, such as DRG error propagation (DRGEP), DRG-aided sensitivity analysis (DRGASA), and DRGEP sensitivity analysis (DRGEPSA) because these methods are characterized by low reduction costs and linear reduction times, making it very efficient to reduce very large mechanisms (Zheng, Lu and Law, 2007; Pepiot-Desjardins and Pitsch, 2008; Niemeyer, Sung and Raju, 2010)

In this work, a seven-step reduction strategy was employed to lower the ignition delay error, which alters the reduction of typical detailed mechanisms. If the mechanism reduction is done with the goal of decreasing the mechanism without going through each phase, the ignition delay has a tendency to produce highly unstable results. A method that reduces the error rate of ignition delay with each stage is consequently required since the results of ignition delay will remain variable as long as the mechanism size is decreased. According to the Figure 1 in Appendix C, each stage of the reduction procedure involved the use of the DRGEP, peak concentration analysis, DRGEPSA, a complete species sensitivity analysis (FSSA), and modification of the A-factor, respectively.

The detailed chemical and thermo-physical properties of methyl palmitate ($C_{17}H_{34}O_2$) and methyl oleate ($C_{19}H_{36}O_2$) were calculated based on the methodologies presented in (An et al., 2013) and assigned to methyl decanoate (md) (saturated methyl ester) and methyl 9-decenoate (md9d) (unsaturated methyl ester), respectively. The CNSL biodiesel like the other biodiesel methyl esters dominantly consists of fatty acid methyl esters (FAME) as shown in Table 7.1.

Table 7.1. CNSL Biodiesel fatty acids methyl esters (Herbinet, Pitz and Westbrook, 2010; Santhanakrishnan and Ramani, 2017; Pandian et al., 2018).

Fatty Acid	Acid code	Formula	CNSL_B100 (wt %)
Methyl palmitate	C16:0M	$C_{17}H_{34}O_2$	23.13 - 38.7
Methyl palmitoleate	C16:1M	$C_{17}H_{32}O_2$	5.16 - 6.63
Methyl stearate	C18:0M	$C_{19}H_{38}O_2$	5.57 - 6.53
Methyl oleate	C18:1M	$C_{19}H_{36}O_2$	31.65 - 42.7
Methyl linoleate	C18:2M	$C_{19}H_{34}O_2$	5.23 - 7.62
Methyl linolenate	C18:3M	$C_{19}H_{32}O_2$	12.33 - 20.71

The properties of diesel, CNSL biodiesel, and blends utilised in the simulation are compared in Table 7.2 (Bayraktar, 2008; Paul et al., 2013; Aksu and Shahin, 2015). CNSL biodiesel has a lower heating value than diesel due to its oxygen content. CNSL biodiesel has a higher kinematic viscosity and flash point than diesel. With the addition of a certain percentage of biodiesel to diesel, a higher flash point has been achieved.

Table 7.2. Properties of CNSL Biodiesel and diesel blends

Properties	Diesel	CNSL B10	CNSL B20	CNSL B30	CNSL B50
Density @ 40 ^oC kg/m^3	817	851	857	865	876
Kinematic Viscosity@ 40^oC	2.2	2.68	3.12	3.65	4.52
Lower Heating Value MJ/kg	42.52	41.75	40.79	40.22	39.35
Cetane Number	50	49.2	48.8	48.4	48.1
Flash Point (^0C)	66	72	82	88	96

7.1.2. CI engine simulation

In this study, ANSYS CHEMKIN-PRO and ANSYS Forte software was used to model a blend of CNSL biodiesel and petroleum diesel using scenarios built for chemical processes before simulating combustion The main engine specifications, injector parameters, operating conditions, and initial boundary conditions in Tables 6.2 and 6.3 of Chapter 6 were used in this model and simulation. A number of sub-models are

used to simulate the CI engine in ANSYS Forte software. The renormalization group k-Ɛ model (Han and Reitz, 1995) was used to model in-cylinder turbulence due to its high accuracy in predicting swirling flows based on Kelvin Helmholtz/Rayleigh-Taylor break-up, discrete multi-component (DMC) vaporization, and radius of influence (ROI), models of atomization and break-up of fuel sprays were developed (Beale and Reitz, 1999; Munnannur and Reitz, 2009; Ra and Reitz, 2009). To simulate the physical properties for CNSL biodiesel, methyl decanoate (md) and methyl-9-decenate (md9d) were represented with methyl palmitate ($C_{17}H_{34}O_2$) and methyl oleate ($C_{19}H_{36}O_2$) as utilised by An et al., 2014. The amount of soot generated in the analysis results was checked using the soot surface mechanism provided by ANSYS Forte. Through the hydrogen abstraction and C_2H_2 addition (HACA) mechanism, soot growth and oxidation are described as part of the soot surface mechanism. (CHOU, 2007)

7.2. Results and discussion

7.2.1. Combustion characteristics

In this simulation, the intake valve is closed at -165° CA BTDC the exhaust valve is opened at 125° CA ATDC, while the engine speed is constant at 1200 rpm The results of the simulations are discussed as follows. It is imperative to note that the air/fuel equivalence ratio distribution within the engine cylinder greatly affects combustion and emission characteristics of a compression ignition diesel engine. In terms of combustion performance, fuel concentration plays a crucial role in in-cylinder pressure, temperature, and apparent heat release. To determine the effect of piston bowl combustion chamber configuration, the cross-sectional equivalence ratio distribution of the optimum bowl designs 1 and 2 with diesel and various CNSL biodiesel blends is shown in Fig. 7.1. Due to better air-fuel mixing in optimum bowl design case 1, there are fewer areas of high equivalence ratio regions than in optimum bowl design 2. Incomplete combustion, inferior engine performance, and soot emissions are caused by these high equivalence ratio regions. When biodiesel blends are used in the engine, the air/fuel equivalence ratio is significantly higher than when mineral diesel is used. As the biodiesel proportion increases, high equivalence ratio regions are observed in each of the investigated combustion chambers.

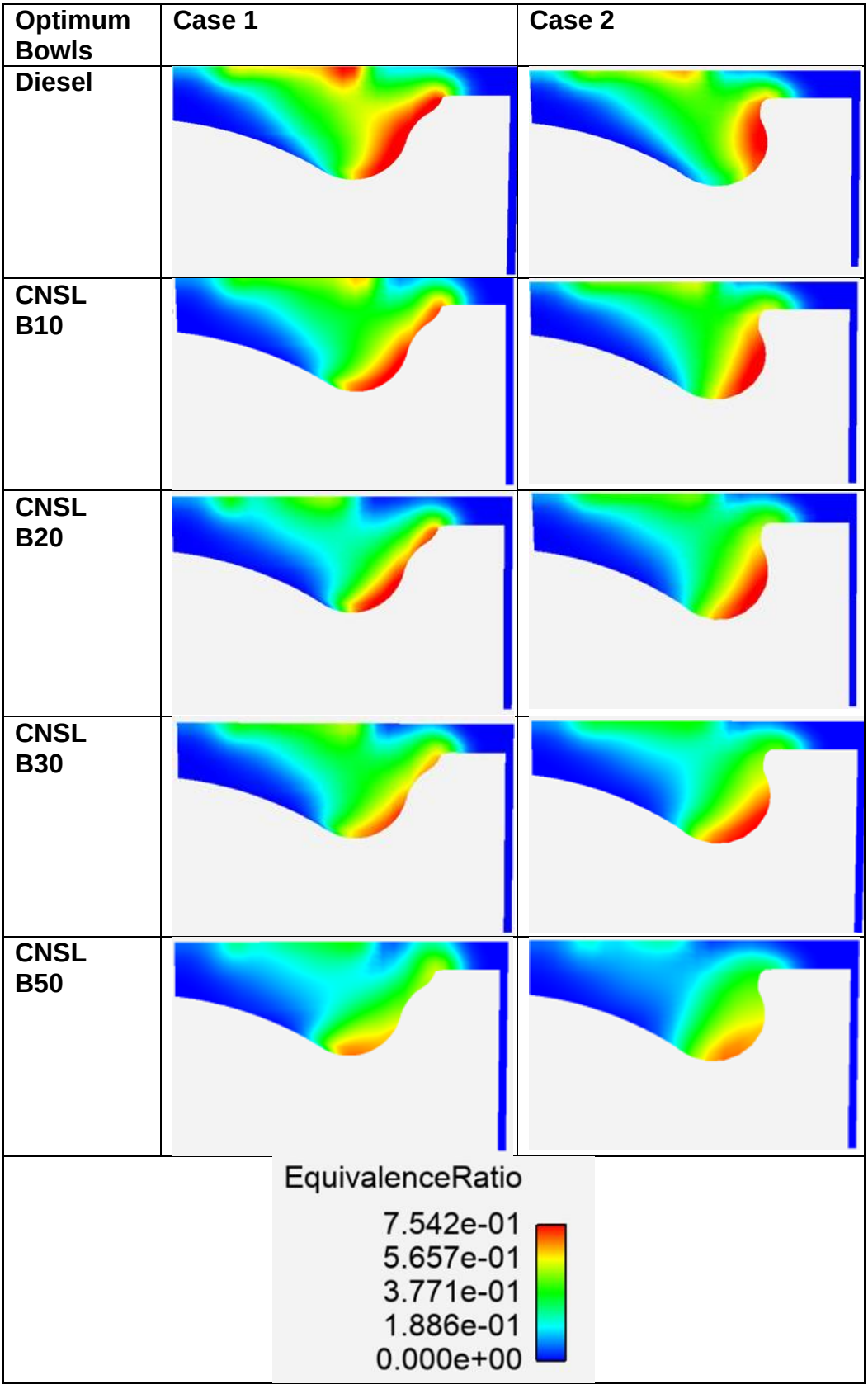

Figure 7.1. Equivalence ratio distribution among the optimum piston bowl design cases 1 and 2 at TDC with diesel and different CNSL biodiesel blends.

A rich mixture provides more energy than a lean mixture, but it has a lower combustion temperature. There is no doubt that biodiesel has a higher density and viscosity than petroleum diesel, which might explain this. Also, diesel fuel is still being injected into the burning zone after the auto-ignition of the fuel-air mixture; as a result, some of the heat from combustion is absorbed by the freshly injected fuel droplets before vaporization (Khan, Panua and Bose, 2019). The combustion of diesel fuel results in a faster rise in pressure in a mixture rich in fuel. In the combustion chamber, as fuel is injected, a combustible mixture is readily formed, resulting in an earlier ignition of the fuel-air mixture (Rahman and Ahmed, 2020).

7.2.2. The variation of peak pressure with crank angle

Figure 7.2 depicts the variations in cylinder pressure with crank angle for various CNSL biodiesel and diesel blends for the optimum bowl design case 1 and 2 combustion chamber. The diesel and CNSL biodiesel blends show higher peak cylinder pressures with the optimum piston bowl case 1 configuration than the optimum piston bowl case 2 configuration. The peak cylinder pressure is raised when more air is added to the injected fuel in case 1 of optimum piston bowls, which improves mixing, evaporation, and combustion. Due to increased turbulence in case 1 combustion chambers, higher premixed fuel, and air availability, it leads to a stronger premixed combustion phase than case 2 combustion chamber, leading to more potent premixed combustion. In the premixed combustion stage, the peak pressure largely depends on the combustion rate. In terms of peak cylinder pressure, diesel is slightly higher than biodiesel blends; this is due to the combustion process for diesel starts earlier than for biodiesel blends because its fire and flash points are lower, resulting in a shorter ignition delay.

The Figure 7.2 shows peak pressures for diesel, CNSL B10, B20, B30, and B50 for optimum piston bowl 1, which are 8.50, 8.81, 8.65, 8.47, and 8.16 MPa, respectively. The predicted peak pressures for optimum piston bowl 2 are 8.74, 8.30, 8.09, 7.91, and 7.58 MPa, respectively.

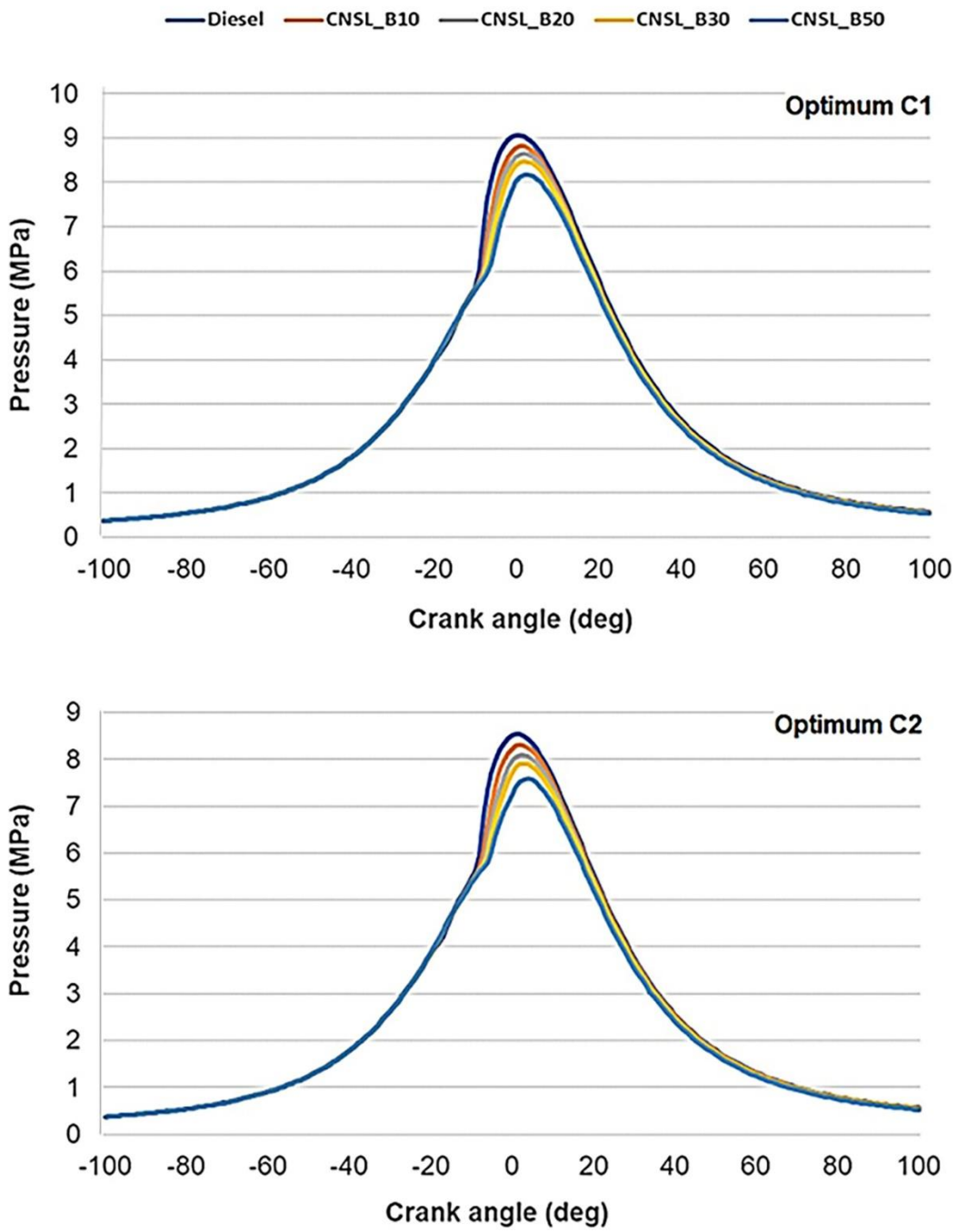

Figure 7.2. The variation of in-cylinder pressure vs crank angle of petroleum diesel and CNSL biodiesel blend for optimum bowl design in cases 1 and 2.

Due to the lower calorific value of biodiesel blends, the maximum cylinder pressure is slightly reduced. There is an overall progressive decline in peak pressure as the CNSL Biodiesel blend with diesel increases from 10% to 50% by volume. This is due to a delay in the combustion process with added biodiesel to diesel (Abu-Jrai et al., 2011 and Can, 2014). Additionally, since biodiesel contains oxygen molecules, the

hydrocarbons achieve complete combustion in some instances, resulting in slightly higher in-cylinder pressure than diesel (Kale, 2017).

7.2.3. In-cylinder Temperature vs. Crank angle

In Figure 7.3, the variation in temperature over crank angle is shown for diesel, CNSL B10, B20, B30, and B50 for optimum piston bowl cases 1 and 2. The highest temperature recorded in optimum bowl case 1 for petroleum diesel followed by CNSL B10, B20, B30, and B50 were 1287,79 K, 1258.25 K, 1239.34 K, 1218.94 K, and 1178.48 K respectively. The optimum piston bowl 2 also recorded a similar trend of the highest temperature for petroleum diesel and declined progressively as the biodiesel concentration increased from 10% to 50%; and the temperature was recorded 1267,41K,1229.39K,1202.58K, 1180.54K, and 1140.69K respectively. The two plots in Figure 7.3 show that the in-cylinder temperature decreases with an increase in CNSL biodiesel concentration because biodiesels have a lower calorific value, therefore, it releases less heat (Bari and Zhang, 2020).

Similar findings from a study conducted by Elkelawy et al., (2021) confirmed that the temperature dropped as biodiesel concentration increased because of incomplete combustion and the low calorific value of fuel blends. Higher viscosity and density of biodiesel with large molecules delay temperature rise, according to a study conducted by Bari and Chang (2020). With CNSL biodiesel, larger droplets lead to a longer evaporation time in the chamber. The evaporation rate is affected by a lower temperature, resulting in poor mixing and combustion. Approximately 0.19 W/m-K and 0.13 W/m-K are the thermal conductivities of diesel and biodiesel, respectively (Liu et al., 2010).

Lower thermal conductivity results in lower heat transfer inside the molecules, which results in a lower evaporation rate. Another significant property is the latent heat of evaporation. There is approximately 250 kJ/kg of latent heat of evaporation in diesel and 350 kJ/kg in biodiesel (Liu et al., 2010; Tripathi and Subramanian, 2018). This delays the occurrence of a rise in temperature and at a higher crank angle which causes lower temperatures (Bari and Zhang, 2020). It can be seen from this simulation that the CNSLB50 combustion temperature appears to be lower than that of petroleum

diesel and CNSLB10. This confirms the study conducted by Tat et al., (2004) that lower combustion temperatures reduce NOx emissions.

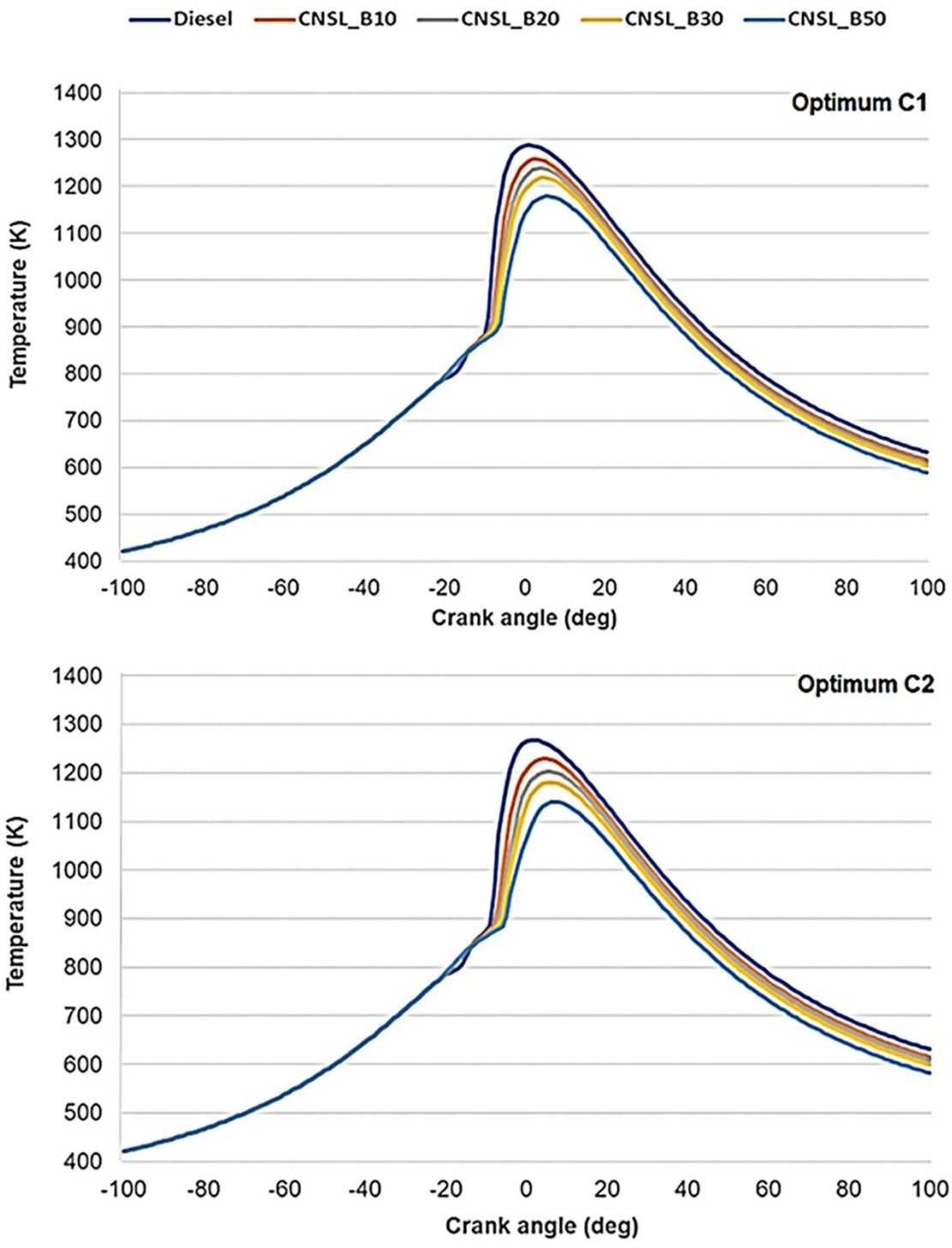

Figure 7.3. The variation of temperature vs crank angle of petroleum diesel and CNSL biodiesel blend for optimum bowl design in cases 1 and 2.

Figure 7.4 depicts the in-cylinder temperature distribution for the optimum piston bowl cases 1 and 2 with diesel and various CNSL biodiesel blends at 100 crank angles after ATDC.

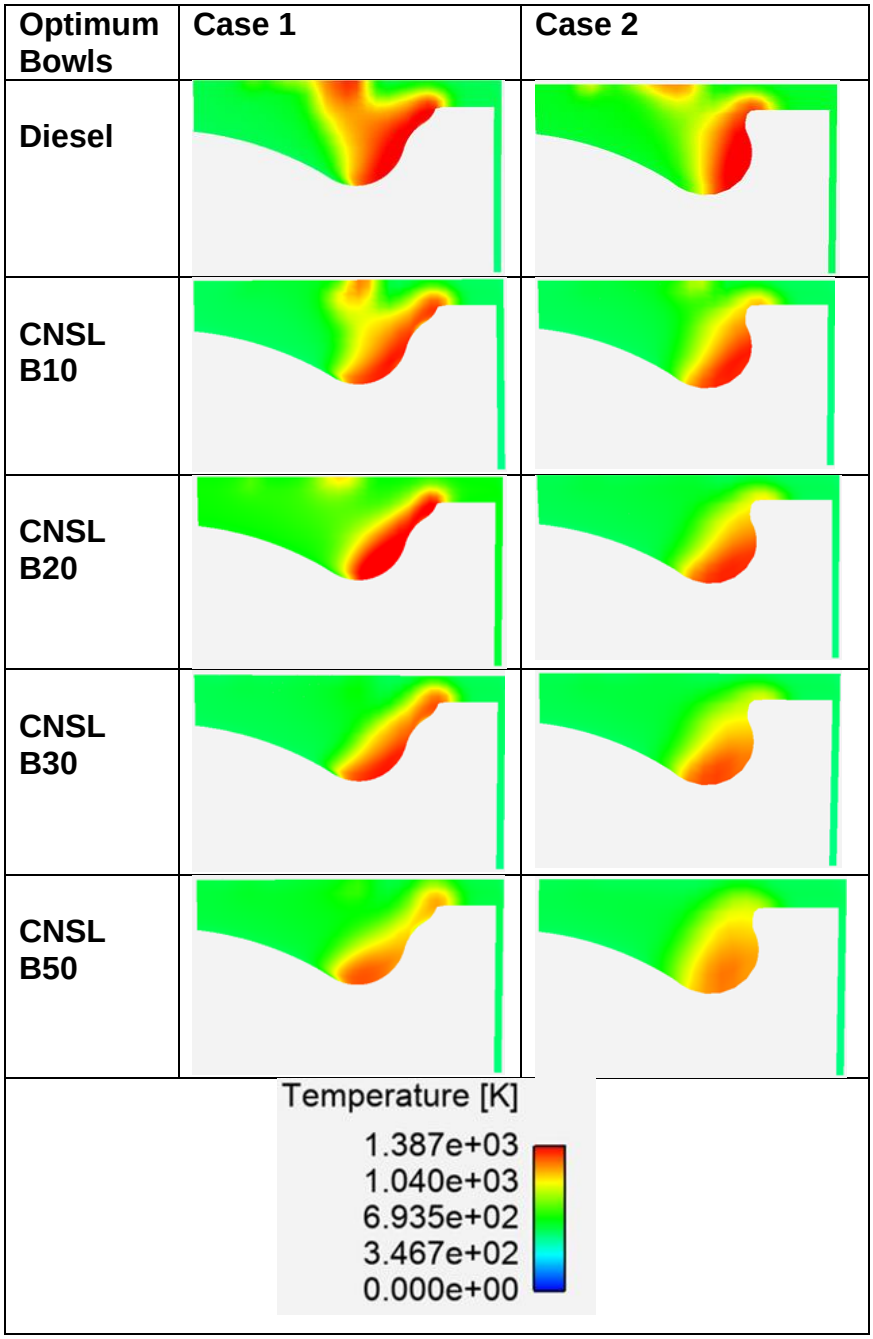

Figure 7.4. The distribution of temperature among combustion chambers in a cross-section view of the optimum bowl design cases 1 and 2 at 10° after ATDC with petroleum diesel and CNSL blends.

The figure shows that higher biodiesel substitution decreases temperature intensity in all the optimum bowl cases. Furthermore, optimum bowl case one topologies result in

a larger area of high-intensity combustion temperature than optimum bowl case 1 topologies due to improved combustion.

7.2.4. Apparent heat release rate

In combustion systems, the apparent rate of heat release (AHRR) is crucial because it determines how much heat energy can be converted into practical mechanical work. Figure 7.5 depicts the apparent heat release rate as a function of crank angle in two optimal piston bowl designs for petroleum diesel and CNSL biodiesel blends. The results of the apparent heat release rate for diesel and CNSL (B10, B20, 30, and B50) for optimum bowl design case 1 are 628, 415, 389, 350, and 280 (J/deg), respectively. When compared to optimum bowl design case 2, the results for diesel and CNSL (B10, B20, 30, and B50) are lower at 577, 362, 284, 265, and 220.8 (J/deg), respectively. The results show that diesel had a high peak apparent heat release rate, and this rate decreased as the blend concentration of CNSL biodiesel increased from 10% to 50%. As the amount of CNSL biodiesel increases in the fuel, the viscosity of the fuel increases as well. In contrast, when the viscosity is lowered, the fuel is atomized more finely, enhancing combustion, especially diffusion combustion, by taking advantage of the oxygen in CNSL biodiesel (Vedharaj et al., 2015).

The optimum piston bowls in case 1 have more air entrainment during fuel injection due to enhanced turbulence than case 2, which leads to better air-fuel mixing and combustion and a higher peak rate of heat release. Due to the short ignition delay and greater heat release during the premixed combustion phase, the heat release rate for diesel is slightly higher. Diesel combustion begins quicker than biodiesel combustion does because it has a shorter ignition delay, a higher heating value, and better spray production. As a result, diesel combustion has a slightly higher peak heat release rate than CNSL biodiesel (Kale, 2017; Khan, Panua and Bose, 2019).

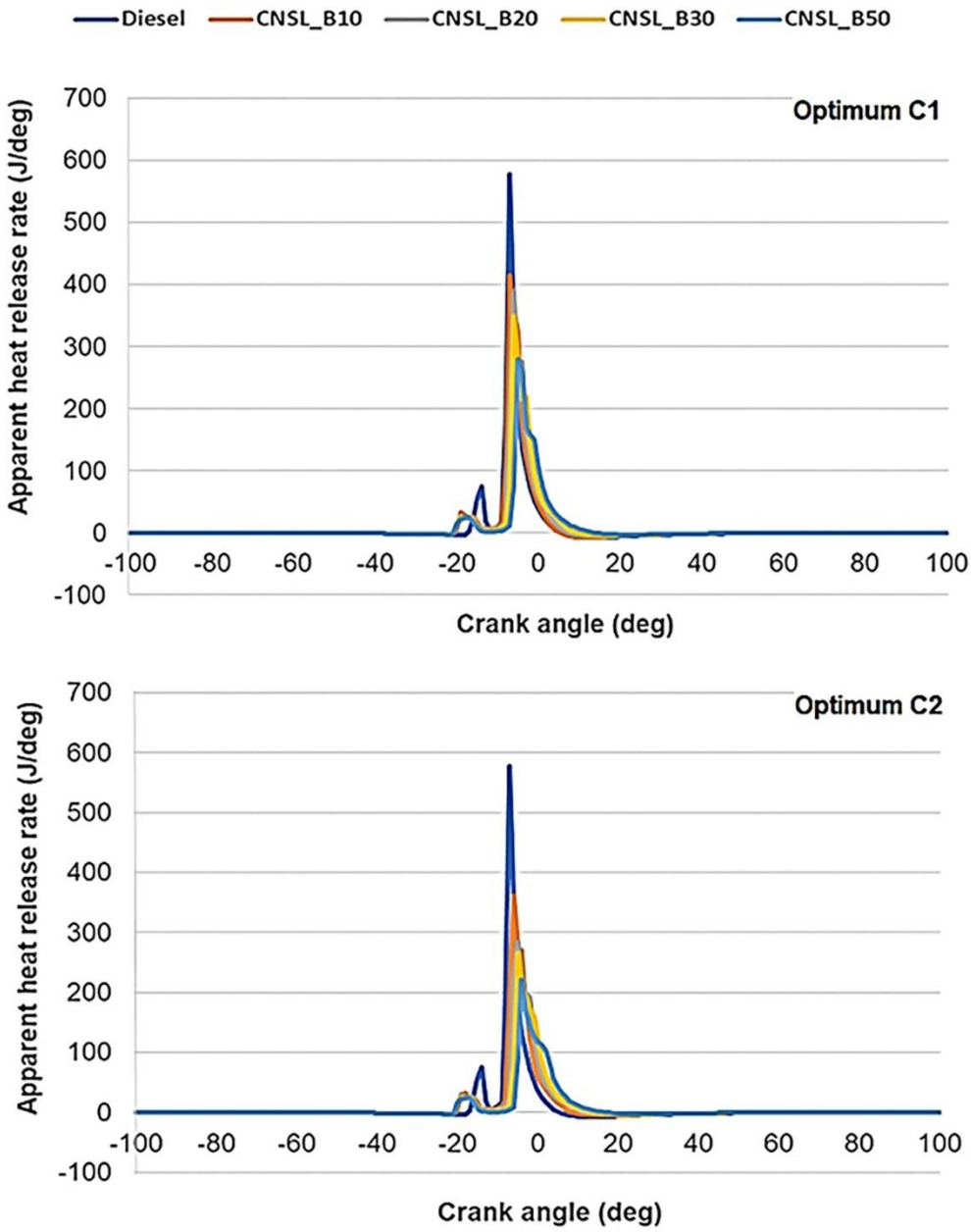

Figure 7.5. Apparent heat release rate vs crank angle for petroleum diesel and CNSL biodiesel blend for optimum bowl design in cases 1 and 2.

7.2.5. Accumulate chemical heat release

Figure 7.6 shows the variation in cumulative heat release (CHR) with crank angles for optimum piston bowl cases 1 and 2 with diesel and CNSL biodiesel (B10, B20, B30, and B50). The optimum piston bowl case 1 recorded high chemical heat release for diesel, followed by CNSL (B10, B20, B30, and B50) as follows: 2399 J, 2309 J, 2238

J, 2165 J, and 2001 J, respectively, whereas the optimum bowl case 2 had slightly low CHR at 2389 J, 2285 J, 2197 J, 2097 J, and 1904 J, respectively.

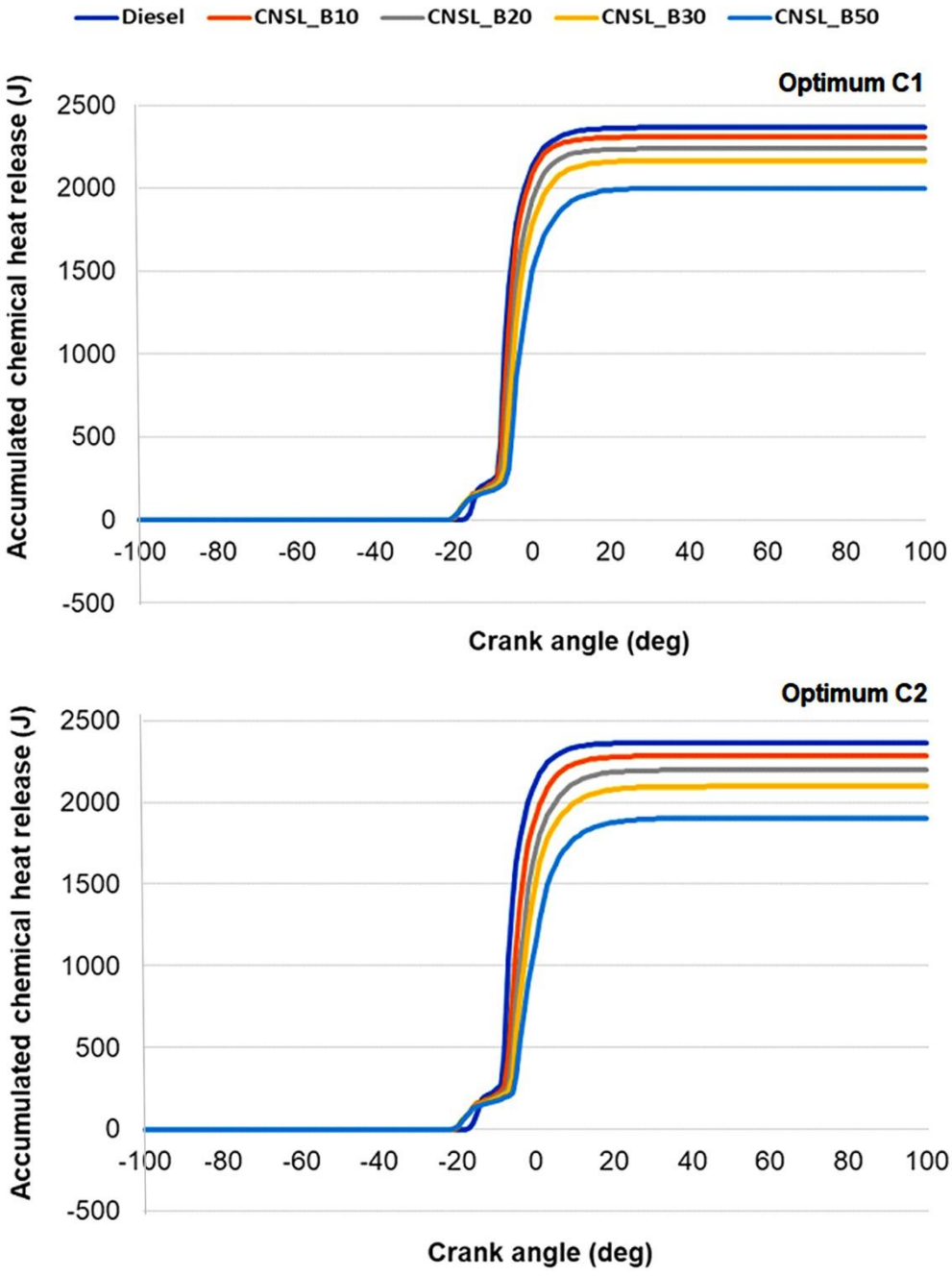

Figure 7.6. Accumulated chemical heat release vs crank angle for petroleum diesel and CNSL biodiesel blends for optimum bowl design in cases 1 and 2.

The graph demonstrates that, when compared to diesel, CNSL biodiesel has a propensity to release heat more slowly during the initial stages of combustion. However, at a later stage of combustion, the CHR value of diesel fuel quickly surpasses the CHR for CNSL biodiesel. CNSL biodiesel has a lower heating value

(LHV) than diesel, which contributes to the CHR decline. Compared to petroleum diesel, the fuel evaporates and absorbs latent heat from the surroundings, causing a negative heat release. This is another reason for the lower molecular temperatures of CNSL biodiesel molecules. This affects the evaporation rate of CNSL biodiesel, resulting in poorer performance than diesel (Shahabuddin et, al. 2013). And again, this is because biodiesel has molecules that are heavier, denser, and have higher viscosities, which extend combustion and give it a longer burn time than diesel. A prolonged combustion indicates that the combustion will remain longer during power strokes, which will lessen the amount of work done by the piston produces (Bari et, al. 2022).

7.3. Exhaust emissions characteristics

The results in this section include an analysis of combustion exhaust gases, one of the most crucial factors in improving compression ignition internal combustion engines. Unburned hydrocarbons (HC), carbon dioxide (CO_2), carbon monoxide (CO), nitrogen oxides (NOx), and oxygen emissions (O_2) from diesel and CNSL biodiesel blends were measured and discussed.

7.3.1. Carbon monoxide (CO) emission

The main cause of carbon monoxide emissions is the incomplete combustion of fuels in the combustion chamber (Heywood, 2018). Figure 7.7 shows the variation in CO emissions for petroleum diesel and CNSL biodiesel fuel. CO emission is predominantly formed due to the lack of oxygen but since biodiesel fuel contains small amount of oxygen, which acts as a combustion promoter inside the cylinder. Compared to diesel, biodiesel fuels have a higher proportion of underlying oxygen molecules and a smaller proportion of carbon molecules (Elkelawy et al., 2021; Nayak, et al., 2021). CNSL biodiesel combustion also lowers CO emissions as the concentration increases due to the presence of more oxygen. The results for diesel and CNSL biodiesel (B10, B20, B30, and B50), are 44.4, 37.7, 35.1, 31.6, and 29.1 g/kg-fuel respectively for optimum bowl design case 1, whereas the optimum bowl design case 2 recorded slightly high CO emissions for all the fuels as 52.8, 48.9, 45.4,

42.6, and 40.9 g/kg-fuel respectively. There are other studies that have reported similar results (Elkelawy et al., 2021; Nayak et al., 2021; Sathyamurthy et al., 2021).

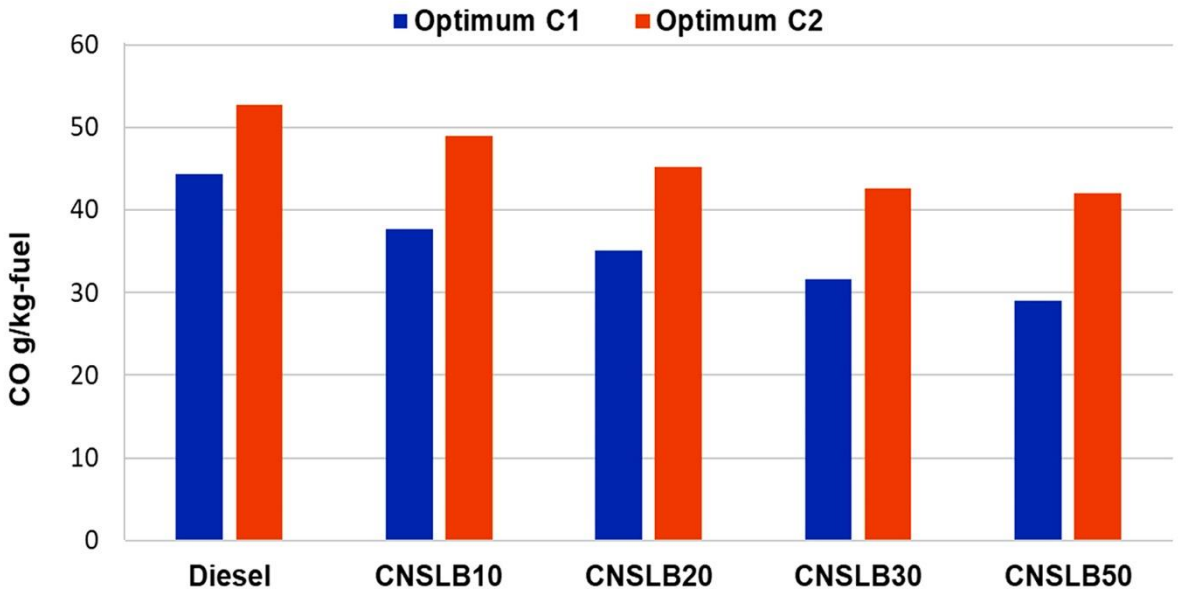

Figure 7.7. Carbon monoxide for diesel and CNSL biodiesel blends for optimum bowl design in cases 1 and 2.

The distribution of CO mass fraction for diesel and CNSL biodiesel at 15° crank angle is shown in Figure. 7.8 for optimum bowl design cases 1 and 2. It is observed that case 2 of the optimum piston bowl configuration has a broader area of high CO regions than case 1. When CNSL biodiesel blend concentrations are increased from B10 to B50, CO emissions are also significantly reduced as shown. The level of CO reduction and ability to reduce exhaust CO emissions appears to be enhanced by introducing CNSL biodiesel.

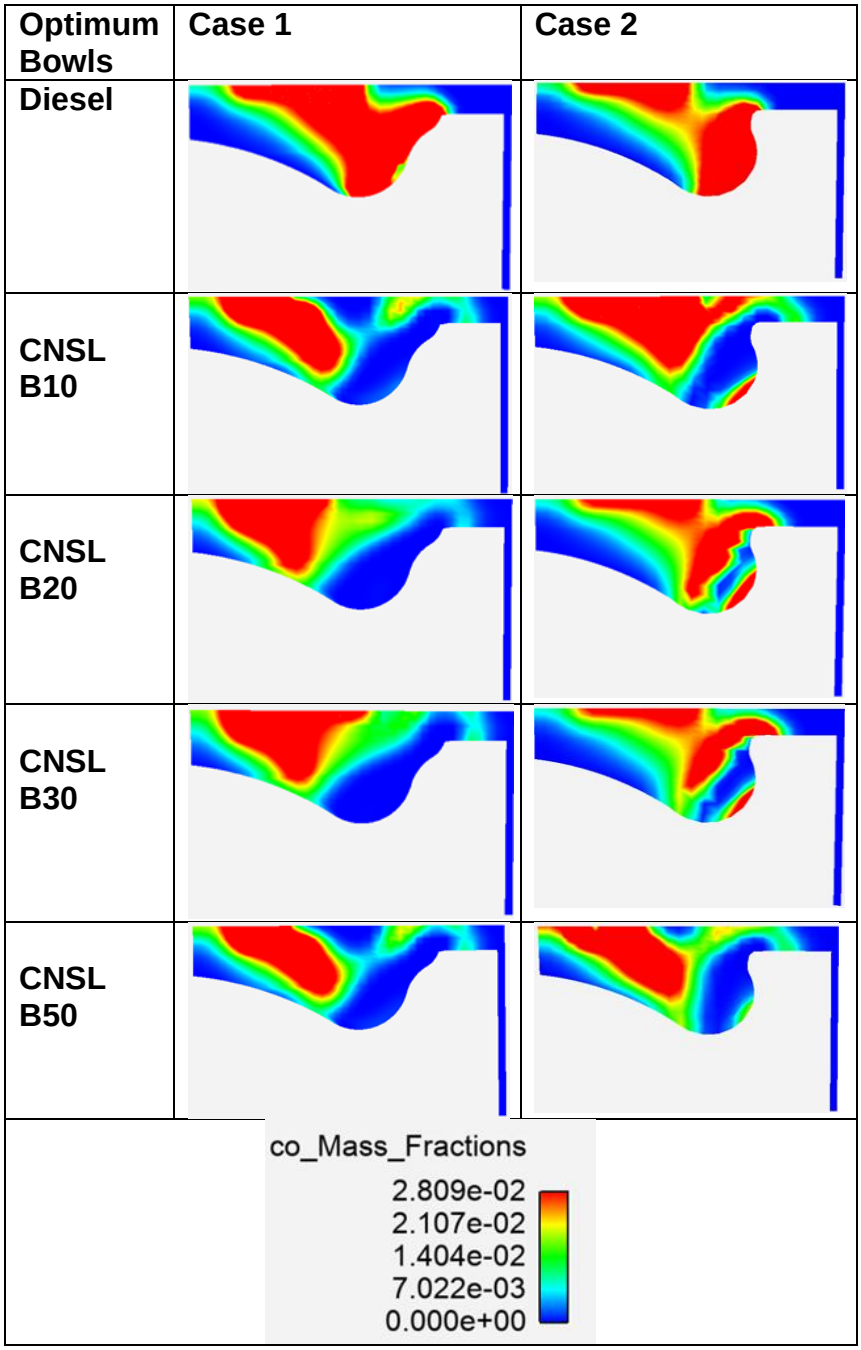

Figure 7.8. carbon monoxide mass fraction distributions in a cross-section view of the optimum bowl design cases 1 and 2 at 15° ATDC with petroleum diesel and CNSL blend.

7.3.2. Unburnt Hydrocarbon (UHC) emissions

The main cause of unburned hydrocarbon (HC) emissions is the incomplete combustion of fuel. Another critical factor affecting engine emissions is how much

unburned hydrocarbon (HC) is present in the combustion chamber (Heywood, 2018). According to Figure 7.9, CNSL biodiesel emits fewer unburn hydrocarbons than diesel.

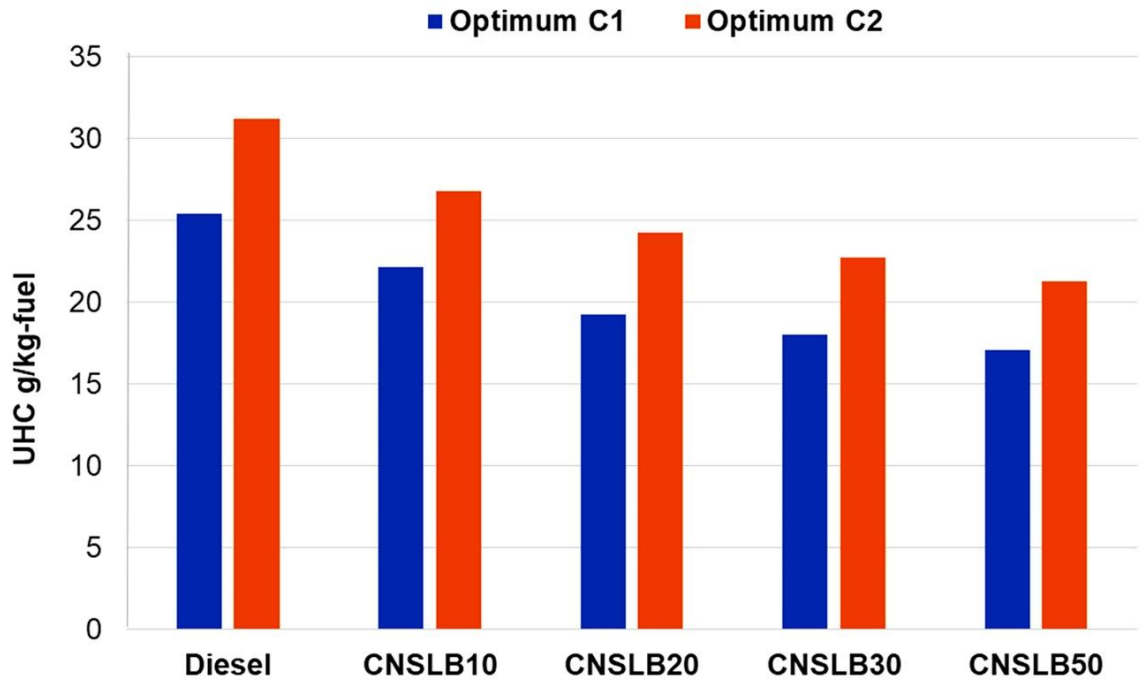

Figure 7.9. Unburned hydrocarbon emissions for diesel and CNSL biodiesel blends for optimum bowl design in cases 1 and 2.

The reason for this is that biodiesel contains more oxygen atoms than regular diesel fuel and thus burns more efficiently in combustion chambers (Nayak et al., 2021; Sathyamurthy, et al., 2021). The results recorded for diesel and CNSL biodiesel (B10, B20, B30, and B50) are 25.4, 22.2, 19.2, 18.04, and 17.1 g/kg-fuel respectively for optimum bowl design case 1; whereas the optimum bowl design case 2 recorded 31.2, 26.8, 24.2, 22.8, and 21.3 g/kg-fuel respectively. Similar results have been reported in other studies (Khan, Panua and Bose, 2019; Elkelawy et al., 2021a; Nayak, et al., 2021) The amount of NOx produced depends greatly on the temperature, oxygen concentration, and reaction time in the cylinder (Heywood, 2018). The combustion of premixed biodiesel fuel is also very strong, and the chemical effects of oxygen in oxygenated fuels increases NOx emissions (Devan and Mahalakshmi, 2009).

7.3.3. Nitrogen oxides (NOx) emissions

This is primarily due to the fuel-bound oxygen content in biodiesel blends, which results in a lean-fuel combustion process (Heywood, 2018). It can be observed from the graph in Figure 7.10, that when CNSL biodiesel blend increases by volume, the NOx increased proportionately compared to petroleum diesel. Figure 7.10 depicts NOx emission results for optimum piston bowl cases 1 and 2 for diesel and CNSL (B10, B20, B30, and B50) biodiesel blends.

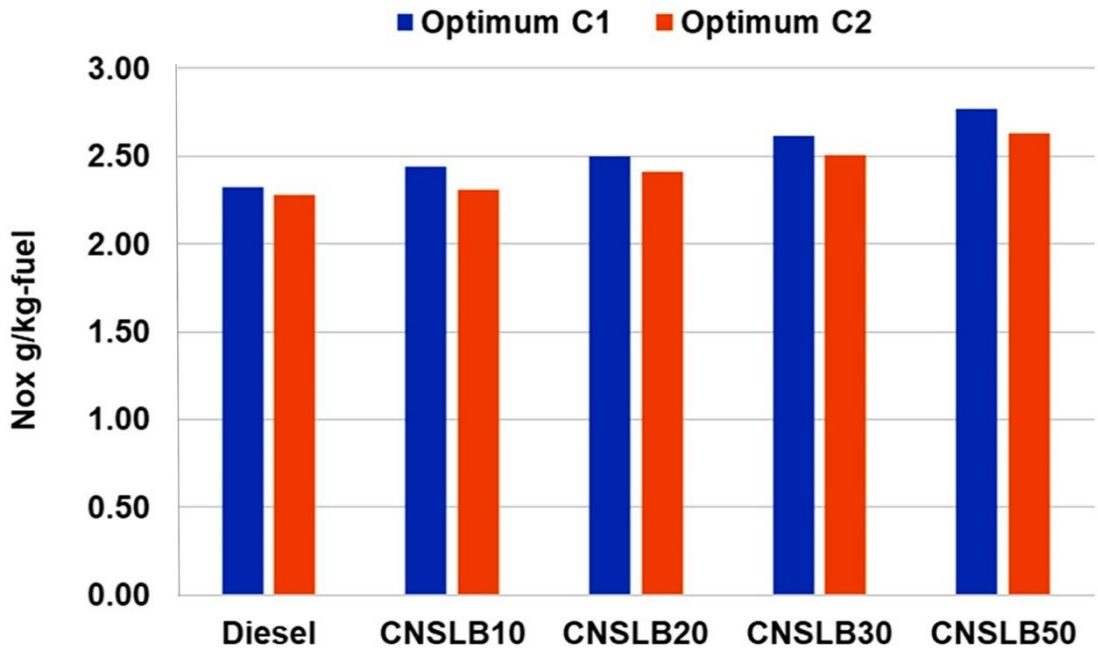

Figure 7.10. Nitrogen oxides (NOx) emissions for diesel and CNSL biodiesel blends for optimum piston bowl design cases 1 and 2.

These results are 2.32, 2.44, 2.50, 2.61, and 2.77g/kg-fuel, respectively, for optimum piston bowl 1, while optimum bowl design case 2 recorded 2.32, 2.44, 2.50, 2.61 and 2.77 g/kg-fuel, respectively. It can be observed from the figure that NOx emission increases with the increasing proportion of CNSL biodiesel for the optimum bowl 1 and 2 configurations. A few studies have reported similar findings (Varatharajan, Cheralathan and Velraj, 2011; Khan, Panua and Bose, 2019; Kafrawi et, al. 2022).

In Figure 7.11, NO mass fractions at 15° crank angle ATDC have been shown for optimum bowl design cases 1 and 2 operated with diesel and CNSL biodiesel blends (B10, B20, B30, and B50). When comparing case 2 of the optimum piston bowl configuration to case 1, a broader area of high NO regions is observed. An increase

in NO emissions from the combustion chamber has also been observed with the addition of biodiesel blends. It is observed that CNSL biodiesel addition increases NO levels as more is introduced into the combustion chamber.

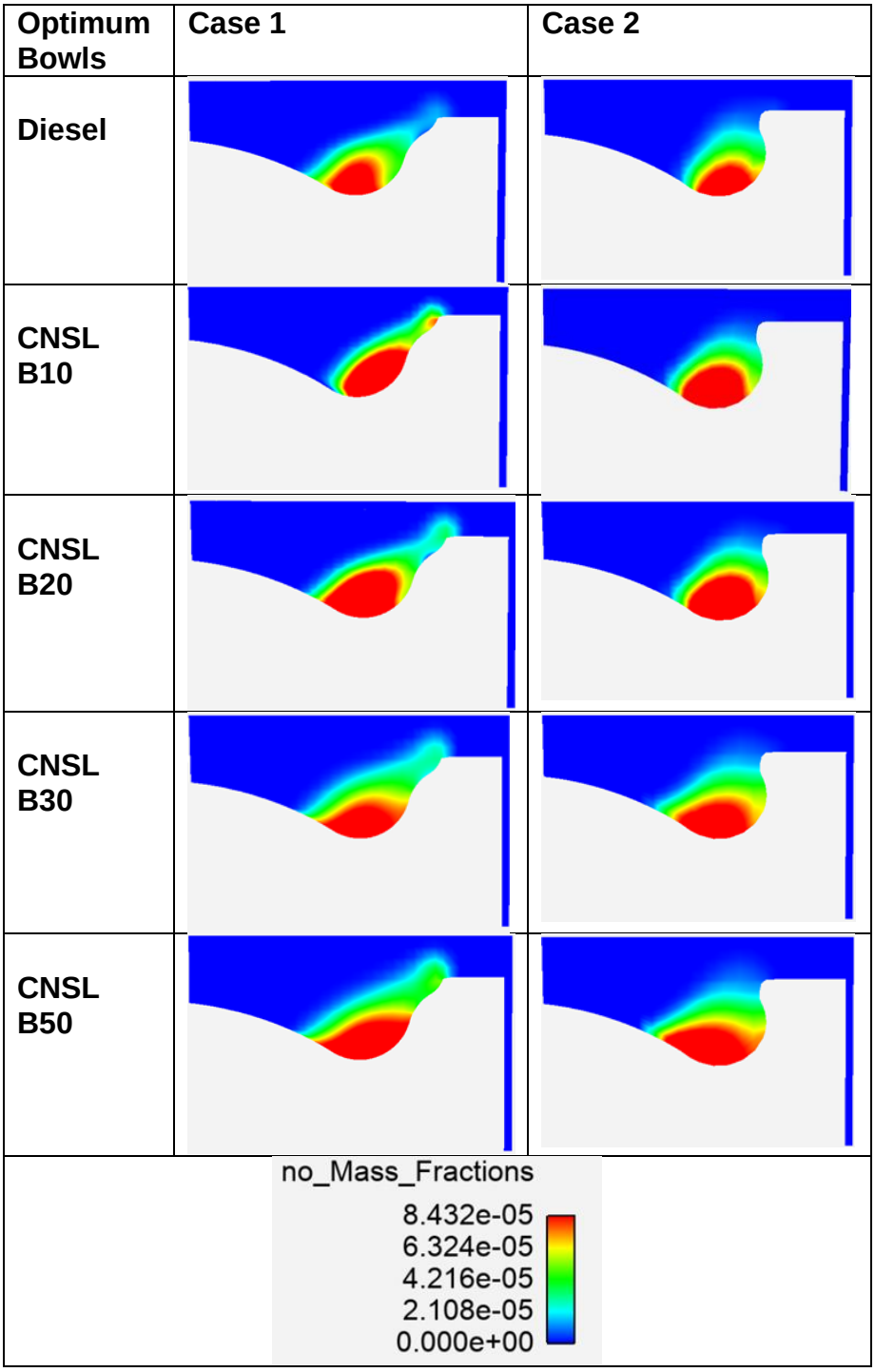

Figure 7.11. NO mass fraction distribution in a cross-section view of the optimum bowl design cases 1 and 2 at 10° after ATDC with different petroleum diesel and CNSL blends.

7.3.4. Soot emissions

Figure 7.12 shows the soot production at 1200 rpm for the optimal piston bowl design cases 1 and 2, with petroleum diesel, and various CNSL biodiesel blends. According to the figures, increasing the proportion of CNSL biodiesel increases soot emission levels because of its high density, kinematic viscosity, low compressibility, and poor air-fuel mixing (Buyukkaya, 2010; Kalam et, al. 2011). The soot emissions in Figure 7.12 show petroleum diesel and CNSL biodiesel (B10, B20, B30, and B50) biodiesel blends, with results of 99 x 10^{-5}, 1.03 x 10^{-5}, 1.06 x 10^{-5}, 1.08 x $10^{-5,}$ and 1.12 x 10^{-5} g/kg-fuel, respectively, for optimum piston bowl 1. The optimum bowl design case 2 recorded marginal increases of 104 x 10^{-5}, 1.12 x 10^{-5}, 1.14 x 10^{-5}, 1.15 x 10^{-5}, and 1.16 x 10^{-5} g/kg-fuel, respectively compared to case 1.

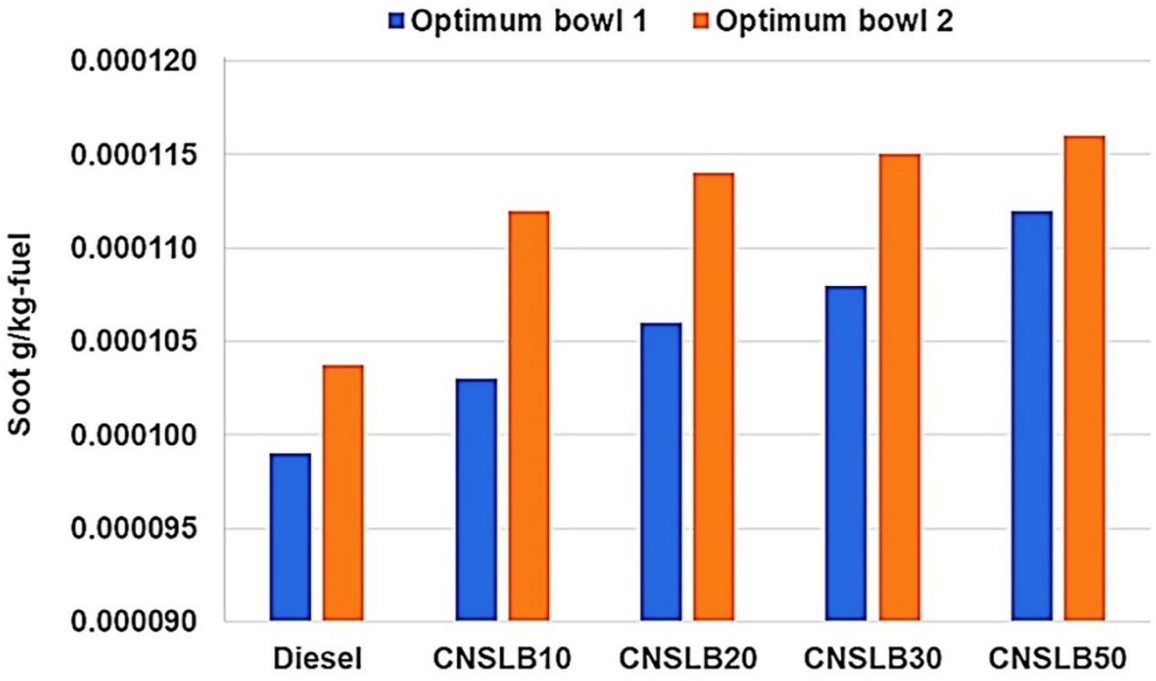

Figure 7.12 Soot emissions for diesel and CNSL biodiesel blends for optimum bowl design cases 1 and 2.

As a result of air-fuel mixing, local temperatures play a major role in soot oxidation. It has been found that piston bowls that have been redesigned produce less soot and oxidizes faster (Khan, Panua and Bose, 2019; Simsek, 2020). A modified piston bowl might have more air entrainment, which could cause greater oxidation than a standard piston bowl (Khan, Panua and Bose, 2019).

7.4. Engine performance

7.4.1 Gross indicate power and Gross indicated specific fuel consumption

A comparison of gross indicated power (GIP) and gross indicated specific fuel consumption (GISFC) is shown in Figure 7.13 (a) and (b) respectively for optimum piston bowl cases 1 and 2 for diesel and CNSL (B10, B20, B30, and B50) biodiesel blends is shown. With more CNSL biodiesel addition, indicated power decreases, while GISFC increases proportionately.

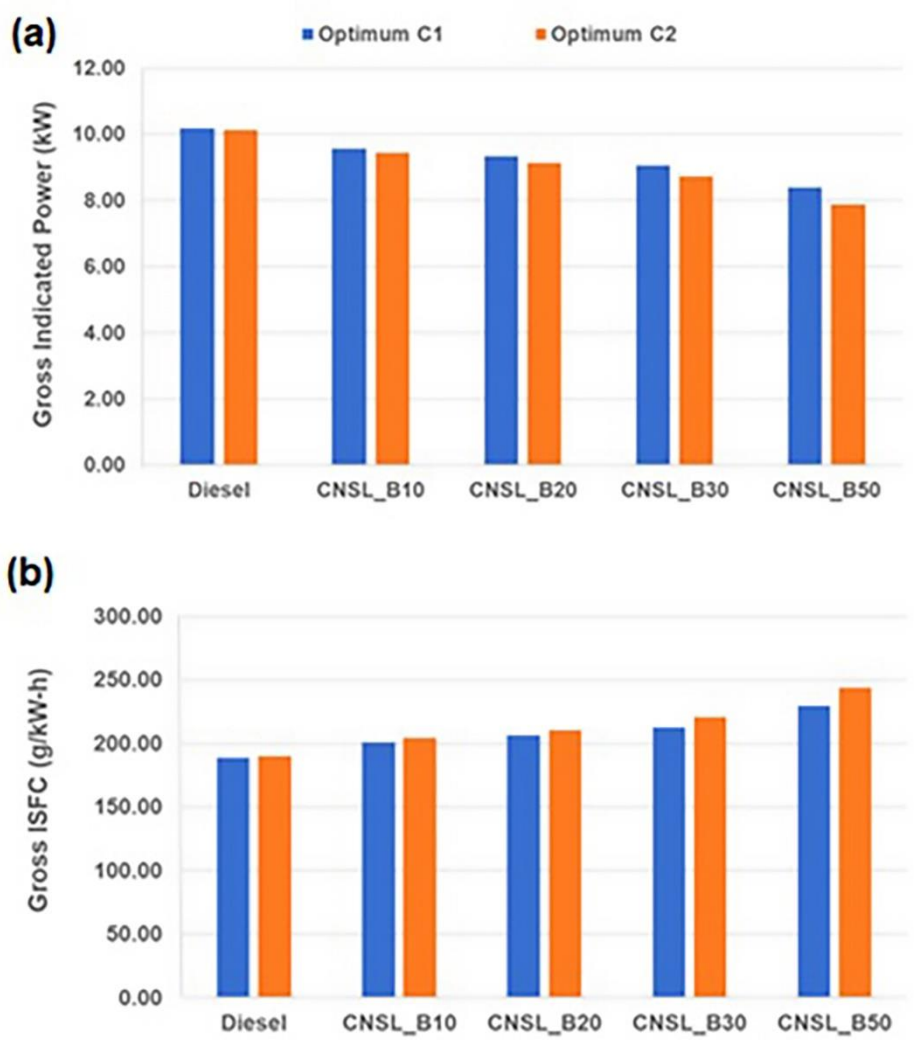

Figure 7.13. (a) Gross Indicate Power and (b) Gross Indicated Specific Fuel Consumption for petroleum diesel and CNSL biodiesel blends for optimum bowl design in cases 1 and 2.

When the gross indicated power for diesel was 9.96 kW and 9.79 kW for optimum bowl design cases 1 and 2, respectively, CNSL Biodiesel B10, B20, B30, and B50 decreased at 3.9%, 7.02%, 9.6%, and 15.9% concurrently in comparison to diesel for optimum case 1. When compared to diesel performance for optimum bowl case 2, the reduction is 5.5%, 8.8%, 12.4%, and 19.7% respectively. Based on Figure 7.13 (a), it can be observed that increasing the proportion of CNSL biodiesel in the blend reduces the indicated power of the engine (Khan, Panua and Bose, 2019).

In optimized bowl case 1, the engine power is marginally higher due to improved fuel-air mixing and more complete combustion than in case 2. The gross indicated specific fuel consumption (GISFC) is an important parameter that reflects the performance of an engine operation (Heywood, 2018). As heating value of CNSL biodiesel is lower compared to mineral diesel, therefore, increasing the proportion of CNSL biodiesel in the blends results in a lower heating value of the fuel, and hence GISFC increases (Dinesha and Mohanan, 2015).

Figure 7.13 (b) shows variation in GISFC with respect to fuel blends for optimum piston bowl cases 1 and 2 for diesel and CNSL (B10, B20, B30, and B50) biodiesel blends. The GISFC in Figure 7.13 (b) shows petroleum diesel and CNSL biodiesel blends (B10, B20, B30, and B50), with results of 193.4, 201.2, 207.3, 214.1, and 230.1 g/kW-h, respectively, for optimum piston bowl 1. The optimum bowl design case 2 recorded marginal increases of 196.76, 204.78, 212.19, 220.98, and 240.84 g/kW-h, respectively, compared to case 1. The GISFC for optimum bowl case 2 is marginally higher than that of optimum bowl case 1 for all fuel blends due to improved fuel-air mixing and more complete combustion for case 1. The lower GISFC of optimum piston bowl case 1 may be attributed to more efficient fuel utilisation due to increased turbulence, as fuel-air mixing leads to more complete combustion. When diesel mixed with CNSL biodiesel to make blends, it is found that the more percentage of CNSL biodiesel in the blends, the higher of the viscosity and the lower the gross calorific value. Pure CNSL biodiesel has the lowest gross calorific value and the highest viscosity.

7.4.2. Indicated thermal efficiency

Figure 7.14 shows the variation of Indicated thermal efficiency (ITE), where with optimum piston bowl case 1, the ITE decreases by 4.7%, 7%, 7%, and 11.6% respectively for CNSL biodiesel blends (B10, B20, B30, and B50) as the volume of blends increases compared to petroleum diesel. Similarly, ITE decreased by 4.8%, 4.8%, 9.5%, and 14.3% for optimum piston bowl case 2 when compared to diesel. It is observed that the thermal efficiency generally decreases as compared to diesel when all the CNSL biodiesel fuel blends are increase.

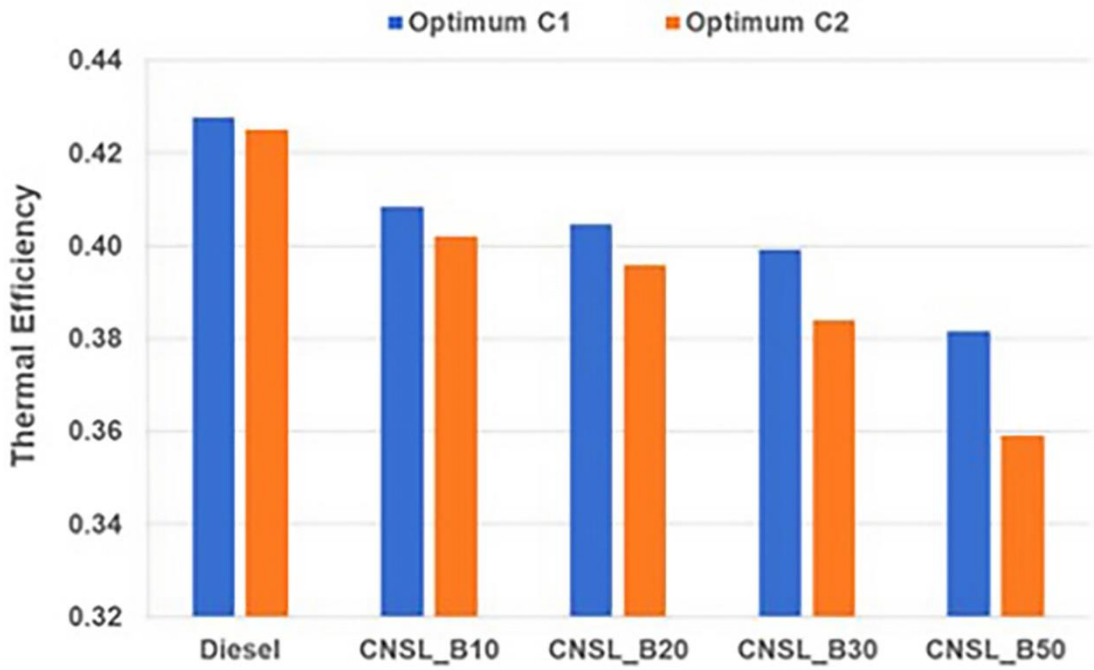

Figure 7.14. Indicate thermal efficiency (ITE) for petroleum diesel and CNSL biodiesel blends for optimum bowl design in cases 1 and 2.

The higher viscosity and lower evaporation of the CNSL biodiesel leads to the formation of large droplets during atomization, resulting in insufficient mixing of air and fuel, thus a reduction in thermal efficiency (Qi et al., 2010; Saravanan, 2015). The thermal efficiency of CNSL biodiesel is lower compared to diesel; and this may be due to the higher fuel viscosity, density, and higher latent heat of vaporization required to initiate combustion (Saravanan, 2015; Channapattana, Pawar and Kamble; 2017). A similar trend is observed in other studies which is in-line with this study (Saravanan, 2015; Channapattana, Pawar and Kamble; 2017; Srihari, Thirumalini and Prashanth 2017).

7.5. Evaluation of the regression model

7.5.1. The effect of parameter on the responses

A variety of response variables were varied in the simulation runs for the model. To determine the impact of explanatory variables on response variables, analysis of variance (ANOVA) was performed on the simulation findings. The interaction effect of piston bowl design (PBD), start of injection (SOI) spray included angle (SIA) and biodiesel on the response parameter such as Gross Indicated Specific Fuel Consumption (GISFC), Nitrogen oxide (NOx), soot, Gross Indicated Power (GIP), Carbon Monoxide (CO) and Unburnt Hydrocarbons (UHC) were used to calculate the regression coefficients and the t value for different response parameters of the model. The model is significant as the t value is more than 1.96 (Shi, and Reitz, 2008).

Results in Table 7.3 show that spray included angle (SIA) had a significant positive effect ($p<0.05$) on GISFC, NOx, soot emission, CO, and UHC. This means that an increase in spray-included angle may lead to high fuel consumption and adversely increase pollutant emissions (Shu et al., 2019). The indicated power may, however, decrease when the SIA is increased. PBD and SOI negatively affected NOx. Besides, SOI had a negative impact on soot emissions, CO, and UHC. On the contrary, PBD has a positive impact on CO. This explains that an increase in the piston bowl and the start of injection decrease nitrogen oxides. The result further indicates that to decrease emissions such as carbon monoxide, unburnt hydrocarbon, and soot emissions significantly, the start of injection is a matter of concern. On the other hand, increasing the geometry of the piston bowl is likely to increase carbon monoxide (Yoon et al., 2010). In addition, biodiesel significantly increases nitrogen oxides but negatively impacts indicated power. Thus, increasing biodiesel is likely to increase nitrogen oxide, but decrease gross indicated power (Shu et al., 2019).

7.5.2. Interaction effect of parameter on responses

The interaction between biodiesel and piston bowl design produces favourable and significant effects on GISFC, CO, and UHC. It does, however, have a major detrimental impact on GIP. This suggests that the combined impact of increased biodiesel and piston bowl design is expected to increase specific fuel consumption, carbon monoxide production, and unburned hydrocarbon production. However, it's

likely that these interactive factors will lower the engine's reported power. Additionally, the combined effect of biodiesel and the beginning of injection showed a notable favourable effect on soot emission, carbon monoxide, and unburned hydrocarbons. This explains why a higher biodiesel content and the beginning of injection settings are more likely to contribute to high vehicle emissions (Ganji et al., 2017). On the other hand, the combined impact of biodiesel and the spray-included angle showed a detrimental, significant influence on nitrogen oxide and soot emissions. This shows that a high biodiesel percentage and a high spraying angle for advanced applications will probably reduce nitrogen oxide and soot emissions. Response variables are not significantly affected by some factors. As a result, it can be said that the parameters have very little influence on the response variables and can be ignored (Shi and Reitz, 2008).

Table 7.3. Regression analyses for parameters

Parameter	GISFC (kWh [g])			NOx (kg-fuel [g])			Soot (kg-fuel [g])		
	Stand. Coefficient	t-value	p-value	Stand. Coefficient	t-value	p-value	Stand. Coefficient	t-value	p-Value
PBD	.000	-.009	.993	-.271	-2.701	.009	.124	.637	.527
SOI	-.077	-1.255	.214	-.489	-3.737	.000	-.778	-3.056	.003
SIA	.304	6.209	.000	.899	8.650	.000	.921	4.557	.000
BD	.063	.142	.888	1.971	2.083	.041	3.256	1.770	.082
PBD*SOI	-.066	-.576	.567	.055	.223	.824	-.096	-.202	.841
PBD*SIA	.087	.785	.436	-.057	-.240	.811	.018	.039	.969
PBD*BD	.474	5.731	.000	.174	.989	.327	-.121	-.353	.725
SOI*SIA	-.010	-.179	.859	-.127	-1.023	.310	.015	.060	.952
SOI*BD	.118	.657	.513	.250	.653	.516	1.991	2.675	.010
SIA*BD	.323	.786	.435	-2.780	-3.183	.002	-5.390	-3.173	.002

Table 7.3.(cont.) Regression analyses for parameters

Parameter	**GIP (kW)**			**CO (g/kg-fuel)**			**UHC (g/kg-fuel)**		
	Stand. Coefficient	t value	p-value	Stand. Coefficient	t value	p-value	Stand. Coefficient	t value	F-Value
PBD	-.050	-1.204	.233	.179	2.171	.034	-.004	-.048	.962
SOI	.069	1.282	.205	-.278	-2.576	.012	-.261	-2.654	.010
SIA	-.388	-9.085	.000	.412	4.811	.000	.302	3.870	.000
BD	-.768	-1.976	.053	-.447	-.574	.568	-1.008	-1.420	.161
PBD*SOI	.025	.250	.804	.186	.926	.358	.084	.456	.650
PBD*SIA	-.043	-.446	.657	-.140	-.719	.475	-.030	-.168	.868
PBD*BD	-.374	-5.180	.000	.615	4.248	.000	1.072	8.130	.000
SOI*SIA	.021	.401	.690	-.083	-.812	.420	-.056	-.597	.553
SOI*BD	-.105	-.668	.507	1.511	4.796	.000	1.436	5.003	.000
SIA*BD	.289	.806	.423	-.802	-1.115	.269	-.573	-.874	.385

7.5.3. Model fitting

The R-squared (R^2) is a statistical measure that represents the proportion of variance in the response variable (the variable the model is trying to predict) that is explained by the parameters (the factors the model considers). In this case, the result in Table 7.4 indicates that the model tested is statistically significant and the variance explained in the response variables spans from 48% to 98%, which suggests that the model's performance varies across different response variables. The R^2 of 0.48 explained in response variable, Soot (kg-fuel[g]) emission implies that the model reasonably predicted 48% of soot emission with 52% unexplained. According to other studies, R^2 value greater than 0.10 (10%) indicates an improved and acceptable model fit (Ulfarsson, Kim and Booth, 2010; Ganji et al., 2017; Raihan et al., 2022). Therefore, the variance explained in the soot emission is within the acceptable fit threshold.
Conversely, model explains a substantial variance in GISFC (kW-h [g]), NOx (kg-fuel [g]), GIP(KW), CO(g/kg-fuel), UHC (g/kg-fuel). This suggests that the model is exceptionally good at capturing and predicting the response variables, leaving only a small fraction of the variance unexplained. Over all, the observed results are meaningful and not just the result of chance. In practical terms, this means that the model's predictions power is not arbitrary but have a basis in the data.

Table 7.4. Model fitting

Model	GISFC (kW-h [g])	NOx (kg-fuel [g])	Soot (Kg-fuel [g])	GIP (kW)	CO (g/kg-fuel)	UHC (g/kg-fuel)
R^2	0.970	0.863	0.481	0.977	0.907	0.923
Adjusted R^2	0.965	0.840	0.396	0.973	0.892	0.910
Predicted R^2	0.985	0.929	0.694	0.988	0.952	0.961

7.5.4. Interaction effect on GISFC

The interactive effects of piston bowl design and biodiesel on GISFC are shown in Figure 7.15. The increase in bowl design and biodiesel increases the GISFC. Specifically, the combination of piston bowl design and biodiesel resulted in an increase in gross indicated specific fuel consumption (Shi and Reitz, 2008).

7.5.5. Interaction effect on Nitrogen oxide

A study found that late injection consistently reduced NOx emissions by marginal amounts (Shu et al., 2019). A wider spray angle combined with low biodiesel results in increased NOx, as shown in Figure 7.16. This contrasts with the combination of high biodiesel and a narrow spray angle that reduces NOx emissions (Ganji et al., 2017).

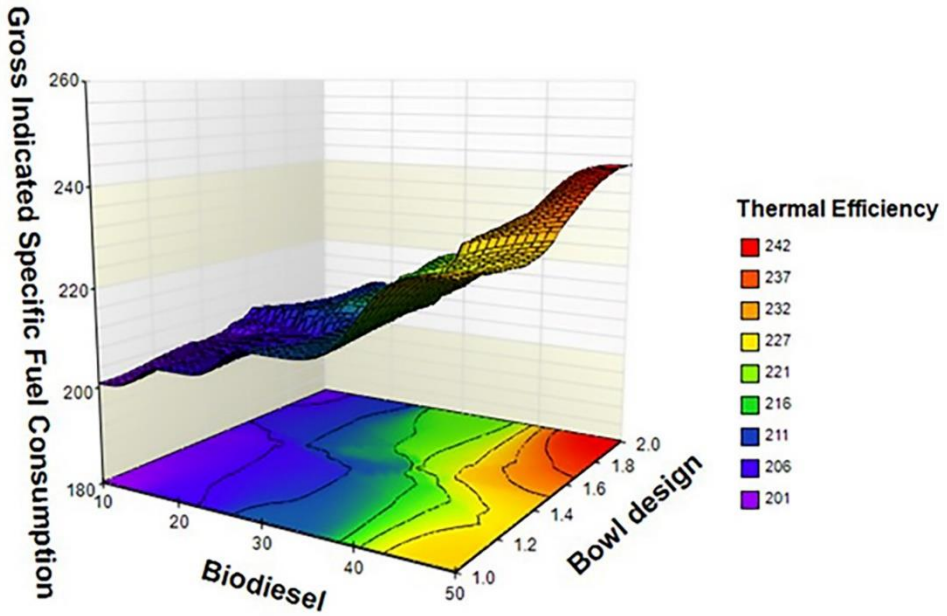

Figure 7.15. GISFC variations against bowl design and biodiesel

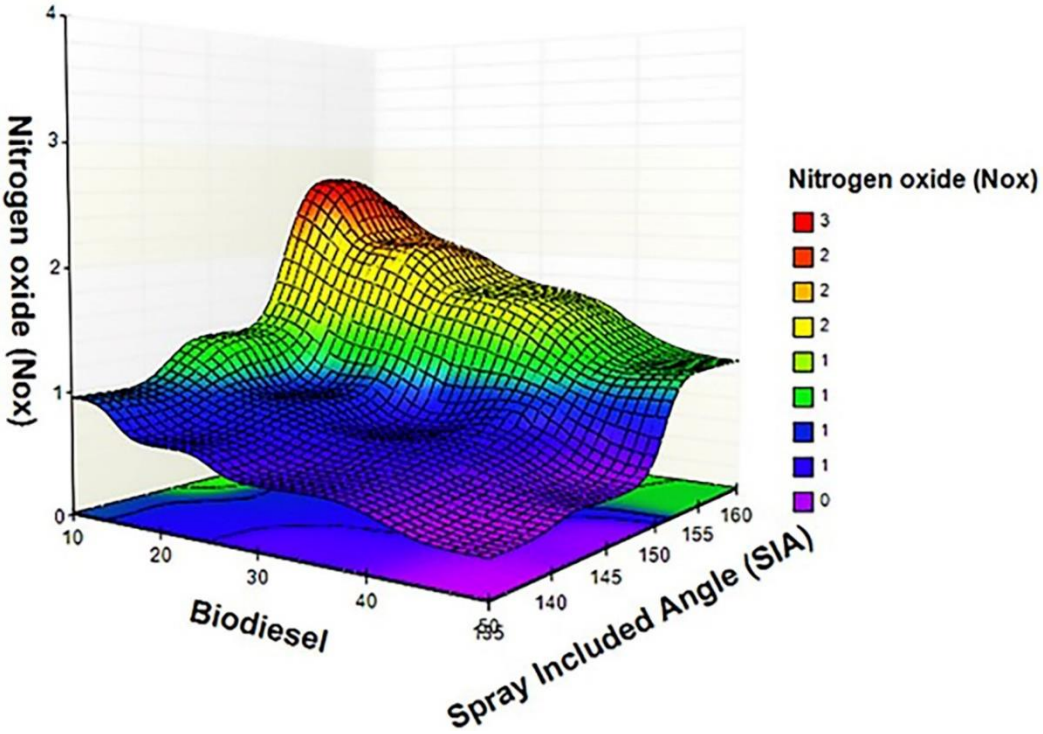

Figure 7.16. Nitrogen oxide variations against Biodiesel and SIA

7.5.6. Interaction effect on Soot

A decrease in biodiesel results in an increase in soot emissions, as shown in Figure 7.17. Subsequently, soot emissions appear to remain constant at low levels, regardless of the spray-included angle or injection time. Therefore, advanced injection timing and starting injection at both narrow and wide angles reduced soot production as shown in Figure 7.18 (Shu et al., 2019).

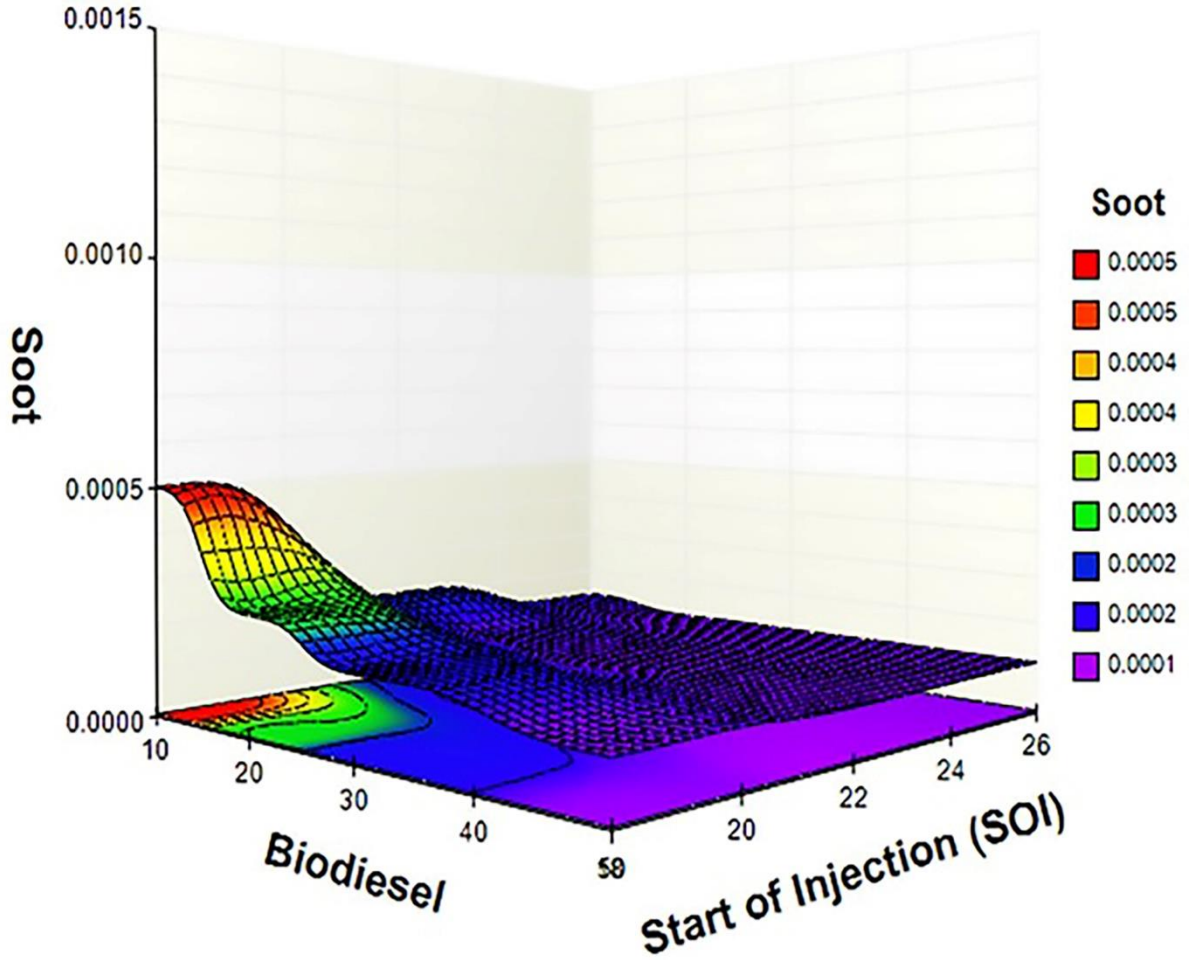

Figure 7.17. Soot variations against biodiesel and SOI

7.5.7. Interaction effect on Gross Indicated Power

An optimized piston bowl design and low biodiesel are key factors in achieving high indicated power, as shown in Figure 7.19. On the other hand, increasing biodiesel and optimized piston bowl designs show increasing trends in indicated power. A study also found that optimum engine performance was achieved with a 126° included-spray angle and an optimized injection strategy.

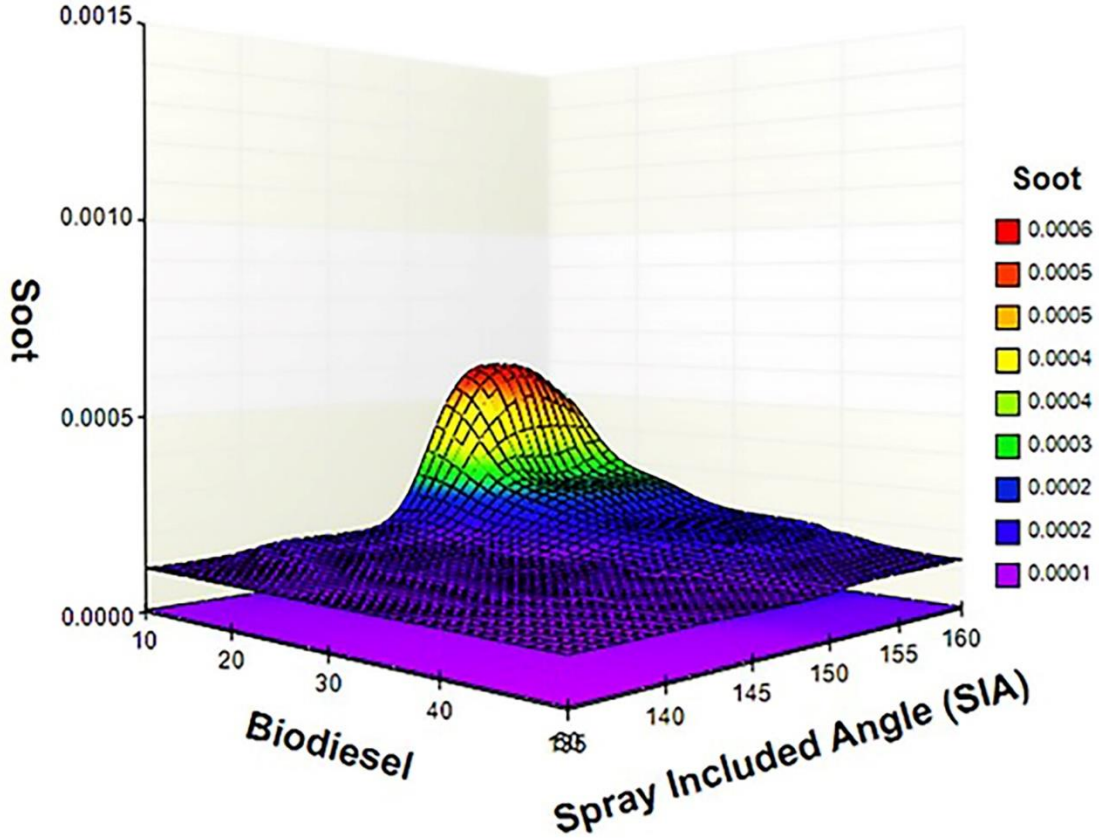

Figure 7.18. Soot variations against SOI and SIA

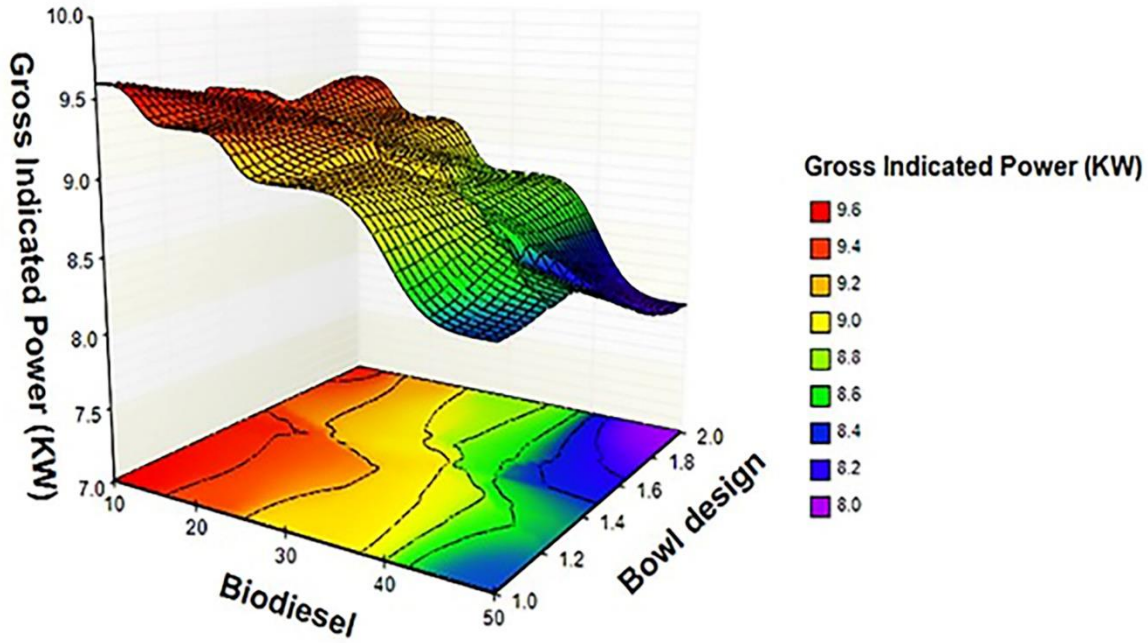

Figure 7.19. Indicated power variations against biodiesel and bowl design

7.5.8. Interaction effect on carbon monoxide

As a sustainable and renewable replacement for conventional fossil fuels, biodiesel can reduce greenhouse gas emissions and address climate change. In spite of this, biodiesel fuel may burn differently than petroleum-based fuels, resulting in pollution emissions like carbon monoxide (Kumar et al., 2018). A combination of biodiesel and the piton bowl design reduces carbon monoxide as seen in Figures 7.20 and 7.21. As a result of raising the biodiesel content, moving forward the injection time, and adjusting the piston bowl design, carbon monoxide levels increase. Based on the significant interaction between biodiesel, the start of injection, and the piston bowl form, these elements may enhance the amount of carbon monoxide emissions from an engine. There may be a reason for this, as biodiesel fuel has special combustion properties that require careful injection timing to optimize combustion and minimize emissions (Ghobadian and Kiani, 2014; Sathiyamoorthi and Sankaranarayanan, 2015).

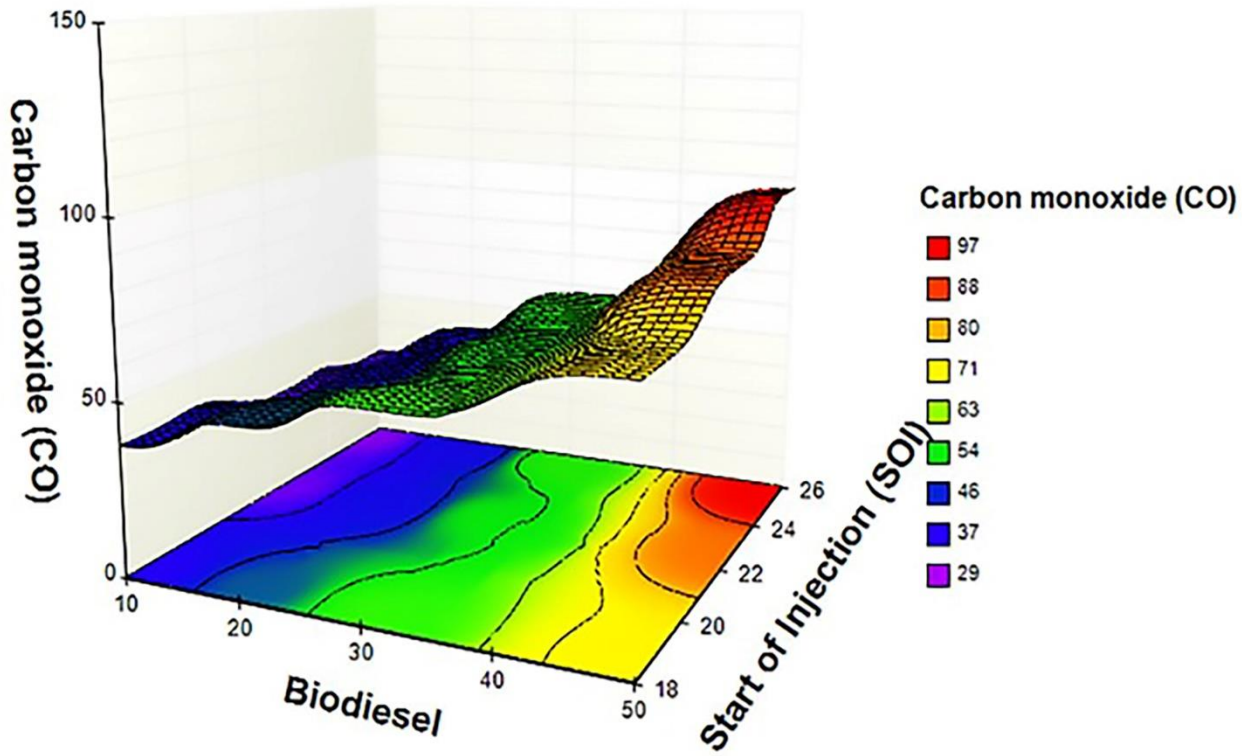

Figure 7.20. Carbon monoxide variations against Biodiesel and SOI

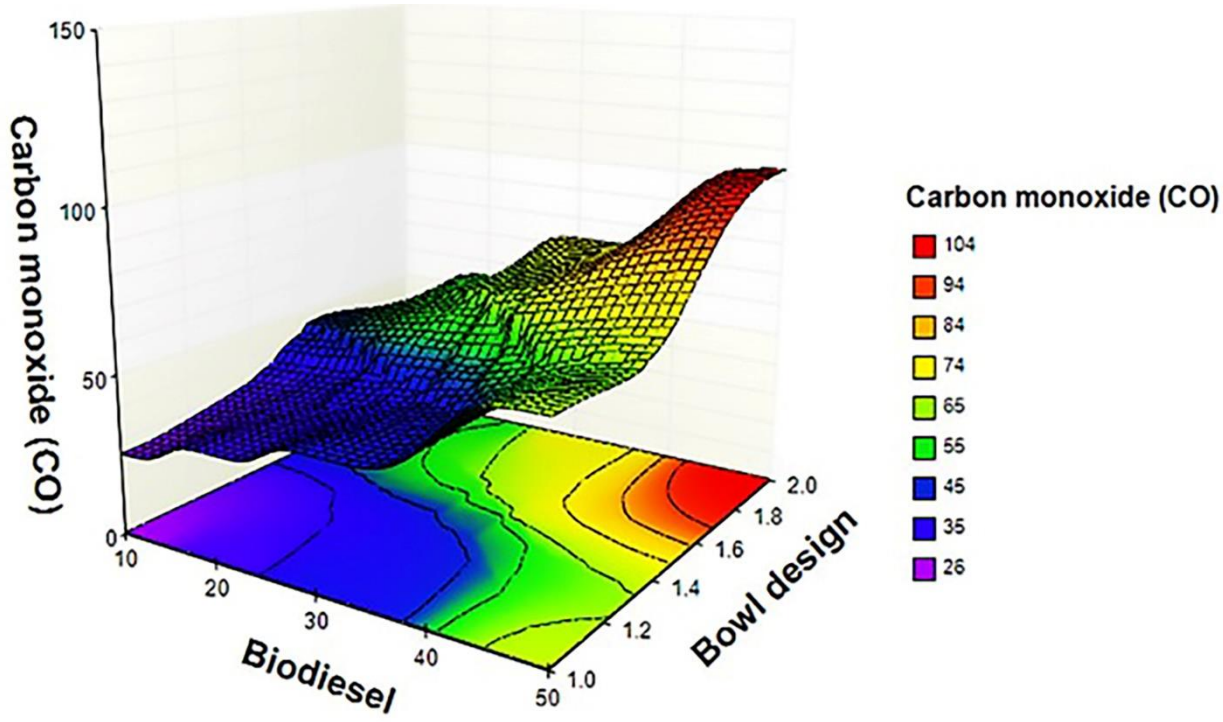

Figure 7.21. Carbon monoxide variations against Biodiesel and bowl design

7.5.9. Interaction effect on unburnt hydrocarbon

Figures 7.22 and 7.23 show the outcome of the combined impact of biodiesel with piston bowl design and injection commencement on unburned hydrocarbons. Increasing biodiesel and modifying the piston bowl design, along with delaying injection, resulted in an increase in unburned hydrocarbons. This explains how the interaction of these three variables may result in insufficient fuel combustion, which generates unburned hydrocarbon emissions. Unburned hydrocarbon levels decrease with low biodiesel levels, delaying SOI through optimize piston bowl design. The findings show that a combination of low biodiesel and piston bowl design is necessary to achieve the reduction of unburned hydrocarbons and enhance fuel efficiency (Ghobadian and Kiani, 2014; Ganji et al., 2017).

It is possible that biodiesel fuel produces a unique mixture of air and fuel, requiring a specific timing for injection to optimize combustion and lower emissions. The fuel is injected later in the combustion process; however, if the injection process is delayed, it may result in a shorter combustion time (Shu et al., 2019). This can therefore result in incomplete combustion and an increase in emissions of unburned hydrocarbons. Furthermore, the particular piston bowl shape tailored to biodiesel fuel might not work

with a later injection timing. As a result, fuel and air may not mix well, and combustion may be incomplete, which may result in increased unburned hydrocarbon emissions (Shi and Reitz, 2008; Ganji et al., 2017).

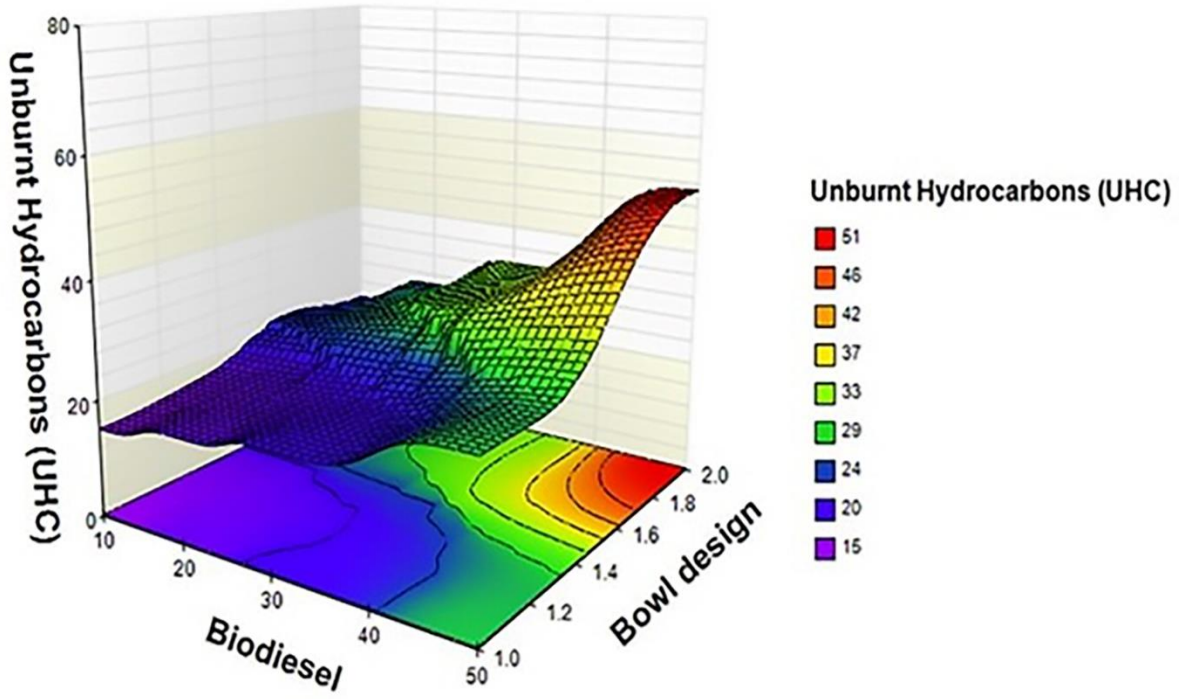

Figure 7.22. Unburnt Hydrocarbon variations against Biodiesel and bowl design

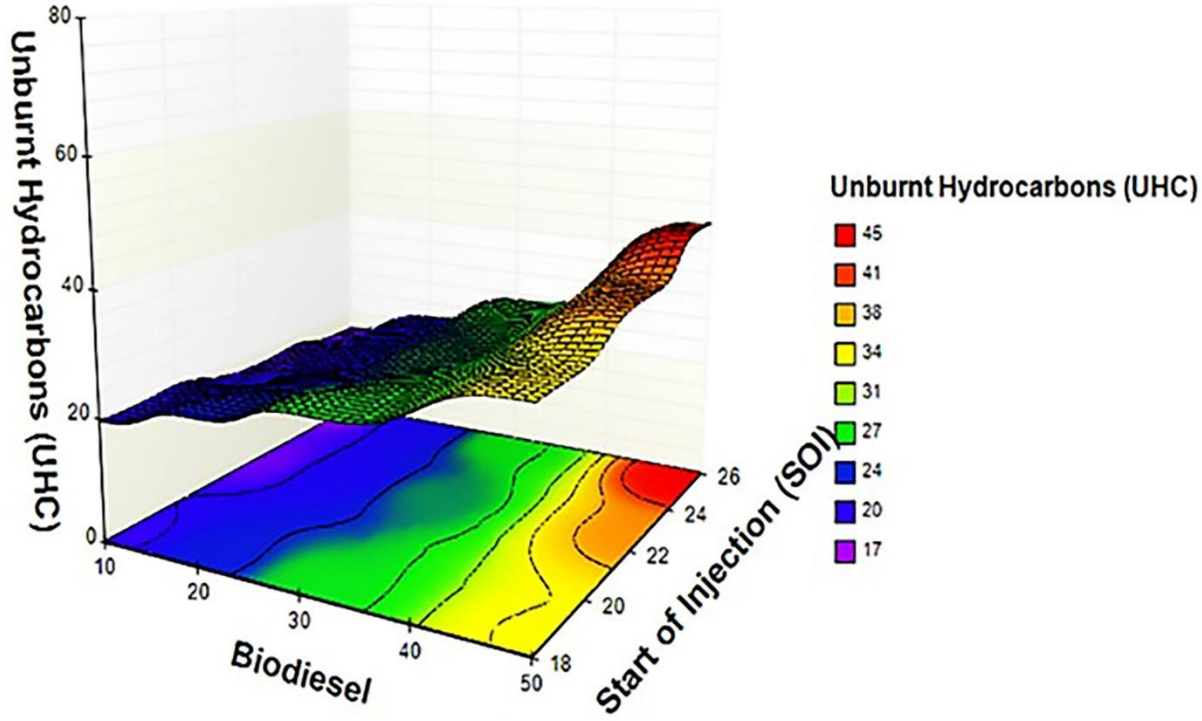

Figure 7.23. Unburnt hydrocarbon variations against biodiesel and SOI.

7.5.10. Model validation

In Table 7.5, standards are compared with regards to baseline setup and the optimized model. In order to ensure that the outcomes were accurate, a comparison was conducted. There was a significant decrease in indicated power, nitrogen oxide, and soot emission between baseline engine performance and the optimized case. When fuel consumption, CO, and unburned hydrocarbons are given, the optimized case is more efficient than the baseline engine. As a result of these findings, the normal model configurations outperformed the experimental configurations in terms of pollutant indicators, soot emissions, and nitrogen oxide emissions.

Table 7.5. Comparison of optimized and baseline cases

Parameters and Responses	**Standard vale**	**Experimental value**	**Difference in value**	**t value**	**Sig. (2-tailed)**
Gross Indicated Power (GIP)	9.58 kW	8.9756	-0.60444	-8.939	0.000
Gross Indicated Specific Fuel Consumption (GISFC)	201.02 g/kg-fuel	215.4826	14.46264	8.552	0.000
Carbon Monoxide (CO)	30.62	54.4767	23.85667	7.359	0.000
Unburnt Hydrocarbons (UHC)	16.09	26.3522	10.26222	7.382	0.000
Nitrogen oxide (NOx)	2.98	1.0956	-1.88444	-18.113	0.000
Soot	0.00022 g/Kg-fuel	0.00017369	-0.000046306	-1.963	0.054
Piston bowl design	0.000	1.50	1.500	-0.980	0.331
Start of injection	22.5	22.167	-0.3333	-0.980	0.331
Spray included angle	152	146.00	-6.000	-6.192	0.000
Biodiesel	1.000	27.50	26.500	15.097	0.000

When compared to experimental values, emissions, the comparison of standards with regards to baseline setup and an optimized model is explained in parameters that were

low compared to standard values. This indicates that the outcome was consistent with the optimized or experimental outcomes. In terms of injection start and spray-included angle, experimental designs performed worse than regular engine configurations based on the parameters measured. In contrast, biodiesel and piston bowl designs demonstrate improved results.

7.5. Summary

In terms of its characteristics, CNSL-produced biodiesel is similar to diesel. The reduced calorific value, higher viscosity, and higher density, and heavier molecules of CNSL biodiesel fuel decrease its performance as compared to petroleum diesel. The impact of combustion chamber geometry on the combustion and emission variables in a diesel engine powered by CNSL biodiesel blended with diesel has been modelled and investigated numerically. When the engine runs at a constant speed of 1200 rpm, the comparison between two optimized combustion chamber bowl geometries is done in terms of cylinder pressure, heat release rate, the temperature distribution in the combustion chamber, and emissions characteristics. In summary, the results were as follows:

i. A systematic mechanism reduction technique has been developed to add precise and detailed kinetics to engine CFD simulations. By converting master mechanisms into surrogate fuel mechanisms, the method can condense master mechanisms to the smallest possible amount with comparable accuracy. The technique produced a reduction of over 90% while keeping predictions accurate to a predetermined level.
ii. The combustion results show that the in-cylinder pressure, temperature, and apparent heat release rate of petroleum diesel are higher and decrease with the CNSL biodiesel concentration increasing from 10% to 50%.
iii. In comparison with petroleum diesel, CNSL biodiesel emits fewer unburned hydrocarbons (UHC). This is because biodiesel contains more oxygen atoms than regular diesel fuel, which helps it burn more efficiently in combustion chambers. The optimal bowl design in case 2 recorded a slightly higher UHC than in case 1.

iv. The emission of NOx from CNSL biodiesel blends is marginally higher than that from petroleum diesel; it can also be observed that NOx emission increases with the increasing proportion of CNSL biodiesel for the optimum bowl 1 and 2 configurations. The optimized piston bowl in case 1 shows high NOx for all the blends compared to case 2. This is primarily due to the fuel-bound oxygen content in biodiesel blends, which results in a lean-fuel combustion process.

v. Within the operational limit, conventional diesel engines can utilise B10 and B20 CNSL biodiesel and petroleum diesel blend as alternative fuels without requiring significant engine modifications. When compared to petroleum diesel, the CO and UHC of CNSL biodiesel blend emissions are lower. A greater reduction in CO and HC emission is attained as the blend proportion is raised.

vi. As CNSL biodiesel was added to the blends, the gross indicated specific fuel consumption (GISFC) increased significantly. This is because CNSL biodiesel has a lower heating value than standard petroleum diesel. However, modified optimize case 1 combustion chamber shows slightly improved GISFC.

vii. A larger spray-included angle and advanced injection increased NOx emissions and reduces soot emissions and GISFC.

viii. The interaction effects of the optimized piston bowl, spray-included angle, and start of injection were dominant for the responses of NOx and soot emissions.

CHAPTER 8

Conclusions and recommendations for future work

This work investigates cashew nut shell liquid (CNSL) as an inedible feedstock for biodiesel production and potentially for use as an alternative fuel in conventional diesel engines. The study further numerically models and simulates the combustion and emissions characteristics of a direct injection compression ignition heavy-duty engine fuelled with CNSL biodiesel. The model also incorporates realistic physical properties in a vaporization model developed for multicomponent fuel sprays in addition to an improved mechanism for CNSL biodiesel combustion chemistry. As a summary of this study, the research findings, conclusions, and recommendations for future works are as follows.

8.1. Conclusions

8.1.1. Conclusions on inedible cashew shell nut liquid (CNSL) as biodiesel

In the study of CNSL biodiesel as a fuel alternative, the following conclusions were drawn:

i. The empty shells of cashew nuts, where inedible CNSL is extracted, are regarded as agricultural and industrial waste. The inedible CNSL, which is touted as a promising, readily accessible, affordable, environmentally responsible, and renewable fuel for biodiesel production, can lessen the heavy reliance on petroleum diesel. This can significantly reduce the demand for fossil fuels, thereby reducing carbon footprints and mitigating global warming. This also supports long-term socioeconomic development for rural communities and the livelihoods of small-holding farmers.

ii. Cashew apple post-harvest waste is widespread in cashew plantations around the world, and it has the potential to be converted into bioethanol for transesterification of CNSL methyl ester into biodiesel or directly blended with gasoline for use in spark ignition engines.

iii. According to the study, it is established that globally, cashew plants are grown throughout the year in regions between 23° North and 23° South of the Equator, where solar energy is readily available. It is possible to process cashew nuts

with their shells, extract CNSL, and refine it into CNSL biodiesel using solar energy technology.

iv. The cashew industry generally uses the waste empty shells of cashew nuts as a cheap, reliable, and sustainable energy source after the extraction of CNSL. This is used to run boilers and to make briquettes that can be used for other energy needs, like traditional home energy sources.

v. The CNSL biodiesel meets ASTM biodiesel standards; and when modified, its viscosity, flash point, cetane number, and calorific value match petroleum diesel for use in heavy duty DICI engines. The use of this energy source in the mix of energy sources is the subject of numerous research and development initiatives.

vi. According to the economic analysis, CNSL is a cheap feedstock for creating biodiesel, and integrating its use in diesel engines will help prevent unnecessary expenses associated with biodiesel production. Additionally, using thermal and chemical extraction methods is more effective because of the higher yield; as a result, the cost of making CNSL biodiesel is low when compared to other feedstocks.

vii. The CNSL biodiesel fuel can be used as a fuel for CI engines since, after modification, its viscosity, flash point, and calorific value are comparable to those of diesel fuel.

8.1.2. Conclusions on the impact of piston bowl designs and injection parameters on combustion and emission characteristics

In this study, the combustion, performance, and emission characteristics of the base bowl and five modified piston bowl designs in low-temperature combustion direct injection compression ignition (DICI) heavy-duty engines are simulated using a reduced normal heptane (n-heptane) kinetic mechanism as a fuel surrogate. The numerical CFD model developed in this study has been validated with the measured data from the base bowl design and in-cylinder pressure was compared to ensure accuracy. The measured data demonstrated a significant and reasonable agreement with the modified bowl design cases 1, 2, 3, 4, and 5, which were used to investigate combustion, performance, and emission characteristics. The following are the summary of the conclusions:

i. In cases 1, 3, 4, and 5, the piston bowl design has a high TKE due to the throat diameter and toroidal radius of the piston cavity, which enhances fuel-air mixing and concentrates airflow in the combustion chamber. As a result of TKE-generating bowl geometries, CO emissions are typically lower and NOx emissions are increased. When the right bowl geometry is used, NOx emissions can be reduced simultaneously, and CO emissions can be reduced as well. The combustion process requires good turbulence velocity and a high TKE at the end of the compression stroke. In case 1, turbulence velocity was 382.39 cm/s; in cases 2, 4, and 5, TKE was higher, resulting in better combustion. In addition, this study has shown that in-cylinder pressures, temperatures, and heat release values are directly affected by rapid turbulence and squish.

ii. The results showed that out of the bowl designs, cases 3, case 4 and 5, with piston curved toroidal inside shape, produced better combustion and emissions performance when compared to other designs. The results led to the conclusion that these bowl designs are effective. Several essential features such as the impingement region, pip curves, and pip heights, as well as the provision for a homogeneous mixture, which directly affects performance, are incorporated into them.

iii. According to the results, the gross indicated power (GIP) for bowl design cases 1, 2, 3, and 5 is marginally high compared to the base bowl design. In contrast, the gross indicated specific fuel consumption (GISFC) for these bowl design cases is marginally lower than for the base bowl design.

iv. With a favourable air-fuel mixture, due to the internal design features of bowl cases 2, 3, and 4, the record showed less than 22% CO compared to the base bowl design. However, bowl design cases 3 and 4 recorded 10% less UHC compared to the base bowl design. The other bowl designs had marginally higher CO and unburned hydrocarbons (UHC) due to incomplete combustion that may be present in the bowl cavity at the end of the compression stroke.

v. The base bowl and the five bowl design cases were compared for emissions of NOx and SOOT, and the trade-offs between NOx and SOOT have been looked at. The bowl design cases 3, 4, and 2 each emit more NOx than the base bowl design (4.09, 3.92, and 3.55 g/kg-fuel, respectively). The generation of NOx gases is primarily associated with higher temperatures and pressures. While the base bowl design has low NOx but high SOOT, cases 1, 2, 3, and 5 have

comparatively low SOOT. As a result, bowl design case 5, which produces low SOOT and NOx emissions, is the optimal bowl design for reducing SOOT and NOx emissions.

vi. The study shows that when injection timing is retarded, the delay period becomes short, and there is a lack of sufficient time for the air-fuel mixture to have complete combustion, resulting in higher CO and UHC. It became evident with SOI 15.5° CA BTDC and 18.5° CA BTDC, which recorded higher CO and UHC for all the bowl designs.

vii. The study shows that when the start of injection is advanced, the in-cylinder peak pressure increases, and when the timing is retarded, it decreases. A longer ignition delay interval is achievable with improved injection timing; and as a result, more fuel accumulates inside the cylinder, hastening the release of heat and increasing temperature and pressure during the premixed combustion stage. The ideal injection timing is when in-cylinder peak pressure is the highest, NOx and soot emissions are the lowest. Therefore, SOI -22.5° CA BTDC showed improved performance and was tipped as the optimum injection timing for the bowl designs in this study. Maximum pressure is reached at SOI -25.5° CA BTDC, but substantial high quantities of NOx and SOOT are generated, so it is not recommended.

viii. The piston bowl cavity design, spray angle, and injection timing all have a significant impact on the impingement target. In the study, injection included angle 136° and 146° showed improved indicated power for bowl design cases 2, 3 and 5, and in the same vein, engine performance recorded slightly reduced gross indicated specific fuel consumption (GISFC) for the same bowl design cases 2, 3 and 5. When the spray angle got wider to 156° there is more wall impingement; this results to low work done therefore the indicated power for all bowl designs became low and the GISFC become high for all the bowl designs.

ix. According to the findings, when the spray impinged on the bowl lip bottom edge at the 146° spray angle, atomization was enhanced in the bowl cavity of the combustion chamber and resulted in a drop in emissions of UHC and CO. However, CO emissions increase as the spray angle decreases below 136° but remain low when the spray angle ranges between 146° and 156°. Therefore, to

balance the emissions of NOx, unburned hydrocarbons (UHC), and CO, the optimal spray angle should range between 136° and 146°.

8.1.3. Conclusions on modelling of combustion and emissions characteristics of CNSL biodiesel fuelled heavy duty DICI engines

The depletion of natural resources on this planet makes it essential to increase the generation of renewable and sustainable energy. In addition to being abundant and inexpensive, CNSL as a waste from cashew industry is also extremely eco-friendly. Biodiesel generated from CNSL is a renewable fuel with characteristics similar to diesel. As a result of its lower calorific value, higher viscosity, density, and heavier molecules, CNSL biodiesel fuel delivers lower performance than diesel fuel. The impact of combustion chamber geometry on the combustion and emission variables in a diesel engine powered by CNSL biodiesel blended with diesel has been investigated numerically. When the engine runs at a constant speed of 1200 rpm, the comparison between two optimized combustion chamber bowl geometries is done in terms of cylinder pressure, heat release rate, the temperature distribution in the combustion chamber, and emissions characteristics. In summary, the results were as follows:

i. A systematic mechanism reduction technique has been developed to add precise and detailed kinetics to engine CFD simulations. By converting master mechanisms into surrogate fuel mechanisms, the method is able to condense master mechanisms to the smallest possible amount with comparable accuracy. The technique produced a reduction of over 90% while keeping predictions accurate to a predetermined level.
ii. The combustion results show that the in-cylinder pressure, temperature, and apparent heat release rate of petroleum diesel are higher and decrease with the CNSL biodiesel concentration increasing from 10% to 50%.
iii. In comparison with petroleum diesel, CNSL biodiesel emits fewer unburned hydrocarbons (UHC). This is because biodiesel contains more oxygen atoms than regular diesel fuel, which helps it burn more efficiently in combustion chambers. The optimal bowl design in case 2 recorded a slightly higher UHC than in case 2.

iv. The emission of NOx from CNSL biodiesel blends is marginally higher than that from petroleum diesel; it can also be observed that NOx emission increases with the increasing proportion of CNSL biodiesel for the optimum bowl 1 and 2 configurations. The optimized piston bowl in case 1 shows high NOx for all the blends compared to case 2. This is primarily due to the fuel-bound oxygen content in biodiesel blends, which results in a lean-fuel combustion process.

v. Within the operational limit, conventional diesel engines can utilise B10 and B20 CNSL biodiesel and petroleum diesel blend as alternative fuels without requiring significant engine modifications. When compared to petroleum diesel, the CO and UHC of CNSL biodiesel blend emissions are lower. A greater reduction in CO and HC emission is attained as the blend proportion is raised.

vi. As CNSL biodiesel was added to the blends, the gross indicated specific fuel consumption (GISFC) increased significantly. This is because CNSL biodiesel has a lower heating value than standard petroleum diesel. However, modified optimize case 1 combustion chamber shows slightly improved GISFC.

vii. A larger spray-included angle and advanced injection increased NOx emissions and reduces soot emissions and GISFC.

viii. The interaction effects of the optimized piston bowl, spray-included angle, and start of injection were dominant for the responses of NOx and soot emissions.

ix. When running with CNSL biodiesel, engine performance was lower than diesel. This can be further enhanced by blending and preheating, adding fuel additives, and oxygenating the intake air. It is possible to substitute CNSL biodiesel by up to 20% without affecting engine performance. The use of CNSL biodiesel blends greatly lowers UHC, CO, and soot but increased NOx emissions marginally.

8.2. Recommendations for future works

To increase efficient and effective engine performance with modified engine designs based on CNSL biodiesel characteristics, more research and studies are required to address long-term issues such as engine deposits, injector choking, and contamination. Further research and investigations need to be conducted before CNLS biodiesel can be fully incorporated into the energy mix of many countries, and are as follows:

i. Further study is necessary to determine the necessary additives for CNSL biodiesel to be commercially viable as a standalone fuel for compression ignition engines.
ii. An assessment of the long-term stability of CNSL biodiesel blends must be conducted, including engine deposits, injector choking, and oil contamination.
iii. Further studies will be needed to determine if CNSL biodiesel or the blends affect the component and material quality of engine parts including cylinders, valves, pistons, and crankshafts.
iv. The usage of NOx reduction techniques like EGR (exhaust gas recirculation) or additional study is required on strategies like water injection to reduce NOx emissions as it has been demonstrated that utilising CNSL biodiesel increases NOx emissions when compared to using diesel fuel.
v. In comparison with conventional diesel fuel, CNSL biodiesel offers some disadvantages, including undesired qualities at low temperatures, a higher viscosity, and a higher indicated specific fuel consumption (GISFC), further studies are needed to overcome these challenges.
vi. Further investigations are needed to evaluate the characteristics of multi-cylinder engines using CNSL biodiesel, since it is evident from a review of the literature that little research has been done despite promising research on the performance, emission, and combustion characteristics of biodiesel in single-cylinder diesel engines.
vii. Further experimental investigations should be conducted on the combustion and emissions of a DICI diesel heavy-duty engine fuelled with cashew nut shell liquid biodiesel with different combustion chamber piston bowl designs and varied injection parameters.
viii. There is a need for further experimental research to elaborate on the issue of the representativeness of fuel characteristics and other design configurations.

References

Abd Alla, G.H., Soliman, H.A., Badr, O.A. and Abd Rabbo, M.F., 2002. Effect of injection timing on the performance of a dual fuel engine. Energy conversion and Management, 43(2), pp.269-277.

Abu-Jrai, A., Yamin, J.A., Ala'a, H. and Hararah, M.A., 2011. Combustion characteristics and engine emissions of a diesel engine fuelled with diesel and treated waste cooking oil blends. Chemical Engineering Journal, 172(1), pp.129-136.

Acharya, N., Nanda, P., Panda, S. and Acharya, S., 2018. Biodiesel from Non-Edible Vegetable Oils: A Review on Engine Performance and Emission Characteristics. Nature Environment and Pollution Technology, 17(3), pp.711-720.

Agyemang, M., Zhu, Q. and Tian, Y. 2016. Analysis of opportunities for greenhouse emission reduction in the global supply chains of cashew industry in West Africa. Journal of Cleaner Production. Elsevier Ltd, 115, pp. 149–161. doi: 10.1016/j.jclepro.2015.12.059.

Akinhanmi, T.F., Atasie, V.N. and Akintokun, P.O., 2008. Chemical composition and physicochemical properties of cashew nut (Anacardium occidentale) oil and cashew nut shell liquid. Journal of Agricultural, Food and Environmental Sciences, 2(1), pp.1-10.

Ali, O.M., Mamat, R. and Faizal, C.K.M., 2013. Review of the effects of additives on biodiesel properties, performance, and emission features. Journal of renewable and sustainable energy, 5(1).

Amate, A.P. and Khairnar, H.P., 2015. Disquisition on Diesel Engine Emissions and Piston Bowl Parameters. International Advanced Research Journal in Science, Engineering and Technology, 2(7).

Amsden, A.A., 1997. KIVA-3V: A block-structured KIVA program for engines with vertical or canted valves. Los Alamos. NM: Los Alamos National Laboratory Report LA-13313-MS.

An, H., Yang, W., Li, J., Maghbouli, A., Chua, K.J. and Chou, S.K., 2014. A numerical modelling on the emission characteristics of a diesel engine fuelled by diesel and biodiesel blend fuels. Applied energy, 130, pp.458-465.

Anbarasu, A. and Karthikeyan, A., 2016. Diesel engine performance and emission evaluation using Canola biodiesel emulsion fuel. Australian Journal of Mechanical Engineering, 14(3), pp.174-181.

Anenberg, S., Miller, J., Henze, D.A.V.E.N. and Minjares, R., 2019. A global snapshot of the air pollution-related health impacts of transportation sector emissions in 2010 and 2015. International Council on Clean Transportation: Washington, DC, USA.

Angeli, P. and Hewitt, G.F., 2000. Drop size distributions in horizontal oil-water dispersed flows. Chemical Engineering Science, 55(16), pp.3133-3143.

Anilkumar, P. ed., 2017. Cashew nut shell liquid: a goldfield for functional materials. Springer.

ANSYS Forte Users Guide, 2020. ANSYS Forte Users Guide, 2021_R1. ANSYS, Inc. and ANSYS Europe, http://www.ansys.com. p 1-270

ANSYS. ANSYS Forte theory manual (ANSYS Version 2020.). Canonsburg, PA: ANSYS Inc, 2020.

ANSYS Forte Theory, 2020. Ansys Forte Theory Manual, 2021_R1. ANSYS, Inc. and ANSYS Europe, http://www.ansys.com. p 1-96

Arai, M., Tabata, M., Hiroyasu, H. and Shimizu, M., 1984. Disintegrating process and spray characterization of fuel jet injected by a diesel nozzle. SAE transactions, pp.358-371.

Arcoumanis, C. and Kamimoto, T. eds., 2009. Flow and combustion in reciprocating engines. Springer Science & Business Media.

Aruna, M. and Vardhan, H., 2017. Investigation on the performance of a variable compression ratio engine operated with raw cardanol kerosene blends. Biofuels. 7269, pp. 1–7. doi: 10.1080/17597269.2017.1389195.

Asadi, A., Zhang, Y., Mohammadi, H., Khorand, H., Rui, Z., Doranehgard, M.H. and Bozorg, M.V., 2019. Combustion and emission characteristics of biomass derived biofuel, premixed in a diesel engine: A CFD study. Renewable Energy, 138, pp.79-89.

Atabani, A.E., Silitonga, A.S., Ong, H.C., Mahlia, T.M.I., Masjuki, H.H., Badruddin, I.A. and Fayaz, H., 2013. Non-edible vegetable oils: a critical evaluation of oil extraction, fatty acid compositions, biodiesel production, characteristics, engine performance and emissions production. Renewable and sustainable energy reviews, 18, pp.211-245.

Bae, C. and Kim, J., 2017. Alternative fuels for internal combustion engines. Proceedings of the Combustion Institute, 36(3), pp.3389-3413.

Balasubramanian, D., Sokkalingam Arumugam, S.R., Subramani, L., Joshua Stephen Chellakumar, I.J.L. and Mani, A., 2018. A numerical study on the effect of various combustion bowl parameters on the performance, combustion, and emission

behaviour on a single cylinder diesel engine. Environmental Science and Pollution Research, 25(3), pp.2273-2284.
Balat, M. and Balat, H., 2010. Progress in biodiesel processing. Applied energy, 87(6), pp.1815-1835.
Bari, S (ed.). 2013, Diesel Engine - Combustion, Emissions and Condition Monitoring, IntechOpen, London. 10.5772/2782
Bari, S. and Zhang, C., 2020. Analysis of Performance and Emission of Diesel Engines Operating on Palm Oil Biodiesel. SAE International Journal of Advances and Current Practices in Mobility, 2(2020-01-0336), pp.1862-1869.
Bari, S., Zhang, C., Kafrawi, F. and Lee, K.H., 2022. Study of Spray Behaviours to Correlate with Engine Performance and Emissions of a Diesel Engine Using Canola-Based Biodiesel. Fuels, 3(1), pp.87-112.
Basha, S.J., Prasad, P.I. and Rajagopal, K., 2009. Simulation of in-cylinder processes in a DI diesel engine with various injection timings. ARPN journal of engineering and applied sciences, 4(1), pp.1-7.
Bastos, F.A. and Tubino, M., 2017. The use of the liquid from cashew nut shells as an antioxidant in biodiesel. Journal of the Brazilian Chemical Society, 28, pp.747-755.
Battistoni, M. and Grimaldi, C.N., 2012. Numerical analysis of injector flow and spray characteristics from diesel injectors using fossil and biodiesel fuels. Applied Energy, 97, pp.656-666.
Baumgarten, C., 2006. Mixture formation in internal combustion engines. Springer Science & Business Media.
Bawankar, C.S. and Gupta, R., 2016. Effects of piston bowl geometry on combustion and emission characteristics on diesel engine: a cfd case study. International Journal of Research in Engineering and Technology, 5, pp.81-93.
Beale, J.C. and Reitz, R.D., 1999. Modelling spray atomization with the Kelvin-Helmholtz/Rayleigh-Taylor hybrid model. Atomization and sprays, 9(6).
Belal, T.M., El Sayed, M.M. and Osman, M.M., 2013. Investigating diesel engine performance and emissions using CFD.
Bellman R. and Pennington R. H., 1954. Effects of Surface Tension and Viscosity on Taylor Instability, Quarterly of Applied Mathematics, 12(2): 151-162.
Bello, E.I., Akinola, A.O., Otu, F. and Owoyemi, T.J., 2013. Fuel and physiochemical properties of cashew (Anarcardium 1 occidentale) nut oil, its biodiesel and blends with diesel. British Journal of Applied Science and Technology, 3(4), pp.1055-1069.

Benajes, J., Pastor, J.V., García, A. and Monsalve-Serrano, J., 2015. An experimental investigation on the influence of piston bowl geometry on RCCI performance and emissions in a heavy-duty engine. energy conversion and management, 103, pp.1019-1030.

Bernard, C. and Rodica, B., 1999. Diesel engine reference book.

Berry, A.D. and Sargent, S.A., 2011. Cashew apple and nut (Anacardium occidentale L.). In postharvest biology and technology of tropical and subtropical fruits (pp. 414-423e). Woodhead Publishing.

Biscoff, R.K. and Enweremadu, C.C., 2023. Cashew nutshell liquid: A potential inedible source of biodiesel for heavy duty vehicles in sub-Saharan Africa. Energy Sources, Part A: Recovery, Utilization, and Environmental Effects, 45(1), pp.905-923.

Bueno, A.V., Velásquez, J.A. and Milanez, L.F., 2011. Heat release and engine performance effects of soybean oil ethyl ester blending into diesel fuel. Energy, 36(6), pp.3907-3916.

Bupesh Raja, V.K. and JayaPrabakar, J., 2019. Performance and emission characteristics of cashew nut shell oil on the CI engine. International Journal of Ambient Energy, 40(6), pp.563-565.

Buyukkaya, E., 2010. Effects of biodiesel on a DI diesel engine performance, emission and combustion characteristics. Fuel, 89(10), pp.3099-3105.

Can, Ö., 2014. Combustion characteristics, performance and exhaust emissions of a diesel engine fuelled with a waste cooking oil biodiesel mixture. Energy Conversion and Management, 87, pp.676-686.

Can, Ö., Öztürk, E. and Yücesu, H.S., 2017. Combustion and exhaust emissions of canola biodiesel blends in a single cylinder DI diesel engine. Renewable Energy, 109, pp.73-82.

Challen, B. and Baranescu, R. eds., 1999. Diesel engine reference book. Butterworth-Heinemann Limited.

Channapattana, S. V., Abhay A. Pawar, and Prashant G Kamble. 2017. Optimisation of Operating Parameters of DI-CI Engine Fuelled with Second Generation bio-Fuel and Development of ANN Based Prediction Model. Applied Energy 187: 84–95.

Channappagoudra, M., Ramesh, K. and Manavendra, G., 2018. Effect of piston bowl geometry on diesel engine performance operated with dairy scum biodiesel', International Journal of Ambient Energy. Taylor & Francis, 0(0), pp. 1–11.

Channappagoudra, M., Ramesh, K. and Manavendra, G., 2019. Comparative study of standard engine and modified engine with different piston bowl geometries operated with B20 fuel blend. Renewable Energy. Elsevier Ltd, 133, pp. 216–232. doi: 10.1016/j.renene.2018.10.027.

Channappagoudra, M., Ramesh, K. and Manavendra, G., 2020. Effect of piston bowl geometry on diesel engine performance operated with dairy scum biodiesel. International Journal of Ambient Energy, 41(14), pp.1628-1638.

Chiodi, M., 2011. An innovative 3D-CFD-approach towards virtual development of internal combustion engines. Braunschweig: Vieweg+ Teubner Verlag.

CHOU, C.P., 2007. Modelling soot growth and activity with heterogeneous kinetics and method of moments. In Proceedings of 5th US Combustion Meeting, 2007.

Correa, S.M., 1993. A review of NOx formation under gas-turbine combustion conditions. Combustion science and technology, 87(1-6), pp.329-362.

Costa, S. and Bocchi, S., 2017. Manual for small-scale cashew cultivation in Sierra Leone. Milan, Italy.

Daioglou, V., Doelman, J.C., Wicke, B., Faaij, A. and van Vuuren, D.P., 2019. Integrated assessment of biomass supply and demand in climate change mitigation scenarios. Global Environmental Change, 54, pp.88-101. (Daioglou et al., 2019)

Dakhore, R., Gandhi, N.G., Gokhale, N., Aghav, Y., Kumar, M.N. and Hulwan, D.B., 2015. Effect of Piston Cavity Geometry on Combustion, Emission and Performance of a Medium Duty DI Diesel Engine (No. 2015-26-0198). SAE Technical Paper.

Date, A.W., 2020. Analytic combustion: with thermodynamics, chemical kinetics and mass transfer. Springer Nature.

Datta, A. and Mandal, B.K., 2016. A comprehensive review of biodiesel as an alternative fuel for compression ignition engine. Renewable and Sustainable Energy Reviews, 57, pp.799-821.

de Abreu, F.P., Dornier, M., Dionisio, A.P., Carail, M., Caris-Veyrat, C. and Dhuique-Mayer, C., 2013. Cashew apple (Anacardium occidentale L.) extract from by-product of juice processing: A focus on carotenoids. Food chemistry, 138(1), pp.25-31.

de Figueirêdo, M.C.B., Potting, J., Serrano, L.A.L., Bezerra, M.A., da Silva Barros, V., Gondim, R.S. and Nemecek, T., 2016. Environmental assessment of tropical perennial crops: the case of the Brazilian cashew. Journal of Cleaner Production, 112, pp.131-140.

de Oliveira, A., Yang, J. and Sodré, J.R., 2021. Numerical and Experimental Study on the Impact of Mild Cold Exhaust Gas Recirculation on Exhaust Emissions in a Biodiesel-Fuelled Diesel Engine. Journal of Engineering for Gas Turbines and Power, 143(11).

Debnath, B.K., Saha, U.K. and Sahoo, N., 2013. Effect of compression ratio and injection timing on the performance characteristics of a diesel engine running on palm oil methyl ester. Proceedings of the Institution of Mechanical Engineers, Part A: Journal of Power and Energy, 227(3), pp.368-382.

Dec, J.E., 1997. A conceptual model of DL diesel combustion based on laser-sheet imaging. SAE transactions, pp.1319-1348.

Design, R., 2008. CHEMKIN-PRO, ed: Reaction Design San Diego.

Devan, P.K. and Mahalakshmi, N.V., 2009. Study of the performance, emission and combustion characteristics of a diesel engine using poon oil-based fuels. Fuel processing technology, 90(4), pp.513-519.

Devarajan, Y., Munuswamy, D.B. and Nagappan, B., 2017. Emissions analysis on diesel engine fuelled with cashew nut shell biodiesel and pentanol blends. Environmental science and pollution research, 24, pp.13136-13141.

Dinesha, P. and Mohanan, P., 2015. Effect of oxygen enrichment of intake air on the performance and emission of single cylinder CI engine fuelled with cardanol blends. Distributed Generation & Alternative Energy Journal, pp.6-14.

Dinesha, P. and Mohanan, P., 2015a. Evaluation of combustion, performance and emissions of a diesel engine fuelled with bio-fuel produced from cashew nut shell liquid. Biofuels, 6(1-2), pp.101-106.

Dinesha, P. and Mohanan, P., 2018. Combined effect of oxygen enrichment and exhaust gas recirculation on the performance and emissions of a diesel engine fuelled with biofuel blends. Biofuels, 9(1), pp.45-51.

Dinesha, P., Nayak, V. and Mohanan, P., 2014. Effect of oxygen enrichment on the performance, combustion, and emission of single cylinder stationary CI engine fueled with cardanol diesel blends. Journal of Mechanical Science and Technology, 28(7), pp.2919-2924.

Dixit, S., Kumar, A., Kumar, S., Waghmare, N., Thakur, H.C. and Khan, S., 2020. CFD analysis of biodiesel blends and combustion using Ansys Fluent. Materials Today: Proceedings, 26, pp.665-670.

Dolak, J. and Reitz, R.D., 2011. Optimization of the piston geometry of a diesel engine using a two-spray-angle nozzle. Proceedings of the Institution of Mechanical Engineers, Part D: Journal of Automobile Engineering, 225(3), pp.406-421.

EIA, U., 2019. International energy outlook 2013 with projections to 2040. Office of Energy Analysis US Department of Energy: Washington, DC, USA.

Elkelawy, M., Bastawissi, H.A.E., El Shenawy, E.A., Shams, M.M., Panchal, H., Sadasivuni, K.K. and Choudhary, A.K., 2021. Influence of lean premixed ratio of PCCI-DI engine fueled by diesel/biodiesel blends on combustion, performance, and emission attributes; a comparison study. Energy Conversion and Management: X, 10, p.100066.

Elkelawy, M., Bastawissi, H.A.E., El Shenawy, E.A., Taha, M., Panchal, H. and Sadasivuni, K.K., 2021. Study of performance, combustion, and emissions parameters of DI-diesel engine fuelled with algae biodiesel/diesel/n-pentane blends. Energy Conversion and Management: X, 10, p.100058.

ENERGY, I.W. and Iea, A., 2020. IEA. Renewable Energy Market Update.

Enweremadu, C.C., Rutto, H.L. and Peleowo, N., 2011. Performance evaluation of a diesel engine fuelled with methyl ester of shea butter. World Academy of Science, Engineering and Technology, 79, pp.142-146.

European Commission, 2015. Directive (EU) 2015/1513 of the European Parliament and of the Council of 9 September 2015 amending Directive 98/70/EC relating to the quality of petrol and diesel fuels and amending Directive 2009/28/EC on the promotion of the use of energy from renewable sources. Off. J. Eur. Union, 239, pp.1-29.

Fang, T., Coverdill, R.E., Chia-fon, F.L. and White, R.A., 2008. Effects of injection angles on combustion processes using multiple injection strategies in an HSDI diesel engine. Fuel, 87(15-16), pp.3232-3239.

FAOSTAT data, 2020.www.fao.org. http://www.fao.org/faostat/en/#search.

Ferguson, C.R. and Kirkpatrick, A.T., 2015. Internal combustion engines: applied thermosciences. John Wiley & Sons.

Fischer, G., Tramberend, S., van Velthuizen, H., Bole-Rentel, T. and Reeler, J., 2019. Sustainable aviation biofuel potential in sub-Saharan Africa. A systems analysis investigation into the current and future potential for biofuel feedstock production.

Fontaras, G., Kalogirou, M., Grigoratos, T., Pistikopoulos, P., Samaras, Z. and Rose, K., 2014. Effect of rapeseed methylester blending on diesel passenger car emissions–Part 1: Regulated pollutants, NO/NOx ratio and particulate emissions. Fuel, 121, pp.260-270.

Ganji, P.R., Raju, R.K.V. and Rao, S.S., 2017. Computational optimization of biodiesel combustion using response surface methodology. Thermal Science, 21(1 Part B), pp.465-473.

Ganji, P.R., Singh, R.N., Raju, V.R.K. and Srinivasa Rao, S., 2018. Design of piston bowl geometry for better combustion in direct-injection compression ignition engine. Sādhanā, 43(6), pp.1-9.

Garrett, T.K., Newton, K. and Steeds, W., 2000. Motor vehicle. Butterworth-Heinemann.

Geng, P., Cao, E., Tan, Q. and Wei, L., 2017. Effects of alternative fuels on the combustion characteristics and emission products from diesel engines: A review. Renewable and Sustainable Energy Reviews, 71, pp.523-534.

GerMan, J., 2012. Estimated cost of emission reduction technologies for light-duty vehicles. The International Council on Clean Transportation. Washington DC (USA).

Ghosh, I., 2020. Visualizing the Human Impact on the Ocean Economy. Visual Capitalist.

Giner, C., Palandri, C. and Debnath, D., 2019. The role of biofuels in a 2 degrees scenario. In Biofuels, Bioenergy and Food Security (pp. 247-263). Academic Press.

Gnansounou, E., Pachón, E.R., Sinsin, B., Teka, O., Togbé, E. and Mahamane, A., 2020. Using agricultural residues for sustainable transportation biofuels in 2050: Case of West Africa. Bioresource technology, 305, p.123080.

Goga, G., Chauhan, B.S., Mahla, S.K. and Cho, H.M., 2019. Performance and emission characteristics of diesel engine fuelled with rice bran biodiesel and n-butanol. Energy Reports, 5, pp.78-83.

Gohrt, G. 2016. ASTM D975 Diesel Fuel. Specification Test. Available at: http://emotor-extreme.cl/assets/astm_d975_specification_test.

Gugulothu, S.K., Kishore, N.P., Babu, V.P. and Sapre, G., 2019. CFD analysis on different piston bowl geometries by using split injection techniques. Acta Mechanica Malaysia, 2(1), pp.23-28.

Gui, M.M., Lee, K.T. and Bhatia, S., 2008. Feasibility of edible oil vs. non-edible oil vs. waste edible oil as biodiesel feedstock. Energy, 33(11), pp.1646-1653.

Gunstone, F.D. and Harwood, J.L., 2007. The lipid handbook with CD-ROM. CRC press.

Gupta H.N., 2009. Fundamentals of internal combustion engines, Asoke K. Ghosh, PHI Learning, New Delhi, India.

Guzzella, L. and Onder, C., 2009. Introduction to modelling and control of internal combustion engine systems. Springer Science & Business Media.

Habchi, C., Verhoeven, D., Huu, C.H., Lambert, L., Vanhemelryck, J.L. and Baritaud, T., 1997. Modeling atomization and break up in high-pressure diesel sprays. SAE transactions, pp.1391-1406.

Han, Z. and Reitz, R.D., 1995. Turbulence modelling of internal combustion engines using RNG κ-ε models. Combustion science and technology, 106(4-6), pp.267-295.

Hao, H., Liu, Z., Zhao, F., Ren, J., Chang, S., Rong, K. and Du, J., 2018. Biofuel for vehicle use in China: Current status, future potential and policy implications. Renewable and Sustainable Energy Reviews, 82, pp.645-653.

Hassan, N.M.S., Rasul, M.G. and Harch, C.A., 2015. Modelling and experimental investigation of engine performance and emissions fuelled with biodiesel produced from Australian Beauty Leaf Tree. Fuel, 150, pp.625-635.

Hawi, M., Abdel-Rahman, A.K., Bady, M. and Ookawara, S., 2017, June. Prediction of Diesel Combustion and Emission Characteristics in CI Engine Using Computational Fluid Dynamics Simulations. In Energy Sustainability (Vol. 57595, p. V001T02A001). American Society of Mechanical Engineers.

Hawi, M., Elwardany, A., Ookawara, S. and Ahmed, M., 2019. Effect of compression ratio on performance, combustion and emissions characteristics of compression ignition engine fueled with jojoba methyl ester. Renewable Energy, 141, pp.632-645.

Hellier, P. and Ladommatos, N., 2015. The influence of biodiesel composition on compression ignition combustion and emissions. Proceedings of the Institution of Mechanical Engineers, Part A: Journal of Power and Energy, 229(7), pp.714-726.

Herbinet, O., Pitz, W.J. and Westbrook, C.K., 2010. Detailed chemical kinetic mechanism for the oxidation of biodiesel fuels blend surrogate. Combustion and flame, 157(5), pp.893-908.

Heywood, J.B., 2018. Internal Combustion Engine Fundamentals. 2nd Edition, McGraw-Hill Education (ISBN 13: 9781260116106)

Hillier, V.A.W. and Coombes, P., 2004. Hillier's fundamentals of motor vehicle technology. 6 Edition. Nelson Thornes.

Hoekman, S.K., Broch, A., Robbins, C., Ceniceros, E. and Natarajan, M., 2012. Review of biodiesel composition, properties, and specifications. Renewable and sustainable energy reviews, 16(1), pp.143-169.
Howell, S., 2007. Biodiesel Progress: ASTM Specification and 2nd Generation Biodiesel. In 2007 Diesel Engine Efficiency and Emissions Research Conference.
Ianda, T.F., Sales, E.A., Nascimento, A.N. and Padula, A.D., 2020. Optimizing the Cooperated “Multi-Countries” Biodiesel Production and Consumption in Sub-Saharan Africa. Energies, 13(18), p.4717.
IEA (International Energy Agency), 2020. Global Energy Review 2021. Paris, French: IEA.
IEA 2020g, Trucks and Buses, IEA, Paris https://www.iea.org/reports/trucks-and-buses.
IEA, 2018f. Clean Energy Transitions Programme (CETP): Annual Report 2018.
IEA, 2019a. Tracking Transport, Track. Transp., no. May 2019, pp. 1–8.
IEA, 2019c. CO_2 emissions from fuel combustion, IEA Publ., pp. 1–165.
IEA, 2020b. Energy Technology Perspectives 2020, Energy Technol. Perspect. 2020,
IEA, 2020d. “Transport Biofuels,” Track. Reports.
IEA, 2020e. World energy outlook 2020. OECD Publishing.
IEA, G.E., 2019. CO_2 Status Report—The Latest Trends in Energy and Emissions in 2018. International Energy Agency (IEA), Paris, France.
IEA, Ukraine. 2020. Global energy review 2020. Ukraine. [Online] https://www. iea. org/countries/ukraine.
Jaichandar, S. and Annamalai, K., 2012. Influences of re-entrant combustion chamber geometry on the performance of Pongamia biodiesel in a DI diesel engine. Energy, 44(1), pp.633-
Jaichandar, S., Kumar, P.S. and Annamalai, K., 2012. Combined effect of injection timing and combustion chamber geometry on the performance of a biodiesel fueled diesel engine. Energy, 47(1), pp.388-394.
Jumbe, C.B., Msiska, F.B. and Madjera, M., 2009. Biofuels development in Sub-Saharan Africa: are the policies conducive. Energy Policy, 37(11), pp.4980-4986.
Kafrawi, F., Lee, K.H., Zhang, C. and Bari, S., 2022. Spray analysis of Palm-Based biodiesel to correlate performance and combustion analysis of a compression ignition engine. Fuel, 319, p.123822.

Kalam, M.A., Masjuki, H.H., Jayed, M.H. and Liaquat, A.M., 2011. Emission and performance characteristics of an indirect ignition diesel engine fuelled with waste cooking oil. Energy, 36(1), pp.397-402.

Kale, P.T., 2017. Combustion of biodiesel in CI engine. International Journal of Applied Research, 3(3), pp.145-149.

Kasiraman, G., Geo, V.E. and Nagalingam, B., 2016. Assessment of cashew nut shell oil as an alternate fuel for CI (Compression ignition) engines. Energy, 101, pp.402-410.

Keating, E.L., 2007. Applied combustion. CRC press.

Kegl, B. and Lešnik, L., 2018. Modelling of macroscopic mineral diesel and biodiesel spray characteristics. Fuel, 222, pp.810-820.

Khan, S., Panua, R. and Bose, P.K., 2018. Combined effects of piston bowl geometry and spray pattern on mixing, combustion and emissions of a diesel engine: A numerical approach. Fuel, 225, pp.203-217.

Khan, S., Panua, R. and Bose, P.K., 2019. The impact of combustion chamber configuration on combustion and emissions of a single cylinder diesel engine fuelled with soybean methyl ester blends with diesel. Renewable Energy, 143, pp.335-351.

Khond, V.W. and Kriplani, V.M., 2016. Effect of nanofluid additives on performances and emissions of emulsified diesel and biodiesel fuelled stationary CI engine: A comprehensive review. Renewable and Sustainable Energy Reviews, 59, pp.1338-1348.

Kim, H.J., Park, S.H. and Lee, C.S., 2016. Impact of fuel spray angles and injection timing on the combustion and emission characteristics of a high-speed diesel engine. Energy, 107, pp.572-579. Kim et al., 2016

Kitamura, T., Ito, T., Senda, J. and Fujimoto, H., 2002. Mechanism of smokeless diesel combustion with oxygenated fuels based on the dependence of the equivalence ration and temperature on soot particle formation. International Journal of Engine Research, 3(4), pp.223-248.

Knothe, G. and Razon, L. F., 2017. Biodiesel fuels, Progress in Energy and Combustion Science. Elsevier Ltd, 58, pp. 36–59.

Knothe, G., 2009. Improving biodiesel fuel properties by modifying fatty ester composition. Energy & Environmental Science, 2(7), pp.759-766.

Knothe, G., 2010. Biodiesel and renewable diesel: a comparison. Progress in energy and combustion science, 36(3), pp.364-373.

Kolhe, A.V., Shelke, R.E. and Khandare, S.S., 2015. Combustion Modelling with CFD in Direct Injection CI Engine Fuelled with Biodiesel. Jordan Journal of Mechanical & Industrial Engineering, 9(1).

Kongre, U.V. and Sunnapwar, V.K., 2010. CFD modelling and experimental validation of combustion in direct ignition engine fuelled with diesel. International Journal of Applied Engineering Research, 1(3), p.508.

Koten, H., 2018. Hydrogen effects on the diesel engine performance and emissions. International journal of hydrogen energy, 43(22), pp.10511-10519.

Kraan, O., Chappin, E., Kramer, G.J. and Nikolic, I., 2019. The influence of the energy transition on the significance of key energy metrics. Renewable and sustainable energy reviews, 111, pp.215-223.

Kumar, A. and Sharma, S., 2011. Potential non-edible oil resources as biodiesel feedstock: an Indian perspective. Renewable and Sustainable Energy Reviews, 15(4), pp.1791-1800.

Kumar, R.S., Sureshkumar, K. and Velraj, R., 2018. Combustion, performance, and emission characteristics of an unmodified diesel engine fuelled with Manilkara Zapota Methyl Ester and its diesel blends. Applied Thermal Engineering, 139, pp.196-202.

Kumar, S. and Rosen, M.A., 2018. Cashew nut shell liquid as a fuel for compression ignition engines: a comprehensive review. Energy & Fuels, 32(7), pp.7237-7244.

Lakshminarayanan, P.A. and Agarwal, A.K. eds., 2019. Design and development of heavy-duty diesel engines: a handbook. Springer Nature.

Lakshminarayanan, P.A., Aghav, Y.V. and Shi, Y., 2010. Modelling diesel combustion (pp. 5-32). New York: Springer.

Leach, F., Ismail, R. and Davy, M., 2018. Engine-out emissions from a modern high speed diesel engine–The importance of Nozzle Tip Protrusion. Applied energy, 226, pp.340-352.

Leach, F., Ismail, R., Davy, M., Weall, A. and Cooper, B., 2018. The effect of a stepped lip piston design on performance and emissions from a high-speed diesel engine. Applied Energy, 215, pp.679-689.

Lee, D.S., Fahey, D.W., Skowron, A., Allen, M.R., Burkhardt, U., Chen, Q., Doherty, S.J., Freeman, S., Forster, P.M., Fuglestvedt, J. and Gettelman, A., 2021. The contribution of global aviation to anthropogenic climate forcing for 2000 to 2018. Atmospheric Environment, 244, p.117834.

Lee, Y. and Huh, K.Y., 2013. Numerical study on spray and combustion characteristics of diesel and soy-based biodiesel in a CI engine. Fuel, 113, pp.537-545.
Levich, V.G., 1962. Physicochemical hydrodynamics, ed N.R. Amundson, Englewood Cliffs, N.J.: PrenticeHall.
Li, F., Fu, W., Yi, B., Song, L., Liu, T., Wang, X., Wang, C., Lei, Y. and Lin, Q., 2018. Comparison of macroscopic spray characteristics between biodiesel-pentanol blends and diesel. Experimental Thermal and Fluid Science, 98, pp.523-533.
Li, H., Yang, W., Zhou, D. and Yu, W., 2019. Skeletal mechanism construction for heavy saturated methyl esters in real biodiesel fuels. Fuel, 239, pp.263-271.
Li, L., Wang, J., Wang, Z. and Liu, H., 2015. Combustion and emissions of compression ignition in a direct injection diesel engine fuelled with pentanol. Energy, 80, pp.575-581.
Li, X., Chen, Y., Su, L. and Liu, F., 2018. Effects of lateral swirl combustion chamber geometries on the combustion and emission characteristics of DI diesel engines and a matching method for the combustion chamber geometry. Fuel, 224, pp.644-660.
Liang, X., Zheng, Z., Zhang, H., Wang, Y. and Yu, H., 2019. A review of early injection strategy in premixed combustion engines. Applied Sciences, 9(18), p.3737.
Liberman, M.A., 2010. Introduction to physics and chemistry of combustion: explosion, flame, detonation. Springer Science & Business Media.
Lipatnikov, A.N. and Chomiak, J., 2002. Turbulent flame speed and thickness: phenomenology, evaluation, and application in multi-dimensional simulations. Progress in energy and combustion science, 28(1), pp.1-74.
Liu, H.P., Strank, S., Werst, M., Hebner, R. and Osara, J., 2010, January. Combustion emissions modeling and testing of neat biodiesel fuels. In Energy Sustainability (Vol. 43949, pp. 131-140).
Loganathan, M., Thanigaivelan, V., Madhavan, V.M., Anbarasu, A. and Velmurugan, A., 2020. The synergetic effect between hydrogen addition and EGR on cashew nut shell liquid biofuel-diesel operated engine. Fuel, 266, p.117004.
Lubi, M.C. and Thachil, E.T., 2000. Cashew nut shell liquid (CNSL)-a versatile monomer for polymer synthesis. Designed Monomers and polymers, 3(2), pp.123-153.
Magnussen, B.F. and Hjertager, B.H., 1977, January. On mathematical modelling of turbulent combustion with special emphasis on soot formation and combustion. In Symposium (international) on Combustion (Vol. 16, No. 1, pp. 719-729). Elsevier.

Mallikappa, D.N., Reddy, R.P. and Murthy, C.S., 2012. Performance and emission characteristics of double cylinder CI engine operated with cardanol bio fuel blends. Renewable energy, 38(1), pp.150-154.

Mauro, S., Şener, R.A.M.A.Z.A.N., Gül, M.Z., Lanzafame, R., Messina, M. and Brusca, S., 2018. Internal combustion engine heat release calculation using single-zone and CFD 3D numerical models. International Journal of Energy and Environmental Engineering, 9(2), pp.215-226.

McAllister, S., Chen, J.Y. and Fernandez-Pello, A.C., 2011. Fundamentals of combustion processes (Vol. 302). New York: Springer.

Mehmet Çelik, İlker Örs, Cihan Bayindirli and Mehmet Demiralp., 2017. Experimental investigation of impact of addition of bioethanol in different biodiesels, on performance, combustion and emission characteristics. Journal of Mechanical Science and Technology, 31 (11) (2017) 5581~5592

Meloni, R. and Naso, V., 2013. An insight into the effect of advanced injection strategies on pollutant emissions of a heavy-duty diesel engine. Energies, 6(9), pp.4331-4351.

Merker, G.P., Schwarz, C. and Teichmann, R. eds., 2011. Combustion engines development: mixture formation, combustion, emissions and simulation. Springer Science & Business Media.

Miller, J. and Jin, L., 2018. Global progress toward soot-free diesel vehicles in 2018. ICCT-International Council on Clean Transportation.

Mobasheri, R. and Peng, Z., 2012. A computational investigation into the effects of included spray angle on heavy-duty diesel engine operating parameters (No. 2012-01-1714). SAE Technical Paper.

Mofijur, M., Masjuki, H.H., Kalam, M.A. and Atabani, A.E., 2013. Evaluation of biodiesel blending, engine performance and emissions characteristics of Jatropha curcas methyl ester: Malaysian perspective. Energy, 55, pp.879-887.

Shameer, P.M., Ramesh, K., Sakthivel, R. and Purnachandran, R., 2017. Effects of fuel injection parameters on emission characteristics of diesel engines operating on various biodiesel: a review. Renewable and Sustainable Energy Reviews, 67, pp.1267-1281.

Mohod, A.G., Khandetod, Y.P. and Sengar, S., 2010. Eco-friendly utilization of parabolic concentrating solar cooker for extraction of cashew nut shell oil and household cooking. International Journal of Sustainable Energy, 29(3), pp.125-132.

Mollenhauer, K. and Tschöke, H. eds., 2010. Handbook of diesel engines (Vol. 1). Berlin: Springer.
Moser, B.R. and Vaughn, S.F., 2012. Efficacy of fatty acid profile as a tool for screening feedstocks for biodiesel production. Biomass and bioenergy, 37, pp.31-41.
Mubofu, E.B., 2016. From cashew nut shell wastes to high value chemicals. Pure and Applied Chemistry, 88(1-2), pp.17-27.
Munnannur, A. and Reitz, R.D., 2009. Comprehensive collision model for multidimensional engine spray computations. Atomization and Sprays, 19(7).
Munroe, D., 2016. Diesel Fuel Properties, S6P4, pp. 1–12. Available at: http://mdec.ca/2016/S6P3_monroe.pdf.
Musculus, M.P., 2004. On the correlation between NOx emissions and the diesel premixed burn. SAE transactions, pp.631-651.
Mwangi, P.M., Kareru, P.G., Thiong'o, G. and Mohammed, A.N., 2013. Cashew nut shell liquid: an agricultural by-product with great potential for commercial exploitation in Kenya. Journal of Agriculture, Science and Technology, 15(1), pp.28-44.
Nayak, S.K., Hoang, A.T., Nayak, B. and Mishra, P.C., 2021. Influence of fish oil and waste cooking oil as post mixed binary biodiesel blends on performance improvement and emission reduction in diesel engine. Fuel, 289, p.119948.
Network, R.E.P., 2017. Renewables global status report. Paris: REN21 Secretariat, 272p.
Newell, R., Raimi, D., Villanueva, S. and Prest, B., 2020. Global Energy Outlook 2020: energy transition or energy addition. Resources for the Future.
Niculescu, R., Clenci, A. and Iorga-Siman, V., 2019. Review on the use of diesel–biodiesel–alcohol blends in compression ignition engines. Energies, 12(7), p.1194.
Noiha Noumi, V., Zapfack, L., Awé Djongmo, V., Witanou, N., Nyeck, B., Ngossomo, J.D., Hamadou, M.R., Chimi, C.D. and Tabue Mbobda, R.B., 2017. Floristic structure and sequestration potential of cashew agroecosystems in Africa: A case study from Cameroon. Journal of Sustainable Forestry, 36(3), pp.277-288.
Nunney M. J. 2007. Light and Heavy Vehicle Technology. Fourth edi. Elsevier Ltd.
OECD/FAO, 2016. OECD-FAO agricultural outlook 2016–2025. Data for tables extracted on 04 Jul 2017 from OECD. Stat. OECD Publishing, Paris.
Ogunkunle, O. and Ahmed, N.A., 2019a. A review of global current scenario of biodiesel adoption and combustion in vehicular diesel engines. Energy Reports, 5, pp.1560-1579.

Ogunkunle, O. and Ahmed, N.A., 2019b. Performance evaluation of a diesel engine using blends of optimized yields of sand apple (Parinari polyandra) oil biodiesel. Renewable Energy, 134, pp.1320-1331.
Ogunkunle, O. and Ahmed, N.A., 2019c. Response surface analysis for optimisation of reaction parameters of biodiesel production from alcoholysis of Parinari polyandra seed oil. International Journal of Sustainable Energy, 38(7), pp.630-648.
Ogunkunle, O. and Ahmed, N.A., 2021. Overview of biodiesel combustion in mitigating the adverse impacts of engine emissions on the sustainable human–environment scenario. Sustainability, 13(10), p.5465.
Oliveira, M.S.C., de Morais, S.M., Magalhães, D.V., Batista, W.P., Vieira, Í.G.P., Craveiro, A.A., de Manezes, J.E.S.A., Carvalho, A.F.U. and de Lima, G.P.G., 2011. Antioxidant, larvicidal and antiacetylcholinesterase activities of cashew nut shell liquid constituents. Acta Tropica, 117(3), pp.165-170.
Onoji, S.E., Iyuke, S.E., Igbafe, A.I. and Nkazi, D.B., 2016. Rubber seed oil: A potential renewable source of biodiesel for sustainable development in sub-Saharan Africa. Energy conversion and management, 110, pp.125-134.
Outlook, B.E. and Dudley, R., 2019. BP Energy Outlook 2019 edition, The Energy Outlook explores the forces shaping the global energy transition out to 2040 and the key uncertainties surrounding that. BP Energy Outlook 2019.
Pandian, A.K., Munuswamy, D.B., Radhakrishanan, S., Devarajan, Y., Ramakrishnan, R.B.B. and Nagappan, B., 2018. Emission and performance analysis of a diesel engine burning cashew nut shell oil bio diesel mixed with hexanol. Petroleum Science, 15(1), pp.176-184.
Park, S., 2012. Optimization of combustion chamber geometry and engine operating conditions for compression ignition engines fueled with dimethyl ether. Fuel, 97, pp.61-71.
Patel, R.N., Bandyopadhyay, S. and Ganesh, A., 2006. Economic appraisal of supercritical fluid extraction of refined cashew nut shell liquid. Journal of Chromatography A, 1124(1-2), pp.130-138.
Patterson, M.A., 1997. Modelling the effects of fuel injection characteristics on diesel combustion and emissions. The University of Wisconsin-Madison.
Patterson, M.A., Kong, S.C., Hampson, G.J. and Reitz, R.D., 1994. Modelling the effects of fuel injection characteristics on diesel engine soot and NOx emissions. SAE transactions, pp.836-852.

Payri, F., Luján, J.M., Martín, J. and Abbad, A., 2010. Digital signal processing of in-cylinder pressure for combustion diagnosis of internal combustion engines. Mechanical Systems and Signal Processing, 24(6), pp.1767-1784.
Pérez de Albéniz Azqueta, S., 2020. ANSYS Forte simulate guide.
Pischinger, F., Schulte, H. and Jansen, J., 1988. Grundlagen und Entwicklungslinien der diesel-motorischen Brennverfahren. VDI-Berichte, 714, pp.61-93.
Pulkrabek, W.W., 2007. Engineering Fundamentals of the Internal Combustion Engine.
Qi, D.H., Chen, H., Geng, L.M. and Bian, Y.Z., 2010. Experimental studies on the combustion characteristics and performance of a direct injection engine fuelled with biodiesel/diesel blends. Energy Conversion and Management, 51(12), pp.2985-2992.
Qi, D.H., Geng, L.M., Chen, H., Bian, Y.Z., Liu, J. and Ren, X.C., 2009. Combustion and performance evaluation of a diesel engine fuelled with biodiesel produced from soybean crude oil. Renewable energy, 34(12), pp.2706-2713.
Ra, Y. and Reitz, R.D., 2009. A vaporization model for discrete multi-component fuel sprays. International Journal of Multiphase Flow, 35(2), pp.101-117.
Raeie, N., Emami, S. and Sadaghiyani, O.K., 2014. Effects of injection timing, before and after top dead centre on the propulsion and power in a diesel engine. Propulsion and power research, 3(2), pp.59-67.
Raghavendra Prasada, S.A., 2014. A Review on CNSL Biodiesel as an Alternative fuel for Diesel Engine. International Journal of Science and Research (IJSR), 3(7), pp.2028-2038.
Rahman, K.M. and Ahmed, Z., 2020. Combustion and emission characteristics of a diesel engine operating with varying equivalence ratio and compression ratio-A CFD simulation. Journal of Engineering Advancements, 1(3), pp.101-10.
Raihan, A., Muhtasim, D.A., Pavel, M.I., Faruk, O. and Rahman, M., 2022. Dynamic impacts of economic growth, renewable energy use, urbanization, and tourism on carbon dioxide emissions in Argentina. Environmental Processes, 9(2), p.38.
Rajasekar, E. and Selvi, S., 2014. Review of combustion characteristics of CI engines fueled with biodiesel. Renewable and Sustainable Energy Reviews, 35, pp.390-399.
Ramadhas, A.S., Muraleedharan, C. and Jayaraj, S., 2005. Performance and emission evaluation of a diesel engine fuelled with methyl esters of rubber seed oil. Renewable energy, 30(12), pp.1789-1800.

Raturi, A.K., 2019. Renewables 2019 global status report.

Ravindra, Aruna, M. and Vardhan, H., 2020. Investigation on the performance of a variable compression ratio engine operated with raw cardanol kerosene blends. Biofuels, 11(6), pp.699-705.

Reif, K. ed., 2014. Diesel engine management. Springer Vieweg.

Reitz, R.D. and Diwakar, R., 1986. Effect of drop breakup on fuel sprays. SAE transactions, pp.218-227.

REN21, 2017. Renewables 2017 global status report (Paris: REN21 Secretariat) REN21-Renewable energy policy network for the 21st century

Ribeiro, B.D., Castro, A.M.D., Coelho, M.A.Z. and Freire, D.M.G., 2011. Production and use of lipases in bioenergy: a review from the feedstocks to biodiesel production. Enzyme research, 2011.

Risfaheri, T.T., Nur, M.A. and Sailah, I., 2009. Isolation of cardanol from cashew nut shell liquid using the vacuum distillation method. Indonesian Journal of agriculture, 2(1), pp.11-20.

Rostami, S., Ghobadian, B. and Kiani, M.K.D., 2014. Effect of the injection timing on the performance of a diesel engine using Diesel-Biodiesel blends. International Journal of Automotive and Mechanical Engineering, 10, p.1945.

Rupa, T.R. and Sajeev, M.V., 2015. Cashew News, July-December 2014, HALF YEARLY NEWSLETTER OF ICAR-DIRECTORATE OF CASHEW RESEARCH, PUTTUR.

Rupa, T.R., Rejani, R. and Bhat, M.G., 2013. Impact of climate change on cashew and adaptation strategies. In Climate-resilient horticulture: adaptation and mitigation strategies (pp. 189-198). Springer, India.

Sadeghinezhad, E., Kazi, S.N., Badarudin, A., Oon, C.S., Zubir, M.N.M. and Mehrali, M., 2013. A comprehensive review of bio-diesel as alternative fuel for compression ignition engines. Renewable and Sustainable Energy Reviews, 28, pp.410-424.

Sahoo, D.K., Rajasekar, R., Kumarasubramanian, R. and Karthik, N., 2019. Emission analysis on cashew nut biofuel in compression-ignition engine. International Journal of Ambient Energy, 40(1), pp.63-68.

Sakthisaravanasenthil, K., Senthilkumar, S. and Sivakumar, G., 2017. A study on effect of piston bowl shape on engine performance and emission characteristics of a diesel engine. In Innovative design and development practices in aerospace and automotive engineering (pp. 579-588). Springer, Singapore.

Sanger, S.H., Mohod, A.G., Khandetode, Y.P., Shrirame, H.Y. and Deshmukh, A.S., 2011. Study of carbonization for cashew nut shell. Research Journal of Chemical Sciences, 1(2), pp.43-55.

Sanjeeva, S.K., Pinto, M.P., Narayanan, M.M., Kini, G.M., Nair, C.B., SubbaRao, P.V., Pullela, P.K., Ramamoorthy, S. and Barrow, C.J., 2014. Distilled technical cashew nut shell liquid (DT-CNSL) as an effective biofuel and additive to stabilize triglyceride biofuels in diesel. Renewable energy, 71, pp.81-88.

Santhanakrishnan, S. and Ramani, B.K.M., 2017. Evaluation of diesel engine performance using diesel–cashew nut shell oil blends. International Journal of Ambient Energy, 38(1), pp.104-107.

Saravanan, S., 2015. Effect of exhaust gas recirculation (EGR) on performance and emissions of a constant speed DI diesel engine fuelled with pentanol/diesel blends. Fuel, 160, pp.217-226.

Sathiyamoorthi, R. and Sankaranarayanan, G., 2015. Fuel injection timings of a direct injection diesel engine running on neat lemongrass oil-diesel blends. International Journal of Automotive and Mechanical Engineering, 11, p.2348.

Sathyamurthy, R., Balaji, D., Gorjian, S., Muthiya, S.J., Bharathwaaj, R., Vasanthaseelan, S. and Essa, F.A., 2021. Performance, combustion and emission characteristics of a DI-CI diesel engine fuelled with corn oil methyl ester biodiesel blends. Sustainable Energy Technologies and Assessments, 43, p.100981.

Sawadogo, M., Tanoh, S.T., Sidibé, S., Kpai, N. and Tankoano, I., 2018. Cleaner production in Burkina Faso: Case study of fuel briquettes made from cashew industry waste. Journal of cleaner production, 195, pp.1047-1056.

Sayin, C. and Canakci, M., 2009. Effects of injection timing on the engine performance and exhaust emissions of a dual-fuel diesel engine. Energy conversion and management, 50(1), pp.203-213.

Şener, R., Özdemir, M.R. and Yangaz, M.U., 2019. Influence of piston bowl geometry on combustion and emission characteristics. Proceedings of the Institution of Mechanical Engineers, Part A: Journal of Power and Energy, 233(5), pp.576-587.

Senthil Kumar, D. and Thirumalini, S., 2020. Investigations on effect of split and retarded injection on the performance characteristics of engines with cashew nut shell biodiesel blends. International Journal of Ambient Energy, pp.1-9.

Setianto, W.B., Yoshikawa, S., Smith Jr, R.L., Inomata, H., Florusse, L.J. and Peters, C.J., 2009. Pressure profile separation of phenolic liquid compounds from cashew

(Anacardium occidentale) shell with supercritical carbon dioxide and aspects of its phase equilibria. The Journal of Supercritical Fluids, 48(3), pp.203-210.
Shahabuddin, M., Liaquat, A.M., Masjuki, H.H., Kalam, M.A. and Mofijur, M., 2013. Ignition delay, combustion and emission characteristics of diesel engine fuelled with biodiesel. Renewable and Sustainable Energy Reviews, 21, pp.623-632.
Shameer, P.M. and Ramesh, K., 2018. Assessment on the consequences of injection timing and injection pressure on combustion characteristics of sustainable biodiesel fuelled engine. Renewable and Sustainable Energy Reviews, 81, pp.45-61.
Shameer, P.M., Ramesh, K., Sakthivel, R. and Purnachandran, R., 2017. Effects of fuel injection parameters on emission characteristics of diesel engines operating on various biodiesel: a review. Renewable and Sustainable Energy Reviews, 67, pp.1267-1281.
Shantharaman, P.P., Pushparaj, T. and Prabhakar, M., 2017. Performance And Emission Studies on Cashew nut Shell Liquid Bio-Oil Fuelled Diesel Engine with Acetone as Additive. Advances in Natural and Applied Sciences, 11(12), pp.56-63.
Shi, Y. and Reitz, R.D., 2008. Optimization study of the effects of bowl geometry, spray targeting, and swirl ratio for a heavy-duty diesel engine operated at low and high load. International Journal of Engine Research, 9(4), pp.325-346.
Shu, J., Fu, J., Liu, J., Ma, Y., Wang, S., Deng, B. and Zeng, D., 2019. Effects of injector spray angle on combustion and emissions characteristics of a natural gas (NG)-diesel dual fuel engine based on CFD coupled with reduced chemical kinetic model. Applied Energy, 233, pp.182-195.
Simsek, S., 2020. Effects of biodiesel obtained from Canola, sefflower oils and waste oils on the engine performance and exhaust emissions. Fuel, 265, p.117026.
Singh, A.P., Sharma, N., Agarwal, R. and Agarwal, A.K. eds., 2020. Advanced combustion techniques and engine technologies for the automotive sector (Vol. 6, pp. 111-147). Singapore: Springer.
Singh, A.P., Shukla, P.C., Hwang, J. and Agarwal, A.K., 2020. Simulations and Optical Diagnostics for Internal Combustion Engines. Springer Singapore.
Singh, H.C.P., Rao, N.K.S. and Shivashankar, K.S. eds., 2013. Climate-resilient horticulture: adaptation and mitigation strategies (pp. 81-88). India: Springer India.
Singh, P., Chauhan, S.R. and Kumar, N., 2016. A review on methodology for complete elimination of diesel from CI engines using mixed feedstock. Renewable and Sustainable Energy Reviews, 57, pp.1110-1125.

Singh, P., Tiwari, S.K., Singh, R. and Kumar, N., 2017. Modification in combustion chamber geometry of CI engines for suitability of biodiesel: A review. Renewable and Sustainable Energy Reviews, 79, pp.1016-1033.

Singh, S., Reitz, R.D. and Musculus, M.P., 2006. Comparison of the characteristic time (CTC), representative interactive flamelet (RIF), and direct integration with detailed chemistry combustion models against optical diagnostic data for multi-mode combustion in a heavy-duty DI diesel engine. SAE Transactions, pp.61-82.

Singh, S.P. and Singh, D., 2010. Biodiesel production through the use of different sources and characterization of oils and their esters as the substitute of diesel: a review. Renewable and sustainable energy reviews, 14(1), pp.200-216.

Solanki, J.H. and Javiya, T.V., 2012. Cashew Nut shell liquid fuel an substitute for diesel fuel to be used in CI engine. International Journal of Advance Research in Science, Engineering and Technology, 1(2), pp.8-12.

Som, S. and Longman, D.E., 2011. Numerical study comparing the combustion and emission characteristics of biodiesel to petrodiesel. Energy & Fuels, 25(4), pp.1373-1386.

Sreedharan, S.N. and Krishnan, R., 2018, August. Development of Tool to Design Piston Bowl Considering Spray Parameters to Reduce Emissions. In IOP Conference Series: Materials Science and Engineering (Vol. 396, No. 1, p. 012055). IOP Publishing.

Srihari, S., S. Thirumalini, and K. Prashanth. 2017. “An Experimental Study on the Performance and Emissions Characteristics of PCCI-DI Engine Fuelled with Diethyl Ether –Diesel-Biodiesel Blends.” Renewable Energy 107: 440–447.

Srinivas, V. and Posangiri, A.R., 2018. Performance and emission characteristics of methyl ester mango seed biodiesel on four stroke single cylinder diesel engine with 200 bar injection pressure. International Journal of Engineering and Techniques, 4(2), pp.327-32.

Stiesch, G., 2003. Modelling engine spray and combustion processes. Springer Science & Business Media.

Stolarski, T, Nakasone, Yand Yoshimoto, S. (2018) Engineering analysis with ANSYS software. Second Edi. Butterworth-Heinemann.

Stone, R., 1999. Introduction to internal combustion engines (Vol. 3). London: Macmillan.

Su, T.F., Patterson, M.A., Reitz, R.D. and Farrell, P.V., 1996. Experimental and numerical studies of high-pressure multiple injection sprays. SAE transactions, pp.1281-1292.

Suarez-Bertoa, R., Kousoulidou, M., Clairotte, M., Giechaskiel, B., Nuottimäki, J., Sarjovaara, T. and Lonza, L., 2019. Impact of HVO blends on modern diesel passenger cars emissions during real world operation. Fuel, 235, pp.1427-1435.

Subbarao, C.N., Krishna Prasad, K.M.M. and Prasad, V.S.R.K., 2011. Review on applications, extraction, isolation and analysis of cashew nut shell liquid (CNSL). The Pharma Research Journal, 6(1), pp.21-41.

Sugihara, T., Shimano, K., Enomoto, Y., Suzuki, Y. and Emi, M., 2007. Direct heat loss to combustion chamber walls in a DI diesel engine-development of measurement technique and evaluation of direct heat loss to cylinder liner wall. SAE Transactions, pp.1467-1482.

Suresh, M., Jawahar, C.P. and Richard, A., 2018. A review on biodiesel production, combustion, performance, and emission characteristics of non-edible oils in variable compression ratio diesel engine using biodiesel and its blends. Renewable and Sustainable Energy Reviews, 92, pp.38-49.

Taiwo, E.A., 2015. Cashew nut shell oil—a renewable and reliable petrochemical feedstock. Advances in Petrochemicals, 1, p.13.

Tamilselvan, P., Nallusamy, N. and Rajkumar, S., 2017. A comprehensive review on performance, combustion and emission characteristics of biodiesel fuelled diesel engines. Renewable and Sustainable Energy Reviews, 79, pp.1134-1159.

Tan, Z., 2003. Multi-dimensional modelling of ignition and combustion in premixed and DIS/CI (direct injection spark/compression ignition) engines. The University of Wisconsin-Madison.

Tat, M.E., Van Gerpen, J.H. and Wang, P.S., 2004. Fuel property effects on injection timing, ignition timing and oxides of nitrogen emissions from biodiesel-fuelled engines. In 2004 ASAE Annual Meeting (p. 1). American Society of Agricultural and Biological Engineers.

TATSCHL, R. and PRIESCHING, P., 2009. 3D-CFD Simulation of DI-Diesel engine combustion and pollutant formation. University of Pitesti Scientific Bulletin Faculty of Mechanics and Technology Automotive series, year XVI, (20).

Tay, K.L., Yang, W., Zhao, F., Yu, W. and Mohan, B., 2017. Numerical investigation on the combined effects of varying piston bowl geometries and ramp injection rate-

shapes on the combustion characteristics of a kerosene-diesel fuelled direct injection compression ignition engine. Energy conversion and management, 136, pp.1-10.
Tchanche, B., 2017. Energy consumption analysis of the transportation sector of Senegal. AIMS Energy, 5(6), pp.912-929.
Tesfa, B., Mishra, R., Zhang, C., Gu, F. and Ball, A.D., 2013. Combustion and performance characteristics of CI (compression ignition) engine running with biodiesel. Energy, 51, pp.101-115. Tesfa et al., 2013
Thompson, P. A., 1972. Compressible-fluid Dynamics, McGraw-Hill: New York,
Tripathi, S. and Subramanian, K.A., 2018. Control of fuel spray wall impingement on piston bowl in palm acid oil biodiesel fuelled direct injection automotive engine using retarded injection timing, EGR and increased compression ratio. Applied Thermal Engineering, 142, pp.241-254.
Tvaronavičienė, M., Baublys, J., Raudeliūnienė, J. and Jatautaitė, D., 2020. Global energy consumption peculiarities and energy sources: Role of renewables. In Energy Transformation Towards Sustainability (pp. 1-49). Elsevier.
Uherek, E., Halenka, T., Borken-Kleefeld, J., Balkanski, Y., Berntsen, T., Borrego, C., Gauss, M., Hoor, P., Juda-Rezler, K., Lelieveld, J. and Melas, D., 2010. Transport impacts on atmosphere and climate: Land transport. Atmospheric environment, 44(37), pp.4772-4816.
Ulfarsson, G.F., Kim, S. and Booth, K.M., 2010. Analyzing fault in pedestrian–motor vehicle crashes in North Carolina. Accident Analysis & Prevention, 42(6), pp.1805-1813.
United Nations., 2015 Transforming our world: the 2030 Agenda for Sustainable Development. General Assembly 70 session, 16301(October), pp. 1–35. doi: 10.1007/s13398-014-0173-7.2.
Uyumaz, A., 2018. Combustion, performance and emission characteristics of a DI diesel engine fuelled with mustard oil biodiesel fuel blends at different engine loads. Fuel, 212, pp.256-267.
Van Basshuysen, R. and Schäfer, F., 2004. Internal combustion engine handbook-basics, components, systems and perspectives (Vol. 345).
Varatharajan, K., Cheralathan, M. and Velraj, R., 2011. Mitigation of NOx emissions from a jatropha biodiesel fuelled DI diesel engine using antioxidant additives. Fuel, 90(8), pp.2721-2725.

Vedharaj, S., Vallinayagam, R., Yang, W.M., Chou, S.K., Chua, K.J.E. and Lee, P.S., 2015. Performance emission and economic analysis of preheated CNSL biodiesel as an alternate fuel for a diesel engine. International Journal of Green Energy, 12(4), pp.359-367.

Vedharaj, S., Vallinayagam, R., Yang, W.M., Saravanan, C.G. and Roberts, W.L., 2016. Synthesis and utilization of catalytically cracked cashew nut shell liquid in a diesel engine. Experimental Thermal and Fluid Science, 70, pp.316-324.

Velmurugan, A., Loganathan, M. and Gunasekaran, E.J., 2014. Experimental investigations on combustion, performance and emission characteristics of thermal cracked cashew nut shell liquid (TC-CNSL)–diesel blends in a diesel engine. Fuel, 132, pp.236-245.

Vishwanathan, G. and Reitz, R.D., 2008. Numerical predictions of diesel flame lift-off length and soot distributions under low temperature combustion conditions (No. 2008-01-1331). SAE Technical Paper.

Voca, N. and Ribic, B., 2020. Biofuel production and utilization through smart and sustainable biowaste management. Journal of cleaner production, 259, p.120742.

Wada, Y. and Senda, J., ICLASS06-106 Cavitation Induced Breakup Model for Multi-Component Fuel Spray.

Wakuri, Y., Takasaki, K. and Yang, Y., 1990. Studies on the fuel-spray combustion characteristics in a diesel engine by the aid of photographic visualization. American Society of Mechanical Engineers, Internal Combustion Engine Division (Publication) ICE, 10, pp.77-85.

Wang, H. and Liu, W., 2015. Simulation studies of diesel engine combustion characteristics with oxygen enriched air. Journal of Power and Energy Engineering, 3(08), p.15.

Wang, Y., Ge, H.W. and Reitz, R.D., 2010. Validation of mesh-and timestep-independent spray models for multi-dimensional engine CFD simulation. SAE International Journal of Fuels and Lubricants, 3(1), pp.277-302.

Wang, Y.D., Al-Shemmeri, T., Eames, P., McMullan, J., Hewitt, N., Huang, Y. and Rezvani, S., 2006. An experimental investigation of the performance and gaseous exhaust emissions of a diesel engine using blends of a vegetable oil. Applied thermal engineering, 26(14-15), pp.1684-1691.

Wentsch, M., 2019. Analysis of Injection Processes in an Innovative 3D-CFD Tool for the Simulation of Internal Combustion Engines. Springer Fachmedien Wiesbaden.

Xin, Q., 2011. Diesel engine system design. Elsevier.
Xu, X., Wei, Z., Ji, Q., Wang, C. and Gao, G., 2019. Global renewable energy development: Influencing factors, trend predictions and countermeasures. Resources Policy, 63, p.101470.
Xue, J., 2013. Combustion characteristics, engine performances and emissions of waste edible oil biodiesel in diesel engine. Renewable and Sustainable Energy Reviews, 23, pp.350-365.
Yakhot, V., and Orszag, S. A. 1986. Renormalization Group Analysis of Turbulence: I. Basic Theory. Journal of Scientific Computing, 1:3
Yamada, Y., Emi, M., Ishii, H., Suzuki, Y., Kimura, S. and Enomoto, Y., 2002. Heat loss to the combustion chamber wall with deposit in DI diesel engine: variation of instantaneous heat flux on piston surface with deposit. JSAE review, 23(4), pp.415-421.
Yang, H., Li, X., Mu, M., Kou, G. and Li, L., 2017. Performance and emissions analysis of a diesel engine directly fuelled with waste cooking oil biodiesel. International Journal of Ambient Energy, 38(4), pp.428-434.
Yao, M., Ma, T., Wang, H., Zheng, Z., Liu, H. and Zhang, Y., 2018. A theoretical study on the effects of thermal barrier coating on diesel engine combustion and emission characteristics. Energy, 162, pp.744-752.
Yoon, S.H., Cha, J.P. and Lee, C.S., 2010. An investigation of the effects of spray angle and injection strategy on dimethyl ether (DME) combustion and exhaust emission characteristics in a common-rail diesel engine. Fuel Processing Technology, 91(11), pp.1364-1372.
Yousefi, A., Birouk, M. and Guo, H., 2017. An experimental and numerical study of the effect of diesel injection timing on natural gas/diesel dual-fuel combustion at low load. Fuel, 203, pp.642-657.
Yu, S., Yin, B., Jia, H., Wen, S., Li, X. and Yu, J., 2017. Theoretical and experimental comparison of internal flow and spray characteristics between diesel and biodiesel. Fuel, 208, pp.20-29.
Zhao, D., Gutmark, E. and de Goey, P., 2018. A review of cavity-based trapped vortex, ultra-compact, high-g, inter-turbine combustors. Progress in Energy and Combustion Science, 66, pp.42-82.
Zhao, H. ed., 2009. Advanced direct injection combustion engine technologies and development: diesel engines (Vol. 2). Elsevier.

Zhou, H., Li, X., Chen, Y., Kang, Y., Liu, D. and Liu, F., 2020. The effect of spray angle on the combustion and emission performance of a separated swirl combustion system in a diesel engine. Energy, 190, p.116481.

Zimont, V.L., Biagioli, F. and Syed, K., 2001. Modelling turbulent premixed combustion in the intermediate steady propagation regime. Progress in Computational Fluid Dynamics, An International Journal, 1(1-3), pp.14-28.

Appendix A

ANSYS FORTE 2020_R2 SIMULATION INTERFACE

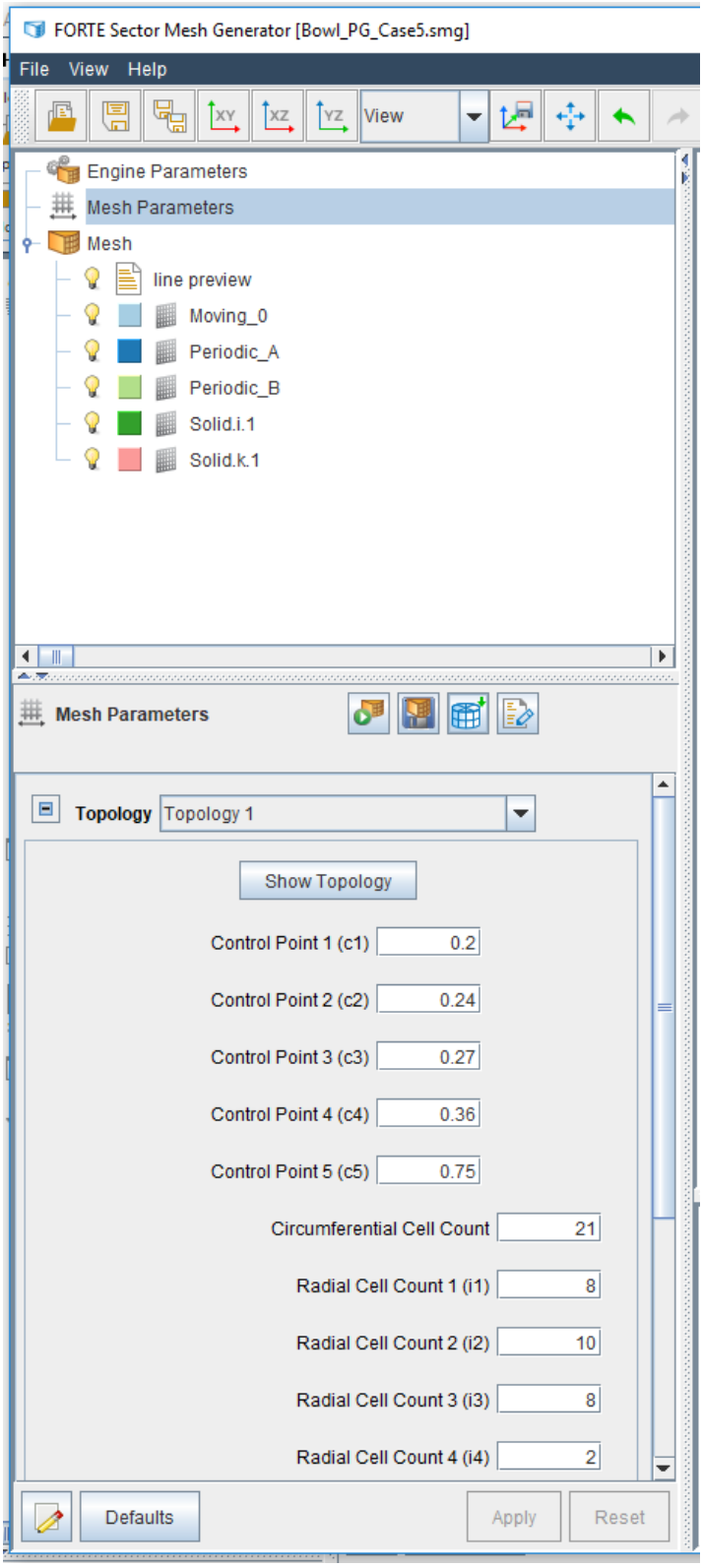

Figure A1. FORTE sector mesh generator

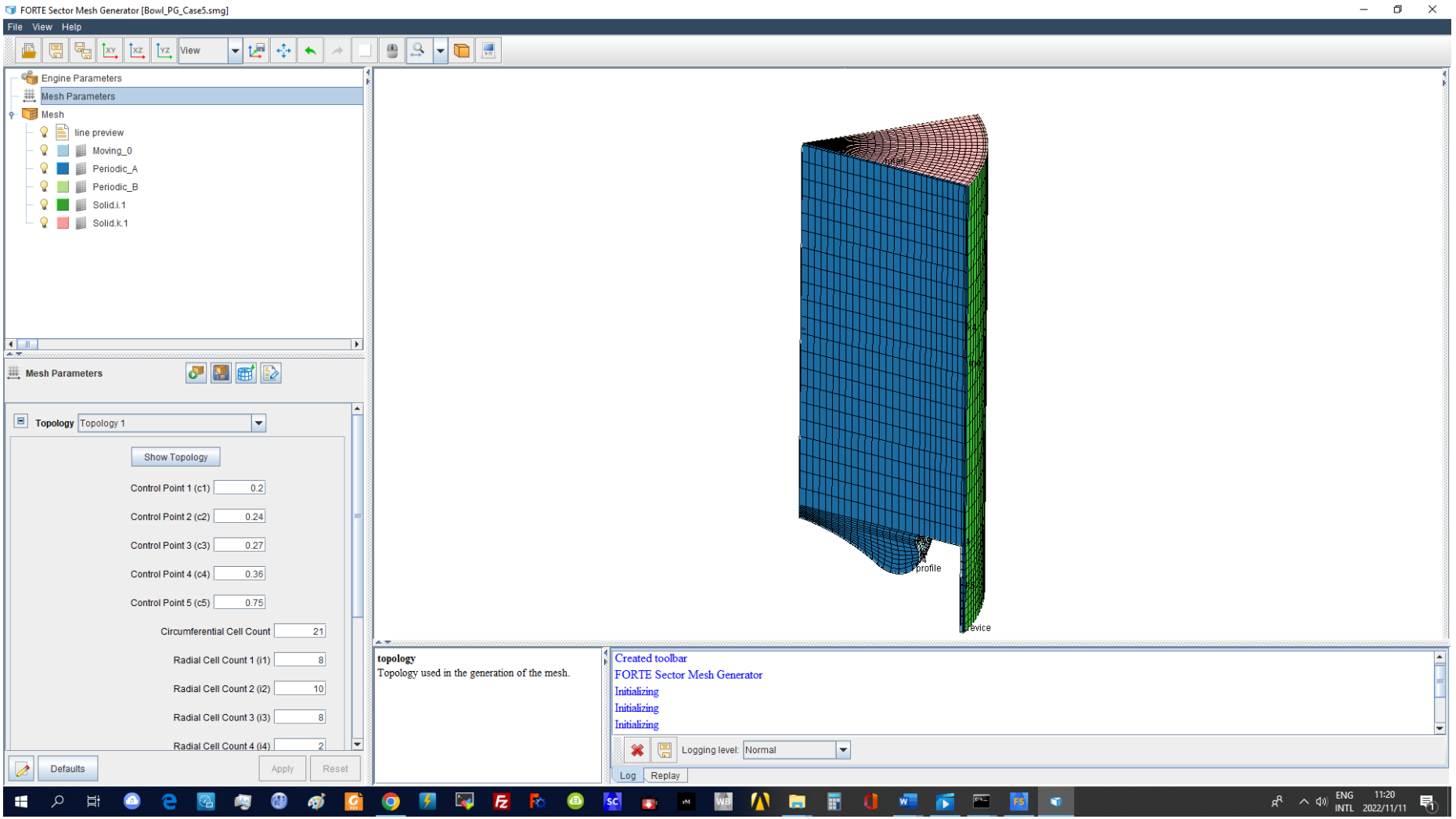

Figure A2. FORTE sector mesh generator-2

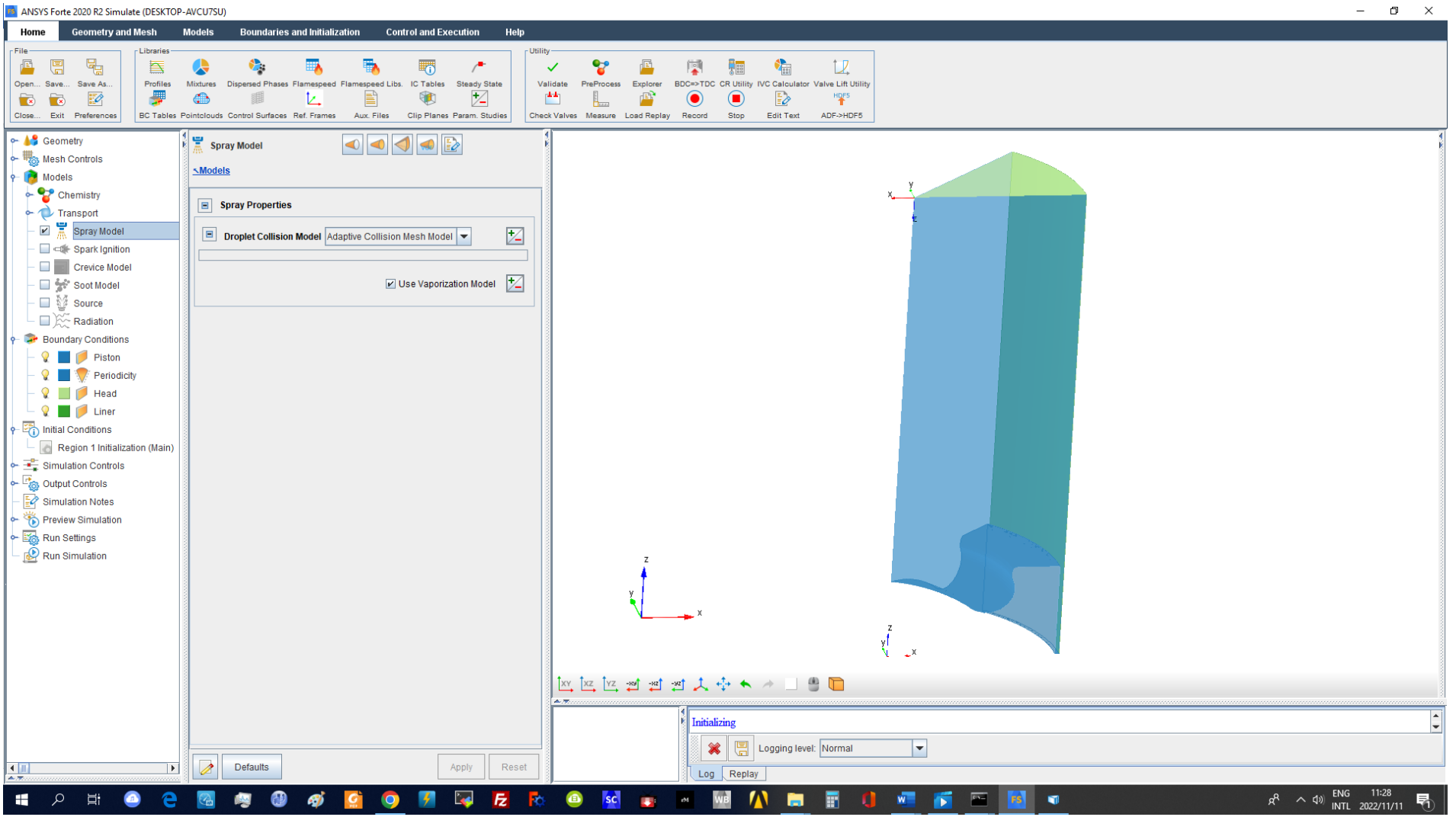

Figure A3. ANSYS Forte 2020 R2 simulation.

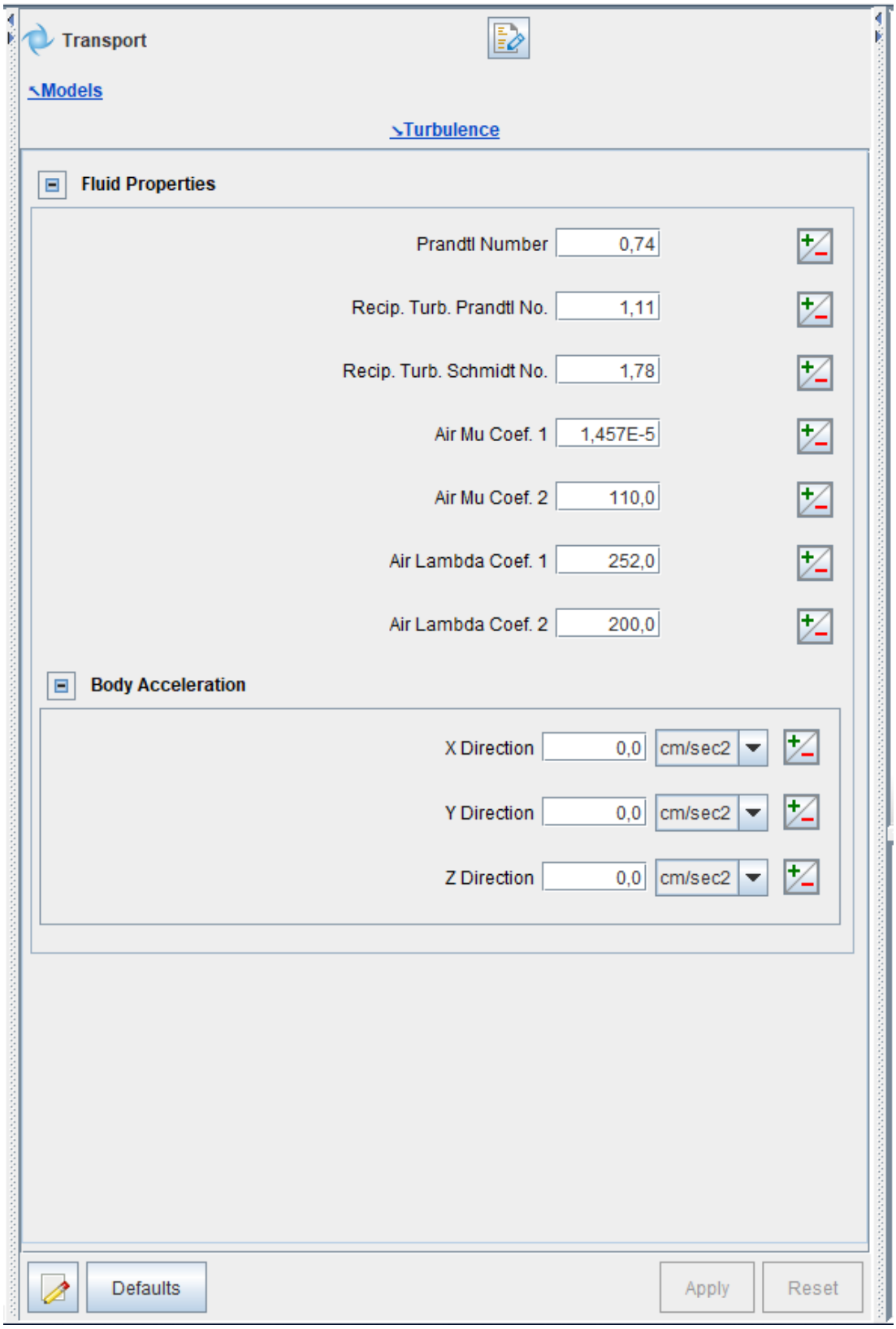

Figure A4. Transport model and turbulence model settings.

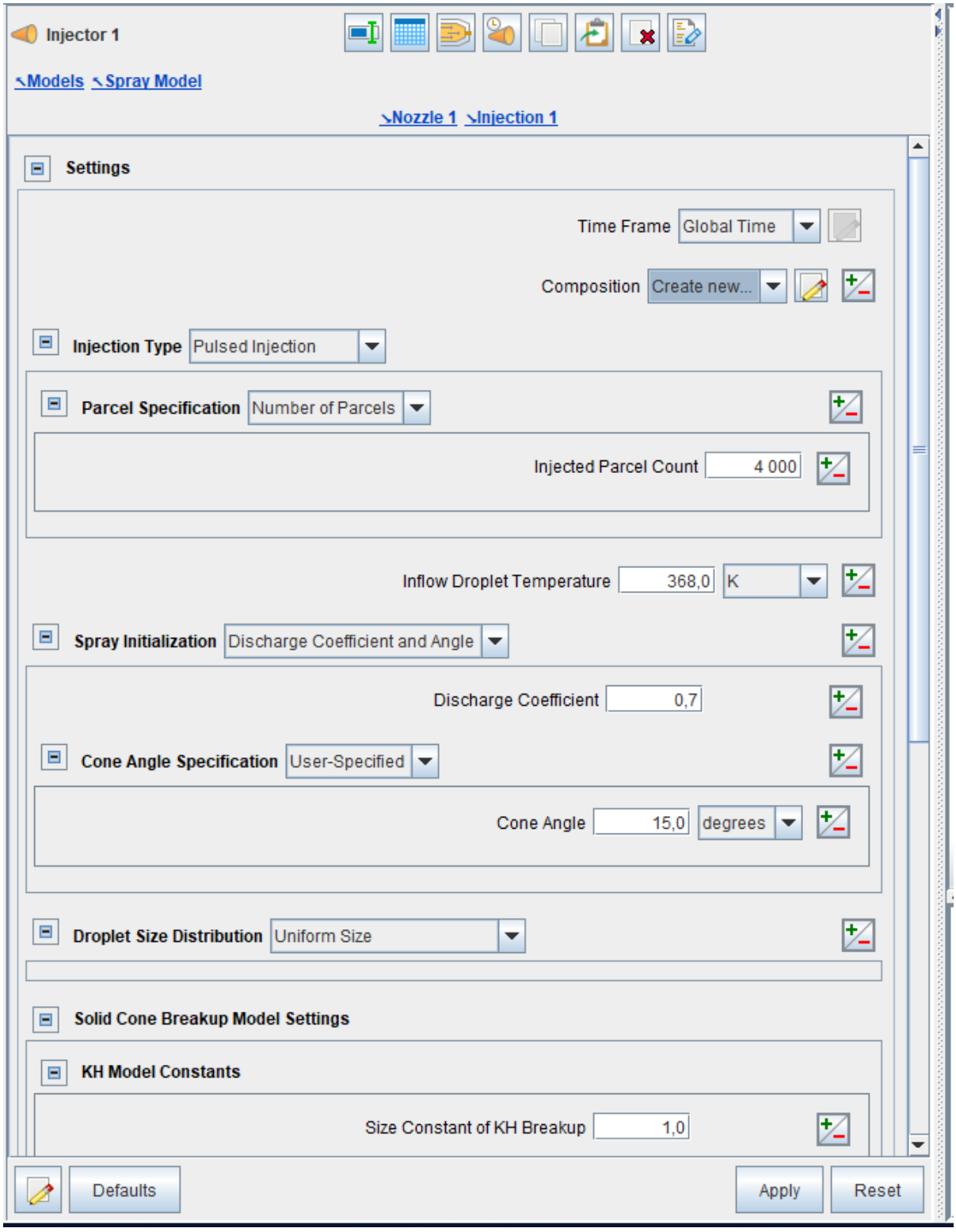

Figure A5. Spray model settings.

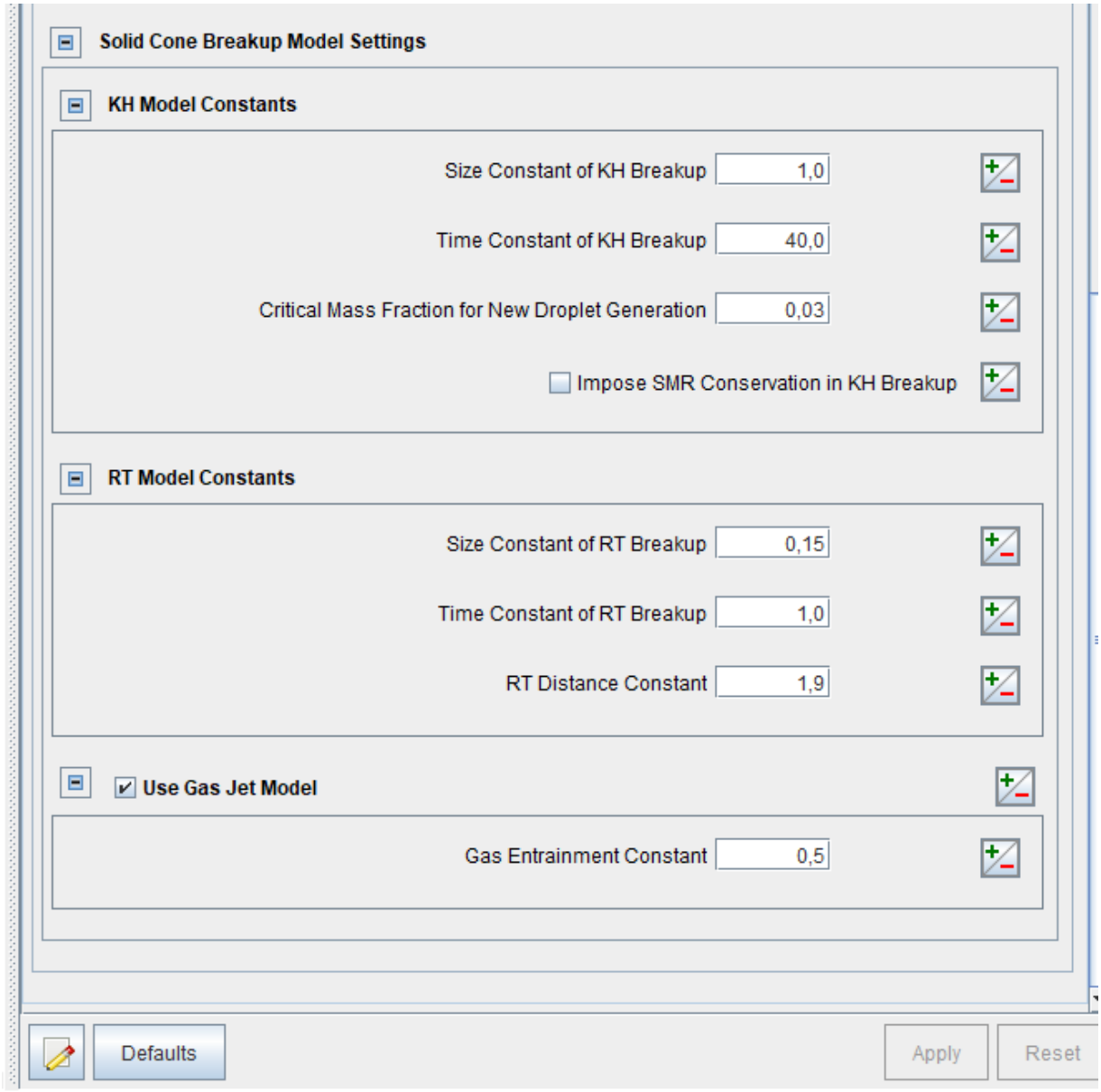

Figure A6. Solid breakup model setting.

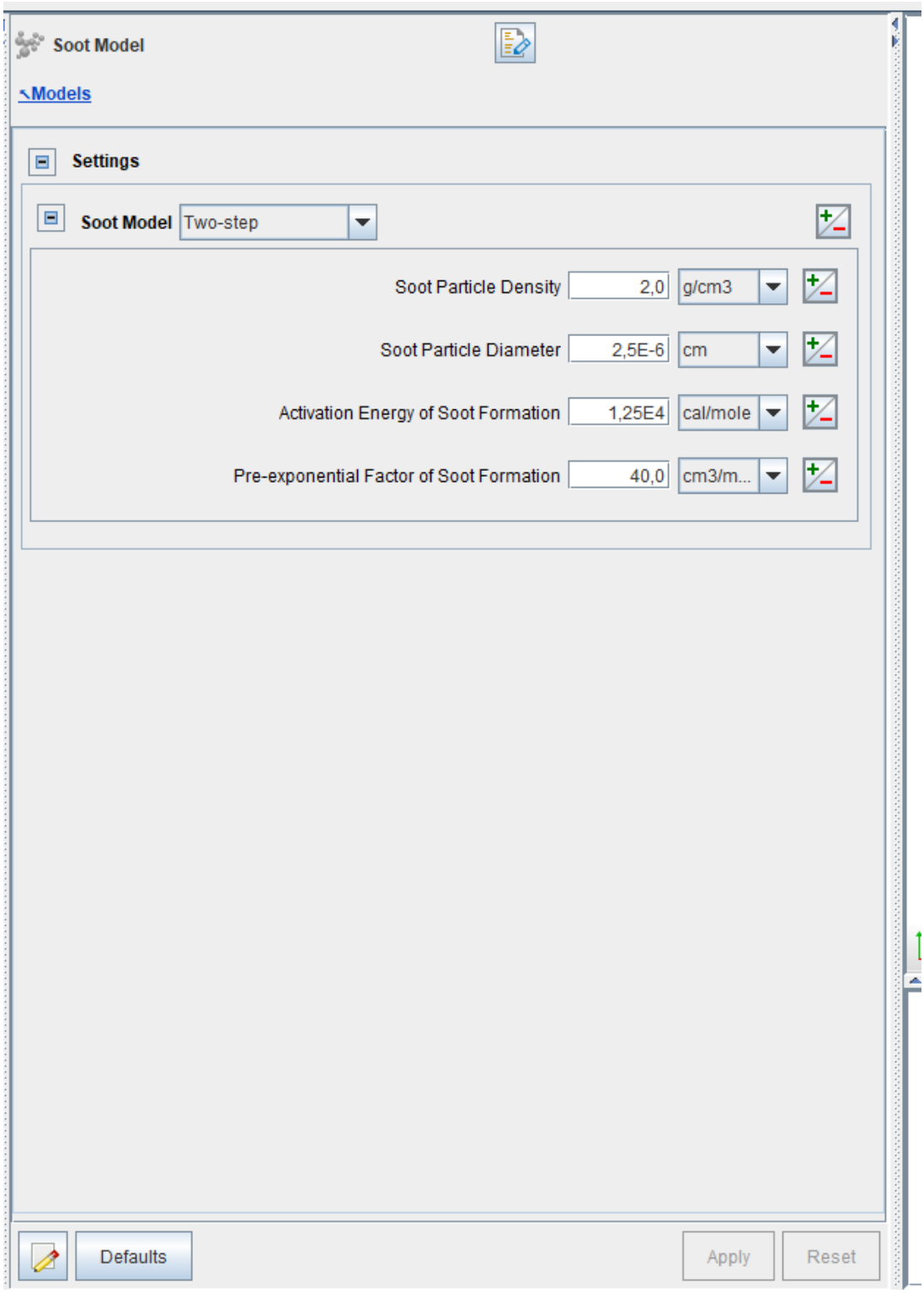

Figure A7. Soot model settings.

Appendix B

Table B1. Results from n-heptane (diesel fuel) in DICI engine ANSYS Forte simulation

Base Bowl Design_0, is the standard Engine performance	
Parameters	
Base Bowl Designs	**0**
Bowl Design Case 1	**1**
Bowl Design case 2	**2**
Bowl Design Case 3	**3**
Bowl Design Case 4	**4**
Bowl Design Case 5	**5**
Start of Injection (Injection Timing)	**SOI**
15.50	**15.5**
18.50	**18.5**
22.50	**22.5**
25.50	**25.5**
Spray Included Angle	**SIA**
126.0	**126**
136.0	**136**
146.0	**146**
156.0	**156**

Table B2. Detailed results from n-heptane (diesel fuel) in DICI engine ANSYS Forte simulation

S. NO.	**Parameters**			**Responses**					
	Bolw Design	**SOI**	**SIA**	**Gross Indicated Power (KW)**	**GISFC (g/KW-h)**	**CO (g/kg-fuel)**	**UHC (g/kg-fuel)**	**NOx (g/Kg-fuel)**	**Soot (g/Kg-fuel)**
0	0	22.5	152	9.58	201.02	30.62	16.09	2.98	0.00022
1	1	15.5	126	10.06	191.37	28.88	15.91	3.23	0.00996
2	2	15.5	126	10.20	188.79	23.34	13.21	3.63	0.011
3	3	15.5	126	10.13	190.08	19.10	11.00	3.86	0.014
4	4	15.5	126	9.99	192.75	16.42	10.51	3.46	0.0068

5	5	15.5	126	10.00	192.65	24.50	14.66	2.69	0.0039
6	1	18.5	126	10.05	191.72	21.82	12.78	3.73	0.0045
7	2	18.5	126	10.16	189.45	17.88	10.45	4.12	0.0038
8	3	18.5	126	10.09	190.84	15.79	9.40	4.42	0.0041
9	4	18.5	126	9.94	193.85	13.86	9.15	3.61	0.0024
10	5	18.5	126	9.96	193.36	20.06	12.49	2.73	0.00088
11	1	22.5	126	9.99	192.82	17.33	17.33	3.57	0.00018
12	2	22.5	126	10.06	191.55	14.95	14.95	3.77	0.000062
13	3	22.5	126	9.97	193.27	14.69	14.69	3.85	0.00016
14	4	22.5	126	9.79	196.66	12.84	12.84	3.58	0.00028
15	5	22.5	126	9.86	195.29	18.51	18.51	2.41	0.00012
16	1	25.5	126	9.98	193.00	17.13	17.80	2.04	0.000093
17	2	25.5	126	10.02	192.13	16.14	15.35	2.18	0.000089
18	3	25.5	126	9.97	193.18	14.72	15.76	2.05	0.000084
19	4	25.5	126	9.81	196.42	15.48	17.74	2.68	0.000096
20	5	25.5	126	9.90	194.56	20.12	17.58	1.01	0.000095
21	1	15.5	136	10.07	191.30	35.47	19.31	2.70	0.000201
22	2	15.5	136	10.17	189.30	27.93	16.56	2.89	0.00047
23	3	15.5	136	10.19	189.00	19.67	13.03	2.97	0.00013
24	4	15.5	136	9.89	194.79	19.42	13.56	2.82	0.00059
25	5	15.5	136	9.94	193.86	35.17	20.56	1.58	0.00013
26	1	18.5	136	10.10	190.64	21.64	14.28	2.01	0.000121
27	2	18.5	136	10.16	189.55	20.73	13.49	2.36	0.000117
28	3	18.5	136	10.15	189.75	15.46	11.15	2.20	0.000115
29	4	18.5	136	9.83	195.99	16.31	12.10	2.61	0.000133
30	5	18.5	136	9.98	192.92	25.46	16.54	1.20	0.000124
31	1	22.5	136	10.06	191.51	15.88	11.65	0.98	0.000114
32	2	22.5	136	10.13	190.12	14.86	10.33	1.31	0.000109
33	3	22.5	136	10.12	190.37	10.89	8.60	1.15	0.000106
34	4	22.5	136	9.84	195.71	14.07	9.86	2.09	0.00011
35	5	22.5	136	10.04	191.91	17.12	12.22	0.68	0.00012
36	1	25.5	136	10.17	189.35	14.61	10.50	0.30	0.0001032
37	2	25.5	136	10.22	188.41	15.11	9.69	0.38	0.00009
38	3	25.5	136	10.16	189.62	11.40	8.24	0.42	0.000097
39	4	25.5	136	9.91	194.29	13.15	8.69	0.82	0.000099
40	5	25.5	136	10.12	190.27	15.45	10.79	0.26	0.000104
41	1	15.5	146	9.93	194.04	47.41	23.90	1.66	0.00015
42	2	15.5	146	10.01	192.44	42.39	21.42	1.90	0.00021
43	3	15.5	146	10.00	192.66	31.73	18.16	2.45	0.00023
44	4	15.5	146	9.82	196.07	28.10	16.57	2.72	0.00029
45	5	15.5	146	9.77	197.08	52.94	25.96	1.59	0.00021

46	1	18.5	146	9.96	193.46	34.06	19.38	1.35	0.000123
47	2	18.5	146	10.01	192.33	30.08	17.32	1.68	0.000124
48	3	18.5	146	9.96	193.36	24.39	15.38	2.24	0.00013
49	4	18.5	146	9.78	196.86	22.64	14.73	2.63	0.000145
50	5	18.5	146	9.79	196.76	39.77	21.21	1.54	0.00012
51	1	22.5	146	9.87	195.07	24.98	15.85	1.40	0.00012
52	2	22.5	146	10.17	189.34	14.86	8.76	7.17	0.00061
53	3	22.5	146	10.18	189.12	11.41	7.34	8.32	0.001003
54	4	22.5	146	9.68	199.04	19.20	12.98	2.80	0.00012
55	5	22.5	146	10.12	190.28	16.91	10.04	6.02	0.000503
56	1	25.5	146	9.78	196.84	24.34	13.79	1.35	0.000105
57	2	25.5	146	10.02	192.14	21.44	13.55	0.78	0.000105
58	3	25.5	146	9.89	194.79	18.11	12.49	1.52	0.00011
59	4	25.5	146	9.68	199.00	17.88	12.01	2.31	0.000108
60	5	25.5	146	9.81	196.29	27.36	15.88	1.06	0.00011
61	1	15.5	156	9.69	198.82	66.37	29.27	2.82	0.00087
62	2	15.5	156	9.80	196.49	57.20	25.74	3.06	0.00174
63	3	15.5	156	9.84	195.82	44.12	20.94	3.44	0.00196
64	4	15.5	156	9.64	199.71	43.22	20.59	2.94	0.0042
65	5	15.5	156	9.57	201.34	66.54	29.99	2.25	0.0023
66	1	18.5	156	9.71	198.28	48.26	22.78	3.25	0.000424
67	2	18.5	156	9.79	196.72	43.01	20.65	3.53	0.00076
68	3	18.5	156	9.79	196.71	33.63	17.74	3.88	0.0012
69	4	18.5	156	9.64	199.85	34.26	17.74	3.32	0.0026
70	5	18.5	156	9.60	200.53	51.32	23.37	2.72	0.00171
71	1	22.5	156	9.66	199.47	34.87	18.00	2.94	0.00044
72	2	22.5	156	9.77	197.23	31.27	16.87	3.43	0.00047
73	3	22.5	156	9.68	198.96	26.16	14.80	3.65	0.00083
74	4	22.5	156	9.59	200.74	26.46	14.75	3.30	0.00128
75	5	22.5	156	9.62	200.15	36.49	18.07	2.58	0.00077
76	1	25.5	156	9.68	199.00	33.72	17.80	1.88	0.000171
77	2	25.5	156	9.91	194.40	25.79	15.35	2.38	0.000112
78	3	25.5	156	9.67	199.18	27.88	15.76	2.08	0.00027
79	4	25.5	156	9.63	200.04	23.88	13.91	2.39	0.000461
80	5	25.5	156	9.70	198.49	35.88	17.58	1.70	0.000201

Appendix C

Procedure for Biodiesel mechanism reduction in ANSYS Reaction Workbench.

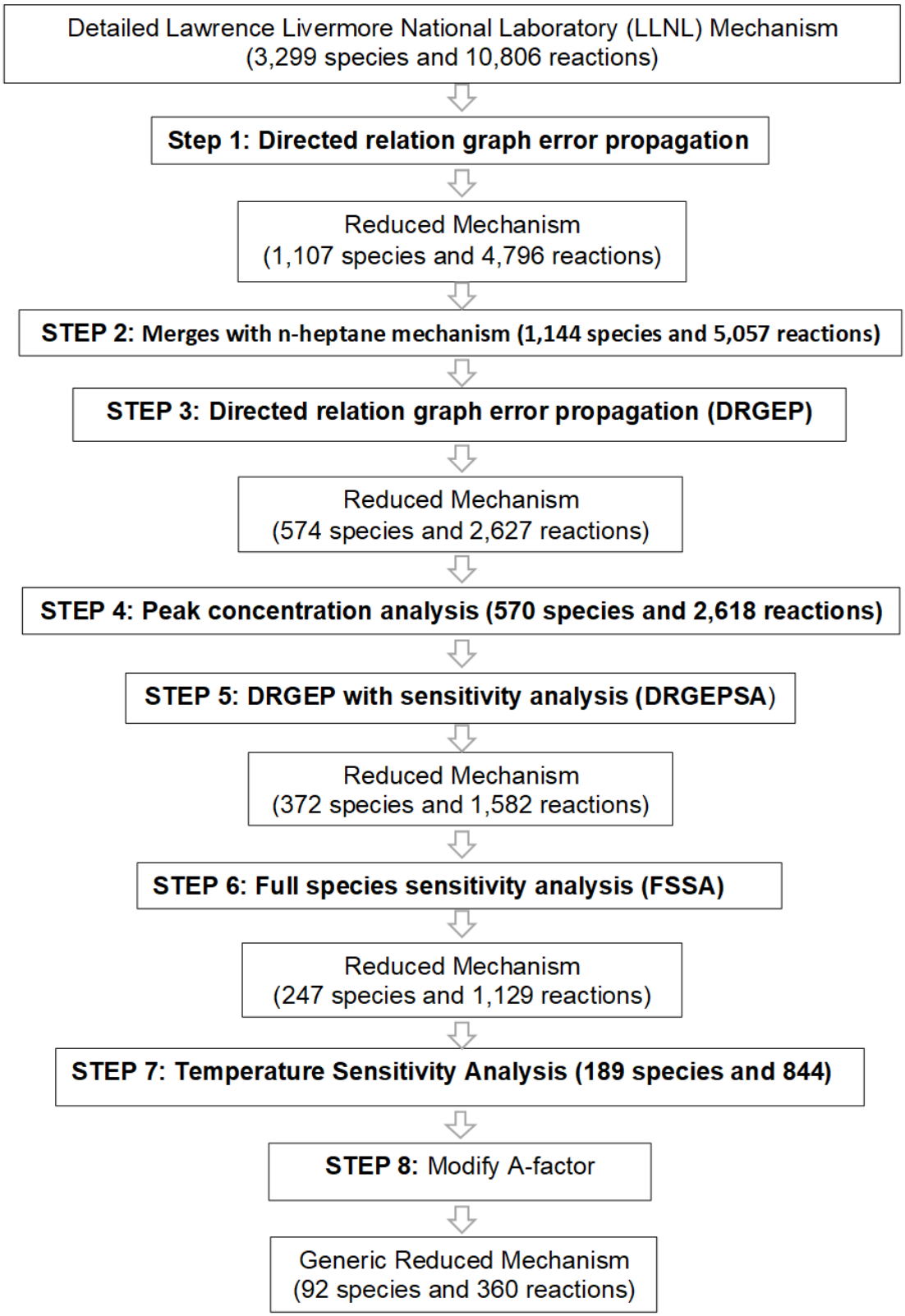

Figure 1. Procedure for mechanism reduction.

Appendix D

Table D1. Results from CNSL Biodiesel in DICI engine (ANSYS Forte Simulation)

Base Bowl Design_0, is the standard Engine performance	
Parameters	
Standard Case 0	0
Optimum Case 1	1
Optimum case 2	2
Start of Injection (Injection Timing) BTDC	**SOI**
18.5	18.5
22.5	22.5
25.5	25.5
Spray Included Angle	**SIA**
136 degres	136
146 degres	146
156 degres	156
Biodiesel/ Diesel	
Diesel 1	1
CNSL B10	10
CNSL B20	20
CNSL B30	30
CNSL B50	50
Response	
Gross Indicated Power:	GIP
Indicated Thermal Efficiency	ITE
Gross Indicated Specific Fuel Consumption	GISFC
Carbon Monoxide	CO
Unburnt Hydrocarbons	UHC
Nitrogen oxide	NOx
Soot	Soot

Table D2. Detailed results from CNSL Biodiesel in DICI engine (ANSYS Forte Simulation)

S. NO.	Parameters				Responses						
	Bowl Design	SOI	SIA	Biodiesel /Diesel	GIP (KW)	Indicated Thermal Efficiency	GISFC (g/KW-h)	CO (g/kg-fuel)	UHC (g/kg-fuel)	NOx (g/Kg-fuel)	Soot (g/Kg-fuel)
0	0	22.5	152	1	9.58	0.40	201.02	30.62	16.09	2.98	0.00022
1	1	18.5	136	10	9.83	0.42	196.00	18.30	12.50	2.12	0.000120
2	1	18.5	136	20	9.55	0.41	201.71	23.45	14.35	1.65	0.000113
3	1	18.5	136	30	9.26	0.41	207.96	29.01	16.09	1.36	0.000109
4	1	18.5	136	50	8.64	0.39	222.79	38.51	18.56	0.95	0.000102
5	2	18.5	136	10	9.62	0.41	200.22	33.64	19.53	1.18	0.000121
6	2	18.5	136	20	9.30	0.40	207.17	47.17	24.10	0.91	0.000118
7	2	18.5	136	30	8.94	0.39	215.44	63.78	29.86	0.68	0.000116
8	2	18.5	136	50	8.08	0.37	238.38	102.34	46.52	0.41	0.000110
9	1	18.5	146	10	9.57	0.41	201.20	27.66	16.16	2.19	0.000195
10	1	18.5	146	20	9.29	0.40	207.32	35.06	18.23	1.62	0.000148
11	1	18.5	146	30	9.00	0.40	214.11	41.59	20.05	1.30	0.000126
12	1	18.5	146	50	8.37	0.38	229.98	54.06	23.10	0.87	0.000109
13	2	18.5	146	10	9.41	0.40	204.78	48.91	23.76	1.54	0.000173
14	2	18.5	146	20	9.08	0.39	212.19	65.25	29.22	1.13	0.000135

15	2	18.5	146	30	8.72	0.38	220.98	77.62	34.76	0.92	0.000126
16	2	18.5	146	50	8.00	0.36	240.84	88.98	46.27	0.63	0.000119
17	1	18.5	156	10	9.42	0.40	204.45	38.06	18.81	3.82	0.000991
18	1	18.5	156	20	9.12	0.40	211.10	45.79	20.76	3.29	0.000408
19	1	18.5	156	30	8.83	0.39	218.18	52.64	22.49	2.89	0.000226
20	1	18.5	156	50	8.13	0.37	236.80	68.83	27.07	2.32	0.000110
21	2	18.5	156	10	9.21	0.39	209.20	60.77	26.69	2.53	0.001438
22	2	18.5	156	20	8.85	0.38	217.71	73.96	32.23	2.15	0.000600
23	2	18.5	156	30	8.49	0.37	226.95	83.77	37.57	1.83	0.000350
24	2	18.5	156	50	7.82	0.36	246.35	88.48	44.60	1.52	0.000188
25	1	22.5	136	10	9.86	0.42	195.33	15.33	11.37	0.97	0.00011
26	1	22.5	136	20	9.64	0.42	199.78	19.66	13.12	0.60	0.00011
27	1	22.5	136	30	9.38	0.41	205.22	25.02	14.93	0.41	0.00010
28	1	22.5	136	50	8.80	0.40	218.89	39.30	19.23	0.16	0.00010
29	2	22.5	136	10	9.74	0.42	197.82	26.31	16.63	0.58	0.00011
30	2	22.5	136	20	9.45	0.41	203.89	38.03	21.21	0.40	0.00011
31	2	22.5	136	30	9.12	0.40	211.07	50.40	25.71	0.28	0.00011
32	2	22.5	136	50	8.15	0.37	236.27	105.17	47.60	0.12	0.00011
33	1	22.5	146	10	9.58	0.41	201.11	25.27	15.43	1.30	0.00011
34	1	22.5	146	20	9.34	0.40	206.22	32.04	17.62	0.74	0.00011
35	1	22.5	146	30	9.06	0.40	212.50	40.39	20.17	0.52	0.00011

36	1	22.5	146	50	8.38	0.38	229.81	71.21	29.25	0.21	0.00011
37	2	22.5	146	10	9.43	0.40	204.28	40.30	21.43	1.17	0.00012
38	2	22.5	146	20	9.14	0.40	210.82	58.87	27.21	0.75	0.00012
39	2	22.5	146	30	8.72	0.38	220.90	84.35	36.19	0.53	0.00012
40	2	22.5	146	50	7.89	0.36	244.18	109.71	56.32	0.25	0.00011
41	1	22.5	156	10	9.35	0.40	205.95	33.15	17.98	3.14	0.00040
42	1	22.5	156	20	9.09	0.39	211.99	40.58	20.15	2.50	0.00014
43	1	22.5	156	30	8.81	0.39	218.50	49.15	22.46	2.01	0.00011
44	1	22.5	156	50	8.08	0.37	238.24	82.92	32.07	1.27	0.00011
45	2	22.5	156	10	9.24	0.39	208.42	47.06	22.68	2.40	0.00038
46	2	22.5	156	20	8.93	0.39	215.58	61.08	27.46	1.91	0.00017
47	2	22.5	156	30	8.58	0.38	224.42	77.24	33.24	1.51	0.00013
48	2	22.5	156	50	7.84	0.36	245.59	95.72	47.19	0.93	0.00012
49	1	25.5	136	10	9.89	0.42	194.79	13.65	10.51	0.44	0.000103
50	1	25.5	136	20	9.71	0.42	198.29	19.98	13.41	0.21	0.000106
51	1	25.5	136	30	9.49	0.42	203.05	25.02	15.24	0.10	0.000108
52	1	25.5	136	50	8.85	0.40	217.70	47.51	22.58	0.03	0.000112
53	2	25.5	136	10	9.75	0.42	197.53	21.49	14.60	0.44	0.000112
54	2	25.5	136	20	9.51	0.41	202.43	35.46	20.09	0.22	0.000114
55	2	25.5	136	30	9.19	0.40	209.66	50.12	25.66	0.13	0.000114
56	2	25.5	136	50	8.10	0.37	237.64	114.20	53.36	0.05	0.000114

57	1	25.5	146	10	9.59	0.41	200.83	24.59	15.22	0.74	0.000108
58	1	25.5	146	20	9.40	0.41	204.88	34.34	18.55	0.37	0.000107
59	1	25.5	146	30	9.16	0.40	210.16	42.67	21.40	0.20	0.000108
60	1	25.5	146	50	8.37	0.38	230.13	86.89	35.29	0.07	0.000112
61	2	25.5	146	10	9.44	0.40	204.03	37.67	20.19	0.96	0.000114
62	2	25.5	146	20	9.18	0.40	209.72	55.12	26.65	0.50	0.000110
63	2	25.5	146	30	8.71	0.38	221.14	91.08	38.87	0.32	0.000110
64	2	25.5	146	50	7.72	0.35	249.58	130.62	68.40	0.12	0.000103
65	1	25.5	156	10	9.27	0.40	207.75	34.50	18.79	2.12	0.00021
66	1	25.5	156	20	9.10	0.39	211.59	45.70	22.37	1.42	0.00011
67	1	25.5	156	30	8.82	0.39	218.39	58.41	26.20	0.96	0.00011
68	1	25.5	156	50	8.01	0.36	240.39	104.47	40.81	0.43	0.00011
69	2	25.5	156	10	9.21	0.39	209.21	41.83	20.87	2.12	0.00017
70	2	25.5	156	20	9.00	0.39	213.88	55.74	26.47	1.28	0.00012
71	2	25.5	156	30	8.64	0.38	222.79	77.79	34.48	0.85	0.00012
72	2	25.5	156	50	8.00	0.36	240.60	97.58	47.42	0.33	0.00012

Appendix E

Table 1E. Sample Results form Ansys Forte Simulation

Crank Angle	Pressure (MPa)	Temperature (K)	Chemical heat release rate (J/deg)	Accumulated chemical heat release (J)	Accumulated wall heat transfer (J)	Apparent heat release rate (J/deg)
-100	3.75E-01	4.22E+02	0.00E+00	0.00E+00	-6.74E+00	3.20E-02
-99	3.81E-01	4.23E+02	0.00E+00	0.00E+00	-6.77E+00	2.90E-02
-98	3.87E-01	4.25E+02	0.00E+00	0.00E+00	-6.80E+00	2.58E-02
-97	3.93E-01	4.27E+02	0.00E+00	0.00E+00	-6.82E+00	2.23E-02
-96	4.00E-01	4.29E+02	0.00E+00	0.00E+00	-6.84E+00	1.88E-02
-95	4.07E-01	4.31E+02	0.00E+00	0.00E+00	-6.86E+00	1.55E-02
-94	4.14E-01	4.33E+02	0.00E+00	0.00E+00	-6.87E+00	1.19E-02
-93	4.21E-01	4.35E+02	0.00E+00	0.00E+00	-6.88E+00	7.96E-03
-92	4.28E-01	4.38E+02	0.00E+00	0.00E+00	-6.88E+00	3.86E-03
-91	4.36E-01	4.40E+02	0.00E+00	0.00E+00	-6.88E+00	-1.78E-04
-90	4.44E-01	4.42E+02	0.00E+00	0.00E+00	-6.88E+00	-4.29E-03
-89	4.52E-01	4.44E+02	0.00E+00	0.00E+00	-6.87E+00	-8.65E-03
-88	4.61E-01	4.47E+02	0.00E+00	0.00E+00	-6.85E+00	-1.33E-02
-87	4.70E-01	4.49E+02	0.00E+00	0.00E+00	-6.84E+00	-1.82E-02
-86	4.79E-01	4.52E+02	0.00E+00	0.00E+00	-6.81E+00	-2.35E-02
-85	4.89E-01	4.54E+02	0.00E+00	0.00E+00	-6.78E+00	-2.90E-02
-84	4.99E-01	4.57E+02	0.00E+00	0.00E+00	-6.75E+00	-3.44E-02
-83	5.09E-01	4.59E+02	0.00E+00	0.00E+00	-6.71E+00	-4.03E-02
-82	5.20E-01	4.62E+02	0.00E+00	0.00E+00	-6.66E+00	-4.66E-02
-81	5.31E-01	4.65E+02	0.00E+00	0.00E+00	-6.61E+00	-5.30E-02
-80	5.42E-01	4.68E+02	0.00E+00	0.00E+00	-6.55E+00	-5.97E-02
-79	5.55E-01	4.70E+02	0.00E+00	0.00E+00	-6.48E+00	-6.68E-02
-78	5.67E-01	4.73E+02	0.00E+00	0.00E+00	-6.41E+00	-7.41E-02
-77	5.80E-01	4.76E+02	0.00E+00	0.00E+00	-6.33E+00	-8.18E-02
-76	5.94E-01	4.80E+02	0.00E+00	0.00E+00	-6.23E+00	-9.01E-02
-75	6.08E-01	4.83E+02	0.00E+00	0.00E+00	-6.14E+00	-9.84E-02
-74	6.23E-01	4.86E+02	0.00E+00	0.00E+00	-6.03E+00	-1.07E-01
-73	6.38E-01	4.89E+02	0.00E+00	0.00E+00	-5.91E+00	-1.17E-01
-72	6.54E-01	4.93E+02	0.00E+00	0.00E+00	-5.79E+00	-1.26E-01
-71	6.70E-01	4.96E+02	0.00E+00	0.00E+00	-5.65E+00	-1.36E-01
-70	6.88E-01	4.99E+02	0.00E+00	0.00E+00	-5.51E+00	-1.47E-01
-69	7.06E-01	5.03E+02	0.00E+00	0.00E+00	-5.35E+00	-1.58E-01
-68	7.24E-01	5.07E+02	0.00E+00	0.00E+00	-5.18E+00	-1.70E-01
-67	7.44E-01	5.10E+02	0.00E+00	0.00E+00	-4.99E+00	-1.82E-01
-66	7.64E-01	5.14E+02	0.00E+00	0.00E+00	-4.80E+00	-1.95E-01
-65	7.85E-01	5.18E+02	0.00E+00	0.00E+00	-4.59E+00	-2.08E-01
-64	8.08E-01	5.22E+02	0.00E+00	0.00E+00	-4.37E+00	-2.23E-01
-63	8.31E-01	5.26E+02	0.00E+00	0.00E+00	-4.13E+00	-2.38E-01

-62	8.54E-01	5.30E+02	0.00E+00	0.00E+00	-3.88E+00	-2.54E-01
-61	8.80E-01	5.34E+02	0.00E+00	0.00E+00	-3.61E+00	-2.70E-01
-60	9.06E-01	5.39E+02	0.00E+00	0.00E+00	-3.32E+00	-2.88E-01
-59	9.34E-01	5.43E+02	0.00E+00	0.00E+00	-3.01E+00	-3.07E-01
-58	9.63E-01	5.48E+02	0.00E+00	0.00E+00	-2.68E+00	-3.27E-01
-57	9.92E-01	5.52E+02	0.00E+00	0.00E+00	-2.34E+00	-3.47E-01
-56	1.02E+00	5.57E+02	0.00E+00	0.00E+00	-1.97E+00	-3.69E-01
-55	1.06E+00	5.62E+02	0.00E+00	0.00E+00	-1.57E+00	-3.93E-01
-54	1.09E+00	5.67E+02	0.00E+00	0.00E+00	-1.15E+00	-4.18E-01
-53	1.13E+00	5.72E+02	0.00E+00	0.00E+00	-7.21E-01	-4.44E-01
-52	1.17E+00	5.77E+02	0.00E+00	0.00E+00	-2.46E-01	-4.71E-01
-51	1.21E+00	5.82E+02	0.00E+00	0.00E+00	2.59E-01	-5.01E-01
-50	1.25E+00	5.88E+02	8.18E-16	8.24E-16	7.96E-01	-5.33E-01
-49	1.29E+00	5.93E+02	2.26E-14	2.36E-14	1.37E+00	-5.67E-01
-48	1.34E+00	5.99E+02	-1.45E-13	-1.18E-13	1.95E+00	-6.02E-01
-47	1.38E+00	6.04E+02	-4.88E-13	-6.10E-13	2.60E+00	-6.39E-01
-46	1.43E+00	6.10E+02	-7.75E-12	-8.42E-12	3.28E+00	-6.79E-01
-45	1.49E+00	6.16E+02	3.05E-12	-5.35E-12	4.01E+00	-7.21E-01
-44	1.54E+00	6.22E+02	6.91E-12	1.38E-12	4.75E+00	-7.65E-01
-43	1.60E+00	6.28E+02	-1.45E-11	-1.33E-11	5.57E+00	-8.12E-01
-42	1.66E+00	6.34E+02	-7.22E-12	-2.05E-11	6.44E+00	-8.64E-01
-41	1.72E+00	6.41E+02	-1.40E-12	-2.20E-11	7.37E+00	-9.20E-01
-40	1.79E+00	6.47E+02	-1.54E-11	-3.75E-11	8.35E+00	-9.77E-01
-39	1.86E+00	6.53E+02	-2.30E-12	-3.97E-11	9.36E+00	-1.04E+00
-38	1.93E+00	6.60E+02	1.04E-11	-2.92E-11	1.05E+01	-1.10E+00
-37	2.01E+00	6.67E+02	-2.52E-12	-3.17E-11	1.17E+01	-1.17E+00
-36	2.09E+00	6.74E+02	7.20E-13	-3.10E-11	1.29E+01	-1.25E+00
-35	2.17E+00	6.81E+02	9.03E-12	-2.22E-11	1.42E+01	-1.32E+00
-34	2.26E+00	6.88E+02	9.01E-12	-1.31E-11	1.56E+01	-1.41E+00
-33	2.35E+00	6.95E+02	-7.07E-12	-2.03E-11	1.71E+01	-1.49E+00
-32	2.44E+00	7.02E+02	-2.16E-12	-2.24E-11	1.87E+01	-1.59E+00
-31	2.54E+00	7.09E+02	1.02E-11	-1.21E-11	2.04E+01	-1.69E+00
-30	2.64E+00	7.16E+02	5.75E-12	-6.54E-12	2.22E+01	-1.79E+00
-29	2.75E+00	7.24E+02	-8.80E-12	-1.54E-11	2.41E+01	-1.90E+00
-28	2.86E+00	7.31E+02	5.58E-12	-9.79E-12	2.61E+01	-2.02E+00
-27	2.98E+00	7.39E+02	6.08E-12	-3.66E-12	2.83E+01	-2.14E+00
-26	3.10E+00	7.46E+02	-1.62E-11	-1.94E-11	3.05E+01	-2.27E+00
-25	3.22E+00	7.53E+02	-1.18E-11	-3.13E-11	3.29E+01	-2.40E+00
-24	3.35E+00	7.61E+02	-3.43E-12	-3.47E-11	3.55E+01	-2.54E+00
-23	3.48E+00	7.68E+02	-1.16E-12	-3.59E-11	3.82E+01	-2.68E+00
-22	3.62E+00	7.75E+02	5.05E-12	-3.08E-11	4.10E+01	-2.83E+00
-21	3.75E+00	7.82E+02	-7.17E-12	-3.78E-11	4.39E+01	-2.97E+00
-20	3.89E+00	7.90E+02	-6.09E-12	-4.39E-11	4.70E+01	-3.12E+00
-19	4.04E+00	7.96E+02	3.88E-12	-4.00E-11	5.03E+01	-3.26E+00
-18	4.18E+00	8.03E+02	6.23E-13	-3.94E-11	5.38E+01	-3.41E+00

-17	4.32E+00	8.10E+02	1.02E-11	-2.94E-11	5.72E+01	-3.55E+00
-16	4.47E+00	8.16E+02	-1.15E-12	-3.06E-11	6.09E+01	-3.69E+00
-15	4.61E+00	8.22E+02	4.99E-12	-2.57E-11	6.47E+01	-3.82E+00
-14	4.75E+00	8.27E+02	2.37E-04	2.39E-04	6.87E+01	-3.95E+00
-13	4.88E+00	8.31E+02	1.96E+00	1.98E+00	7.29E+01	-2.20E+00
-12	5.02E+00	8.36E+02	1.43E+01	1.63E+01	7.73E+01	9.89E+00
-11	5.16E+00	8.43E+02	2.81E+01	4.47E+01	8.18E+01	2.37E+01
-10	5.33E+00	8.53E+02	4.95E+01	9.25E+01	8.67E+01	4.44E+01
-9	5.47E+00	8.61E+02	3.00E+01	1.23E+02	9.25E+01	2.43E+01
-8	5.62E+00	8.69E+02	3.18E+01	1.55E+02	9.90E+01	2.53E+01
-7	5.75E+00	8.77E+02	2.63E+01	1.81E+02	1.06E+02	1.90E+01
-6	5.87E+00	8.83E+02	2.09E+01	2.02E+02	1.14E+02	1.29E+01
-5	5.98E+00	8.91E+02	2.83E+01	2.30E+02	1.23E+02	1.99E+01
-4	6.28E+00	9.24E+02	1.70E+02	4.02E+02	1.32E+02	1.61E+02
-3	6.94E+00	1.01E+03	4.59E+02	8.61E+02	1.44E+02	4.47E+02
-2	7.41E+00	1.07E+03	3.45E+02	1.20E+03	1.59E+02	3.29E+02
-1	7.78E+00	1.12E+03	2.66E+02	1.46E+03	1.77E+02	2.49E+02
0	8.03E+00	1.16E+03	1.96E+02	1.66E+03	1.96E+02	1.77E+02
1	8.21E+00	1.18E+03	1.54E+02	1.82E+03	2.15E+02	1.35E+02
2	8.32E+00	1.21E+03	1.29E+02	1.95E+03	2.34E+02	1.10E+02
3	8.38E+00	1.22E+03	1.02E+02	2.05E+03	2.53E+02	8.28E+01
4	8.38E+00	1.23E+03	7.64E+01	2.12E+03	2.71E+02	5.81E+01
5	8.34E+00	1.23E+03	5.62E+01	2.18E+03	2.89E+02	3.86E+01
6	8.26E+00	1.24E+03	4.37E+01	2.22E+03	3.06E+02	2.69E+01
7	8.16E+00	1.24E+03	3.36E+01	2.26E+03	3.21E+02	1.78E+01
8	8.02E+00	1.23E+03	2.52E+01	2.28E+03	3.36E+02	1.02E+01
9	7.87E+00	1.23E+03	1.90E+01	2.30E+03	3.50E+02	4.92E+00
10	7.70E+00	1.22E+03	1.49E+01	2.32E+03	3.64E+02	1.71E+00
11	7.51E+00	1.22E+03	1.12E+01	2.33E+03	3.76E+02	-1.18E+00
12	7.32E+00	1.21E+03	8.46E+00	2.34E+03	3.88E+02	-3.12E+00
13	7.12E+00	1.20E+03	6.20E+00	2.34E+03	3.98E+02	-4.63E+00
14	6.91E+00	1.19E+03	4.54E+00	2.35E+03	4.09E+02	-5.58E+00
15	6.69E+00	1.18E+03	3.42E+00	2.35E+03	4.18E+02	-6.03E+00
16	6.49E+00	1.17E+03	2.64E+00	2.35E+03	4.27E+02	-6.20E+00
17	6.27E+00	1.16E+03	2.11E+00	2.35E+03	4.35E+02	-6.17E+00
18	6.05E+00	1.15E+03	1.72E+00	2.36E+03	4.43E+02	-6.01E+00
19	5.84E+00	1.14E+03	1.43E+00	2.36E+03	4.50E+02	-5.80E+00
20	5.63E+00	1.13E+03	1.20E+00	2.36E+03	4.57E+02	-5.56E+00
21	5.43E+00	1.12E+03	1.02E+00	2.36E+03	4.63E+02	-5.31E+00
22	5.23E+00	1.11E+03	8.69E-01	2.36E+03	4.69E+02	-5.06E+00
23	5.03E+00	1.10E+03	7.43E-01	2.36E+03	4.75E+02	-4.80E+00
24	4.84E+00	1.09E+03	6.42E-01	2.36E+03	4.80E+02	-4.54E+00
25	4.66E+00	1.08E+03	5.51E-01	2.36E+03	4.85E+02	-4.30E+00
26	4.47E+00	1.07E+03	4.94E-01	2.36E+03	4.89E+02	-4.11E+00
27	4.30E+00	1.05E+03	4.15E-01	2.36E+03	4.94E+02	-3.88E+00

28	4.13E+00	1.04E+03	3.54E-01	2.36E+03	4.98E+02	-3.65E+00
29	3.97E+00	1.03E+03	3.04E-01	2.36E+03	5.01E+02	-3.45E+00
30	3.82E+00	1.02E+03	2.63E-01	2.36E+03	5.05E+02	-3.26E+00
31	3.67E+00	1.01E+03	2.28E-01	2.36E+03	5.08E+02	-3.06E+00
32	3.53E+00	1.00E+03	1.97E-01	2.36E+03	5.11E+02	-2.88E+00
33	3.39E+00	9.93E+02	1.71E-01	2.36E+03	5.14E+02	-2.70E+00
34	3.26E+00	9.83E+02	1.50E-01	2.37E+03	5.17E+02	-2.53E+00
35	3.14E+00	9.73E+02	1.31E-01	2.37E+03	5.19E+02	-2.36E+00
36	3.02E+00	9.64E+02	1.15E-01	2.37E+03	5.22E+02	-2.21E+00
37	2.90E+00	9.54E+02	1.02E-01	2.37E+03	5.24E+02	-2.06E+00
38	2.79E+00	9.45E+02	9.00E-02	2.37E+03	5.26E+02	-1.93E+00
39	2.69E+00	9.36E+02	8.02E-02	2.37E+03	5.28E+02	-1.81E+00
40	2.59E+00	9.27E+02	7.16E-02	2.37E+03	5.29E+02	-1.70E+00
41	2.50E+00	9.19E+02	6.41E-02	2.37E+03	5.31E+02	-1.60E+00
42	2.41E+00	9.10E+02	5.76E-02	2.37E+03	5.33E+02	-1.50E+00
43	2.32E+00	9.02E+02	5.26E-02	2.37E+03	5.34E+02	-1.42E+00
44	2.24E+00	8.93E+02	4.78E-02	2.37E+03	5.36E+02	-1.35E+00
45	2.16E+00	8.85E+02	4.33E-02	2.37E+03	5.37E+02	-1.26E+00
46	2.08E+00	8.77E+02	3.93E-02	2.37E+03	5.38E+02	-1.19E+00
47	2.01E+00	8.70E+02	3.58E-02	2.37E+03	5.39E+02	-1.12E+00
48	1.95E+00	8.62E+02	3.29E-02	2.37E+03	5.40E+02	-1.05E+00
49	1.88E+00	8.55E+02	3.02E-02	2.37E+03	5.41E+02	-9.91E-01
50	1.82E+00	8.47E+02	2.79E-02	2.37E+03	5.42E+02	-9.33E-01
51	1.76E+00	8.40E+02	2.58E-02	2.37E+03	5.43E+02	-8.80E-01
52	1.70E+00	8.33E+02	2.40E-02	2.37E+03	5.44E+02	-8.30E-01
53	1.65E+00	8.26E+02	2.24E-02	2.37E+03	5.45E+02	-7.84E-01
54	1.60E+00	8.20E+02	2.10E-02	2.37E+03	5.46E+02	-7.40E-01
55	1.55E+00	8.13E+02	1.97E-02	2.37E+03	5.46E+02	-7.01E-01
56	1.50E+00	8.07E+02	1.84E-02	2.37E+03	5.47E+02	-6.63E-01
57	1.45E+00	8.00E+02	1.74E-02	2.37E+03	5.48E+02	-6.28E-01
58	1.41E+00	7.94E+02	1.64E-02	2.37E+03	5.48E+02	-5.94E-01
59	1.37E+00	7.88E+02	1.55E-02	2.37E+03	5.49E+02	-5.62E-01
60	1.33E+00	7.82E+02	1.46E-02	2.37E+03	5.49E+02	-5.32E-01
61	1.29E+00	7.77E+02	1.38E-02	2.37E+03	5.50E+02	-5.05E-01
62	1.26E+00	7.71E+02	1.31E-02	2.37E+03	5.50E+02	-4.79E-01
63	1.22E+00	7.65E+02	1.24E-02	2.37E+03	5.51E+02	-4.53E-01
64	1.19E+00	7.60E+02	1.18E-02	2.37E+03	5.51E+02	-4.29E-01
65	1.16E+00	7.55E+02	1.11E-02	2.37E+03	5.52E+02	-4.06E-01
66	1.13E+00	7.49E+02	1.08E-02	2.37E+03	5.52E+02	-3.91E-01
67	1.10E+00	7.44E+02	1.02E-02	2.37E+03	5.53E+02	-3.71E-01
68	1.07E+00	7.39E+02	9.69E-03	2.37E+03	5.53E+02	-3.51E-01
69	1.04E+00	7.34E+02	9.21E-03	2.37E+03	5.53E+02	-3.32E-01
70	1.02E+00	7.30E+02	8.75E-03	2.37E+03	5.54E+02	-3.14E-01
71	9.91E-01	7.25E+02	8.33E-03	2.37E+03	5.54E+02	-2.97E-01
72	9.67E-01	7.20E+02	7.92E-03	2.37E+03	5.54E+02	-2.81E-01

73	9.44E-01	7.16E+02	7.54E-03	2.37E+03	5.54E+02	-2.66E-01
74	9.22E-01	7.12E+02	7.19E-03	2.37E+03	5.55E+02	-2.51E-01
75	9.01E-01	7.07E+02	6.85E-03	2.37E+03	5.55E+02	-2.38E-01
76	8.81E-01	7.03E+02	6.58E-03	2.37E+03	5.55E+02	-2.26E-01
77	8.61E-01	6.99E+02	6.28E-03	2.37E+03	5.55E+02	-2.14E-01
78	8.42E-01	6.95E+02	6.00E-03	2.37E+03	5.56E+02	-2.02E-01
79	8.24E-01	6.91E+02	5.74E-03	2.37E+03	5.56E+02	-1.91E-01
80	8.07E-01	6.87E+02	5.49E-03	2.37E+03	5.56E+02	-1.81E-01
81	7.90E-01	6.83E+02	5.25E-03	2.37E+03	5.56E+02	-1.71E-01
82	7.73E-01	6.80E+02	5.03E-03	2.37E+03	5.56E+02	-1.62E-01
83	7.58E-01	6.76E+02	4.84E-03	2.37E+03	5.56E+02	-1.53E-01
84	7.43E-01	6.73E+02	4.65E-03	2.37E+03	5.57E+02	-1.44E-01
85	7.28E-01	6.69E+02	4.46E-03	2.37E+03	5.57E+02	-1.36E-01
86	7.14E-01	6.66E+02	4.34E-03	2.37E+03	5.57E+02	-1.29E-01
87	7.01E-01	6.63E+02	4.19E-03	2.37E+03	5.57E+02	-1.22E-01
88	6.88E-01	6.59E+02	4.06E-03	2.37E+03	5.57E+02	-1.14E-01
89	6.76E-01	6.56E+02	3.93E-03	2.37E+03	5.57E+02	-1.07E-01
90	6.63E-01	6.53E+02	3.81E-03	2.37E+03	5.57E+02	-1.00E-01
91	6.52E-01	6.50E+02	3.68E-03	2.37E+03	5.57E+02	-9.35E-02
92	6.40E-01	6.47E+02	3.57E-03	2.37E+03	5.58E+02	-8.71E-02
93	6.30E-01	6.44E+02	3.45E-03	2.37E+03	5.58E+02	-8.10E-02
94	6.19E-01	6.41E+02	3.34E-03	2.37E+03	5.58E+02	-7.51E-02
95	6.09E-01	6.39E+02	3.23E-03	2.37E+03	5.58E+02	-6.93E-02
96	5.99E-01	6.36E+02	3.12E-03	2.37E+03	5.58E+02	-6.39E-02
97	5.90E-01	6.33E+02	3.02E-03	2.37E+03	5.58E+02	-5.91E-02
98	5.81E-01	6.31E+02	2.93E-03	2.37E+03	5.58E+02	-5.40E-02
99	5.72E-01	6.28E+02	2.83E-03	2.37E+03	5.58E+02	-4.90E-02
100	5.63E-01	6.25E+02	2.74E-03	2.37E+03	5.58E+02	-4.43E-02